THE FORMATION AND ERUPTION OF MAGNETIC FLUX ROPES IN SOLAR AND STELLAR CORONAE

Gordon Peter Samuel Gibb

A Thesis Submitted for the Degree of PhD
at the
University of St Andrews

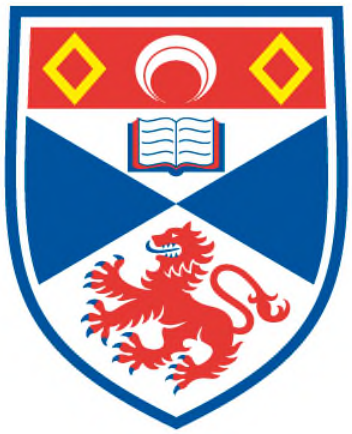

2015

The Formation and Eruption of Magnetic Flux Ropes in Solar and Stellar Coronae

Gordon Peter Samuel Gibb

University of
St Andrews

This thesis is submitted in partial fulfilment for the degree of Doctor of Philsophy at the University of St Andrews

June 26, 2015

Abstract

Flux ropes are magnetic structures commonly found in the solar corona. They are thought to play an important role in solar flares and coronal mass ejections. Understanding their formation and eruption is of paramount importance for our understanding of space weather. In this thesis the magnetofrictional method is applied to simulate the formation of flux ropes and track their evolution up to eruption both in solar and stellar coronae.

Initially, the coronal magnetic field of a solar active region is simulated using observed magnetograms to drive the coronal evolution. From the sequence of magnetograms the formation of a flux rope is simulated, and compared with coronal observations.

Secondly a procedure to produce proxy SOLIS synoptic magnetograms from SDO/HMI and SOHO/MDI magnetograms is presented. This procedure allows SOLIS-like synoptic magnetograms to be produced during times when SOLIS magnetograms are not available.

Thirdly, a series of scaling laws for the formation and life-times of flux ropes in stellar coronae are determined as a function of stellar differential rotation and surface diffusion. These scaling laws can be used to infer the response of stellar coronae to the transport of magnetic fields at their surface.

Finally, global long-term simulations of stellar corona are carried out to determine the coronal response to flux emergence and differential rotation. A bipole emergence model is developed and is used in conjunction with a surface flux transport model in order to drive the global coronal evolution. These global simulations allow the flux, energy and flux rope distributions to be studied as a function of a star's differential rotation and flux emergence rate.

Declarations

I, Gordon Gibb, hereby certify that this thesis, which is approximately 65,000 words in length, has been written by me, and that it is the record of work carried out by me, or principally by myself in collaboration with others as acknowledged, and that it has not been submitted in any previous application for a higher degree.

I was admitted as a research student in September 2011 and as a candidate for the degree of Doctor of Philsophy in September 2012; the higher study for which this is a record was carried out in the University of St Andrews between 2011 and 2015.

Date: _____ Signature of Candidate: _____.

I hereby certify that the candidate has fulfilled the conditions of the Resolution and Regulations appropriate for the degree of Doctor of Philosophy in the University of St Andrews and that the candidate is qualified to submit this thesis in application for that degree.

Date: _____ Signature of Supervisor: _____.

In submitting this thesis to the University of St Andrews I understand that I am giving permission for it to be made available for use in accordance with the regulations of the University Library for the time being in force, subject to any copyright vested in the work not being affected thereby. I also understand that the title and the abstract will be published, and that a copy of the work may be made and supplied to any bona fide library or research worker, that my thesis will be electronically accessible for personal or research use unless exempt by award of an embargo as requested below, and that the library has the right to migrate my thesis into new electronic forms as required to ensure continued access to the thesis. I have obtained any third-party copyright permissions that may be required in order to allow such access and migration, or have requested the appropriate embargo below.

The following is an agreed request by candidate and supervisor regarding the electronic publication of this thesis:

Access to printed copy but embargo of electronic publication of thesis for a period of one year on the following ground(s): publication would preclude future publication.

Date: _____ Signature of Candidate: _____.

Date: _____ Signature of Supervisor: _____.

Acknowledgements

Firstly I would like to thank my supervisor Duncan Mackay for his help throughout my PhD. Also I would like to thank Moira Jardine for her input, in addition to the other members of the solar and astronomy groups for their advice and comments. I also thank Lucie Green for supplying us with the magnetograms and X-ray images of AR10977. I am also grateful to the STFC for their financial support.

Importantly, I need to mention my friends within (and outwith) the solar group whose support kept my spirits high. Also my parents, whose moral support is much appreciated.

I should also mention my high school teachers who helped ignite my interest in mathematics and physics – in particular Mrs Mitchell, Mr Ritchie, Miss Tindall and Miss Strachan.

Publications

The following published papers include material from this thesis:

1. Gibb, G. P. S., Mackay, D. H., Green, L. M. & Meyer, K. A. (2014), 'Simulating the Formation of a Sigmoidal Flux Rope in AR10977 from SOHO/MDI Magnetograms, ApJ **782**, 71.

2. Gibb, G. P. S., Jardine, M. M. & Mackay, D. H. (2014), 'Stellar differential rotation and coronal time-scales, MNRAS **443**, 3251-3259.

"There was something comforting about having a vast hydrogen furnace burning millions of tons of material a second at the centre of a solar system. It was cheery."

– Iain M. Banks, *The Hydrogen Sonata*

Contents

Chapter 1

Introduction

1.1 The Sun

The Sun lies at the centre of the solar system, and is the closest star to the Earth. It is a large sphere of plasma (ionised gas) with a radius of 6.96×10^5 km ($1R_\odot$) and a mass of 1.99×10^{30} kg ($1M_\odot$) resulting in a mean density of 1.4×10^3 kg m^{-3} (1.4 g cm^{-3}). At its current age of approximately 4.6 billion years, it has a sidereal equatorial rotation period of 24.47 days, corresponding to a synodic equatorial rotation period of 26.24 days from the Earth. The Sun provides almost all the energy required for life on Earth. It is threaded with a complex magnetic field, which drives a wide variety of solar phenomena. These phenomena are collectively known as solar activity.

The Sun-Earth connection, mediated by the solar wind – a flow of particles away from the Sun into interplanetary space – has major effects on modern technology. During a geomagnetic storm, currents induced in power grids due to the Earth's fluctuating magnetic field can cause damage to transformers. High energy particles from coronal mass ejections (CMEs) and solar flares can cause damage to satellite electronics. In addition, radio communications can be disrupted by alterations to the ionosphere. High energy particles can heat the outer atmosphere of the Earth, causing it to expand, and hence exert a higher drag force on low-Earth orbit satellites, degrading their orbits. Increased particle flux from CMEs can also be harmful to astronauts in space. Space Weather is the term given to the changing environmental conditions in near-Earth space due to the solar wind, coronal mass ejections and flares. Understanding the sources of solar activity, and their links to space weather is therefore of paramount importance to humanity in the modern age.

1.1.1 Solar Structure

In this section, the structure of the Sun will be described. Figure 1.1 displays a graphic outlining the solar structure.

Core

The core of the Sun extends outwards to about 0.2–0.25$R_\odot$. The maximum core temperature is about 16MK and has a peak density of 150 g cm^{-3}. The high temperatures and densities allow nuclear fusion to occur here, converting hydrogen into helium mostly via the proton-proton chain. This nuclear fusion is the energy source of the Sun, which produces the solar luminosity of $L_\odot = 3.85 \times 10^{26}$ W.

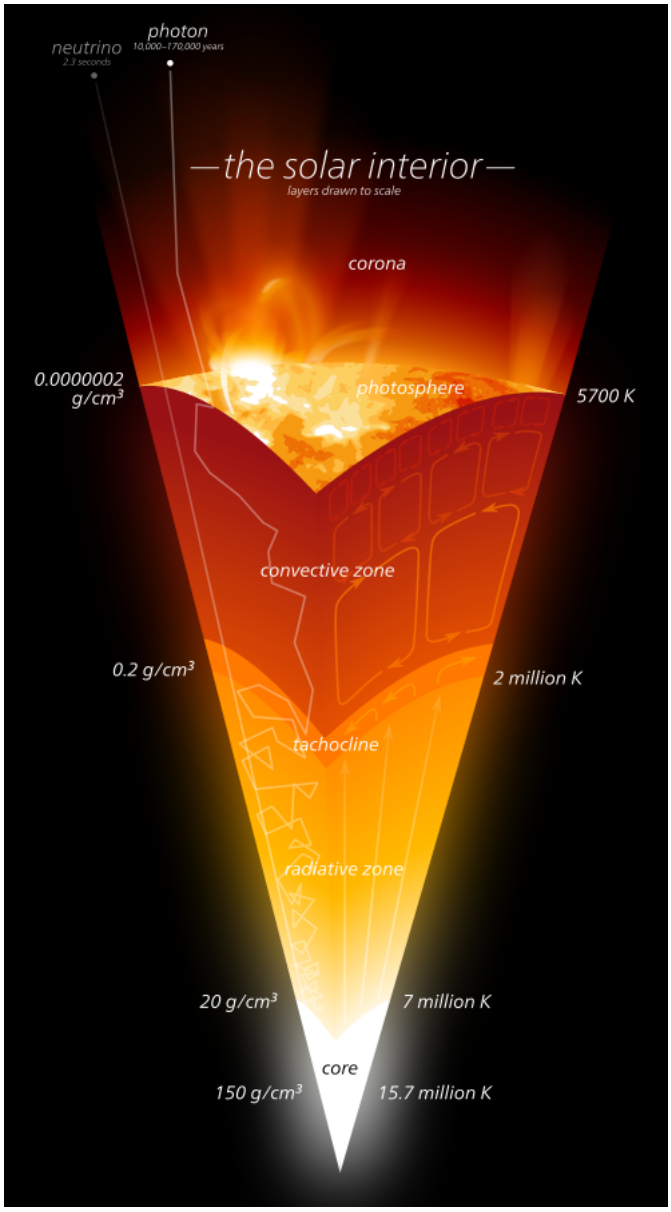

Figure 1.1: A diagram outlining the internal structure of the Sun, in addition to several of its surface features. (Image source: http://commons.wikimedia.org/wiki/File:The_solar_interior.svg)

Radiative zone

Beyond the core lies the radiative zone which extends from the outer edge of the core to about $0.7R_\odot$. Here the plasma is stable to convection, and therefore heat must be transported by radiation. The mean free path of radiation in the radiative zone is only a few millimetres and the travel time for a photon through the radiative zone is estimated to be between ten thousand and one hundred and seventy thousand years. Through the radiative zone, the temperature drops from 7MK to 2MK, and the density drops from 20 g cm^{-3} to 0.2 g cm^{-3}.

Convective zone

From $0.7R_\odot$ to the solar surface the plasma is unstable to convection, and the heat is predominantly transported outwards by convection. At the interface between the convective zone and the radiative zone lies the tachocline, an area of high radial shear in the rotational velocity of the Sun. It is believed that the tachocline is the location of the dynamo which generates the Sun's complex and ever changing magnetic fields. The temperature in the convective zone decreases from 2MK at its base to an effective temperature of 5778K at the solar surface. The convection zone density drops from 0.2 g cm^{-3} at its base to 2×10^{-7}g cm^{-3}.

Photosphere

The photosphere is the visible surface of the Sun, where photons can leave the Sun and travel outward into space. This is therefore the innermost region of the Sun that can be directly imaged. The properties of the solar interior are either inferred from mathematical models or through helioseismology, which utilises the Sun's minute oscillations to probe its inner structure. The dynamics of the photosphere are dominated by the flows of plasma, namely by granulation, differential rotation and meridional flow (see Section 1.1.5 for more detail).

The temperature of the photosphere is quoted as 5778K, which is the temperature of a black body with the same total emissive power as the Sun. Whilst this may be considered the spatial mean temperature of the photosphere, the local photospheric temperature varies. The photosphere is located at the top of the convective zone, and as such consists of the tops of convective cells, known as granules. The centre of these granules are hotter than the mean photospheric temperature as at these locations hot material from the solar interior is rising up to the surface. At the edges of the granules the material is cooler than the mean photospheric temperature, and sinks downwards into the solar interior. Granules have a typical size of 1Mm. In addition to granules, larger convective structures known as supergranules are observed. These are the fingerprints of large convective cells from within the solar interior, and have typical sizes of 14-32Mm. Faculae are bright spots on the photosphere found at the boundaries between (super)granules. They are associated with small bundles of strong (> 1 kG) magnetic fields. The top right panel of Figure 1.2 displays an image of the Sun in a wavelength where the hexagonal shapes of the supergranular boundaries are visible.

Another feature where the temperature of the photosphere deviates from the mean is a sunspot, a dark spot on the surface of the Sun. The first records of sunspot observations were over 2000 years ago. Sunspots are areas where strong magnetic fields in excess of 1.5 kG (Priest 1982) emerge from the solar interior through the photosphere. The first measurement of the magnetic field in sunspots was made over one hundred years ago by Hale (1908), who measured the magnetic field of a sunspot to be almost 3 kG. In addition

to being the first measurement of the field in a sunspot, this was also the first measurement of the Sun's magnetic field. Sunspots appear dark due to the strong magnetic fields in their centres inhibiting convection, causing the material inside them to radiatively cool to around 3700K. It is important to note that although sunspots appear dark, they are in fact still bright objects. They only appear dark relative to the surrounding photosphere because they are cooler, and therefore by the Stefan-Boltzmann law, where the luminosity of an object is proportional to its temperature to the fourth power, emit less radiation. The top left panel of Figure 1.2 displays an image of the photosphere of the Sun, where sunspots are clearly visible.

The photosphere may be easily observed by telescopes on the Earth or in space. Observations may be taken in visible light, either over a continuum to get an image of the photosphere, or at particular wavelengths to observe certain features. Observing the photosphere at wavelengths corresponding to magnetically sensitive absorption lines with a spectropolarimeter, it is possible to determine the spatial distribution of the photospheric magnetic field. Such an image is called a magnetogram, and an example of one is displayed in the top centre panel of Figure 1.2.

Chromosphere

The chromosphere is a thin (compared to the convective zone or the corona) layer (only $\sim$ 2000 km thick) of the Sun's atmosphere above the photosphere. It is known as the chromosphere because of its red colour visible during a solar eclipse. The chromospheric density is much lower than the photospheric density. Interestingly, the temperature in the chromosphere rises from around 4000 K at its inner edge to 35,000 K at its outer edge where it meets the boundary between the chromosphere and the corona, known as the transition region. The chromosphere may be observed in the Hydrogen-alpha (Hα) emission spectral line from telescopes on the Earth. Additionally, it may be observed in the Ca II H and K spectral lines, which display emission surrounding magnetic features such as the edges of supergranules and active regions.

Corona

The corona may be considered as the extended outer layer of the Sun's atmosphere. It is visible during a solar eclipse as a halo around the Sun. The corona's dynamics, in contrast to the photosphere's, are dominated by magnetic forces. Coronal plasma is typically at temperatures of 10^5 K to several times 10^7 K. It is currently not understood why the coronal temperature is orders of magnitude higher than the photospheric temperature. This is known as the coronal heating problem. Solutions to the coronal heating problem fall into two main categories; heating due to waves driven by turbulent photospheric motions (Schatzman 1949) or by magnetic reconnection (Parker 1972).

Regions of the corona may be loosely classified as open-field regions or closed-field regions. A magnetic field line passing through an open-field region will have one of its footpoints in the photosphere, and the other will extend out into interplanetary space. In contrast, a field line in a closed field region will have both of its footpoints in the photosphere. Open field regions are responsible for the solar wind, which flows out into interplanetary space along these open field lines. Coronal holes are open field regions, associated with large monopolar regions of the photospheric magnetic field. They appear as dark regions in X-ray images of the Sun's corona as the particle density in these regions is low. The low particle density results in less X-ray emission, and therefore the coronal hole appears dark. Coronal holes are known to be sources of the fast solar wind. A coronal

hole is visible in the bottom right panel of Figure 1.2 as the dark region covering the north pole of the Sun. In contrast to open field regions, closed-field regions tend to be bright in X-ray images due to hot, relatively dense plasma trapped in the magnetic field. Closed field regions are associated with bipolar and multipolar regions of the magnetic field on the photosphere. Coronal loops (corresponding to magnetic flux tubes) are a feature of the closed field corona, and examples of coronal loops are visible in the bottom centre panel of Figure 1.2.

The vast majority of observations of the solar corona must be made from space-based telescopes, as much of the coronal emission is in the ultraviolet or X-ray, which the Earth's atmosphere absorbs. Current space-born instruments that observe the corona are the Solar Dynamics Observatory (SDO), the SOlar and Heliospheric Observatory (SOHO) and Hinode. Observations from these space telescopes, and those that preceded them have shown that the solar corona is highly dynamic. Magnetic fields cannot at present be routinely measured in the corona, and instead must inferred, either through coronal seismology (e.g Nakariakov et al. (1999), Nakariakov & Ofman (2001)) or through mathematical modelling (for examples see Section 1.5 and Chapter 2).

1.1.2 Active Regions

Active regions are locations where intense magnetic fields emerge from the solar interior and into the corona. They are frequently associated with sunspots. Active regions are so named because they tend to be the sources of magnetic flares and coronal mass ejections, from which solar activity originates. They are typically located between $\pm 35^{\circ}$ latitude (Priest 1982). In X-ray and UV images of the Sun, active regions are bright due to their relatively high density, high temperature plasma. Active regions may be rather simple bipolar features, with well-defined positive and negative flux regions, or may be composed of far more complex multipolar configurations of flux. More complex active regions are more likely to have eruptions and higher energy flares (Bai 1988, Canfield et al. 1999, Benz 2008). In all the panels of Figure 1.2 active regions are visible. In the top left panel of Figure 1.2 the active regions are visible as sunspots. In the top centre panel of Figure 1.2 the active regions are visible as the black and white bipolar regions on the magnetogram. In the top left panel of Figure 1.2 the active regions are visible both as the dark sunspots and as the brighter regions surrounding the sunspots. In the bottom panels of Figure 1.2 the active regions are visible as bright emission from the corona.

Active regions go through an emergence phase, followed by a decay phase. During the emergence phase, a magnetic flux tube from the solar interior rises through the photosphere and emerges into the corona (e.g. Fan (2001)). This is observed as a strong bipolar or multipolar magnetic feature appearing over a period of hours to days in magnetogram observations. During the emergence, the absolute magnetic flux ($\int |\mathbf{B}| \cdot \mathrm{d}\mathbf{A}$) is observed to increase. Frequently, a sunspot is visible in one or both of the magnetic polarities since the magnetic field in the newly-emerged active region may be strong enough to inhibit convection (Priest 1982). In the decay phase of the active region's life, the magnetic flux decreases, due to cancellation of positive and negative polarity flux at the polarity inversion line (PIL) between two magnetic polarities. The active region also spreads out spatially due to the diffusion mechanism described in Section 1.1.5, resulting in a lower mean magnetic field.

The coronal magnetic fields of active regions can become twisted, storing vast amounts of magnetic energy. This energy is released via the process of magnetic reconnection (see Section 1.4.3). The energy release results in a solar flare – an impulsive brightening associated with intense heating of the coronal plasma, accelerated electrons and a re-

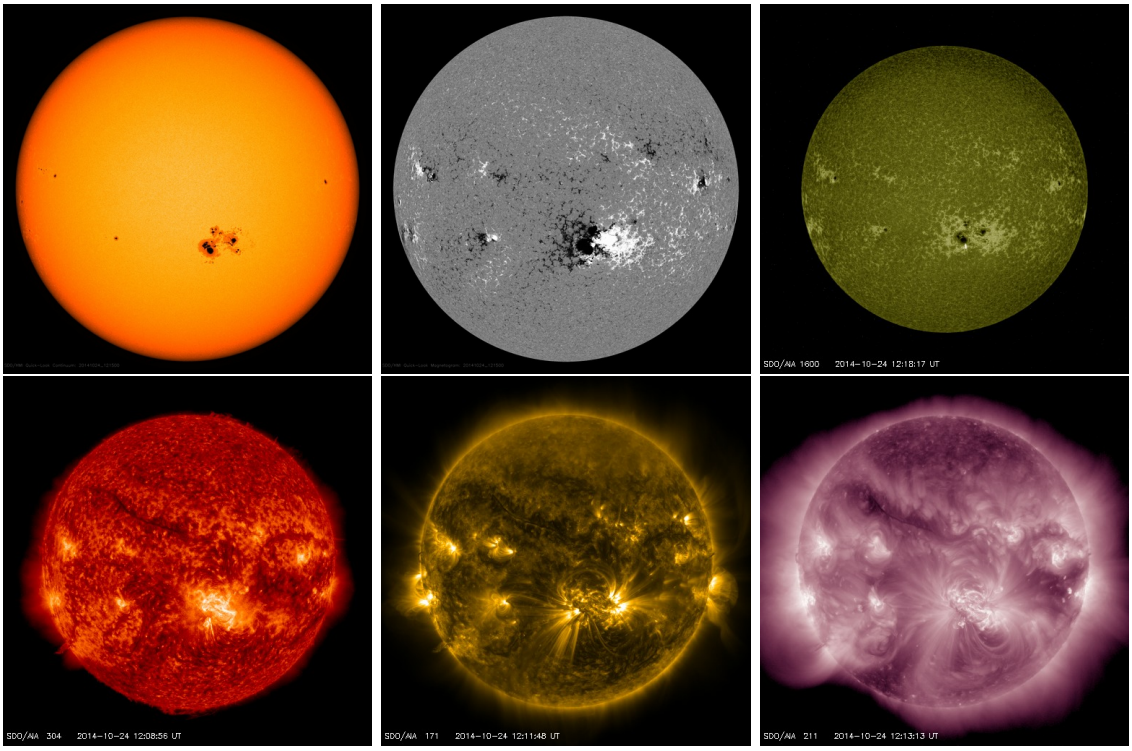

Figure 1.2: The Sun on 24/10/2014 in various wavelengths. Top left: 6173Å, giving a representation of the photosphere. Visible are dark sunspots. Top centre: A magnetogram of the Sun. This displays the magnetic field at the photosphere, where white and black denote positive and negative magnetic flux respectively. Visible are many bipolar active regions. Top right: 1600Å, corresponding to a temperature of approximately 10,000K, highlighting features in the photosphere and transition region. The hexagonal-shaped supergranular boundaries are visible. Bottom left: 304Å, corresponding to a temperature of around 50,000K. This highlights features in the chromosphere and upper transition region. Visible in this image is a prominence/filament, which appears dark as it is absorbing emission from underneath it. Bottom centre: 171Å, corresponding to a temperature of around 600,000K. This wavelength probes the cool corona. Visible in this image are coronal loops. Bottom right: 211Å, corresponding to around 2,000,000K. This image displays the hot corona. Visible are the bright closed-field regions such as the active regions, and dark regions corresponding to the open-field coronal holes. Images are from SDO/HMI and SDO/AIA and were downloaded from http://sdo.gsfc.nasa.gov.

organisation of the magnetic field. Flares are also sometimes associated with coronal mass ejections (CMEs), where material is ejected into space.

Some active regions display S- or inverted S-shaped X-ray emission features. These features are called sigmoids (Rust & Kumar 1996), and active regions that host sigmoids are statistically more likely to be the sources of eruptions than active regions without sigmoids (Canfield et al. 1999, Glover et al. 2000). Rust & Kumar (1996) found that sigmoids tended to be inverse S-shaped in the northern hemisphere, and S-shaped in the southern hemisphere. Sigmoids are further discussed in Section 1.8.

1.1.3 Solar Prominences

Prominences (also known as filaments) have been known about for over a century. During a solar eclipse, prominences are observed as bright features protruding from the solar limb. When the Sun is observed in Hα, dark filaments are observed on the disk. Filaments and prominences are in fact the same object, just viewed in different projections. In this thesis, the terms 'prominence' and 'filament' will be used interchangeably. In Figure 1.2 a filament is visible as a dark linear feature in the top left quadrant of the solar disk in the bottom left and centre images.

Prominences are found along polarity inversion lines, which separate regions of different magnetic polarity. They are long thin structures of cool dense plasma suspended above the photosphere by magnetic fields. Prominences found within active regions are known as active region prominences. These short, unstable prominences are associated with solar flares, and tend to be short-lived, with lifetimes of less than two days (Tandberg-Hanssen 1995, Lites et al. 1995, Lites & Low 1997, Mackay et al. 2010). Quiescent prominences are found at the boundaries between active regions, or within decaying active regions. Unlike active region prominences, quiescent prominences are long-lived structures, and can be observed over several solar rotations. Prominences of both types may become unstable and erupt to produce CMEs. Prominences are typically located at heights of at most 100Mm (Priest 1982, Tandberg-Hanssen 1995, Mackay et al. 2010).

In order for the cool dense prominence plasma to be supported against gravity, it must be contained within dips of the magnetic field. As such, the downwards weight of the plasma may be balanced by the upwards magnetic tension force of the magnetic field (Kippenhahn & Schlüter 1957). Flux ropes – twisted flux tubes – have been proposed as magnetic structures that can support prominence plasma, as they contain dips in the magnetic field lines (Kuperus & Raadu 1974, Pneuman 1983, Priest et al. 1989, van Ballegooijen & Martens 1989, Rust & Kumar 1994, Aulanier & Demoulin 1998, Gibson & Fan 2006), see Section 1.8. van Ballegooijen & Martens (1989) proposed that a sheared arcade may be transformed into a flux rope due to flux cancellation (see DeVore & Antiochos (2000) for an alternate formation mechanism). For quiescent prominences, one of the sources of shear in the corona is likely to be due to the Sun's differential rotation (van Ballegooijen et al. 2000, Mackay & van Ballegooijen 2006), see Section 1.1.5. Additional sources of shear may be from the emergence of sheared field (Pevtsov et al. 1995, Leka et al. 1996), the evolution of the large scale properties of active regions (Mackay et al. 2011) or from small scale vortical motions (Antiochos 2013, Mackay et al. 2014).

There are three main mechanisms by which prominences may become mass loaded. Plasma may be injected into the coronal loops by reconnection at their footpoints forcing cool plasma up into the prominence (Wang 1999, Chae 2001). Alternatively, cool plasma from the photosphere may be lifted into the corona with the rising magnetic fields during the formation of a flux rope (Deng et al. 2000, van Ballegooijen & Martens 1989). The plasma may also accumulate in the dips of the magnetic field by an evaporation-

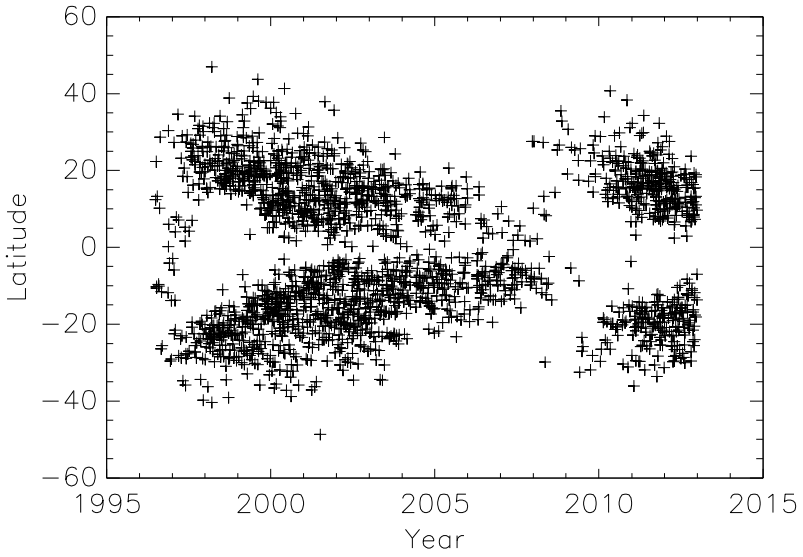

Figure 1.3: A butterfly diagram of the sunspots on the Sun between January 1996 and January 2013. Note that the pattern follows approximately an eleven year cycle. *Data supplied by A. R. Yeates.*

condensation mechanism. In this scenario, heating at the footpoints of coronal loops causes chromospheric material to be evaporated into the loop and heated to coronal temperatures. If the loop is sufficiently long this plasma may then condense at the centre of the loop (Serio et al. 1981, Mok et al. 1990, Antiochos & Klimchuk 1991, Dahlburg et al. 1998) and cool down to chromospheric temperatures (Hood & Anzer 1988).

1.1.4 The Solar Cycle

The latitudinal distribution of sunspots on the Sun as a function of time follows an approximate eleven year cycle. The cycle has a mean period of 10.92 years, with a standard deviation of 1.16 years (Hathaway et al. 2002). At the beginning of the cycle, sunspots are located at high latitudes (±20-25°) and as the cycle progresses the sunspots migrate towards the equator. A scatterplot of the sunspot latitudes with time displays a butterfly shape, and such diagrams are called butterfly diagrams (Maunder (1904) – for an example of one, see Figure 1.3). The solar cycle was first discovered by Schwabe (1844) who noticed that the number of sunspots on the Sun increased and decreased with a period of about 10 years. Hale et al. (1919) used measurements of sunspots over more than one cycle and concluded that "the preceding and following spots of binary groups, with few exceptions, are of opposite polarity, and that the corresponding spots of such groups in the Northern and Southern hemispheres are also of opposite sign. Furthermore, the spots of the present cycle are opposite in polarity to those of the last cycle." To summarise, Hale et al. (1919) found that the magnetic polarity of the leading sunspot in a sunspot pair in a given hemisphere switched polarity from cycle to cycle. It was also found that the polarity of the Sun's polar field swapped from cycle to cycle. It is therefore better to think of the Sun's magnetic cycle to be 22 years, as two 11 year activity cycles are needed to return the Sun's polar field to its original configuration.

1.1.5 Surface flows

As stated above, the photosphere's dynamics are dominated by plasma flows. Since the corona is coupled to the photosphere through magnetic fields, the photospheric flows contribute to the evolution of the coronal magnetic field. In this section several coherent surface flows, which exist over long periods of time, and their effects will be outlined.

Differential Rotation

As the Sun is composed of a fluid, it need not necessarily rotate as a solid body. Indeed, observations show that the Sun exhibits differential rotation, where the equator rotates more quickly than the poles. The rotation is also a function of radius. This differential rotation is thought to arise from the interaction between the Sun's rotation and its convection. Snodgrass (1983) determined that the surface rotation profile best be described by the following relation:

$$\Omega(\theta) = 14.71 - 2.30\cos^2\theta - 1.62\cos^4\theta \text{ deg day}^{-1}, \tag{1.1}$$

where Ω is the sidereal angular velocity of rotation and θ is the polar angle (also known as the co-latitude). An important timescale of differential rotation is the equator-pole lap time, defined as the time required for the equator to have rotated 2π further than the pole. For the above rotation profile, the lap time is

$$\tau_{\text{Lap}} = \frac{360^\circ}{\Omega(90^\circ) - \Omega(0^\circ)} = 91.8 \text{ days}. \tag{1.2}$$

Although the Sun's equatorial rotation period is 24.47 days, a rotation period that is commonly quoted is the Carrington rotation period. The sidereal Carrington rotation period is 25.37 days, and the synodic period is 27.2753 days. This corresponds to a latitude of approximately 26°. This is a useful latitude to define the solar rotation by, as it roughly corresponds to the latitude bands where the active regions are on the Sun.

Meridional Flow

The meridional flow is a slow polewards flow at the photosphere along lines of constant longitude. Its peak velocity is found to be around 10-20 m s^{-1} (DeVore et al. 1985). In this thesis, the peak velocity is taken to be $v_m = 15$ m s^{-1}. The timescale to transport a feature from the equator to the pole is

$$\tau_{\text{Merid}} = \frac{\pi}{2}\frac{R_\odot}{v_m} = 2.3 \text{ years}. \tag{1.3}$$

Due to the meridional flow at the surface, within the Sun there must be a return flow from the poles to the equator in order for mass to be conserved. The meridional flow is thought to play an important role in the solar cycle, as it transports the magnetic flux from active regions towards the pole, helping aid the reversal of the polar field (Babcock 1961).

Granulation

As mentioned before, the top of the convection zone manifests in the photosphere as convective cells known as granules, and larger scale convection patterns known as supergranules. The flows in the constantly changing (super)granular flows can be considered as randomly jostling small scale features about on the solar surface. If a small bundle

of magnetic flux is considered, its motion in these flows may be considered as a random walk. For an ensemble of such small bundles, the collective random walks may be regarded as a diffusion of the mean field (Leighton 1964). As such, the large-scale effects of (super)granulation on the large scale magnetic field may be characterised by a surface diffusion equation of the form:

$$\frac{\partial B_r}{\partial t} = D\nabla^2 B_r, \tag{1.4}$$

where B_r is the magnetic field normal to the solar surface, and the diffusion constant, D, lies in the range of approximately 200-600 km^2 s^{-1} (DeVore et al. 1985, Wang et al. 1989, 2002). In this thesis, we take the solar surface diffusion constant to be 450 km^2 s^{-1}, in line with the work of Yeates et al. (2007). The timescale for surface diffusion can be expressed by

$$\tau_{\text{Diff}} = \frac{L^2}{D}, \tag{1.5}$$

where L is the length scale over which the diffusion acts. The global diffusion time ($L = R_\odot$) is 34 years, however this timescale is shorter for small-scale objects.

1.2 Stars

The Sun is but one of approximately 10^{11} stars within the Galaxy. The Hertzsprung Russell (HR) diagram (Figure 1.4) provides a method to classify stars. It is a scatter plot of stars' luminosities against their effective temperatures. It shows several distinct populations of stars, namely the white dwarfs, the main sequence, subgiants, giants, bright giants and supergiants. Each of these populations (excluding the white dwarfs) is assigned a roman numeral ranging from I to V. This is called the luminosity class. Stars are also classified according to their colour. From blue (hottest) to red (coolest) the spectral classifications are O, B, A, F, G, K and M. Each spectral classification is split into 10 subclasses, numbered 0–9, with 0 referring to the hottest star in that spectral class, and 9 being the coolest. A nomenclature which is frequently used is to use the adjectives 'early' and 'late' to describe hotter and cooler stars respectively. The full classification of a star is a combination of the spectral class and the luminosity class. For example, the Sun's classification is G2V, meaning that it is a relatively hot G-class main sequence star.

1.2.1 The Main Sequence

The majority of stars inhabit the main sequence, a band which spans the HR diagram from the bottom right to the top left. Stars on the main sequence are burning hydrogen into helium in their cores via thermonuclear fusion. On the main sequence, hotter stars are more luminous, and contain higher mass. The hottest main sequence stars can have mass in excess of $100M_\odot$, beyond which the radiation pressure blows the star apart, whilst the coolest of M stars have a mass of $0.08M_\odot$, below which the star is not massive enough to sustain the burning of hydrogen into helium.

Along the main sequence the internal structure of stars varies. Figure 1.5 outlines the internal structure of stars of various masses. In contrast to the Sun, which has a radiative core with a convective outer envelope, stars below a mass of around $0.35M_\odot$ (Baraffe et al. 1998) are fully convective. Stars with masses between $0.35M_\odot$ and $1.5M_\odot$, like the Sun, have radiative cores and convective envelopes, with the depth of the convective envelope decreasing with increasing stellar mass. Stars with masses above $1.5M_\odot$ have convective cores, but radiative outer envelopes.

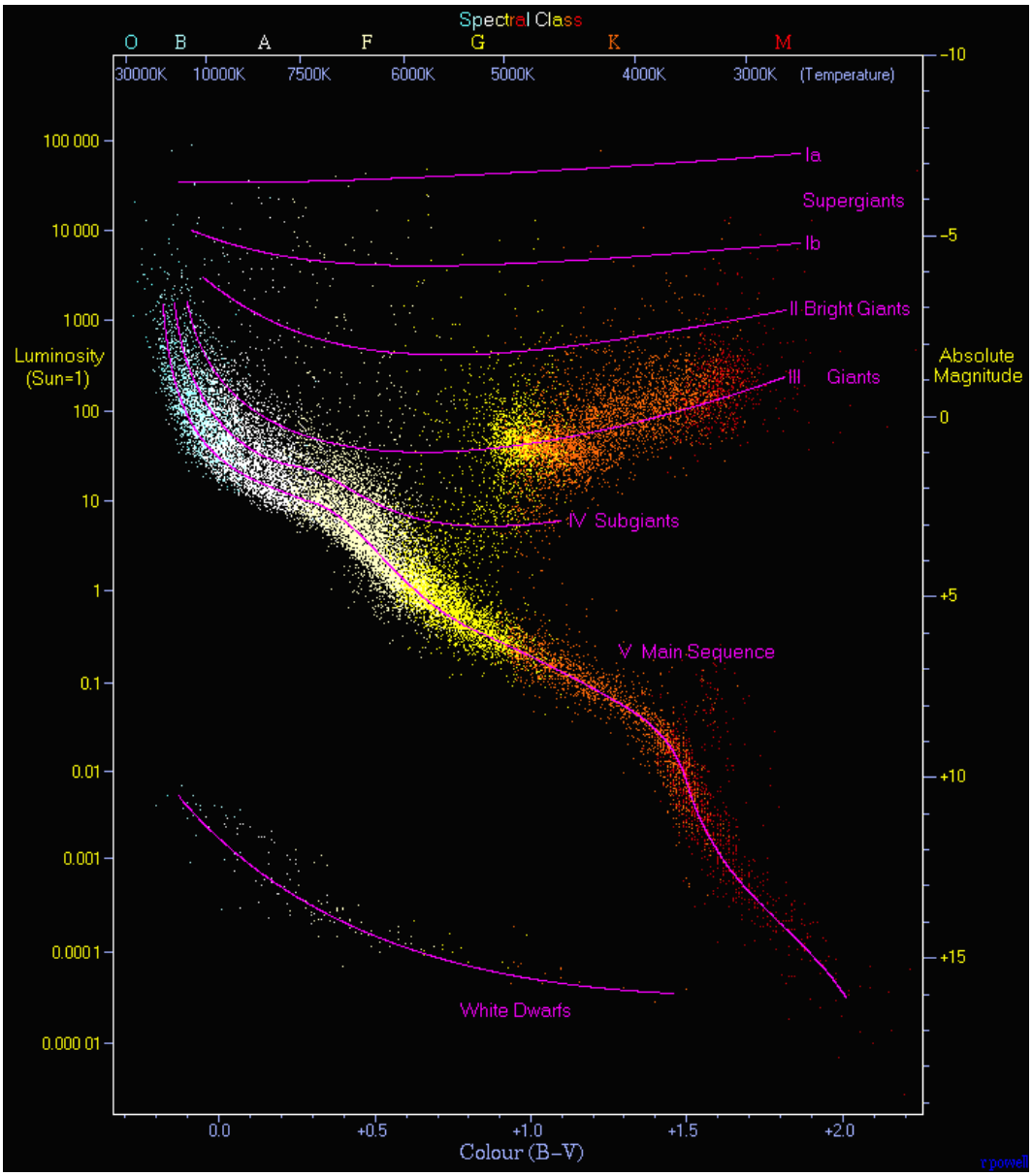

Figure 1.4: The Hertzsprung Russell Diagram, a scatter plot of stars' effective temperatures against their luminosities. The diagram highlights the distinct popultions of stars, the most prominent and populous being the main sequence. (Image source: http://www.atlasoftheuniverse.com/hr.html).

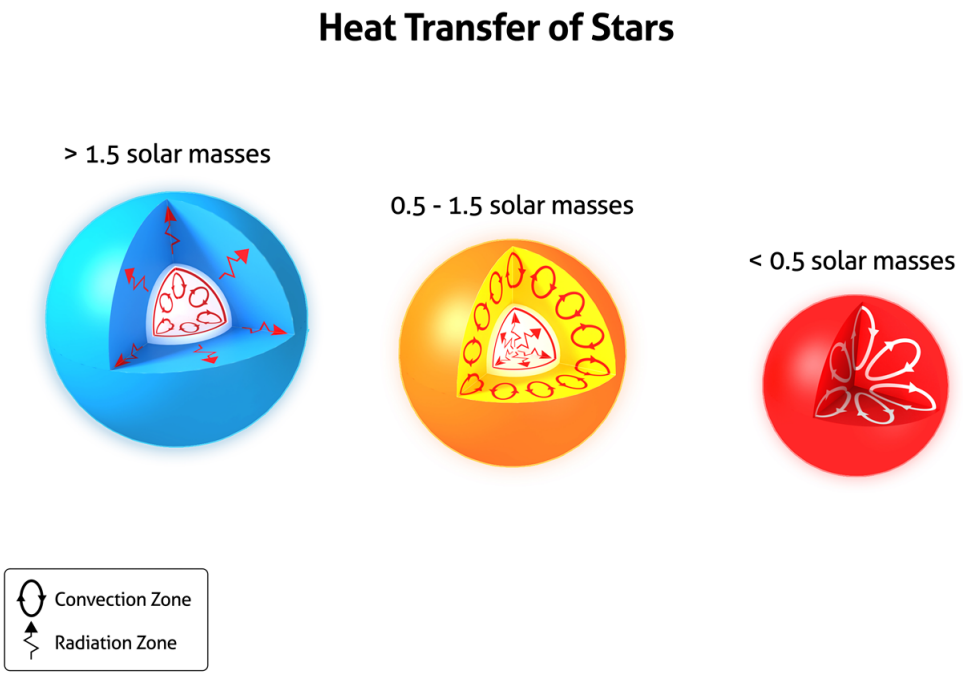

Figure 1.5: The internal structure of stars of different masses. High mass stars have convective cores and radiative envelopes. Intermediate mass stars have radiative cores and convective outer envelopes, whilst low mass stars are fully convective. (Image source: http://www.sun.org/encyclopedia/stars).

As mentioned in Section 1.1.1, the Sun's magnetic field is thought to be generated at the tachocline, the interface between the convective zone and the radiative zone. The fully convective stars with masses below $0.35M_{\odot}$ do not have tachoclines due to the absence of a radiative core, and thus any magnetic field they possess must be generated by a different mechanism. Similarly, high mass ($M > 1.5M_{\odot}$) stars, which have convective cores and radiative envelopes must generate their magnetic fields in different ways from the Sun. In this thesis only intermediate mass stars ($0.35M_{\odot} \leq M \leq 1.5M_{\odot}$) are considered as the generation of their magnetic fields is likely due to a solar-like process. These stars approximately cover the spectral class range F-K.

1.2.2 Magnetic Fields in Solar-Like Stars

Since the Sun is known to have a magnetic field, it is reasonable to expect that solar-like stars have similar magnetic fields. Indirect evidence of solar-like stars' magnetic fields include X-ray emission from hot coronae (e.g. Feigelson & Montmerle (1999), Favata & Micela (2003)) and emission from chromospheric activity-sensitive lines such as Ca II H and K. Additionally, star spots, the stellar analogues to sunspots have been determined to be present on stellar surfaces, both through the use of topographical techniques such as Doppler imaging (see below) and through exoplanet transit lightcurves (Pont et al. 2007, Rabus et al. 2009). Wilson (1978) found long term cyclical variations in the Ca II H and K emission from a number of main sequence solar-like stars. These variations were concluded to be analogous of the solar magnetic cycle, implying that these stars

also hosted magnetic cycles. Indeed, Donati et al. (2008) and Fares et al. (2009) claim to have observed the visible pole of the star τ Boötis undergo a polarity reversal, which they interpret as evidence that it has a magnetic cycle.

Zeeman Broadening

The first direct measurements of the magnetic fields of solar-like stars was by Robinson et al. (1980). On two stars they found magnetic fields of around 2 kG by measuring the Zeeman splitting of magnetically sensitive spectral lines using high resolution spectrometry. This method, called Zeeman broadening (ZB), which uses unpolarised light, can measure the strength of the magnetic field on stars and approximate the area of their surface covered by the strong magnetic field, however cannot obtain any information on the spatial distribution of the field.

Doppler Imaging

Doppler imaging (DI) techniques may been used to determine the spatial location of spots on stellar surfaces. A star's spectral lines are broadened due to the stellar rotation, which produces a Doppler shift in the emitted light, whereby one half of the star's visible hemisphere is moving towards the observer producing a blueshift, and the other half of the visible hemisphere is moving away from the observer producing a redshift. A dark spot on the star's surface will produce a notch in the spectral line due to the reduction in light being emitted from that region of the star. As the stellar rotation moves this spot towards and then away from the observer, the notch moves through the spectral line from the blueshifted side to the redshifted side. An ensemble of starspots on the surface of the star will produce an ensemble of notches in the spectral line that continuously move through it as the star rotates. Using tomographical techniques, the surface brightness profile of the star may be obtained. Vogt & Penrod (1983) first presented Doppler images which showed a dark polar spot on a star. Since then, many stars have had their spot distributions mapped, and results have shown that stars exhibit both high latitude polar spots and lower latitude spots (Strassmeier 1996, Korhonen et al. 2001, Strassmeier 2002, Berdyugina 2005). These stellar spots are interpreted to be analagus to solar sunspots. Namely, they are assumed to be due to strong magnetic fields inhibiting convection.

Zeeman Doppler Imaging

Zeeman Doppler Imaging (ZDI) is an extension to DI which takes advantage of the polarisation properties of Zeeman splitting to determine the magnetic topology of stars (Semel 1989, Brown et al. 1991, Donati & Brown 1997). This technique allows the radial, azimuthal and meridional components of the magnetic field to be measured across the whole visible surface of the star (Donati et al. 2000, 2008, Marsden et al. 2006, 2011, Waite et al. 2011). It is important to note that ZDI can only measure the large-scale magnetic toplolgy of a star as the polarisation signals from small-scale bipolar regions such as active regions cancel out. Although ZDI misses the small magnetic features, a study by Lang et al. (2014) found that any small-scale field present on a star will have a minimal effect on the large-scale topology of the magnetic field as derived by ZDI.

From ZDI maps of a star's magnetic field, the coronal magnetic field may be extrapolated. The extrapolations typically use the 'potential field source surface' method (Altschuler & Newkirk 1969), which assumes that the coronal magnetic field is current-free (Jardine et al. 2002, Donati et al. 2007, Marsden et al. 2011). Potential extrapolations

may provide a snapshot of the star's global magnetic field, but give no information on the time evolution of the coronal field. ZDI maps for a single star may be obtained at several different epochs, and used to obtain a series of coronal magnetic fields (Donati et al. 2008, Fares et al. 2009). It is important to note that these coronal magnetic field extrapolations are produced independently of each other at different times, and cannot represent a continuous time evolution of the coronal field.

Effects of Mass and Rotation on Stellar Magnetism

It has long been known that the rotation periods of stars decrease with age (Skumanich 1972). This is because the magnetised stellar winds carry away angular momentum, causing the star to spin down (Weber & Davis 1967). The stellar dynamo, which generates the stellar magnetic fields, is more efficient with faster stellar rotation and as a consequence produces stronger magnetic fields (Parker 1955) and therefore more active stars. As a result, as the star ages, its decreasing rotation decreases the strength of its magnetic field and activity (Skumanich 1972, Ayres 1997, Güdel 2007, Gondoin et al. 2012, Reiners 2012). This magnetic activity-rotation breaks down for fast rotating stars, whereby the activity becomes independent of rotation (Vilhu 1984). This is thought to be due to the dynamo becoming saturated and unable to generate stronger magnetic fields as the rotation increases. A possible cause of the dynamo saturation is the stellar surface becoming completely filled with active regions. Stellar activity is found to correlate better with the Rossby number (Ro) – the ratio of the stellar rotation period to the convective turnover time – than the stellar rotation (Noyes et al. 1984, Vilhu 1984).

A recent study by Vidotto et al. (2014) has used ZDI measurements of 104 stars to characterise the dependence of the mean large-scale stellar magnetic fields on the Rossby number, rotation period and stellar age. They found that the mean magnetic field ($\langle B \rangle$) was proportional to the Rossby number as $\langle B \rangle \propto Ro^{-1.4}$, the rotation period as $\langle B \rangle \propto P^{-1.3}$ and to the stellar age as $\langle B \rangle \propto t^{-0.66}$. They also found that the surface flux scaled with the Rossby number as $\Phi \propto Ro^{-1.19}$, and the X-ray luminosity scaled with the flux as $L_x \propto \Phi^{1.8}$. The above findings state that as a star ages and spins down (Rossby number increases) its mean magnetic field, flux and X-ray luminosity decreases. Similarly, as the stellar mass decreases (Rossby number decreases) the star has a higher mean surface field, flux and X-ray luminosity.

A number of stars with different masses and rotation periods have had their magnetic topologies mapped by ZDI. With this information, it is possible to begin to understand how the mass of a star and its rotation/Rossby number affects the star's magnetic topology. Such a study was carried out by Donati et al. (2009), who found the following trends: The mean field strengths of stars decrease from around 1.5 kG for low mass ($M < 0.5 M_{\odot}$) stars to around 3 G for solar mass stars. This trend may be explained by the convective turnover times increasing with decreasing stellar mass, resulting in smaller Rossby numbers and hence stronger magnetic fields. Stars with Rossby numbers of around 10^{-2} have large-scale axisymmetric poloidal magnetic topologies. As the Rossby number increases to around 10^{-1} the stellar large-scale magnetic topologies become mostly toroidal with non-axisymmetric poloidal components. For stars with Rossby numbers of approximately 1 the large-scale magnetic fields are axisymmetric and poloidal. For a detailed review of stellar magnetism, please refer to Donati & Landstreet (2009).

1.2.3 Stellar Differential Rotation

Like the Sun, it is assumed that stars can possess differential rotation. Stellar differential rotation may be estimated in a number of ways. The variation in the stellar rotation period as determined by the rotational modulation of Ca II H and K emission may be used to estimate the differential rotation (Donahue et al. 1996). A similar approach uses the rotational modulation of X-ray emission from stars. In a more sophisticated manner, the numerical techniques that facilitate the reconstruction of spot features in DI and the magnetic features in ZDI incorporate differential rotation into their models. Therefore, using DI and ZDI the differential rotation of a star may be measured (Donati & Collier Cameron 1997, Petit et al. 2002). It may even be possible to use photometry from the Kepler spacecraft to measure differential rotation (Reinhold et al. 2013), however the results of a study carried out by Aigrain et al. (2015) suggests that this may be very inaccurate.

Stellar differential rotation profiles are modelled in a similar manner to the Sun's (Equation 1.1), however only include the $\cos^2\theta$ dependence as there is insufficient information to constrain the $\cos^4\theta$ present in the solar differential rotation profile. Stellar differential rotation profiles are of the form

$$\Omega(\theta) = \Omega_0 - d\Omega \cos^2\theta. \tag{1.6}$$

The differential rotation equator-pole lap time is defined as

$$\tau_{\text{Lap}} = \frac{2\pi}{d\Omega}. \tag{1.7}$$

The differential rotation profiles for a number of stars have been measured using ZDI or DI (e.g Donati et al. (2000), Marsden et al. (2006), Donati et al. (2008), Marsden et al. (2011), Waite et al. (2011)). Stars have been found with differential rotation rates of up to around 10 times the solar amount (lap times of one-tenth of the solar lap time). Using a sample of stars with measured differential rotation, Barnes et al. (2005) found that the lap times decrease ($d\Omega$ increases) with increasing effective temperature of the star, with early-G and F type stars having shorter lap times than that of the Sun. They found a scaling between the differential rotation and effective temperature of

$$d\Omega \propto T_{\text{eff}}^{8.92}, \tag{1.8}$$

valid in the temperature range of $3500K \leq T_{\text{eff}} \leq 6000K$. Using a larger sample of stars covering the temperature range $3000K \leq T_{\text{eff}} \leq 7000K$, Collier Cameron (2007) found a slightly shallower temperature dependence, namely

$$d\Omega = 3.03\left(\frac{T_{\text{eff}}}{5130\ \text{K}}\right)^{8.6}\ \text{deg day}^{-1}. \tag{1.9}$$

Using numerical modelling of stellar interiors, Küker & Rüdiger (2011) instead find a broken power law of the form

$$d\Omega = \begin{cases} 4.06\left(\frac{T_{\text{eff}}}{5500\ \text{K}}\right)^{2}\ \text{deg day}^{-1} & 3800\ \text{K} \leq T_{\text{eff}} \leq 5800\ \text{K} \\ 0.68\left(\frac{T_{\text{eff}}}{5500\ \text{K}}\right)^{20}\ \text{deg day}^{-1} & 6000\ \text{K} \leq T_{\text{eff}} \leq 6700\ \text{K}. \end{cases} \tag{1.10}$$

Differential rotation measurements from Kepler photometry (Reinhold et al. 2013) agree with the Küker & Rüdiger (2011) model, however as stated above the validity of Kepler

differential rotation measurements is in question. Although the above relations between differential rotation and stellar effective temperature are quantitatively different, it is important to note that they are qualitatively similar. Morin et al. (2008) found that M-class stars exhibit solid body rotation. The interpretation of the above findings is that differential rotation ($d\Omega$) is inversely proportional to the depth of the convection zone, such that stars with a deep convective zone have very low differential rotation, and stars with very shallow convective zones have very strong differential rotation.

Whilst there is a strong correlation between the effective temperature and differential rotation, the same is not so for the stellar rotation and differential rotation. Using the long term variation in the rotational period measured from rotational modulation due to starspots as a proxy for differential rotation, Henry et al. (1995) found a relationship between the stellar rotation and differential rotation of $d\Omega \propto \Omega^{0.24}$. Similarly, Donahue et al. (1996) used the long term variation in the rotation period measured from the rotational modulation of Ca II H and K emission line flux to infer a stellar rotation-differential rotation relationship of $d\Omega \propto \Omega^{0.7}$. It is important to note that these two studies did not measure differential rotation directly, and so their results may be subject to considerable uncertainty. Barnes et al. (2005), using differential rotation measured by DI found a relationship between stellar rotation and differential rotation of $d\Omega \propto \Omega^{0.15}$. From the above three studies, it can be concluded that the differential rotation is far more weakly dependent upon stellar rotation than it is upon stellar effective temperature.

1.3 Magnetohydrodynamics (MHD)

Magnetohydrodynamics (MHD) is a method by which electrically conducting fluids (such as a plasma) can be modelled. It is governed by eight equations, which consist of an amalgamation of Maxwell's equations and the fluid equations. The eight equations of MHD will be described below.

The first equation is the mass continuity equation,

$$\frac{\partial \rho}{\partial t} + \nabla \cdot (\rho \mathbf{v}) = 0, \tag{1.11}$$

where ρ is the mass density, t is time, and $\mathbf{v}$ is the fluid velocity. This equation states mass is conserved – that the rate of change of mass in a volume must be equal to the flux of mass through the closed surface bounding the volume.

Secondly, is the equation of motion,

$$\rho \frac{D\mathbf{v}}{Dt} = \rho \frac{\partial \mathbf{v}}{\partial t} + \rho(\mathbf{v} \cdot \nabla)\mathbf{v} = \rho \mathbf{g} - \nabla p + \mathbf{j} \times \mathbf{B} + \text{viscous terms} , \tag{1.12}$$

where the acceleration due to gravity is $\mathbf{g} = -\nabla\Phi$ (where $\nabla^2\Phi = 4\pi G\rho$), p is the gas pressure, and $\mathbf{j}$ is the electric current density. The equation of motion details the various forces on a plasma element, namely pressure gradients, gravity and the Lorenz force. The Lorentz force may be written as

$$\mathbf{j} \times \mathbf{B} = \frac{1}{\mu_0}(\mathbf{B} \cdot \nabla)\mathbf{B} - \nabla \left(\frac{B^2}{2\mu_0} \right), \tag{1.13}$$

where the Lorentz force (LHS) is split into magnetic tension (first term on RHS) and magnetic pressure (second term on RHS) components. Other forces can be included in the equation of motion as necessary, such as viscous forces and the Coriolis force.

Thirdly, the energy equation is given by,

$$\frac{\partial}{\partial t}\left(\rho e + \frac{1}{2}\rho v^2\right) + \nabla \cdot \left(\left[\rho e + \frac{1}{2}\rho v^2 + p + \rho\Phi\right]\mathbf{v}\right) = -\mathcal{L}, \tag{1.14}$$

where e is the internal energy per unit mass, given by

$$e = \frac{3}{2}\frac{k_B T}{\bar{\mu}},$$

assuming that the ratio of specific heats is 5/3, and $\mathcal{L}$ is the loss function. This states that the rate of change of energy within a volume (internal and kinetic) is equal to the flux of energy through the boundary of the volume, forces (pressure and gravity) on the boundary of the volume, and due to energy losses in the volume, as described by the loss function. The loss function is of the form

$$-\mathcal{L} = \nabla \cdot (\kappa \nabla T) - \rho^2 Q(T) + \frac{j^2}{\sigma} + \text{viscous heating}\ , \tag{1.15}$$

which includes thermal conduction (where κ is the conductivity), radiative losses (where $Q(T)$ is the radiative loss function), and Joule heating (where σ is the conductivity). If viscous terms are included within the equation of motion, a viscous loss term is required in $\mathcal{L}$.

The fourth equation is the ideal gas law,

$$p = \frac{\rho k_B T}{\bar{\mu}}, \tag{1.16}$$

where $\bar{\mu}$ is the mean mass of particles in the solar atmosphere, and k_B is the Boltzmann constant. The ideal gas law provides a link between the thermodynamic observables: temperature (T), pressure and density.

The solenoidal constraint,

$$\nabla \cdot \mathbf{B} = 0, \tag{1.17}$$

makes up the fifth equation of MHD. It states that magnetic fields are divergence-free, in other words that there are no sources of magnetic 'charge.' This allows us to express the magnetic flux density in terms of a magnetic vector potential, $\mathbf{A}$, through the relation

$$\mathbf{B} = \nabla \times \mathbf{A}. \tag{1.18}$$

The sixth equation is Ampère's law,

$$\mathbf{j} = \frac{1}{\mu_0}\nabla \times \mathbf{B}, \tag{1.19}$$

which gives the relationship between the current density and the magnetic flux density.

Faraday's law,

$$\frac{\partial \mathbf{B}}{\partial t} = -\nabla \times \mathbf{E}, \tag{1.20}$$

the penultimate equation, states that a time-changing magnetic field induces an electric field, $\mathbf{E}$.

Finally, Ohm's law,

$$\frac{\mathbf{j}}{\sigma} = \mathbf{E} + \mathbf{v} \times \mathbf{B}, \tag{1.21}$$

relates the current density to the electric field and the cross product of the plasma velocity with the magnetic flux density.

1.4 The Induction Equation

The equations of MHD can be simplified by eliminating the electric field. In order to do this, we first take the curl of Ohm's Law (Equation 1.21):

$$\begin{aligned} \nabla \times \frac{\mathbf{j}}{\sigma} &= \\ \frac{1}{\sigma}\left[\nabla \times \left(\frac{1}{\mu_0}\nabla \times B\right)\right] &= \\ \frac{1}{\mu_0 \sigma}\left(\nabla(\nabla \cdot \mathbf{B}) - \nabla^2 \mathbf{B}\right) &= \nabla \times (\mathbf{v} \times \mathbf{B}) + \nabla \times \mathbf{E}. \end{aligned}$$

Using the solenoidal constraint (Equation 1.17), Faraday's law (Equation 1.20) and rearranging we get the induction equation,

$$\frac{\partial \mathbf{B}}{\partial t} = \underbrace{\nabla \times (\mathbf{v} \times \mathbf{B})}_{\text{Advection}} + \underbrace{\eta \nabla^2 \mathbf{B}}_{\text{Diffusion}}, \tag{1.22}$$

where we have defined the diffusivity as $\eta = 1/\mu_0 \sigma$. The induction equation states that a changing magnetic field may occur either by advection, whereby the plasma velocity moves the magnetic field, or by diffusion, which reduces gradients in the magnetic field.

It is sometimes useful to express the induction equation in terms of the magnetic vector potential. In this form, the induction equation becomes

$$\frac{\partial \mathbf{A}}{\partial t} = \mathbf{v} \times \mathbf{B} - \frac{\mathbf{j}}{\sigma}. \tag{1.23}$$

1.4.1 Magnetic Reynolds Number

It is useful to consider the ratio of the advective term to the diffusive term in the induction equation. The magnetic Reynolds number is defined as the ratio of the advective to the diffusive terms. Using dimensional analysis, we obtain

$$R_m = \frac{\nabla \times (\mathbf{v} \times \mathbf{B})}{\eta \nabla^2 \mathbf{B}} \approx \frac{vB/L}{\eta B/L^2} = \frac{Lv}{\eta} = \frac{L^2}{\eta t}. \tag{1.24}$$

If $R_m \gg 1$ advection dominates the induction equation and diffusion may be neglected. Similarly, if $R_m \ll 1$ then diffusion dominates the induction equation, and advection may be neglected.

We can define the timescales involved for advective and diffusive processes as:

$$\tau_{\text{adv}} = \frac{L}{v}, \tag{1.25}$$

$$\tau_{\text{diff}} = \frac{L^2}{\eta}. \tag{1.26}$$

Thus, the magnetic Reynolds number may also be expressed as

$$R_m = \frac{\tau_{\text{diff}}}{\tau_{\text{adv}}}. \tag{1.27}$$

1.4.2 The Ideal Limit

In the corona, $\eta \approx 10^9 T^{-3/2}$ m^{2}s^{-1} (Priest 1982), and so for coronal temperatures ($T > 10^5$ K), is less than 30 m^{2}s^{-1}. The typical length scales in the corona, however, are on the order of tens to hundreds of Mm. Therefore, in the corona, generally $R_m \gg 1$ and we may neglect the diffusive term in the induction equation. Thus, for the majority of the solar corona the induction equation reduces to:

$$\frac{\partial \mathbf{B}}{\partial t} = \nabla \times (\mathbf{v} \times \mathbf{B}). \tag{1.28}$$

This is known as the ideal induction equation. In the ideal limit, the magnetic field is regarded as being 'frozen' into the plasma, whereby the magnetic field moves with the fluid, and a given plasma element is always associated with the same magnetic field line.

1.4.3 Magnetic Reconnection

Whilst it is the case that in the corona the magnetic Reynolds number is generally much greater than 1, in the case of small-scale structures such as current sheets the magnetic Reynolds number may approach or even drop below 1. In such a case, diffusion becomes important and cannot be neglected. At these locations, the magnetic field lines may change their connectivity. This process is called magnetic reconnection. Reconnection allows the magnetic field to change its topology, and is a process whereby vast amounts of energy may be released, in the form of heat, bulk plasma kinetic energy and accelerated electrons. Magnetic reconnection drives the impulsive energy release in solar flares, where the connectivity of the magnetic field changes. Reconnection also plays a role in CMEs, as by changing the connectivity of the magnetic field allowing material that was once held down by magnetic field lines to be ejected.

1.5 The Force-Free Approximation

Solving the equations of MHD is very computationally expensive. It is therefore desirable to apply some approximations in order to reduce the number of equations that must be solved. One such approximation is the 'force-free' approximation, which considers magnetic equilibria. In the force-free approximation, the inviscid equation of motion (Equation 1.12) is simplified. In an equilibrium (no net force acting on a plasma element) then the inviscid equation of motion reduces to

$$0 = \rho \mathbf{g} - \nabla p + \mathbf{j} \times \mathbf{B}$$

If the length scales being investigated are smaller than the gravitational pressure scale height, Λ where

$$\Lambda = \frac{k_b T}{\bar{\mu} g}$$

then the gravitational term can be neglected. Finally, assuming the magnetic pressure, given by

$$p_m = \frac{B^2}{2\mu_0}$$

is much greater than the plasma pressure then the equation of motion can be reduced to

$$\mathbf{j} \times \mathbf{B} = 0 \tag{1.29}$$

In the solar corona, magnetic loops are observed to remain unchanged for hours to days. They can thus be assumed to be in equilibrium. The pressure scale height (typically on the order of 100Mm in the solar corona) is larger than the length of a coronal loop, and the magnetic pressure is much greater than the plasma pressure. The force-free approximation can be thus used to model the corona.

The force-free condition, $\mathbf{j}\times\mathbf{B} = 0$, constrains the current density, as it must be parallel to the magnetic flux density. There are therefore three possible cases:

- $\mathbf{j} = 0$ - This is known as a potential field, and is the lowest energy field configuration for a given photospheric magnetic field configuration. Potential fields are unique, and reasonably easy to calculate. They are thus widely used in the solar and stellar communities to study the topology of solar and stellar magnetic fields. Potential fields are however not useful for determining the energy available for eruptions as they are the lowest energy field configurations and therefore no energy can be extracted from them to power eruptions.

- $\mathbf{j} = \alpha_0\mathbf{B}$ - This is a linear force-free (LFF) field. Here the current density is a scalar constant multiple of the magnetic flux density. LFF fields are unphysical however, as if the whole corona was described by a LFF field the magnetic energy content would be infinite (Seehafer 1978).

- $\mathbf{j} = \alpha(\mathbf{r})\mathbf{B}$ - This is a non-linear force-free (NLFF) field. Here the current density is a scalar multiple of the magnetic flux density, but this scalar quantity varies with spatial position. The solenoidal constraint (Equation 1.17) requires α to be constant along a field line, but allows it to vary across field lines. This is the most realistic force-free field. Although NLFF fields are the most realistic, they are not unique (given a specified boundary magnetic field) and are difficult to calculate. Much work has been carried out in developing methods of generating NLFF fields from magnetogram data. This can be achieved by either extrapolating the NLFF field from a single vector magnetogram directly, or by evolving an initial field – typically a potential or LFF – into a NLFF state. Examples of extrapolations are Low & Lou (1990), Wheatland et al. (2000), Liu et al. (2002), Yan & Sakurai (1997, 2000), Régnier et al. (2002). The magnetofrictional method is an example of an evolution method, and will be used extensively in this thesis. Chapter 2 will discuss the magnetofrictional method in detail.

In applying the force-free approximation, the equation of motion's dependence on the plasma pressure and density is removed. This allows us to discard the mass continuity equation, the energy equation and the ideal gas law (Equations 1.11, 1.14, 1.16). The reduced equations of MHD thus consist of the force-free equation (Equation 1.29), Ampère's law (Equation 1.19) and the induction equation (Equation 1.22). This simplified set of the MHD equations is much easier to solve than the full set of MHD equations. Although it is easier to solve, the force-free condition is only valid for magnetic equilibria, and so cannot be used to simulate non-equilibrium situations, such as eruptions of flux ropes.

1.6 Magnetic Energy

The energy contained within a magnetic field is given by:

$$U = \frac{1}{8\pi}\int B^2 dV, \tag{1.30}$$

in Gaussian units. Since the potential field is known to be the lowest energy field configuration (and hence no energy can be removed from it), a better measure of the energy of a magnetic field configuration is the free magnetic energy, given by:

$$U_f = \frac{1}{8\pi} \int \left(B^2 - B_p^2\right) dV, \tag{1.31}$$

where B_p is the potential field corresponding to the same photospheric magnetic field as the actual field. The free magnetic energy is thus an indication of the energy that is available to be converted into another form (e.g. heat, particle acceleration, radiation). An active region with a build-up of free magnetic energy is thus more likely to produce flare, as the field can release this free energy whilst relaxing to a configuration that more closely resembles a potential field.

1.7 Magnetic Helicity

Magnetic helicity is a quantity which characterises the degree of twist of a magnetic field configuration. It is defined as

$$H = \int (\mathbf{A} \cdot \mathbf{B}) dV, \tag{1.32}$$

(Berger & Field 1984). This quantity is conserved within a volume enclosed by a magnetic surface in an ideal plasma, and decays on the global diffusion time in a non-ideal plasma. Under reconnection the helicity is approximately conserved (Berger 1999). For a volume not bounded by a magnetic surface it is more convenient to define the relative helicity. This is the helicity relative to a potential reference field, $\mathbf{B}_p$ and $\mathbf{A}_p$, whose field is assumed to be identical outwith the volume. The relative helicity is defined as

$$H_r = \int (\mathbf{A} + \mathbf{A}_p) \cdot (\mathbf{B} - \mathbf{B}_p) dV, \tag{1.33}$$

and is gauge-invariant (Finn & Antonsen 1985).

Helicity can be injected into a volume through the surface. Helicity in the corona is injected via photospheric motions or through the emergence of new magnetic fields into the corona. The helicity is generally negative in the northern hemisphere of the Sun, and positive in the southern hemisphere (Berger 1999).

1.8 Flux Ropes

Flux ropes are twisted flux tubes, where the magnetic field lines are twisted round the axis like the fibres of a rope, hence its name. Flux ropes are of interest to both the solar physics and stellar astrophysics communities as they contain free magnetic energy, and thus are good candidates for the energy source that drives magnetic flares. Indeed, the standard flare model of Shibata et al. (1995) involves the eruption of a flux rope. The structure of the magnetic field in magnetic clouds in interplanetary space is consistent with flux ropes (Burlaga et al. 1981, Marubashi 1986) and their origins can be traced back to solar CMEs (Wilson & Hildner 1984). Magnetic clouds frequently cause geomagnetic storms when they impact upon the Earth (Leamon et al. 2002). Understanding the formation and eruptions of flux ropes is thus very important to understand the Sun-Earth connection.

The origin of flux ropes in the corona is now discussed. van Ballegooijen & Martens (1989) proposed a mechanism whereby a flux rope may form in-situ in the corona. In

this scenario, a sheared arcade is gradually transformed into a flux rope by shearing and converging photospheric motions driving reconnection at a polarity inversion line (PIL). Multiple reconnection events then produce the flux rope. In contrast, Rust & Kumar (1994) suggested that a flux rope produced in the convective zone may rise due to magnetic buoyancy and emerge through the photosphere into the corona. Numerous numerical studies have shown, however, that the axis of the flux rope is unable to rise through the photosphere and results in a sheared arcade in the corona (Fan 2001, Moreno-Insertis 2004, Archontis et al. 2004, Archontis 2008). Even though this is the case, a flux rope may still form from these sheared arcade field lines, either through rotation of the emerged flux, twisting the arcade into a flux rope (Magara 2006, Fan 2009, Leake et al. 2013), or through reconnection transforming the arcade into a flux rope in a manner consistent with the van Ballegooijen & Martens (1989) mechanism (Manchester et al. 2004, Archontis & Török 2008, Archontis & Hood 2010).

There are several mechanisms by which a flux rope can become unstable and erupt. The flux rope may undergo a loss of equilibrium through an ideal MHD instability (Hood & Priest 1981, Kliem & Török 2006). The flux rope could also experience a force imbalance between itself and the arcade above it, whereby the upward Lorentz force from the flux rope dominates over the downward tension force of the arcade (Mackay & van Ballegooijen 2006). Several studies (Bobra et al. 2008, Su et al. 2009, Savcheva & van Ballegooijen 2009) have shown that the force imbalance occurs when the ratio of flux rope flux to active region flux exceeds 10-14%.

Rust & Kumar (1996) proposed that sigmoids are the projections of helically kinked flux ropes along the line of sight (LOS). To appear as an S-shape in projection, they argue that the flux rope would require a twist around its axis of around 2π. They calculated that the majority of flux ropes with such a twist would be kink unstable and thus would eventually erupt. Titov & Démoulin (1999), however, suggested that sigmoids are emission from a current layer in a separatrix surface formed by bald patch field lines underneath a flux rope. The works of Canfield et al. (2007) and Green et al. (2007) favour the Titov & Démoulin (1999) sigmoid model over the Rust & Kumar (1996) model.

1.9 Thesis Outline

In this thesis the formation and evolution of flux ropes in solar and stellar coronae is investigated. In particular, the effects of the evolution of the photospheric magnetic field on the formation and evolution of flux ropes are investigated. Both observed and idealised photospheric magnetic flux distributions are used to drive the evolution of the solar/stellar coronal magnetic field using the magnetofrictional method.

This thesis is structured as follows. Chapter 2 describes the models used to simulate the coronal field, and the algorithms developed to detect and characterise flux ropes. Chapters 3 and 4 describe simulations of the coronal magnetic field of the NOAA active region AR10977. In particular, the formation and evolution of a flux rope which was associated with an X-ray sigmoid is analysed. In Chapter 5 the development of an IDL routine that is capable of producing proxy SOLIS synoptic magnetograms from SDO/HMI and SOHO/MDI magnetograms is presented. In Chapter 6 a series of scaling relations are determined for the formation times and lifetimes of magnetic flux ropes in stellar coronae as a function of differential rotation and surface diffusion. In Chapter 7 this work is extended to include long-term global simulations of stellar coronae. In particular the effects of flux emergence and differential rotation on the coronal evolution are investigated. Finally, in Chapter 8 the findings from the thesis are described, and future work is discussed.

Chapter 2

Numerical Techniques

In this chapter the numerical techniques used in this thesis are presented. Firstly, the magnetofrictional method is described (Section 2.1). Secondly, the two codes that use the magnetofrictional method to obtain a continuous time evolution of NLFF fields are summarised. These are Hexa (Section 2.2) and FFF3 (Section 2.3). Thirdly, the parallelisation that allows Hexa and FFF3 to run on a supercomputer is explained (Section 2.4). Finally, the two algorithms that were developed to detect flux ropes from the outputs of Hexa and FFF3 are described. Section 2.5 outlines the algorithm that uses the Lorentz force to detect flux ropes, and Section 2.6 outlines the algorithm that uses the shear angle of the magnetic fields along polarity inversion lines to detect flux ropes. We use two different flux rope identification methods to ensure that the quantities determined from our analysis are robust and independent of the nature of the description of the flux rope chosen. Whilst this chapter describes the workings of Hexa and FFF3, Appendix A provides a more detailed description of Hexa and FFF3, including a detailed description of the finite difference scheme carried out.

2.1 The Magnetofrictional Method

Since the magnetic field within the corona cannot presently be routinely measured, it must be inferred from simulations or from extrapolations of the measured photospheric magnetic field. The corona is frequently treated as being force-free (see Section 1.5), whereby the coronal field is constrained to be either potential, linear force-free, or most realistically, non-linear force-free (NLFF).

The magnetofrictional method (Yang et al. 1986) is a relaxation technique that can be used to produce a NLFF field. Once a magnetic field has been perturbed, the magnetofrictional method acts to relax the magnetic field into an equilibrium state, which is generally NLFF. The magnetofrictional method evolves the 3D magnetic field, $\mathbf{B}$, according to the induction equation,

$$\frac{\partial \mathbf{A}}{\partial t} = \mathbf{v} \times \mathbf{B} + \mathbf{D}, \tag{2.1}$$

where $\mathbf{A}$ is the magnetic vector potential such that $\mathbf{B} = \nabla \times \mathbf{A}$, $\mathbf{v}$ is the magnetofrictional velocity and $\mathbf{D}$ represents any non-ideal terms.

In the magnetofrictional approach, the equation of motion of MHD is modified to include an artificial frictional term of the form $\nu'\mathbf{v}$, where ν' is a frictional coefficient:

$$\rho \frac{D\mathbf{v}}{Dt} = \rho \mathbf{g} - \nabla p + \mathbf{j} \times \mathbf{B} - \nu' \mathbf{v}. \tag{2.2}$$

Under the force-free approximation (steady state, with gravity and pressure being neglected), the equation of motion reduces to:

$$\mathbf{j} \times \mathbf{B} - \nu' \mathbf{v} = 0, \tag{2.3}$$

where $\mathbf{j} = \nabla \times \mathbf{B}$. The magnetofrictional velocity $\mathbf{v}$ can thus be prescribed as:

$$\mathbf{v} = \frac{\mathbf{j} \times \mathbf{B}}{\nu'}. \tag{2.4}$$

It is important to note that this is a relaxation velocity, not a physical velocity. The form of the frictional coefficient can be taken to be:

$$\nu' = \nu B^2 \tag{2.5}$$

where ν is a spatial variable, which results in the frictional relaxation velocity being independent of the magnetic field strength. This aids the field to relax more quickly in low-field regions, The relaxation velocity is aligned in the direction of the Lorentz force and acts to restore any non-equilibrium perturbed field towards a force-free equilibrium.

The magnetofrictional method (Yang et al. 1986) has been used by a number of authors to produce single snapshots of NLFF fields. One method is to take a potential field extrapolated from a magnetogram and set the photospheric field to be that of the vector magnetogram. The coronal field is then allowed to relax to a NLFF state (Valori et al. 2005). An alternative method involves inserting a flux rope into a potential field, and relaxing the field into a NLFF state (van Ballegooijen 2004, Savcheva et al. 2012). A key feature of the above methods is that they take a single magnetogram frame, and from it derive a single NLFF field. Using these methods and taking a time series of magnetograms, a time series of NLFF fields may be extrapolated. It is important to note, however, that each NLFF field produced is independent of the previous fields in the time series, and hence this technique does not reflect a true time-evolution of the coronal field, as no information is transferred between subsequent times.

In contrast to the single extrapolation method, the magnetofrictional method may also be used to generate a continuous time series of NLFF fields. This is carried out by evolving an initial coronal field through continuously varying the photospheric magnetic field according to a time series of synthetic or observed magnetgrams (van Ballegooijen et al. 2000, Mackay & van Ballegooijen 2006, Yeates et al. 2007, Mackay et al. 2011, Cheung & DeRosa 2012, Meyer, Sabol, Mackay & van Ballegooijen 2013). Using this method, the time series of NLFF fields is now dependent upon previous magnetic configurations and field line connectivity. This allows the buildup of free magnetic energy and helicity to be studied – in addition to the continuous evolution of the magnetic field. This is the method applied in this thesis to determine the evolution of the coronal field.

2.2 Hexa

Hexa is a code that applies the magnetofrictional method to evolve a coronal field through a time series of NLFF equilibria in a Cartesian frame of reference. As such it is designed to simulate a small portion of the Sun whose size (l_0) is much smaller than the solar radius ($l_0 \ll R_\odot$). This small portion may be considered as cartesian, with a flat photosphere. It was written by Aad van Ballegooijen (CfA, Harvard), and was later parallelised by Duncan Mackay (Mathematical Institute, St Andrews). Hexa solves the un-curled induction equation (Equation 2.1).

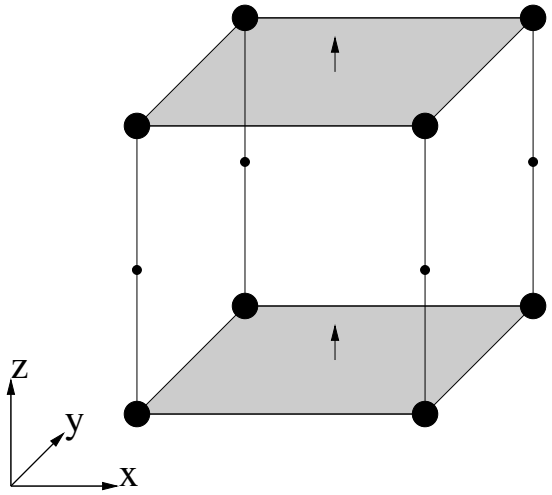

Figure 2.1: The locations of the z-components of variables. Corner variables are shown by the "•" symbols (for example v_z), ribs are shown by the "·" symbols (for example A_z) and the faces are shaded in grey, with the centres indicated by the arrows (for example B_z).

2.2.1 The Numerical Grid

Hexa uses a staggered grid to ensure second order accuracy and ensure $\nabla \cdot \mathbf{B} = 0$. Variables are either located on cell faces, cell corners, or cell ribs. The magnetic vector potential and currents are located on cell ribs. The magnetofrictional velocity is located on the cell corners, and the magnetic field is located on the cell faces. Figure 2.1 displays the faces, ribs and corners for the z-components of variables. The primary variable is the magnetic vector potential, $\mathbf{A}$, as its use on a staggered grid automatically ensures that $\nabla \cdot \mathbf{B} = 0$ at cell centres, since $\mathbf{B} = \nabla \times \mathbf{A}$ and the divergence of a curl is zero. All the other variables $(\mathbf{v}, \mathbf{B}, \mathbf{j})$ are derived from the magnetic vector potential.

Hexa is defined to have N_x, N_y and N_z grid cells in the x, y and z-directions respectively. The grid thus has $N_x + 1, N_y + 1$ and $N_z + 1$ corners in the x, y and z directions respectively. In this chapter, the coordinates of cell corners within the grid will have integer values that range from $1 : N_{X_i} + 1$, where X_i refers to either x, y or z. Cell centres have integer $+\frac{1}{2}$ values, ranging from $1 + \frac{1}{2} : N_{X_i} + \frac{1}{2}$. By default, the ranges of x, y and z are scaled to be $[0, 6]$. The grid separations $(\Delta x, \Delta y, \Delta z)$ are thus $(6/N_x, 6/N_y, 6/N_z)$. Figure 2.2 outlines the positions of all the variables and their indices in the plane of the z face of a grid cell whose bottom left corner is located at (i, j, k).

In solving the induction equation, spatial derivatives must be taken. For cells located at the edge of the grid, this cannot be achieved without the inclusion of ghost cells (a.k.a. halo cells), which are cells located outside the boundary of the grid. The values within these cells must be specified using boundary conditions, which are discussed in Section 2.2.3. Ghost cells are located either at rib or cell face locations, and have coordinates of either $\frac{1}{2}$ or $N_{X_i} + \frac{3}{2}$ in the direction that they extend beyond the grid.

2.2.2 Solution of the Induction Equation

Hexa solves the induction equation using the Eulerian method of numerical integration:

$$\mathbf{A}(t + \Delta t) = \mathbf{A}(t) + [\mathbf{v}(t) \times \mathbf{B}(t) + \mathbf{D}(t)]\, \Delta t \tag{2.6}$$

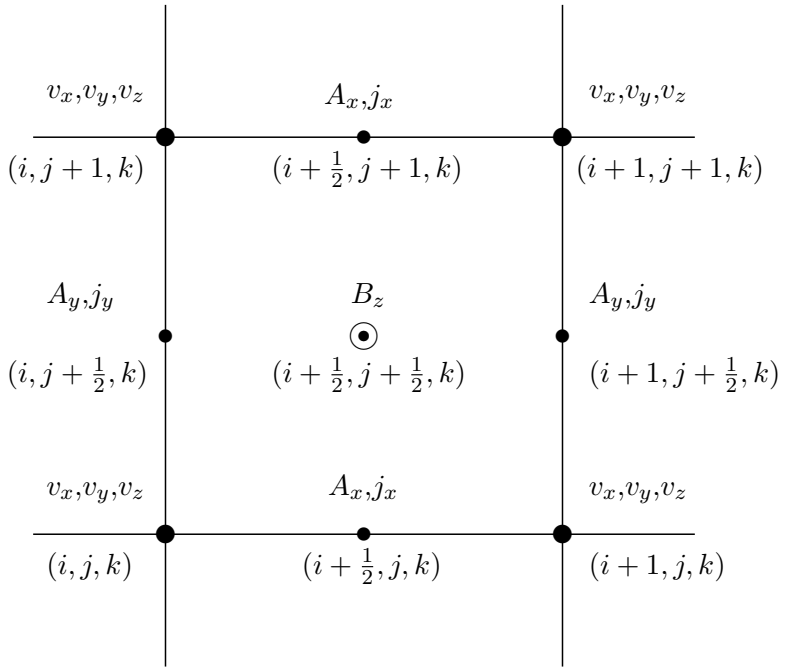

Figure 2.2: The location of variables located in the plane of the z face of a grid cell. The coordinates of the variables are given in parenthesis. Cell corners ($\bullet$) have coordinates of the form (i, j, k), cell centres ($\odot$) of $(i+\frac{1}{2}, j+\frac{1}{2}, k)$, y-ribs ($\cdot$) of $(i, j+\frac{1}{2}, k)$ and x-ribs ($\cdot$) of $(i+\frac{1}{2}, j, k)$.

Where for each timestep (Δt) the RHS of Equation 2.1 must be calculated. In brief, this is carried out by:

1. A_x and A_y, corresponding to B_z at the photosphere, are updated on the base ($z = 0$) according to the prescribed photospheric evolution. This is described in Chapter 3.

2. The 3D magnetic field is calculated on the cell faces from the 3D vector potential, boundary conditions are applied and then the magnetic field is averaged onto cell corners.

3. The 3D current density is calculated on cell ribs from the 3D magnetic field on the cell faces and is then averaged onto cell corners.

4. The 3D magnetofrictional velocity is calculated at cell corners.

5. $\mathbf{v} \times \mathbf{B}$ is calculated at cell corners and averaged onto the cell ribs.

6. Non-ideal terms are calculated on cell ribs.

7. The vector potential is updated by: $\mathbf{A} \rightarrow \mathbf{A} + (\mathbf{v} \times \mathbf{B} + \mathbf{D})\Delta t$.

The following subsections detail the above calculation steps. In this chapter the steps will be described briefly, and in general will only provide a description of the calculation of the z variables so as to demonstrate the process. For a more detailed description of how Hexa carries out the calculations, please see Appendix A.

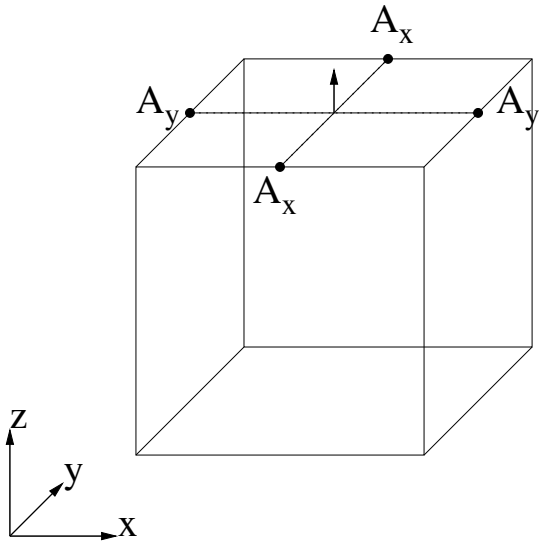

Figure 2.3: The calculation of B_z from A_x and A_y, outlined in Equation 2.8. B_z (indicated by the upward facing arrow) is calculated on the cell face from the values of A_x and A_y on the ribs surrounding the face. Δx and Δy are represented by the dotted lines joining the A_y values and A_x values respectively.

2.2.3 Calculation of B

Firstly the magnetic field is calculated on the cell faces within the grid (i.e. neglecting ghost cells). In order to calculate this, we take the spatial derivatives of the magnetic vector potentials. For example, we calculate B_z by calculating

$$B_z = \frac{\partial A_y}{\partial x} - \frac{\partial A_x}{\partial y}. \tag{2.7}$$

Since in Hexa the variables are located on a grid, they are discrete rather than continuous. Therefore, to calculate derivatives, a finite difference scheme is used. Under this, B_z is calculated by

$$B_z(i+\tfrac{1}{2}, j+\tfrac{1}{2}, k) = \frac{A_y(i+1, j+\tfrac{1}{2}, k) - A_y(i, j+\tfrac{1}{2}, k)}{\Delta x} - \frac{A_x(i+\tfrac{1}{2}, j+1, k) - A_x(i+\tfrac{1}{2}, j, k)}{\Delta y}, \tag{2.8}$$

for $i = 1 : N_x$, $j = 1 : N_y$ and $k = 1 : N_z + 1$. Figure 2.3 outlines the calculation of B_z from A_x and A_y, showing the positions of the variables on the grid.

Now the boundary conditions must be applied. These are set such that the current density parallel to the boundary planes is zero. Since the magnetofrictional velocity, $\mathbf{v}$, is proportional to $\mathbf{j} \times \mathbf{B}$ this ensures that the component of the magnetofrictional velocity normal to the boundary planes is zero. The magnetofrictional velocity cannot, therefore, transport any magnetic field in or out of the computational box. At the top and side boundaries, we set the derivative of the magnetic field in the direction normal to the boundary plane to be zero. For example, at the top boundary ($z = 6$) we set

$$\frac{\partial B_x}{\partial z} = \frac{\partial B_y}{\partial z} = 0 \tag{2.9}$$

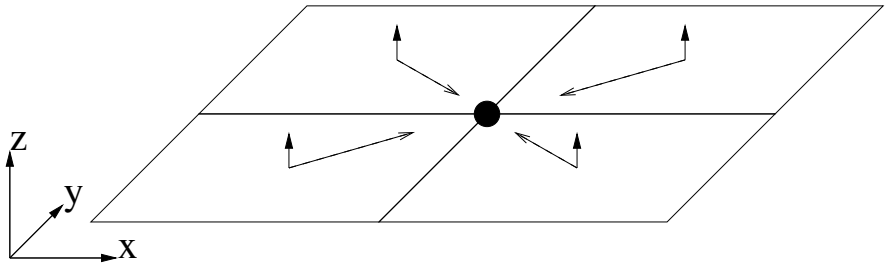

Figure 2.4: Averaging B_z from cell faces onto cell corners. The values at the four faces (denoted by the upward pointing arrows) surrounding the corner (•) are averaged together.

This condition ensures that j_x and j_y are

$$j_x = \frac{\partial B_z}{\partial y} \tag{2.10}$$

$$j_y = -\frac{\partial B_z}{\partial x} \tag{2.11}$$

If the initial condition coronal field has $B_z = 0$ on the upper boundary (closed boundary condition) then j_x and j_y are zero on the boundary plane, ensuring that $\mathbf{v}$ lies in the boundary plane. At the lower boundary, where B_z is not necessarily zero, we instead specify

$$\frac{\partial B_y}{\partial z} = \frac{\partial B_z}{\partial y} \tag{2.12}$$

$$\frac{\partial B_x}{\partial z} = \frac{\partial B_z}{\partial x} \tag{2.13}$$

which ensures that j_x and j_y are zero on the lower boundary, resulting in $\mathbf{v}$ being parallel to the boundary.

Lastly the magnetic field is averaged onto cell corners. The magnetic field at the cell corner is defined to be the average of the magnetic field from the corner's four surrounding faces. Figure 2.4 illustrates this averaging process for B_z. Further details on the calculation of $\mathbf{B}$ and its boundary conditions can be found in Section A.1.1 of Appendix A.

2.2.4 Calculation of j

The current density is calculated by $\mathbf{j} = \nabla \times \mathbf{B}$. It is calculated from the face values of $\mathbf{B}$, and is calculated onto the ribs - including ribs located in the ghost cells. For example, the z component of the current is calculated by

$$j_z(i,j,k+\tfrac{1}{2}) = \frac{B_y(i+\frac{1}{2},j,k+\frac{1}{2}) - B_y(i-\frac{1}{2},j,k+\frac{1}{2})}{\Delta x} - \frac{B_x(i,j+\frac{1}{2},k+\frac{1}{2}) - B_x(i,j-\frac{1}{2},k+\frac{1}{2})}{\Delta y} \tag{2.14}$$

for $i = 1 : N_x + 1$; $j = 1 : N_y + 1$ and $k = 0 : N_z + 1$. Figure 2.5 illustrates the calculation of j_z.

The current density is then averaged onto the cell corners. Each component of $\mathbf{j}$ at the cell corner is calculated from the average of the two nearest rib values. This process is illustrated for j_z in Figure 2.6. Further details on the calculation of $\mathbf{j}$ can be found in Section A.1.2 of Appendix A.

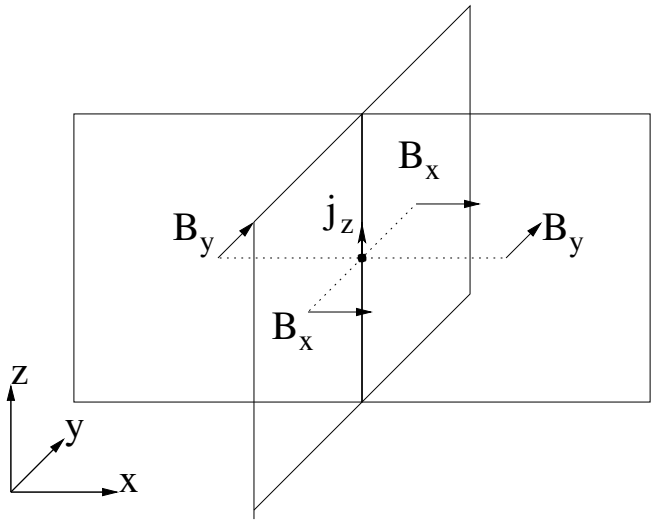

Figure 2.5: Calculating j_z from B_x and B_y. j_z (upward pointing arrow) is calculated on the z-rib from the values of B_x and B_y on the faces surrounding that rib. Δx is represented by the dotted line joining the two B_y values, and Δy is represented by the dotted line joining the two B_x values.

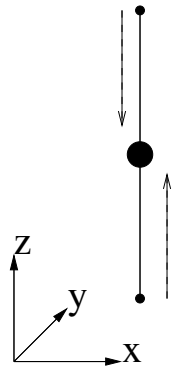

Figure 2.6: Averaging j_z onto cell corners. The two rib values of j_z ($\cdot$) either side of the cell corner are averaged onto the cell corner ($\bullet$).

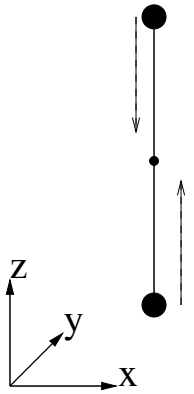

Figure 2.7: Averaging the z-component of the advective term from the cell corners onto the cell ribs. The two corner values ($\bullet$) either side of the rib ($\cdot$) are averaged together, and the averaged value is located at the rib.

2.2.5 Magnetofrictional Velocity

The magnetofrictional velocity is defined as

$$\mathbf{v} = \frac{1}{\nu}\frac{\mathbf{j}\times\mathbf{B}}{B^2}, \tag{2.15}$$

and is calculated on the cell corners. The frictional coefficient is set to be

$$\nu = 10\frac{\Delta t}{\Delta x^2}. \tag{2.16}$$

B^2 is calculated at cell corners. The maximum value of B^2, B^2_{max} is determined. For any point on the grid where B^2 is less than $0.0001B^2_{\text{max}}$, the value of B^2 is set to $0.0001B^2_{\text{max}}$. This is to prevent dividing by very small numbers, causing the magnetofrictional velocity to become anomalously large.

We then calculate the advective term in the induction equation ($\mathbf{v}\times\mathbf{B}$) at the cell corners, and average this quantity onto cell ribs. Figure 2.7 illustrates how the z-component of the advective term is averaged onto the cell rib. Further details on the calculation of $\mathbf{v}$ can be found in Section A.1.3 of Appendix A.

2.2.6 Non-Ideal Terms

There are three different non-ideal terms that are implemented by Hexa. These are Ohmic diffusion, hyperdiffusion, and the diffusion of $\nabla\cdot\mathbf{A}$. Whilst the use of Ohmic diffusion and hyperdiffusion are optional when running Hexa, the diffusion of $\nabla\cdot\mathbf{A}$ is always carried out.

Ohmic Diffusion

Ohmic diffusion ($\eta\mathbf{j}$) is the only physical diffusion term, with its origins in the resistive induction equation. The resistive coefficient, η is defined within Hexa as:

$$\eta = \eta'\frac{\Delta x^2}{\Delta t} \tag{2.17}$$

where η' is a user-defined dimensionless parameter. The diffusion term is calculated on the cell ribs, where $\mathbf{j}$ is already defined.

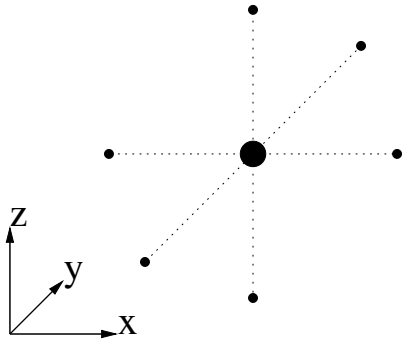

Figure 2.8: Calculating the divergence of a quantity. The divergence is calculated from rib values ($\cdot$) and is located at a cell corner ($\bullet$). Δx, Δy and Δz are denoted by the dotted lines in the x, y and z directions respectively.

Hyperdiffusion

Hyperdiffusion is a form of artificial diffusion which is used to smooth out gradients in the force-free parameter, α, whilst conserving the magnetic helicity. Its form is:

$$\frac{\mathbf{B}}{B^2}\nabla\cdot\left(\eta_4 B^2\nabla\alpha\right) \tag{2.18}$$

where η_4 is the coefficient of hyperdiffusion, defined within Hexa as:

$$\eta_4 = \eta_4'\frac{\Delta x^4}{\Delta t} \tag{2.19}$$

where η_4' is a user-defined dimensionless parameter. In calculating the hyperdiffusion, α must be calculated. This is achieved by calculating

$$\alpha = \frac{j_x B_x + j_y B_y + j_z B_z}{B^2} \tag{2.20}$$

at cell corners. Next the gradient of α is calculated on the ribs using a finite difference scheme. For example, the z derivative of α is calculated by

$$(\nabla\alpha)_z(i,j,k+\tfrac{1}{2}) = \frac{\alpha(i,j,k+1)-\alpha(i,j,k)}{\Delta z} \tag{2.21}$$

for $i = 1 : N_x + 1$; $j = 1 : N_y + 1$ and $k = 1 : N_z$. B^2 must then be averaged onto the cell ribs. This is carried out by the same process as that for averaging the advective term onto the ribs (e.g. see Figure 2.7). Now the divergence of $\eta_4 B^2\nabla\alpha$ must be determined. In order to determine the divergence at the boundaries, ghost cells of $\eta_4 B^2\nabla\alpha$ are required. These ghost cells are set so that the gradients of $\eta_4 B^2\nabla\alpha$ normal to the boundaries are set to zero. The divergence of this quantity is then calculated on the cell corners. A schematic of the calculation of the divergence is displayed in Figure 2.8. Next $\frac{\mathbf{B}}{B^2}\nabla\cdot\left(\eta_4 B^2\nabla\alpha\right)$ is calculated on the cell corners, and is finally averaged onto the cell ribs. Further details on the calculation of hyperdiffusion can be found in Section A.1.4 of Appendix A.

Diffusion of $\nabla\cdot\mathbf{A}$

The initial condition vector potentials providing the coronal fields used in Hexa use the Coulomb gauge: $\nabla\cdot\mathbf{A} = 0$. For consistency, it is desired that the Coulomb gauge is retained

throughout the simulation. To this end a diffusive term is included in the induction equation which acts to maintain the Coulomb gauge by ensuring any deviations of $\nabla \cdot \mathbf{A}$ are diffused away. The diffusive term used is

$$\eta_0 \nabla(\nabla \cdot \mathbf{A}) \tag{2.22}$$

where η_0 is defined within Hexa as

$$\eta_0 = 0.05 \frac{\Delta x^2}{\Delta t} \tag{2.23}$$

In order to understand why this term diffuses $\nabla \cdot \mathbf{A}$, consider the induction equation with this diffusive term included:

$$\frac{\partial \mathbf{A}}{\partial t} = \ldots + \eta_0 \nabla(\nabla \cdot \mathbf{A}), \tag{2.24}$$

where the ellipsis denotes the advective and any other non-ideal terms. If we take the divergence of the induction equation,

$$\frac{\partial}{\partial t}(\nabla \cdot \mathbf{A}) = \nabla \cdot (\ldots) + \eta_0 \nabla^2 (\nabla \cdot \mathbf{A}), \tag{2.25}$$

it is clear that this extra diffusive term included in the induction equation acts to diffuse $\nabla \cdot \mathbf{A}$.

In order to calculate this term, first the divergence of the vector potential is found at cell corners. $\nabla \cdot \mathbf{A}$ is set to zero along the top and side boundaries of the computational box, and the assumption

$$\frac{\partial A_z}{\partial z} = 0 \tag{2.26}$$

is made along the base of the computational box. Finally, the gradient of $\nabla \cdot \mathbf{A}$ is calculated on the cell ribs and is then multiplied by η_0. Further details on the calculation of the diffusion of $\nabla \cdot \mathbf{A}$ term can be found in Section A.1.5 of Appendix A.

2.3 FFF3

Unlike Hexa, which is designed to solve the induction equation for a small portion of the corona on a Cartesian grid, FFF3 is designed to be able to evolve the global corona, and thus employs a spherical coordinate system. FFF3 was written by Duncan Mackay.

2.3.1 Numerical Grid

FFF3 employs the spherical coordinate system (r, θ, ϕ) where r is the distance from centre of the Sun/star, θ is the co-latitude, related to the latitude, λ, by $\lambda = \pi/2 - \theta$, and ϕ is the azimuthal angle. Either the whole corona or only a segment of the corona may be simulated. The corona is simulated between the photosphere ($1R_*$) and $2.5R_*$.

FFF3 employs a uniformly spaced numerical grid using the variables (x, y, z) defined by:

$$x(\phi) = \frac{\phi}{\Delta} \tag{2.27}$$

$$y(\theta) = \frac{-\ln\left(\tan\frac{\theta}{2}\right)}{\Delta} \tag{2.28}$$

$$z(r) = \frac{\ln\left(\frac{r}{R_*}\right)}{\Delta} \tag{2.29}$$

and therefore

$$\phi(x) = x\Delta \tag{2.30}$$

$$\theta(y) = 2\arctan\left(e^{-y\Delta}\right) \tag{2.31}$$

$$r(z) = R_{\odot}e^{z\Delta} \tag{2.32}$$

where Δ is the grid spacing in radians. This choice of variables ensures that the horizontal cell size is $h_x = h_y = r\Delta\sin\theta$ and the vertical cell size is $h_z = r\Delta$. Thus, the size of a cell decreases towards the poles and increases with radial distance away from the surface of the star. Like with Hexa, a staggered grid is used in order to achieve second order accuracy for the computation of derivatives and to ensure $\nabla \cdot \mathbf{B} = 0$ at cell centres. Integer values of (x, y, z) lie on the cell corners, integer $+\frac{1}{2}$ values of (x, y, z) correspond to ribs and cell centres. The grid contains N_x, N_y and N_z cells in the x, y and z directions respectively. A periodic boundary condition on the longitudinal boundaries and a closed boundary condition on the latitudinal boundaries is applied. At the upper ($r = 2.5R_*$) boundary the magnetic field, $\mathbf{B}$, is assumed to be radial with the electric currents horizontal. The lower ($r = R_*$) boundary is specified by the radial photospheric magnetic field as deduced from a 2D surface flux transport model (Sheeley 2005). This is described in Chapter 6.

Since the grid spacing $(h_x, h_y, h_z) = (r\Delta\sin\theta, r\Delta\sin\theta, r\Delta)$ is dependent upon r and θ, this must be taken into account in derivatives. On the staggered grid, since different quantities are located on different points of a grid cell, each quantity has its own (h_x, h_y, h_z) value. In FFF3, all of these length variables must be defined. Further details on the calculation of the grid spacings can be found in Section A.2.1 of Appendix A.

2.3.2 Solution of the Induction Equation

FFF3 solves the induction equation in a very similar way to that of Hexa:

1. A_x and A_y are updated on the base ($z = 0$) according to the prescribed photospheric evolution (See Chapter 6).
2. The 3D magnetic field is calculated on the cell faces from the 3D vector potential using Stokes' theorem and is then averaged onto cell corners.
3. The 3D current density is calculated on cell ribs from the 3D magnetic field on the cell faces using Stokes' theorem and is then averaged onto cell corners.
4. The 3D magnetofrictional velocity is calculated at cell corners.
5. The outflow velocity is determined.
6. $\mathbf{v}\times\mathbf{B}$, where $\mathbf{v}$ is the sum of the magnetofrictional and outflow velocities, is calculated at cell corners, then averaged onto the cell ribs.
7. Diffusive terms are calculated on cell ribs.
8. The vector potential is updated by: $\mathbf{A} \rightarrow \mathbf{A} + (\mathbf{v} \times \mathbf{B} + \mathbf{D})\Delta t$.

The main difference between how Hexa and FFF3 solve the induction equation is the way in which FFF3 calculates the curl of the magnetic vector potential and the magnetic field. Whilst in Hexa the curl is calculated by differentiation, FFF3 uses Stokes' theorem to calculate the curl. Stokes' theorem states

$$\int_S (\nabla \times \mathbf{V}) \cdot d\mathbf{a} = \oint_P \mathbf{V} \cdot d\mathbf{l}, \tag{2.33}$$

where $\mathbf{V}$ is a vector field, and the path, P, on the RHS goes around the boundary of the surface, S. Since $\mathbf{B} = \nabla \times \mathbf{A}$ and $\mathbf{j} = \nabla \times \mathbf{B}$ we may write

$$\int_S \mathbf{B} \cdot d\mathbf{a} = \oint_P \mathbf{A} \cdot d\mathbf{l} \tag{2.34}$$

and

$$\int_S \mathbf{j} \cdot d\mathbf{a} = \oint_P \mathbf{B} \cdot d\mathbf{l}. \tag{2.35}$$

2.3.3 Calculation of B using Stokes' Theorem

Like in Hexa, the magnetic field is calculated at cell faces from the magnetic vector potential located at cell ribs. Instead of differentiating the magnetic vector potential, however, the magnetic vector potential is integrated along a closed path around the face that the magnetic field is to be calculated on (Equation 2.34). For example, to calculate B_z on the cell face, the path integral of $\mathbf{A} \cdot d\mathbf{l}$ around the edges of the face is calculated, and the path integral is divided by the area of the face. Numerically this is achieved by

$$B_z(i+\tfrac{1}{2}, j+\tfrac{1}{2}, k) = \frac{[A_y h_{y_{A_y}}](i+1, j+\frac{1}{2}, k) - [A_x h_{x_{A_x}}](i+\frac{1}{2}, j+1, k) - [A_y h_{y_{A_y}}](i, j+\frac{1}{2}, k) + [A_x h_{x_{A_x}}](i+\frac{1}{2}, j, k)}{[h_{x_{B_z}} h_{y_{B_z}}](i+\frac{1}{2}, j+\frac{1}{2}, k)} \tag{2.36}$$

for $i = 1, ...N_x$, $j = 1, ..., N_y$ and $k = 1, ..., N_z + 1$, where $h_{x_{A_x}}$ is the grid spacing centred at A_x in the x direction, $h_{y_{A_y}}$ is the grid spacing centred at A_y in the y direction, $h_{x_{B_z}}$ and $h_{y_{B_z}}$ are the x and y grid spacings defined on the B_z variable. We have also used the shorthand $[AB](i, j, k) = A(i, j, k)B(i, j, k)$. The process to calculate B_z is illustrated in Figure 2.9.

Boundary conditions are then applied to fill the ghost cells. They are open at the upper ($R = 2.5R_*$) boundary, closed at the latitudinal boundaries, and periodic at the longitudinal boundaries. At the upper boundary we set

$$\frac{\partial B_x}{\partial z} = \frac{\partial B_y}{\partial z} = 0. \tag{2.37}$$

At the latitudinal boundaries, B_x and B_z are specified such that j_x and j_z are solely dependent upon the spatial variation of B_y in the boundary plane. Choosing an initial condition where B_y is zero on the latitudinal boundaries results in $j_x = j_z = 0$ and consequently the magnetofrictional velocity lies in the plane of the boundary. This ensures that no field is transported through the y boundary, resulting in a closed boundary condition. Below the photosphere, B_x and B_y are specified such that $j_x = j_y = 0$ on the photosphere, constraining the magnetofrictional velocity to lie in the plane of the photosphere. Further details on the calculation of $\mathbf{B}$, and its boundary conditions can be found in Section A.2.2 of Appendix A.

2.3.4 Calculation of j using Stokes' Theorem

The current density ($\mathbf{j}$) is calculated at the ribs using Stokes' theorem. The closed path integral of $\mathbf{B} \cdot d\mathbf{l}$, centred on the cell rib where $\mathbf{j}$ is to be located, is calculated from the magnetic field values on the faces of cells, and is divided by the area enclosed by the path.

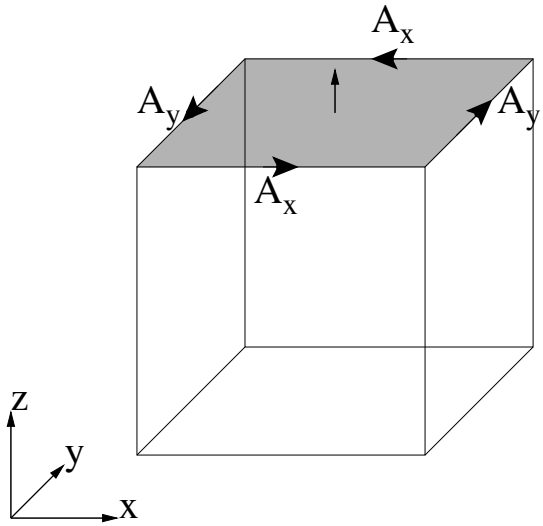

Figure 2.9: The calculation of B_z on the cell face using Stokes' theorem. The path integral of $\mathbf{A} \cdot d\mathbf{l}$ is taken around the edge of the face (the direction indicated by arrows) and this is divided by the area of the face (shaded area).

Numerically, for j_z this is carried out by calculating

$$j_z(i,j,k+\tfrac{1}{2}) = \frac{[B_y h_{y_{B_y}}](i+\frac{1}{2},j,k+\frac{1}{2}) - [B_x h_{x_{B_x}}](i,j+\frac{1}{2},k+\frac{1}{2}) - [B_y h_{y_{B_y}}](i-\frac{1}{2},j,k+\frac{1}{2}) + [B_x h_{x_{B_x}}](i,j-\frac{1}{2},k+\frac{1}{2})}{[h_{x_{A_z}} h_{y_{A_z}}](i,j,k+\frac{1}{2})} \tag{2.38}$$

for $i = 1, ...N_x + 1$, $j = 1, ..., N_y + 1$ and $k = 0, ..., N_z + 1$, where $h_{y_{B_y}}$ and $h_{x_{B_x}}$ are the grid spacings in the y and x directions respectively at the y and x faces of cells, and $h_{x_{A_z}}$ and $h_{y_{A_z}}$ are the grid spacings in the x and y directions at the z-rib of a variable. Once again we have used the shorthand $[AB](i,j,k) = A(i,j,k)B(i,j,k)$. Figure 2.10 shows diagrammatically how calculating j_z is achieved. Further details on the calculation of $\mathbf{j}$ can be found in Section A.2.3 of Appendix A.

Magnetofrictional Velocity

In FFF3, as the grid spacing is not uniform, the magnetofrictional coefficient, ν, is a function of position within the simulation. It is

$$\nu = 5\frac{\Delta t}{{h_x}^2} = 5\frac{\Delta t}{(r\Delta \sin\theta)^2}. \tag{2.39}$$

Outflow velocity

In addition to the magnetofrictional velocity, a radial outflow velocity of the form

$$\mathbf{v}_{\text{out}} = v_0 \exp\left(\frac{z - z_{\max}}{z_w}\right)\hat{\mathbf{z}}, \tag{2.40}$$

is applied, where $v_0 = 100$ km s^{-1} and $z_w = 10$ is the e-folding length over which the radial velocity falls off at the outer boundary. This outflow velocity is chosen to ensure that the coronal magnetic field at the upper boundary is radial, and also allows any features such

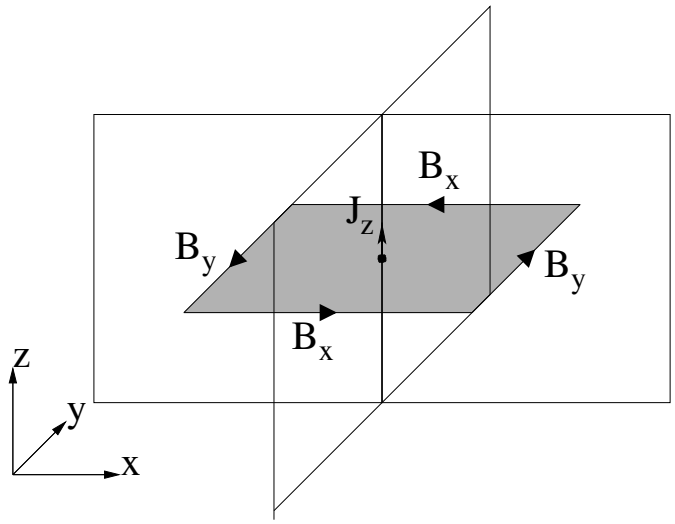

Figure 2.10: The calculation of j_z on the z-rib using Stokes' theorem. The path integral of $\mathbf{B} \cdot d\mathbf{l}$ is taken around the rib (the direction of the path indicated by arrows) and this is divided by the area enclosed by the path (shaded area).

as rising flux ropes to be removed from the computational box. The choice of $z_w \ll N_z$ ensures that the outflow velocity is negligible in the lower closed-field corona. Note that once the field lines become radial near the outer boundary the outflow velocity has no effect on the evolution of the magnetic field.

2.4 Parallelisation

In order to make Hexa and FFF3 run more quickly, they were parallelised using the Message-Passing Interface (MPI) implementation. In MPI, individual processes running on different processors - even other machines - may communicate with each other. As such they can cooperatively carry out a task - in this case solve the induction equation. This is achieved by taking the computational grid, and splitting it up into several sub-grids. Each sub-grid is solved by a single process, with each process communicating with the processes owning adjacent sub-grids to ensure that the sub-grids are 'stitched' together to make the complete grid. This is important, as if the processes did not communicate with each other, then each sub-grid would be independent of the other, and something happening in one sub-grid would not be able to affect something happening in another.

2.4.1 Sub-Grids

In both codes, the grid is parallelised in two dimensions, namely x and y. In a given direction, each subgrid must be divided equally. For example, if there are four processes in the x direction, and $N_x = 100$ then each subgrid must possess $n_x = 25$ cells in the x direction. It is possible to have a different number of processes in each direction. For example, if there were $L = O \times P$ processes in total, with O being a factor of N_x, and P a factor of N_y, then there would be O sub-grids in the x-direction, and P in the y-direction, such that for each subgrid $(n_x, n_y) = (N_x/O, N_y/P)$. As there is no parallelisation in the z-direction, $N_z = n_z$.

Like the global grid, each subgrid has a halo of ghost cells around it. Unlike in the global grid, these ghost cells contain values of the magnetic potential belonging to adjacent

sub-grids. For each subgrid, the A_x variable has indices ranging from $i = 0 : n_x + 1$, $j = 0 : n_y + 2$, $k = 1 : n_z + 1$, with the ghost cells located at $i = 0, n_x + 1$ and $j = 0, n_y + 1, n_y + 2$. Similarly, for A_y the indices range from $i = 0 : n_x + 2$, $j = 0 : n_y + 1$, $k = 1 : n_z + 1$, with the ghost cells located at $i = 0, n_x + 1, n_x + 2$ and $j = 0, n_y + 1$. Finally, for A_z the indices range from $i = 0 : n_x + 2$, $j = 0 : n_y + 2$, $k = 1 : n_z$, with the ghost cells located at $i = 0, n_x + 1, n_x + 2$ and $j = 0, n_y + 1, n_y + 2$. For the x- and y-directions, each process only owns the magnetic vector potential indices $i = 1 : n_x$ and $j = 1 : n_y$. Figures 2.11 to 2.13 illustrate the boundary conditions between two sub-grids in the x-direction for A_x, A_y and A_z. For sub-grids whose ghost cells are located at the boundary of the global grid, the boundary conditions differ to these illustrated in Figures 2.11 to 2.13. The very outer values of the ghost cells are set to zero. For sub-grids containing the maximum of x, the elements of A_y and A_z which possess the index $i = n_x + 1$, which would normally belong to an adjacent sub-grid, instead belong to that grid as there is no adjacent grid in that direction. Similarly, for sub-grids containing the maximum of y, the elements of A_x and A_z which possess the index $j = n_y + 1$, which would normally belong to an adjacent grid, instead belong to that grid due to the absence of an adjacent sub-grid in that direction.

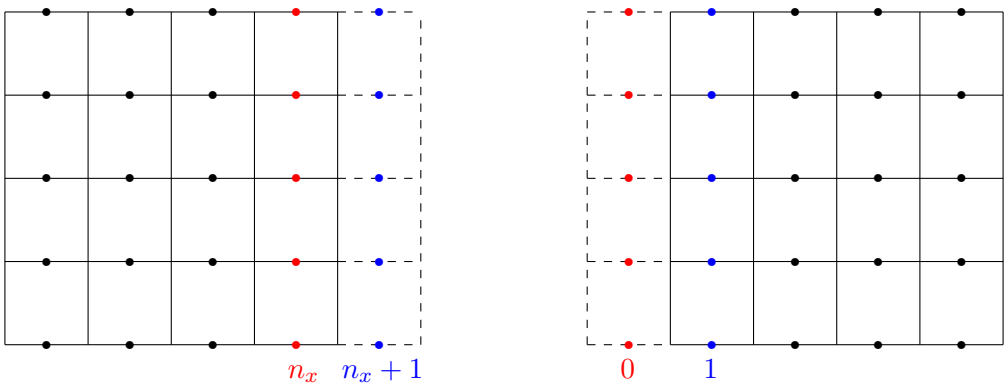

Figure 2.11: The boundary conditions between two adjacent sub-grids in the x-direction for the A_x variable, showing how the values on the two grids match up at the boundaries. Ghost cells are the cells bounded by dashed lines, and cells within the sub-grid are bounded by solid lines. The columns coloured red possess the same values in the left and right sub-grids. The same applies for the columns coloured blue.

2.4.2 Parallelised Solution of the Induction Equation

The methods by which the induction equation is solved in parallel by Hexa and FFF3 are very similar to that outlined in Sections 2.2.2 and 2.3.2 but there are a few differences, which will be outlined here:

- When B_x, B_y and B_z are calculated on the cell faces, the ghost values of the vector potential are used, so the values of the ghost cells for the magnetic field are calculated using the ghost cells of the vector potential instead of the boundary conditions applied in Section 2.2.3. The exception is for ghost cells belonging to the edge of

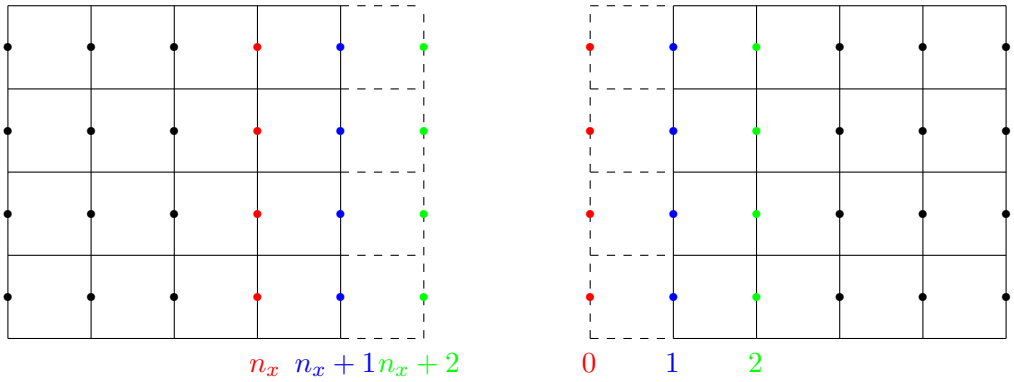

Figure 2.12: The boundary conditions between two adjacent sub-grids in the x-direction for the A_y variable, showing how the values on the two grids match up at the boundaries. It is important to note that the column labeled $n_x + 1$ in the left sub-grid belongs to the right sub-grid. The exception to this case is when the sub-grid is the right-most sub-grid, as then it owns the column labeled $n_x + 1$, which corresponds to the $N_x + 1^{\text{th}}$ column in the global grid.

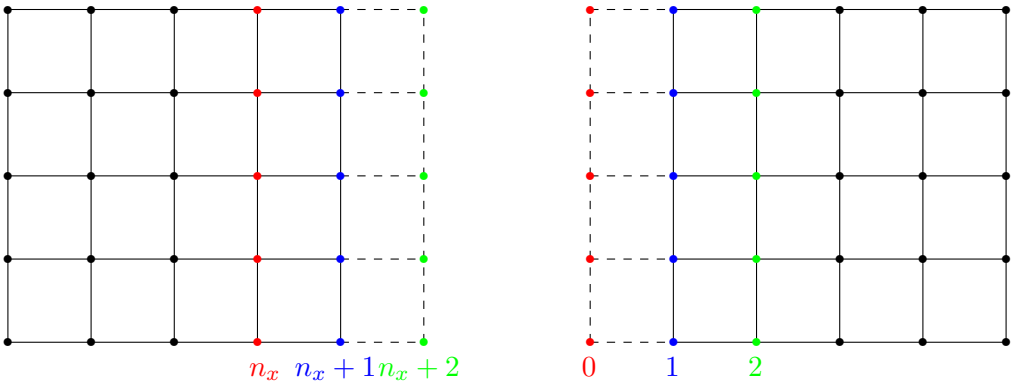

Figure 2.13: The boundary conditions between two adjacent sub-grids in the x-direction for the A_z variable, showing how the values on the two grids match up at the boundaries. It is important to note that the column labeled $n_x + 1$ in the left sub-grid belongs to the right sub-grid. The exception to this case is when the sub-grid is the right-most sub-grid, as then it owns the column labeled $n_x + 1$, which corresponds to the $N_x + 1^{\text{th}}$ column in the global grid.

the global grid, where the the boundary conditions applied are those specified in Sections 2.2.3 and 2.3.3.

- In calculating the maximum value of B^2, the local maximum of B^2 in each subgrid is determined, then the processes communicate to each other what their local maxima are so that a global maximum may be determined, and passed onto every process.
- When calculating the hyperdiffusive term, the quantity $\eta_4 B^2 \nabla \alpha$ is calculated on the cell ribs within the sub-grid (excluding the ghost cells). The ghost cells are populated with the values of $\eta_4 B^2 \nabla \alpha$ from adjacent sub-grids, or using the boundary conditions outlined in Section 2.2.6 for ghost cells located on the edge of the global grid. This allows $\nabla \cdot (\eta_4 B^2 \nabla \alpha)$ to be calculated correctly on the cell corners.
- When calculating $\nabla \cdot \mathbf{A}$, the ghost values of $\mathbf{A}$ are used. Values of $\nabla \cdot \mathbf{A}$ located at the edge of the global grid are set to zero as in Section 2.2.6.
- At the end of every timestep the processes pass on the values of $\mathbf{A}$ around the edge of their sub-grids to the processes owning adjacent subgrids, thus updating the ghost cells for $\mathbf{A}$ in each subgrid.

2.5 Flux Rope Detection: Magnetic Forces

In this section the routine FRfinder, which was written to detect flux ropes in the output from Hexa and FFF3, is described. FRfinder considers the geometry of the magnetic field by investigating the magnetic forces. The Lorentz force may be written as:

$$\mathbf{j} \times \mathbf{B} = \frac{1}{\mu_0}(\mathbf{B} \cdot \nabla)\mathbf{B} - \nabla\left(\frac{B^2}{2\mu_0}\right), \tag{2.41}$$

where the first term on the right hand side of the equation is the magnetic tension force, and the second term is the magnetic pressure force. In this thesis, force-free magnetic fields are studied. As such, the left hand side of the above equation is equal to zero.

In a plane normal to a flux rope's axis, the magnetic tension force due to the twisted field lines must be directed inwards. In order to balance this and ensure that $\mathbf{j} \times \mathbf{B} = 0$, the magnetic pressure force must be directed outwards. These force criteria allow us to determine the points belonging to a flux rope axis in our simulations by looking for locations within the grid where the above criteria are met. This is pictorially represented in Figure 2.14, where the blue arrows denote the tension force, and the red arrows denote the magnetic pressure force. In order to locate a flux rope, the magnetic pressure and tension forces are determined everywhere in the numerical grid, and locations with outwards directed pressure and inwards directed tension are flagged as flux ropes. In the following subsections the calculation of the magnetic tension and pressure forces are described (Sections 2.5.1 and 2.5.2), then the algorithm to detect flux ropes is outlined (Section 2.5.3).

2.5.1 Magnetic Tension

The magnetic tension force is expressed by

$$(\mathbf{B} \cdot \nabla)\mathbf{B} = \left(B_x \frac{\partial}{\partial x} + B_y \frac{\partial}{\partial y} + B_z \frac{\partial}{\partial z}\right)\mathbf{B}, \tag{2.42}$$

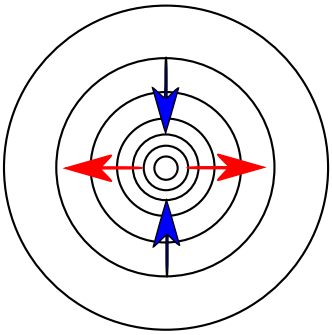

Figure 2.14: The magnetic forces in a flux rope. The blue arrows represent the inwards directed magnetic tension force, and the red arrows denote the outwards directed magnetic pressure force. The black circles represent the projection of the helical flux rope field lines in the plane normal to the flux rope axis.

and will be calculated on the cell corners. To do this, we begin with the B_x, B_y and B_z variables defined at cell corners. Below the calculation of the q^{th} component of the magnetic tension (where q could be x, y or z) will be described.

The expression for the q^{th} component of the tension is

$$T_q = \left(B_x \frac{\partial B_q}{\partial x} + B_y \frac{\partial B_q}{\partial y} + B_z \frac{\partial B_q}{\partial z} \right). \tag{2.43}$$

Firstly, we must calculate the spatial derivatives of B_q. These are determined at the x, y and z ribs. They are calculated by

$$\frac{\partial B_q}{\partial x}(i+\tfrac{1}{2},j,k) = \frac{B_q(i+1,j,k) - B_q(i,j,k)}{\Delta x} \tag{2.44}$$

$$\frac{\partial B_q}{\partial y}(i,j+\tfrac{1}{2},k) = \frac{B_q(i,j+1,k) - B_q(i,j,k)}{\Delta y} \tag{2.45}$$

$$\frac{\partial B_q}{\partial z}(i,j,k+\tfrac{1}{2}) = \frac{B_q(i,j,k+1) - B_q(i,j,k)}{\Delta z}. \tag{2.46}$$

These derivatives are then averaged back onto the cell corners by the same process as is described in Figure 2.6.

2.5.2 Magnetic Pressure

The magnetic pressure force is expressed by

$$-\nabla\left(\frac{B^2}{2}\right) = -\frac{1}{2}\left(\frac{\partial B^2}{\partial x}\hat{\mathbf{x}} + \frac{\partial B^2}{\partial y}\hat{\mathbf{y}} + \frac{\partial B^2}{\partial z}\hat{\mathbf{z}}\right) \tag{2.47}$$

and is calculated onto the cell corners. We will briefly describe the calculation of P_z, the z component of the magnetic pressure. Firstly, we take the z derivative of B^2. B^2 is defined at cell corners, and the derivative is therefore located at the z ribs. The derivative is calculated by

$$\frac{\partial B^2}{\partial z}(i,j,k+\tfrac{1}{2}) = \frac{B^2(i,j,k+1) - B^2(i,j,k)}{\Delta z}. \tag{2.48}$$

This value is then averaged onto the cell corners, as described in Figure 2.6.

2.5.3 Locating a flux rope

Now that the magnetic tension and pressure are calculated, we may determined the locations of flux ropes. Below the algorithm to do this will be described. First, it must be noted that the criteria for a flux rope (tension directed inwards and pressure directed outwards) are only applicable in the plane normal to the flux rope's axis. In the direction parallel to the axis, this condition does not necessarily apply. This could be problematic as we do not necessarily know the orientation of the flux rope's axis. In order to overcome this problem, the assumption is made that the axis of the flux rope lies in the x-y plane. From this assumption it follows that the force criteria apply in the z direction. This is a reasonable assumption to make since the axes of structures associated with stable flux ropes in the solar corona (prominences, sigmoids) tend to lie parallel to the photosphere. During an eruption the flux rope axis may be directed upwards, but an eruption is not an equilibrium state, and the magnetofrictional method is therefore incapable of accurately simulating this portion of a flux rope's evolution.

In order for FRfinder to locate points belonging to flux rope axes, the following criteria are tested on every point (i, j, k) in the grid:

1. Check if $B^2(i, j, k) > \text{Tol}^2$, where Tol is magnetic field strength below which no flux rope is detected. This step is to avoid the code misidentifying noise in low-field regions as flux ropes. It can also be chosen such that FRfinder only finds flux ropes with a sufficiently high axial field strength.

2. Check if $T_z(i, j, k-1) > 0$ and $T_z(i, j, k+1) < 0$

3. Check if $P_z(i, j, k-1) < 0$ and $P_z(i, j, k+1) > 0$

4. Check if $T_x(i-1, j, k) > 0$ and $T_x(i+1, j, k) < 0$ or if $T_y(i, j-1, k) > 0$ and $T_y(i, j+1, k) < 0$

5. Check if $P_x(i-1, j, k) < 0$ and $P_x(i+1, j, k) > 0$ or if $P_y(i, j-1, k) < 0$ and $P_y(i, j+1, k) > 0$

Points that satisfy all of these criteria are defined as belonging to flux rope axes. Figure 2.15 displays the x, y, and z components of the pressure and tension forces around a point identified by FRfinder as belonging to a flux rope axis. It shows that the force criteria apply in the x (red) and z (blue) directions, but not in the y (green) direction. This implies the flux rope axis lies in the y direction.

FRfinder is then also able to characterise the direction of twist of a flux rope by determining the value of the force-free parameter, α, at the points along the flux rope axis. α is calculated in the way described in Equation 2.20. If α is positive, the flux rope has a sinistral chirality. If α is negative, the flux rope has a dextral chirality. Figure 2.16 displays the locations of flux rope axes points (crosses) in the x-y plane, coloured blue if $\alpha > 0$ and magenta if $\alpha < 0$. The red and green contours denote positive and negative photospheric magnetic field respectively.

It must be noted that Sections 2.5.1 and 2.5.2 describe how the pressure and tension are calculated on the Hexa grid with spacings Δx, Δy and Δz. In order to calculate the tension and pressure on the FFF3 grid, the same process is carried out, but it uses h_{xA_x}, h_{yA_y} and h_{zA_z} in place of Δx, Δy and Δz.

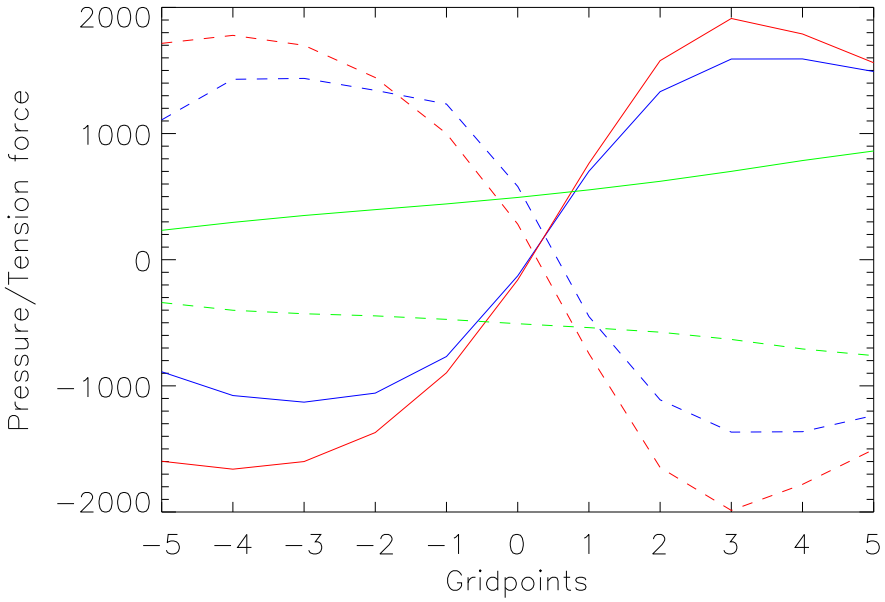

Figure 2.15: The magnetic pressure (solid line) and tension (dashed line) forces in the x (red), y (green) and z (blue) directions about a point determined by FRfinder to belong to a flux rope axis.

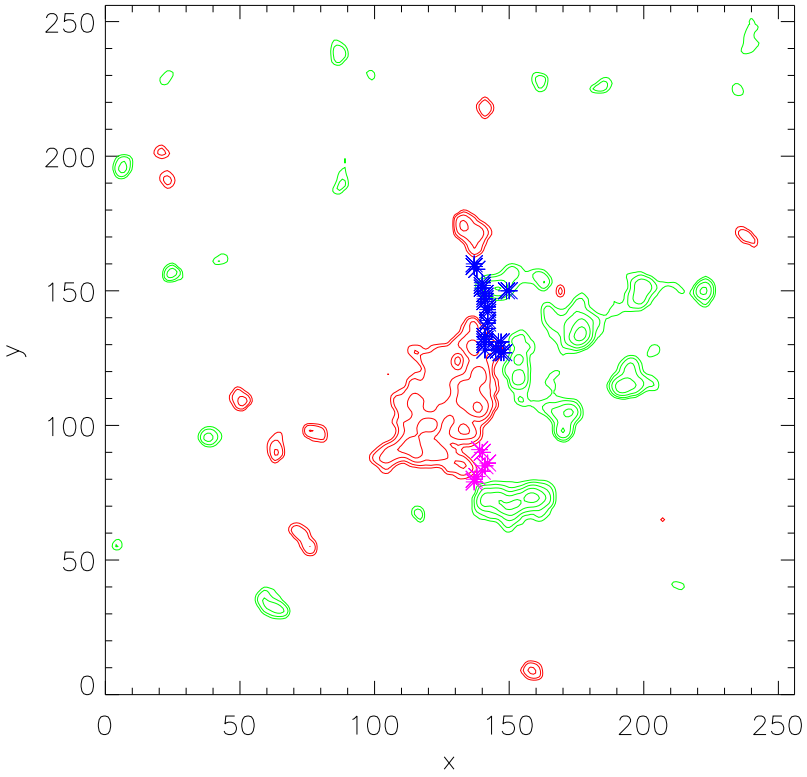

Figure 2.16: The locations (crosses) of flux rope axis points as determined by FRfinder. Blue and magenta crosses denote flux ropes with positive and negative force free parameters respectively. The red and green contours denote positive and negative photospheric magnetic field respectively.

2.6 Flux Rope Detection: Polarity Inversion Line

In the van Ballegooijen & Martens (1989) flux rope formation mechanism, a flux rope is formed at a polarity inversion line (PIL) by flux cancellation of a sheared arcade. It is therefore likely that a flux rope will be found over a polarity inversion line. In this section, a method of detecting flux ropes at PILs that was developed as part of the work in this thesis will be described. The routine is called PILfinder. Firstly, let us consider different possible field configurations across a PIL. Figure 2.17 displays images illustrating the field across a PIL from a potential arcade (left), a sheared arcade (centre) and a flux rope (right). Let us consider the horizontal component of the magnetic field above the PIL, and define the shear angle to be the angle the horizontal field makes with the normal to the PIL. It is clear in the case of the potential arcade, the field is parallel to the normal of the PIL, and so the shear angle is zero. In the case of the sheared arcade, the shear angle is non-zero, but is less than 90°. For the flux rope, the shear angle at the centre of the flux rope is greater than 90° where the flux rope field line makes an inverse-crossing of the PIL. By determining the shear angle at the PIL we can thus infer the presence of a flux rope by the presence of a shear angle greater than 90°. Indeed, it is possible to track the formation of a flux rope by examining the evolution of the shear angle from less than 90° – corresponding to a (sheared) arcade – to greater than 90° – corresponding to a flux rope. It should be noted that the shear angle can be negative. In such a case, a shear angle of less than −90° also implies the presence of a flux rope. In order to detect flux ropes using PILfinder, firstly the PILs must be located. Once they are located the horizontal field above the PIL must be determined, and the shear angle must be calculated.

2.6.1 Location of PIL

In order to look for the PIL, locations where B_z changes sign need to be located. To do this we consider the cell corner values of B_z on the photosphere ($B_z(i,j,1) = B_z(i,j)$). For every point we test

(a) If $[B_z(i+1,j) - B_z(i,j)]/\Delta x >$ Tol and if $B_z(i+1,j) \times B_z(i,j) < 0$ (looking for a PIL crossing the bottom edge of the cell).

(b) If $[B_z(i,j+1) - B_z(i,j)]/\Delta y >$ Tol and if $B_z(i,j+1) \times B_z(i,j) < 0$ (looking for a PIL crossing the left edge of the cell).

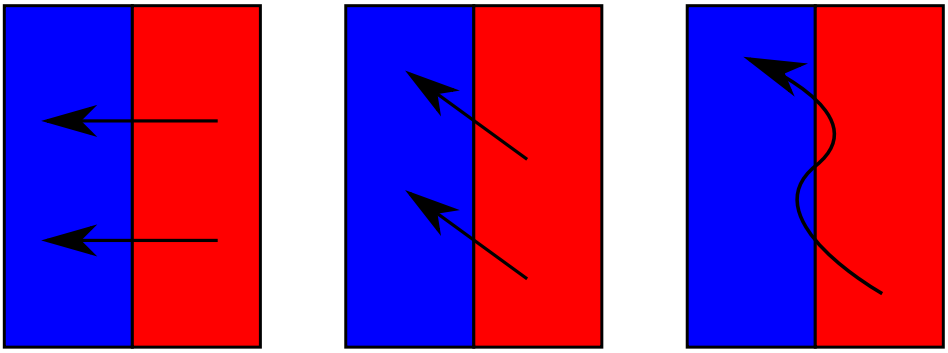

Figure 2.17: A potential arcade (left), a sheared arcade (centre) and a flux rope (right) across a polarity inversion line. The polarity inversion line is the vertical line separating the positive (red) and negative (blue) magnetic polarities. The field lines are represented by black arrows. The normal to the PIL is directed to the left.

Tol is chosen to be 0.05 such that the code only identifies a PIL where the gradient of B_z is sufficiently large. This ensures that the code does not identify numerical noise in low field regions as PILs. For the (i, j) where criteria (a) or (b) are met we know that a PIL crosses somewhere between $(i + 1, j)$ and (i, j) (criterion (a)) or $(i, j + 1)$ and (i, j) (criterion (b)). We determine the location of the PIL along the cell edge in the x (criterion (a)) and y (criterion (b)) directions by assuming B_z is linear between the two corner points and finding the point (ξ) along the edge where $B_z = 0$.

2.6.2 Determining the Shear Angle

In order to calculate the shear angle, we need to determine the normal to the PIL and the horizontal field. The normal to the PIL is is found by calculating

$$\hat{\mathbf{N}}_{\mathrm{PIL}} = -\frac{\nabla B_z}{|\nabla B_z|}. \tag{2.49}$$

The horizontal field, $\mathbf{B}_H = (B_x, B_y)$, is taken to be field one grid point up from the photosphere, so $B_x(i, j) = B_x(i, j, 2)$ and $B_y(i, j) = B_y(i, j, 2)$. The shear angle is calculated by

$$\cos\theta_s = \frac{\mathbf{B}_H \cdot \hat{\mathbf{N}}_{\mathrm{PIL}}}{|\mathbf{B}_H|}. \tag{2.50}$$

Due to the nature of the locations of the PILs as determined from Criterion (a) and Criterion (b), the way to calculate $\hat{\mathbf{N}}_{\mathrm{PIL}}$ and $\mathbf{B}_H$ differs slightly between each criterion. Below we describe these calculations.

Criterion (a)

In criterion (a) the PIL is located at $(i + \xi, j)$. We must thus calculate $\hat{\mathbf{N}}_{\mathrm{PIL}}$ and $\mathbf{B}_H$ at this location. In order to calculate the normal of the PIL we need to calculate $\frac{\partial B_z}{\partial x}$ and $\frac{\partial B_z}{\partial y}$. To determine the x derivative of B_z at $i + \xi$ we simply calculate

$$\frac{\partial B_z}{\partial x}(x, y) = \frac{B_z(i + 1, j) - B_z(i, j)}{\Delta x}, \tag{2.51}$$

as the derivative is assumed to be constant along the cell edge. In order to determine the y derivative of B_z at $i+\xi$ we need to take a weighted four-point average of the y derivatives surrounding $(i + \xi, j)$. This is accomplished by

$$\begin{aligned}\frac{\partial B_z}{\partial y}(x, y) = &\left(\frac{1 - \xi}{2}\right)\left(\frac{B_z(i, j + 1) - B_z(i, j)}{\Delta y} + \frac{B_z(i, j) - B_z(i, j - 1)}{\Delta y}\right) \\ &+ \left(\frac{\xi}{2}\right)\left(\frac{B_z(i + 1, j + 1) - B_z(i + 1, j)}{\Delta y} + \frac{B_z(i + 1, j) - B_z(i + 1, j - 1)}{\Delta y}\right).\end{aligned} \tag{2.52}$$

We must now calculate $\mathbf{B}_H(x, y)$. This is simply accomplished by calculating

$$B_x(x, y) = (1 - \xi)B_x(i, j) + (\xi)B_x(i + 1, j) \tag{2.53}$$

$$B_y(x, y) = (1 - \xi)B_y(i, j) + (\xi)B_y(i + 1, j) \tag{2.54}$$

Criterion (b)

In criterion (b) the PIL is located at $(i, j+\xi)$. To determine the normal to the PIL we calculate

$$\frac{\partial B_z}{\partial x}(x,y) = \left(\frac{1-\xi}{2}\right)\left(\frac{B_z(i,j)-B_z(i-1,j)}{\Delta x}+\frac{B_z(i+1,j)-B_z(i,j)}{\Delta x}\right) + \left(\frac{\xi}{2}\right)\left(\frac{B_z(i,j+1)-B_z(i-1,j+1)}{\Delta x}+\frac{B_z(i+1,j+1)-B_z(i,j+1)}{\Delta x}\right). \quad (2.55)$$

and

$$\frac{\partial B_z}{\partial y}(x,y) = \frac{B_z(i,j+1)-B_z(i,j)}{\Delta y}. \quad (2.56)$$

$\mathbf{B}_H(x,y)$ is then calculated by

$$B_x(x,y) = (1-\xi)B_x(i,j)+\xi B_x(i,j+1) \quad (2.57)$$
$$B_y(x,y) = (1-\xi)B_y(i,j)+\xi B_y(i,j+1) \quad (2.58)$$

Figure 2.18 displays an example of the graphical output of PILfinder. It displays the direction (arrows) of the horizontal field across the PIL. The normal to the PIL points in the direction from red to green. Towards the centre of the bipole, the horizontal field across the PIL is oriented in the opposite direction to the normal to the PIL, implying a flux rope is located here. Similarly, Figure 2.19 displays the shear angle along the PIL as a function of latitude, and shows that the shear angle is greater than 90° between 22° and 42° latitude, implying the presence of a flux rope here. Using PILfinder we may thus characterise the degree of shear across a PIL, and determine the time when a flux rope forms and the time that it lifts off from the photosphere. With PILfinder the length of a flux rope may be measured by determining the length of the region containing shear angle $> 90°$. It should be noted that the length as determined by this method underestimates the true length of the flux rope as it only locates where the dips in the flux rope are – the so called 'bald patch' – and does not detect the extent of the footpoints of the flux rope. Whilst this is the case, for prominences – where the plasma can only be located in the dips of the magnetic field – by measuring the length of the bald patch, we measure the length of the observable prominence.

As with FRfinder it must be noted that Sections 2.6.1 and 2.6.2 describe how a PIL is found and how the shear angle is calculated on the Hexa grid with spacings Δx and Δy. In order to find the PIL and calculate the shear angle on the FFF3 grid, the same process is carried out, but it uses h_{xA_x} and h_{yA_y} in place of Δx and Δy.

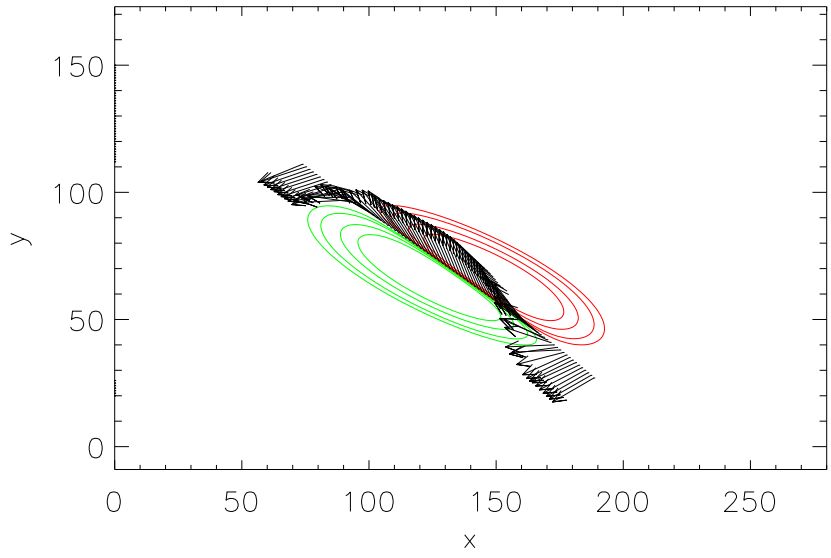

Figure 2.18: An example of the graphical output of PILfinder, showing the direction (arrows) of the horizontal field across the PIL in a magnetic bipole. The contours denote the positive (red) and negative (green) magnetic flux density on the photosphere. The normal to the PIL is directed from red to green. At the centre of the bipole the field is oriented in the opposite direction to the normal of the PIL, implying the presence of a flux rope.

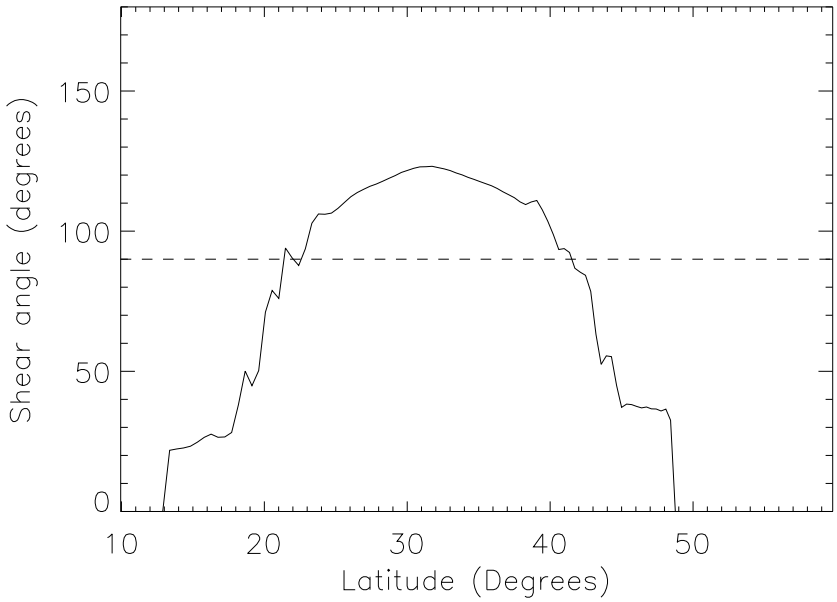

Figure 2.19: The shear angle as a function of latitude along the PIL for the same magnetic field configuration as depicted in Figure 2.18. The shear angle is greater than 90° between 22° and 42° latitude, implying a flux rope lies above the PIL in this latitudinal range.

Chapter 3

Modelling the Coronal Field of AR10977 I: Potential Field Initial Condition

3.1 Introduction

In this chapter, the photospheric and coronal modelling of the NOAA active region AR10977 is described. In order to do this, a time series of line of sight magnetograms are used to drive the coronal evolution of the active region's magnetic field using the magnetofrictional method, in a manner similar to that employed by Mackay et al. (2011).

AR10977 was an isolated active region, which hosted an X-ray sigmoid that erupted. During the active region's passage over the solar disk, several significant flux cancellation events occurred. The active region has previously been studied by Green et al. (2011) and Savcheva et al. (2012). Green et al. (2011) used observations to determine that the sigmoid was associated with a flux rope, and that the formation mechanism of the flux rope was consistent with that of the mechanism proposed by van Ballegooijen & Martens (1989). Additionally they found that the magnetic flux contained within the flux rope was at most 60% of the active region flux, though more likely to be around 30%. Savcheva et al. (2012) carried out NLFF field extrapolations of AR10977's coronal field using the flux rope insertion method of van Ballegooijen (2004). This process was carried out at various times to obtain an estimate for the variation of the active region's properties. The results from this study showed that the best fit flux rope contained roughly 50% of the active region's flux, the free magnetic energy was roughly 6×10^{30} erg and the helicity was 3×10^{41} Mx^2.

Mackay et al. (2011) applied the magnetofrictional method along with line of sight magnetograms in order to simulate the evolution of the coronal magnetic field AR8005, a dispersing active region. Through doing so they quantified the energy and helicity input into the corona. They did not, however, carry out any comparison of the simulation with coronal images. Additionally, the four day period simulated by Mackay et al. (2011) did not include any significant flux cancellation. In order to determine the validity of the modelling method of Mackay et al. (2011), the previously considered AR10977 is studied so that a qualitative and quantitative comparison of our results with those of previous studies of this active region can be made. Only through doing this can we determine if the modelling technique of Mackay et al. (2011), which solely uses normal component magnetograms, is a viable method of simulating the coronal field. While AR10977 has been studied before, this chapter presents the first study which considers a continuous time

evolution of its photospheric and coronal magnetic field though simulation. We note here that Cheung & DeRosa (2012) carried out a similar simulation of a different active region. They found that the use of normal component magnetograms alone was insufficient to reproduce the coronal images. In order to produce a good agreement an extra twisting motion on the boundary had to be applied.

In this chapter, Hexa (See Chapter 2 Section 2.2 for details) is used to simulate the evolution of the coronal field of AR10977 – in particular its emergence phase, followed by a decay phase with significant flux cancellation and formation of an observed X-ray sigmoid. As such, this chapter may be considered a follow on study to Mackay et al. (2011). A key new feature of the present study over that of Mackay et al. (2011) is that we apply a simple method to produce emission proxy images such that we may directly compare the simulation results with coronal observations of the active region. Through doing so we may determine whether or not the photospheric boundary technique of Mackay et al. (2011) can reproduce the evolution seen in the coronal images. The work in this chapter is published in Gibb, Mackay, Green & Meyer (2014).

This chapter is structured as follows. Section 3.2 describes the observations of AR10977 used in this study. The cleaning procedure applied to the magnetograms is described in Section 3.3. The properties of the active region as determined from the cleaned magnetograms are presented in Section 3.4. Section 3.5 describes preparing the data for use in the simulation, along with the process of generating the initial condition. In Section 3.6 the primary simulation results are described. Sections 3.7, 3.8 and 3.9 describe the simulations which used uncleaned magnetograms, Ohmic diffusion and hyperdiffusion respectively. Finally, in Section 3.10 the results of the primary simulation are discussed in detail, along with the effects of using uncleaned magnetograms, hyperdiffusion and Ohmic diffusion.

In Chapter 4 further simulations of AR10977 are described. These simulations include running a simulation at a later start-time, using linear force-free initial conditions and running higher resolution simulations.

3.2 Observations

AR10977 was observed on the Sun's southern hemisphere between the 2^{nd} and 10^{th} of December 2007. During this period, the active region's full lifetime - from emergence to decay - was observed. The evolution of the active region's photospheric magnetic field as observed by SOHO/MDI over this period of time can be seen in Figure 3.1. At the start of the observations (2^{nd} Dec 2007) the active region has a simple bipolar configuration, aligned east-west (top left, Figure 3.1). For the first two days of the observations the active region was still in the emergence phase. During this time, it rotated in the clockwise sense (top centre, Figure 3.1). Starting on the 4^{th} Dec 2007 and continuing on the 5^{th} Dec 2007, flux cancellation occurred across the polarity inversion line (PIL) between the two polarities. With this the negative polarity region fragmented (top right - Figure 3.1) where the fragmentation of the negative polarity continued over the next few days. On the 5^{th} Dec 2007 the active region began to rotate in the counter-clockwise sense (bottom left - Figure 3.1). A second flux cancellation event occurred late on the 7^{th}, continuing into the 8^{th} Dec 2007 (bottom centre - Figure 3.1). Finally, the active region began to diffuse away, and continued to rotate counter-clockwise (bottom right - Figure 3.1).

The evolution of the coronal magnetic field above the active region can be seen through X-ray images taken by the X-Ray Telescope (XRT) on the Japan Aerospace Exploration Agency (JAXA)'s Hinode space telescope. Figure 3.2 shows a collection of four images

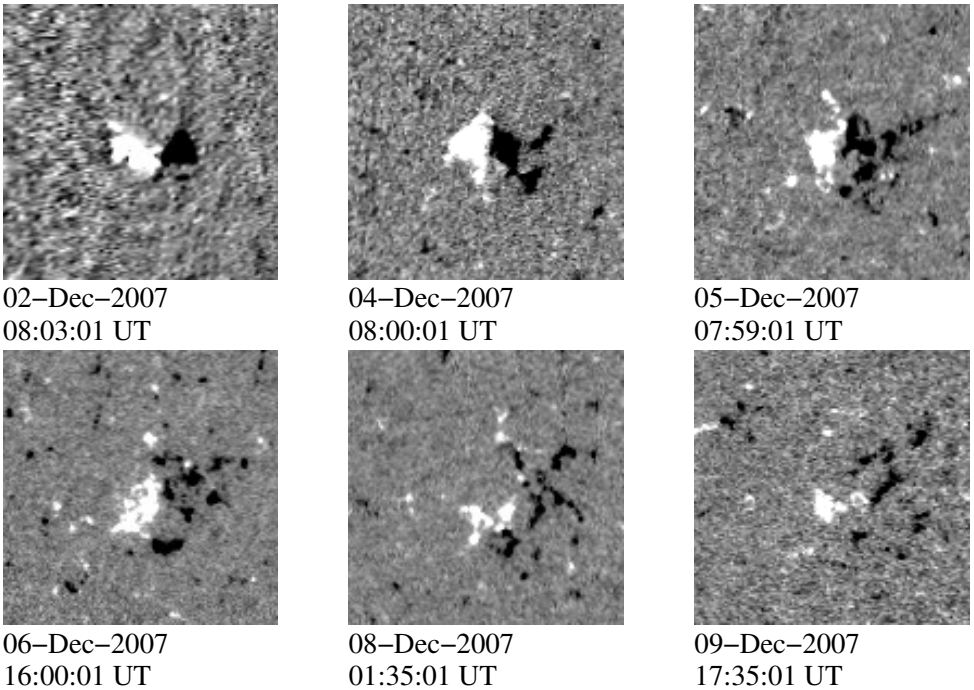

Figure 3.1: Time sequence of de-rotated SOHO MDI line-of-sight magnetograms of AR10977 from 2 Dec 2007 to 9 Dec 2007. The white areas represent positive magnetic polarities and black areas represent negative magnetic polarities. The images saturate at ±100G. *A movie version of this figure, 'raw.mpg', can be found in the 'chapter3' directory on the accompanying CD.*

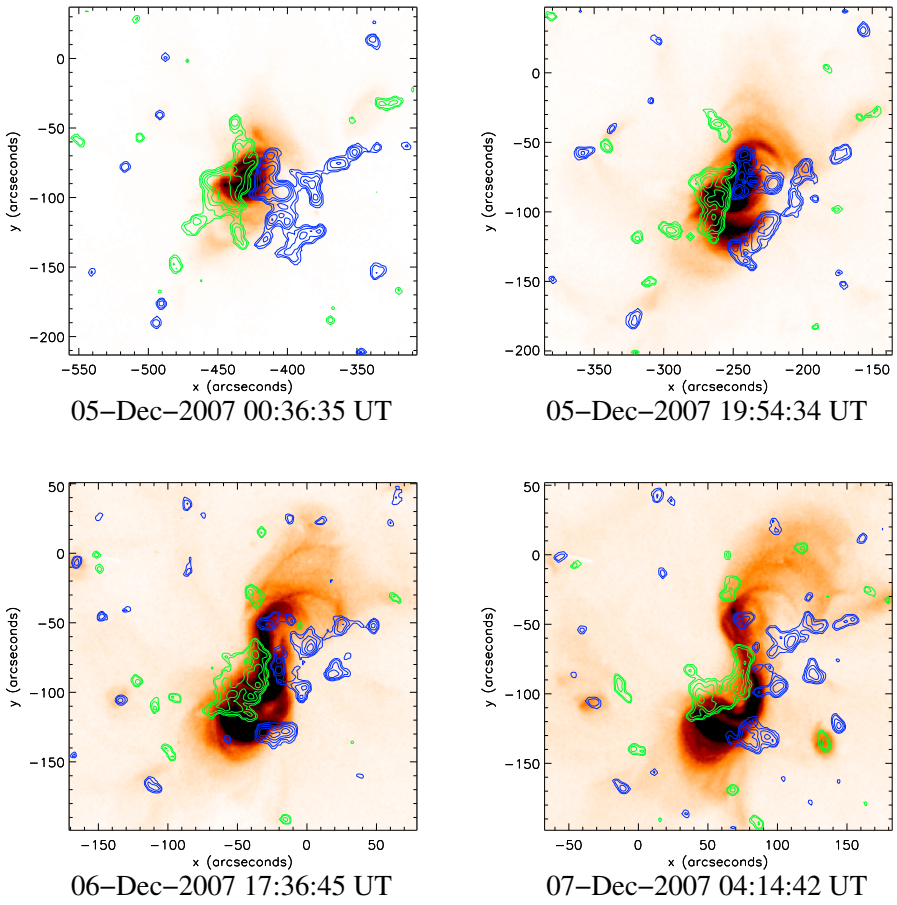

Figure 3.2: Selection of XRT images outlining the evolution of the emission from an unsheared arcade field (top left), to a sheared field (top right), a sigmoid (bottom left) which increases in size (bottom right). The green contours denote positive magnetic flux on the photosphere, and the blue contours denote negative magnetic flux. *A movie version of this figure, 'xrt.mpg', can be found in the 'chapter3' directory on the accompanying CD.*

from XRT illustrating the later stages of the evolution of the active region's coronal field. The images show a magnetic field structure that initially looks like an arcade (Figure 3.2 - top left), then becomes more sheared due to the bipole's rotation (Figure 3.2 - top right). On the 6$^{\text{th}}$ Dec 2007 the X-ray emission takes on the appearance of a continuous forward S-shape - a sigmoid (Figure 3.2 - bottom left). This sigmoid grows in size (Figure 3.2 - bottom right) and then a B1.4-class GOES flare occurs at around 04:20 UT on the 7$^{\text{th}}$ Dec 2007. The flare was associated with an eruption and the temporary disappearance of the sigmoid. Green et al. (2011) proposed that the sigmoid contained a flux rope which became unstable and then either fully or partly erupted.

3.3 Data Preparation

The magnetograms used in this study were taken by the Michelson Doppler Imager (MDI) onboard the Solar and Heliospheric Observatory (SOHO) spacecraft. Each magnetogram provides the line of sight (LOS) magnetic flux density (Mx cm^{-2}). In total 129 full disk magnetograms are used, each with a spatial resolution of 1.97790" per pixel and cadence of 96 minutes. The first observation is at 00:03 UT on the 2nd of December 2007, while the final observation is at 22:23 UT on the 10$^{\text{th}}$ December 2007. Each full disk magnetogram was de-rotated so that AR10977 – which was in the southern hemisphere of the Sun – lies at disk centre. Following this, each magnetogram was corrected for line of sight effects so that each pixel corresponded to the component of magnetic flux density normal to the photosphere. From the de-rotated and corrected images a 127 $\times$ 127 pixel image was extracted centered on the active region.

It is clear from Figure 3.1 that significant noise exists in the magnetogram frames over all times, but this is especially true in the early and late frames (e.g. the top-left and bottom-right frames of Figure 3.1) where the active region was close to the limb of the Sun. In order to reduce the noise and prepare the magnetograms so that they can be used as boundary conditions in the simulation several cleanup procedures were applied:

1. Noise Reduction.
2. Low Flux Removal.
3. Flux Balance.

The following subsections describe each of these procedures. Further preparation steps required to prepare the data for being used as a boundary condition in Hexa are also detailed.

3.3.1 Noise Reduction

Noise reduction was carried out in two phases. Firstly, frames were time averaged in order to try and remove noise. Secondly, small features were removed.

Time Averaging

In order to carry out the time averaging, the following operation was applied to each frame:

$$C_i = \left(\sum_{j=1}^{129} W_{ij} F_j \right) \left(\sum_{j=1}^{129} W_{ij} \right)^{-1} \tag{3.1}$$

Where C_i is the i^{th} cleaned frame, F_j is the j^{th} raw frame, and W_{ij} is the weighting function. Each cleaned frame is a linear combination of the 129 raw frames. This reduces the noise as assuming that the noise is random, averaging frames together will average the noise term towards zero.

Gaussian weighting and uniform (boxcar) weighting were both tested, and compared with no weighting. Gaussian weighting corresponds to the weighting function

$$W_{ij} = \exp\left(-\left[\frac{i-j}{\tau}\right]^2\right) \tag{3.2}$$

This means that the weighting of frames falls off as a Gaussian away from the i^{th} frame. τ is the separation at which the weighting falls to $1/e$, and was chosen to be 2 frames.

Uniform weighting is when a certain number of frames either side of the i^{th} frame are combined with equal weighting. In this case, each cleaned frame was an average of three raw frames. The weighting function that corresponds to this is:

$$W_{ij} = \sum_{k=i-1}^{i+1} \delta_{jk}, \tag{3.3}$$

where δ_{jk} is the Kronneker delta, such that $C_i = (F_{i-1} + F_i + F_{i+1})/3$

For the case of no time averaging, $W_{ij} = \delta_{ij}$, or simply, $C_i = F_i$. A comparison of Gaussian, boxcar and no time averaging is given at the end of Section 3.3.2.

Small Feature Removal

As well as removing the noise, small isolated magnetic flux features were removed since in the present study we are interested in the large-scale evolution of the active region and not the small-scale features such as network magnetic elements found at the boundaries of super-granular cells. This was achieved on a pixel-by-pixel basis, where for each pixel its eight neighbours were considered. If fewer than four of its neighbours had the same sign of flux then that pixel's value was set to zero. Pixels along the edges of the magnetograms - who had fewer than eight neighbours - had their values set to zero.

3.3.2 Low Flux Removal

Figure 3.3 shows example histograms of the cleaned and uncleaned magnetograms. In the Figure, it can be seen that up to about 25 Mx cm^{-2} the histogram of the raw data (top left panel) is roughly flat. These values are interpreted to be background flux values, related to the 'quiet' regions around the active region. All pixels with absolute flux less than 25 Mx cm^{-2} were set to zero in the cleaned magnetograms.

Figure 3.4 shows frame 13 for each time averaging method, after small feature and low flux removal. A comparison of the different time averaging methods showed that the Gaussian time averaging was the most effective at removing noise, followed by the uniform time averaging, and then no time averaging. Gaussian averaging was thus used as the time averaging method for the data to be fed into Hexa.

3.3.3 Flux Balance

Finally, each magnetogram frame was adjusted so that it was in exact flux balance. Due to the closed boundary conditions on the sides and top of the computational box in Hexa, in order to keep the magnetic field divergence-free, the flux through the magnetogram

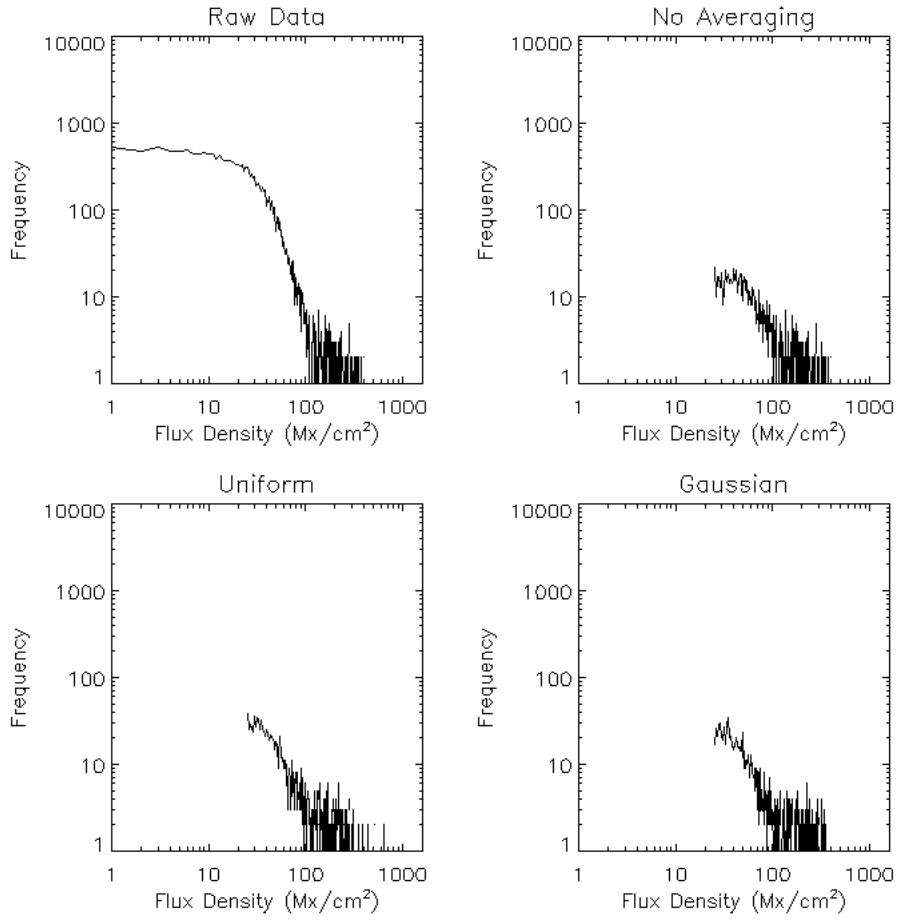

Figure 3.3: A histogram of $|B_z|$ for the 10^{th} frame for the raw, Gaussian time averaged, boxcar (uniform) averaged and no time averaged magnetograms. Note that for the raw frame, the histogram is roughly flat for flux values less than about 25 Mx cm^{-2}.

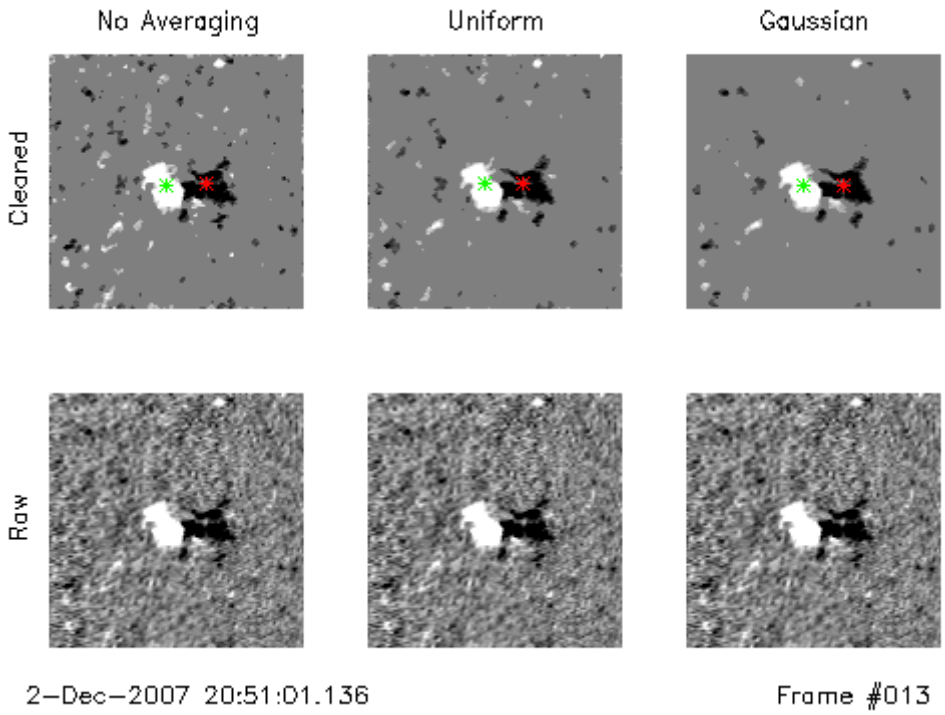

Figure 3.4: A comparison of the time averaging methods (after small feature and low flux removal) for the thirteenth frame. Also displayed is the raw frame (repeated three times) for comparison. The green and red stars are the centres of flux for the positive and negative flux regions. The images are saturated at ±100 G. *A movie version of this figure, 'cleaning.mpg', can be found in the 'chapter3' directory on the accompanying CD.*

must be zero. Flux balance was achieved by calculating the signed flux of each frame. For each frame the number of non-zero-valued pixels was counted, and the signed flux was then divided by this number. Finally, the imbalanced flux per non-zero valued pixel was subtracted from every non-zero valued pixel. This method ensured that pixels that initially had zero flux, remained at zero flux and adjusted every non-zero valued pixel equally. The mean correction per pixel was 8 Mx cm^{-2}, with a maximum correction of 17 Mx cm^{-2}. Since at an earlier stage all pixels with absolute values of flux density lower than 25 Mx cm^{-2} were set to zero, no pixels changed sign during the flux balancing procedure. Figure 3.5 shows the flux imbalance before and after the correction.

In this study, we have applied several cleanup procedures, namely time averaging, removal of isolated features, removal of low flux values and flux balancing. This is in contrast to Mackay et al. (2011) who only carried out the flux balancing necessary for the magnetograms to be used as a lower boundary condition in their simulation. The motivations for carrying out the additional cleanup procedures in this study are as follows. Firstly, AR10977 was close to the limb of the Sun at the beginning and end of the observations, resulting in the de-rotated magnetograms being very noisy at these times. This was not the case for the observations used in the Mackay et al. (2011) study, whose time series covered the evolution of the active region in a four day window centred around the time of central meridian passage. Secondly, the cleaned magnetograms describe a smooth, continuous evolution of the photospheric magnetic field, which is numerically easier to simulate.

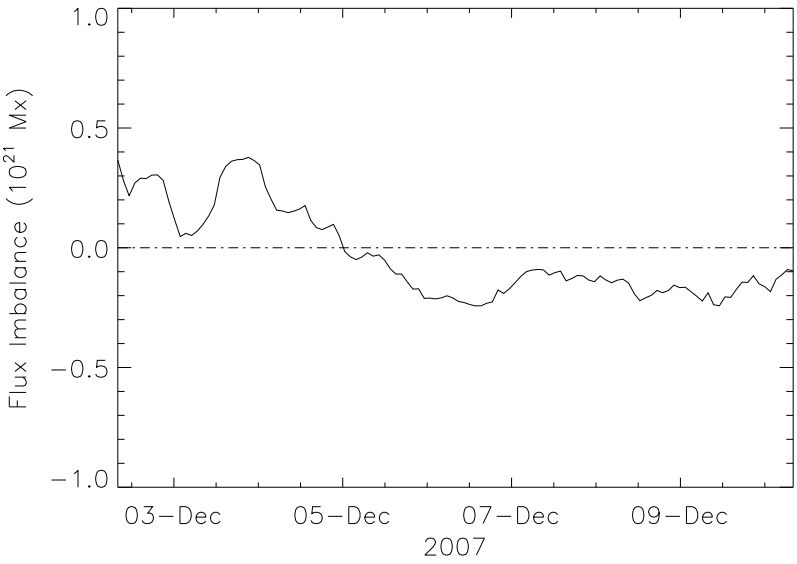

Figure 3.5: Flux imbalance of the active region as a function of time from 2007 December 2 08:03 UT before (solid line) and after (dot-dashed line) flux balancing.

Such a description is a more desirable driver for the magnetofrictional simulation than the noisy uncleaned magnetograms, as significant noise and numerical problems can occur in the simulation due to small, rapidly varying unresolved features. In Section 3.7 a simulation is run using uncleaned magnetograms so that the effect the cleaning has on the evolution of the simulated active region can be determined.

3.4 Active Region Properties

To simulate the evolution of the coronal magnetic field of AR10977 the magnetograms discussed in Section 3.2 are used as lower boundary conditions in the simulation. Due to their noisy nature it is useful to clean them up before they are used. The clean-up process is described in Section 3.3, where a number of steps are applied (e.g. noise reduction, removal of isolated fields below |25|G and flux balancing). These steps are designed to remove small scale random magnetic elements, but retain the overall evolution of the large-scale polarities within the active region. In this section the properties of AR10977 deduced from the cleaned magnetograms are presented.

Figure 3.6 shows the variation of the positive (dashed line) and unsigned negative flux (dotted line) prior to flux balance, and the flux-balanced total flux divided by two (solid line) within the active region. From this figure it is clear that both the positive and negative polarities follow a similar behaviour before and after the flux balancing has been applied. The plot starts at 08:03 UT on the 2^{nd} Dec 2007, corresponding to the sixth frame from the original set of observations. From Figure 3.6 it can be seen that both the positive and negative active region flux increases over the first two days of observations due to flux emergence. After the second day it decreases mainly due to two significant flux cancellation events on the 5^{th} and 7^{th} Dec 2007. Within each of these events approximately 3×10^{20} Mx is cancelled. These correspond to the cancellation events seen in Figure 3.1

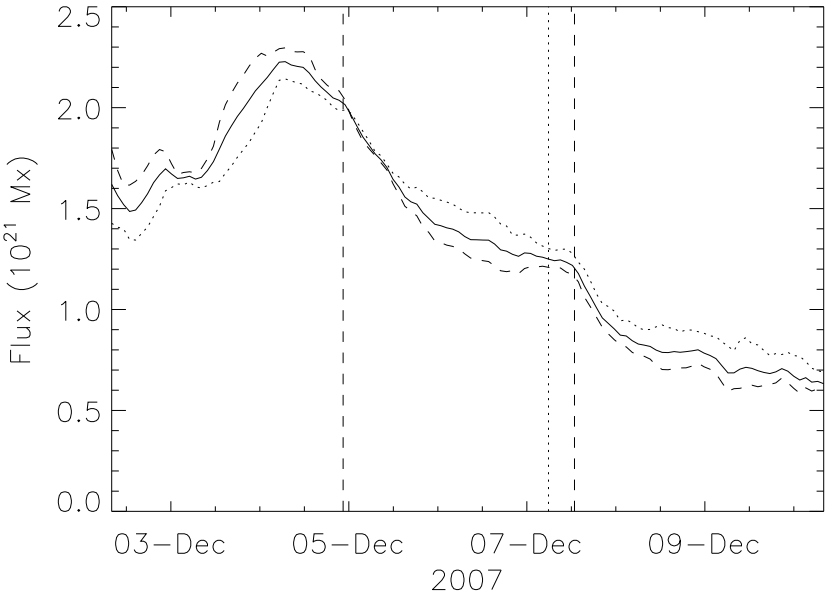

Figure 3.6: Positive (dashed line), negative (dotted line) and flux-balanced total flux divided by two (solid line) flux of the active region as a function of time from 2007 December 2 08:03 UT. The vertical dashed lines denote the time of onset of the two main flux cancellation events. The dotted vertical line is the time of the observed B1.4-class GOES flare.

(top centre and bottom centre).

A useful quantity to calculate is the tilt angle of the active region - the angle the line between the centres of positive and negative flux makes with the east-west line. First the centres of flux for the positive and negative polarities are calculated by

$$\mathbf{r}_{\pm} = \left(\int \mathbf{r} B_{\pm} dA \right) \left(\int B_{\pm} dA \right)^{-1}$$

where $\pm$ represents either the positive or negative flux, $\mathbf{r}$ is a position vector and A is the area. The tilt angle (θ) was then calculated by

$$\theta = \arctan \left(\frac{(\mathbf{r}_{-} - \mathbf{r}_{+})_y}{(\mathbf{r}_{-} - \mathbf{r}_{+})_x} \right)$$

where the x and y subscripts denote the x and y components of the vector $\mathbf{r}_{\pm}$.

In Figure 3.7 the variation of the tilt angle as a function of time is plotted. The solid line is the tilt angle after flux balance while the stars denote the tilt angle prior to flux balancing. Both tilt angles show a similar evolution where it can be seen that the flux correction – which is necessary to run the 3D simulation – does not change the overall behaviour of the active region. From the start of the observations until the 4^{th} Dec 2007, the negative polarity region rotates in a clockwise sense, with the tilt angle becoming negative, peaking around $-10°$. However late on the 5^{th} Dec 2007 the sense of the rotation of the negative polarity reverses to counter-clockwise, where the tilt angle increases towards positive values almost linearly for the remaining duration of the observations.

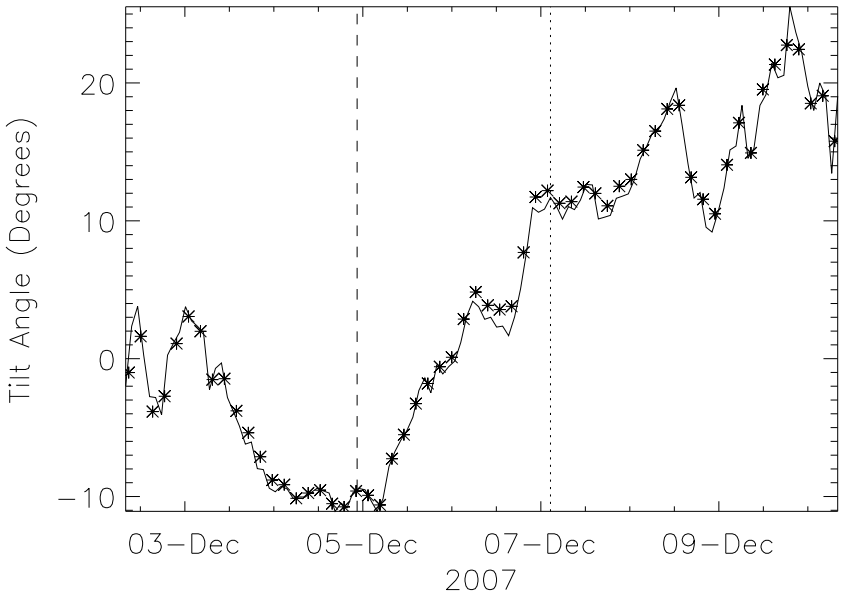

Figure 3.7: Tilt angle of the active region in degrees as a function of time from 2007 December 2 08:03 UT. The vertical dashed line denotes the time of onset of the first main flux cancellation event. The dotted vertical line denotes the time of the flare.

3.5 Further Preparation Steps

3.5.1 Generation of the Lower Boundary Condition

Before the magnetograms can be used as boundary conditions in Hexa, several more preparation steps have to be taken. Firstly, frames 1-5 and 125-129 were discarded as the active region was very close to the limb of the Sun, and thus the signal was very noisy. In addition, the time averaging was less effective for the first few and last few frames as each cleaned frame was made from fewer highly-weighted raw frames. This resulted in 120 cleaned frames that could be used in the simulation. Secondly, the 127×127 magnetograms were resized to 254×254 and placed in a square of size 256×256. This was so that the computational box in Hexa had a higher spatial resolution. Thirdly, as Hexa solves the un-curled induction equation, with $\mathbf{A}$ as the primary variable, we must determine the magnetic vector potentials on the base, A_{xb} and A_{yb}, which correspond to B_z from the cleaned magnetograms. This is carried out as follows:

1. Each of the observed magnetograms, $B_z(x, y, k)$ – for $k = 1 \rightarrow 120$, are taken, where k represents the discrete 96 min time index.

2. Next the horizontal components of the vector potential at the base, $z = 0$, are written in the form,

$$A_{xb}(x, y, k) = \frac{\partial \Phi}{\partial y},$$
$$A_{yb}(x, y, k) = -\frac{\partial \Phi}{\partial x}$$

where Φ is a scalar potential.

3. For each discrete time index k, the equation

$$B_z = \frac{\partial A_{yb}}{\partial x} - \frac{\partial A_{xb}}{\partial y}$$

then becomes,

$$\frac{\partial^2 \Phi}{\partial x^2} + \frac{\partial^2 \Phi}{\partial y^2} = -B_z. \tag{3.4}$$

which is solved using a multigrid numerical method. Details of this method can be found in the papers by Finn et al. (1994) and Longbottom (1998) and references therein.

On solving for the scalar potential, Φ, this determines the horizontal components of the vector potential on the base (A_{xb}, A_{yb}) for each discrete time interval, 96 minutes apart. To produce a continuous time sequence between each of the observed distributions, a linear interpolation of A_{xb} and A_{yb} between each time interval k and $k+1$ is carried out. Between each observation 500 interpolation steps are used. By linearly interpolating the horizontal components of the vector potential on the base, this effectively evolves the magnetic field from one state to the other. Numerically, it also means that undesirable effects such as numerical overshoot or flux pile up at cancellation sites do not occur and no additional numerical techniques to remove these are required.

The technique described above means that there are two timescales involved in the evolution of the lower boundary condition. The first which is 96 minutes is the time scale between observations, the second which is 11.52 seconds is the time-scale introduced to produce the advection of the magnetic polarities between observed states by interpolation, along with the relaxation of the coronal field. The process described above exactly reproduces the cleaned magnetograms at each 96 min discrete time interval and therefore produces a highly accurate description of the magnetogram observations and the life of the active region.

The vector potentials at the base are incorporated into Hexa's grid by

$$A_x(i+\tfrac{1}{2}, j, 1) = A_{xb}(i+\tfrac{1}{2}, j), \tag{3.5}$$
$$A_y(i, j+\tfrac{1}{2}, 1) = A_{yb}(i, j+\tfrac{1}{2}), \tag{3.6}$$

for $i = 1, N_x$ and $j = 1, N_y$ and where A_x and A_y are the Hexa variables.

Figure 3.8 displays a comparison on the cleaned magnetogram (left) and the normal magnetic field component used as the lower boundary condition in the simulation (right) at 07:59 UT on the 5th December 2007. A good agreement between the two is found. A movie comparing the full time series can be viewed in movie1.mpg. At this point it should be noted that the above technique only specifies A_{xb}, A_{yb} at $z = 0$. It however does not specify A_z which lies one-half of a grid point up and is determined by the induction equation (Equation 2.1). Non-potential effects near the base, as a result of the evolving lower boundary condition, may be contained within this term. In Section 4.6 the limitations of using line of sight magnetograms (which only prescribe B_z) are discussed.

3.5.2 Generation of an Initial Coronal field

An initial coronal field for the active region must now be prescribed which will be evolved using the cleaned magnetograms with the magnetofrictional method. This is extrapolated from the cleaned magnetogram frame corresponding to 08:03 UT on December 2$^{\text{nd}}$ 2007 on

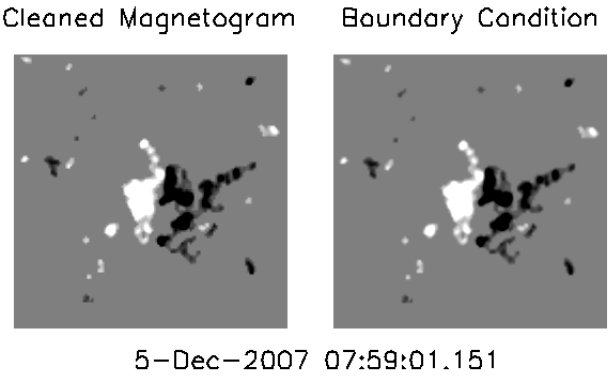

Figure 3.8: Comparison of a cleaned magnetogram (left) and the corresponding lower boundary condition used within the simulation (right) at 07:59:01 UT on the 5th December 2007. The images saturate at ±100 G. *A movie version of this figure, 'compare.mpg', can be found in the 'chapter3' directory on the accompanying CD.*

a grid of 256^3 cells. The sides of the cube range from $0 < x, y, z < 6$ in non-dimensionalised units, where one unit in length is equal to 30,352 km on the Sun. This means that $\Delta_x = \Delta y = \Delta z = 711$ km.

The method used to produce the initial condition is described in Finn et al. (1994) and for further details see Mackay et al. (2011). Since no vector magnetic field data is available to constrain the initial condition, a potential field is used. This potential initial condition is displayed in Figure 3.9. Although unique, a potential field has the limitation that no electric current systems exist within it and correspondingly it is the field of lowest energy for any given boundary conditions. It should be noted that while we use a potential field for the initial condition, we do not expect the field of the active region to be potential at this time. Due to this additional simulations were also run using LFF fields. These simulations are described in Sections 4.3 and 4.5.

3.5.3 Solution of the Induction Equation

Hexa solves the un-curled induction equation,

$$\frac{\partial \mathbf{A}}{\partial t} = \mathbf{v} \times \mathbf{B} - \eta \mathbf{j} + \frac{\mathbf{B}}{B^2} \nabla \cdot \left(\eta_4 B^2 \nabla \alpha\right) + \eta_0 \nabla (\nabla \cdot \mathbf{A}), \tag{3.7}$$

Where $\mathbf{v}$ is the magnetofrictional velocity, expressed by

$$\mathbf{v} = \frac{1}{\nu} \frac{\mathbf{j} \times \mathbf{B}}{B^2}, \tag{3.8}$$

η is the Ohmic diffusivity coefficient, η_4 is the hyperdiffusivity coefficient and η_0 is the diffusivity coefficient designed to ensure the Coulomb gauge is maintained throughout the simulation. Unless otherwise stated, η and η_4 are zero, whilst

$$\eta_0 = 0.05 \frac{\Delta x^2}{\Delta t}, \tag{3.9}$$

where Δx and Δt are the grid spacings and timesteps in Hexa respectively. For a full description of Hexa, please see Chapter 2 Section 2.2.

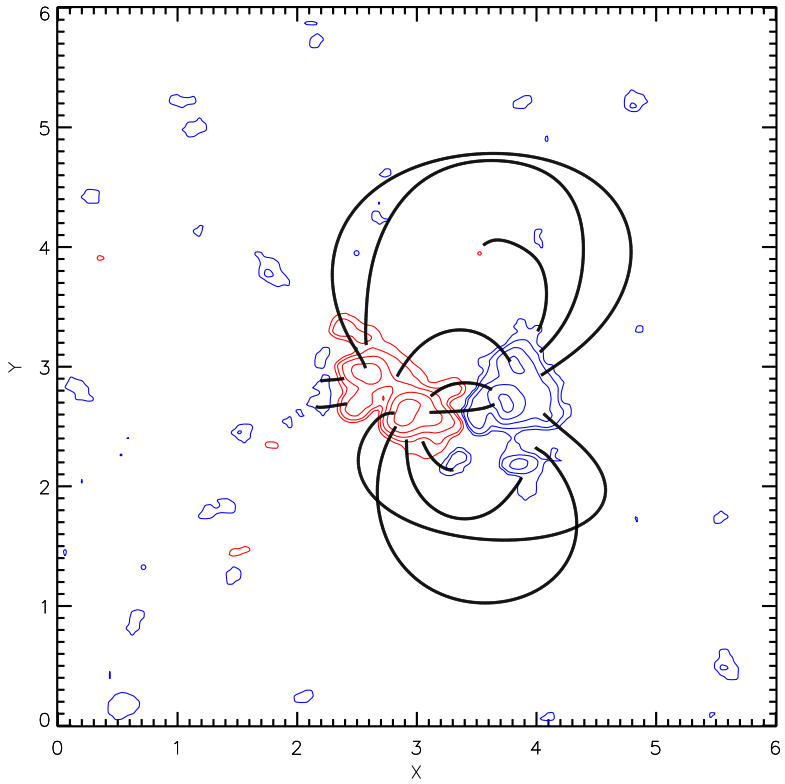

Figure 3.9: Selection of field lines (solid black lines) illustrating the potential field initial condition where red and blue contours denote positive and negative flux respectively. This corresponds to 08:03 UT on 02-Dec-2007.

3.6 The Primary Simulation

In this section the results of the main simulation that was run will be described in detail. This simulation used cleaned magnetograms and did not use Ohmic diffusion or hyperdiffusion. Sections 3.7, 3.8 and 3.9 describe the results of simulations using uncleaned magnetograms, Ohmic diffusion and hyperdiffusion respectively.

3.6.1 Magnetic Field Line Evolution

The evolution of the coronal field in the simulation will now be described. To describe sheared field lines across the PIL, first the shear of the field must be defined. The shear is defined relative to the normal of the PIL. Consider a field line that has a component that lies parallel to the PIL. When viewed from the positive polarity side of the PIL, if the component parallel to the PIL is directed to the left/right then the field line is defined to have sinistral/dextral shear. This is pictorially represented in Figure 3.10.

Figure 3.11 displays a selection of field line plots from the simulation, at times approximately corresponding to the XRT observations presented in Figure 3.2. The field lines plotted in Figure 3.11 highlight the features observed by XRT that are reproduced by the simulation. In the top left panel of Figure 3.11 - corresponding to the top left panel of Figure 3.2 - arcade field is visible in the simulation at the same location as the observed XRT arcade field. While this shows good agreement, the simulated field has almost no shear

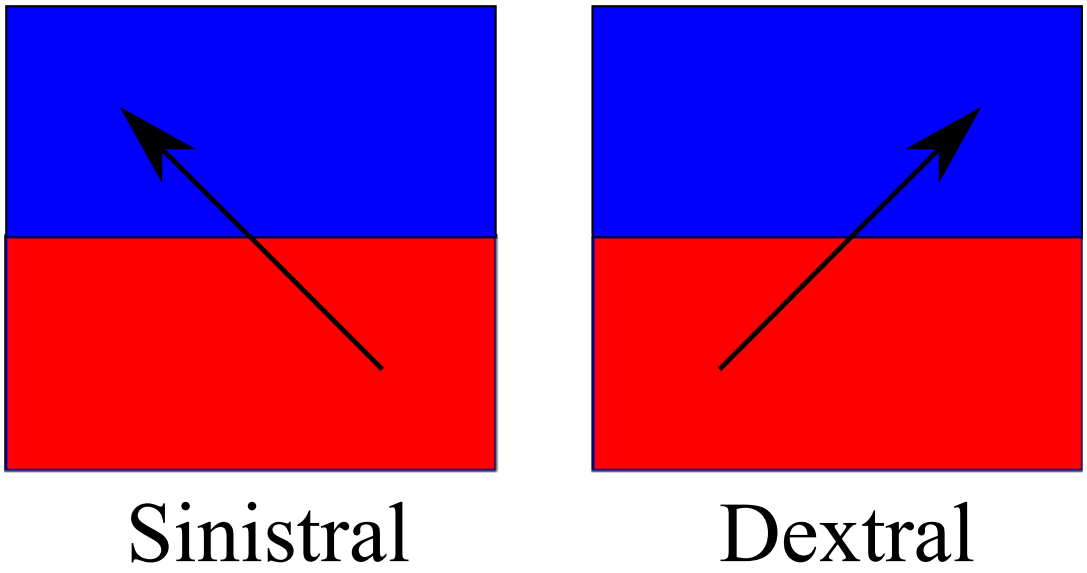

Figure 3.10: Schematic explaining the sinistral and dextral classifications for shear as used in this thesis, where red and blue represent positive and negative magnetic flux respectively. The arrows represent magnetic field lines.

whilst the observed field has a slight sinistral shear. This difference is most likely due to the potential initial condition. The curved J-shaped arcade field in the south of the field line plot is in good agreement with the faint J-shaped emission in the XRT observation.

In the top right panel of Figure 3.11 - corresponding to the top right panel of Figure 3.2 - a flux rope with S-shaped field lines as seen in projection has formed at the location of the strongly sheared field observed by XRT. The extent of the simulated flux rope is in very good agreement with the extent of the observed emission. The arcade field lines in the south of the active region match well with the arcade-like emission in the XRT observations. The curved field lines in the north of the active region also match with the faint loops in the XRT observations.

In the bottom left panel of Figure 3.11 - corresponding to the bottom left panel of Figure 3.2 - the S-shaped field lines are clearly visible at the location of the observed sigmoid. The northern half of the sigmoid is very well described by the simulation, however the southern half of the flux rope terminates further north than the observed sigmoid. Arcade field lines are present in the south of the active region as is seen in the observations. The simulated arcade agrees relatively well with the observed arcade. One difference between the simulated and observed arcade is that the foot-points of the arcade in the negative polarity region in the simulation are on the leading (relative to rotation) side of the flux fragment, whilst in the observations the foot-points appear to be on the trailing side of the flux fragment.

In the bottom right panel of Figure 3.11 - corresponding to the bottom right panel of Figure 3.2 - the S-shaped field lines belonging to the flux rope have increased in length, resulting in a larger S-shaped feature. This is also seen in the XRT observations. Whilst in the XRT observations the southern foot-point of the sigmoid has extended further south, in the simulation the southern foot-points of the flux rope have extended further west (to the left in Figure 3.11). The arcade in the south of the active region present in the observations is also visible in the field line plot, and is in general agreement with the observed arcade.

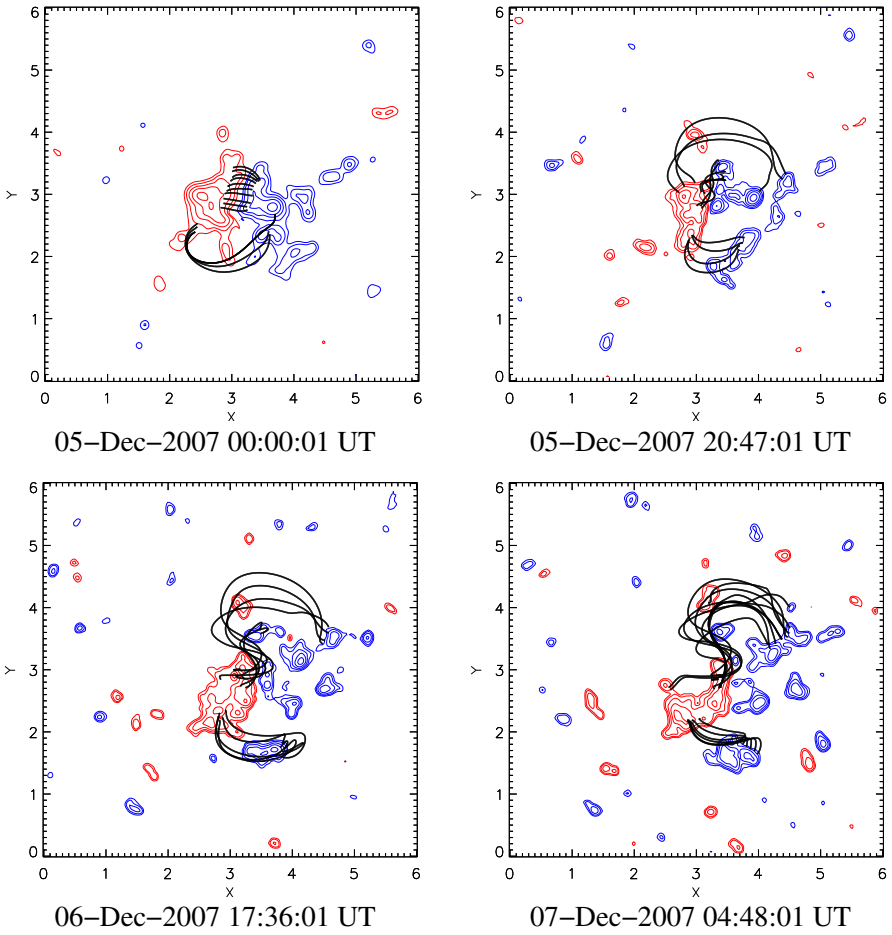

Figure 3.11: Field line plots generated from the primary simulation at various times approximately corresponding to the times in Figure 3.2. The red and blue contours denote positive and negative photospheric flux respectively.

The formation of the flux rope present in the top-right and bottom panels of Figure 3.11 will now be described in detail. In the simulation the flux rope had formed by 14:23 UT on the 5th December 2007. Figure 3.12 outlines the formation of the flux rope field lines. In Figure 3.12 (left) two sheared arcade field lines can be seen. As a result of the convergence of the positive and negative magnetic polarities - leading to flux cancellation - the footpoints are advected towards the PIL. Reconnection occurs at the PIL, producing a long, helical field line (Figure 3.12 – right), and a small loop, which was then removed by the flux cancellation. This is in agreement with the flux rope formation mechanism proposed by van Ballegooijen & Martens (1989).

By the fifth day of the simulation (07-Dec-2007 - 09:36 UT) the field lines have become strongly twisted and the magnetofrictional method can no longer properly describe the coronal evolution. These twisted field lines are especially apparent in the flux rope, and imply that it has become unstable. The magnetofricional method, which is designed to relax a field to a NLFF equilibrium therefore breaks down as there is not an equilibrium state for the field to relax to. Such twisted field lines are visible in Figure 3.13. The simulation's results are therefore not to be trusted after the fifth day (denoted by a solid vertical line in Figure 3.16). It is interesting to note that this time is just after the occurrence of a flare which was observed at 04:20 UT on 7 Dec 2007. This indicates that

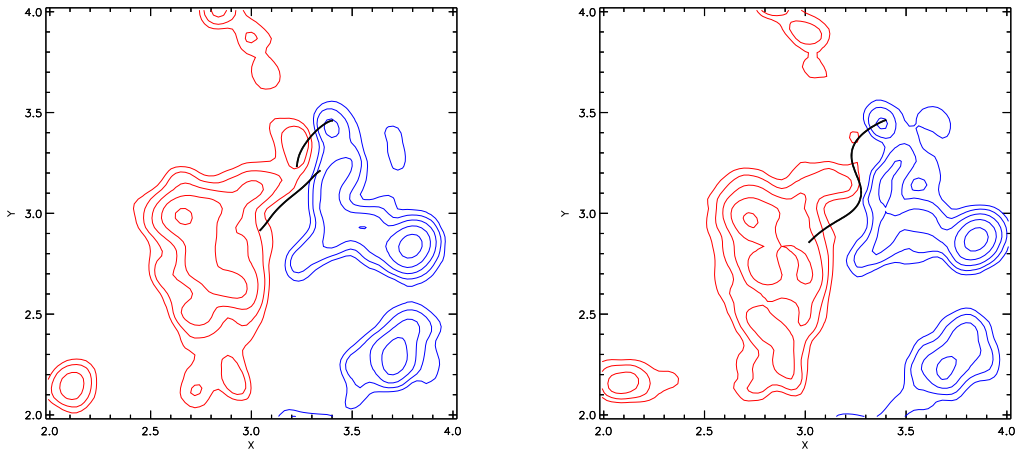

Figure 3.12: Formation of the flux rope. Left: The sheared arcade is advected towards the polarity inversion line (PIL). Right: Reconnection occurs between the northerly footpoint of the southern field line, and the southerly footpoint of the northerly field line, producing a long helical field line and a short field line which is removed by flux cancellation. The left and right panels correspond to 09:35 UT and 14:23 UT on the 5$^{\text{th}}$ Dec 2007 respectively. The red and blue contours denote the positive and negative photospheric field respectively.

the build-up phase to eruption has been successfully followed in the simulation. To follow the dynamics of the eruption a full MHD simulation would have to be run, for example see Pagano et al. (2013).

3.6.2 Flux Rope Properties

The flux content within the flux rope and its height are calculated as a function of time. To compute these quantities, a cut of B_y in the x-z plane centred at $y = 3.4$ is taken. This y coordinate approximates the location of the mid-point of the flux rope axis throughout the duration of the simulation. The location (x_0, z_0) of the maximum of B_y in the cut is determined. From this the height of the flux rope from the photosphere is defined as z_0. Figure 3.14 (left) displays the height of the flux rope with time. It shows a near linear increase, implying that the flux rope was rising at almost constant velocity, calculated to be 63 m s^{-1}. The centre of the flux rope reached a height of 11 Mm by the time of the observed flare (dotted line in Figure 3.14 (left)).

In order to calculate the flux contained within the flux rope, first the full width half maximum (FWHM) of the peak of B_y about (x_0, z_0) in the cut is determined. This is found in the x-direction by determining the points x_1 and x_2 either side of the maximum, x_0, where B_y decreases to one half of the value at x_0. The FWHM is then calculated by $r_{\text{FWHM}} = |(x_1 - x_2)|/2$ and the flux of the flux rope is calculated by integrating B_y within a circle of radius $4r_{\text{FWHM}}$ centred around the point of maximum B_y. Upon investigating various radii of circles to determine the flux in the flux rope, it was found that the vast majority of the flux rope flux was contained within a radius of $4r_{\text{FWHM}}$. This was thus chosen as the radius of the circle through which the flux values quoted in this study are determined.

Figure 3.14 (right) shows the evolution of the flux rope's flux with time. The flux

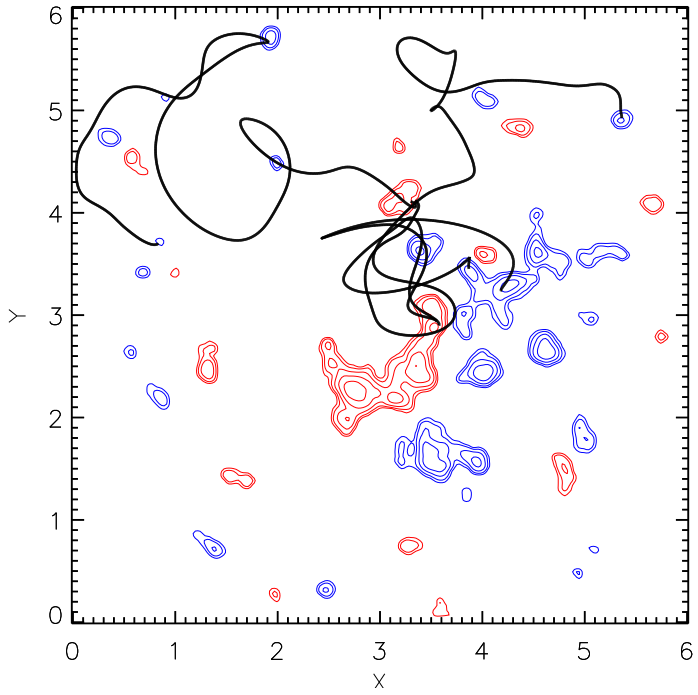

Figure 3.13: A series of twisted field lines belonging to the flux rope at 09:36UT on the 7th December 2007.

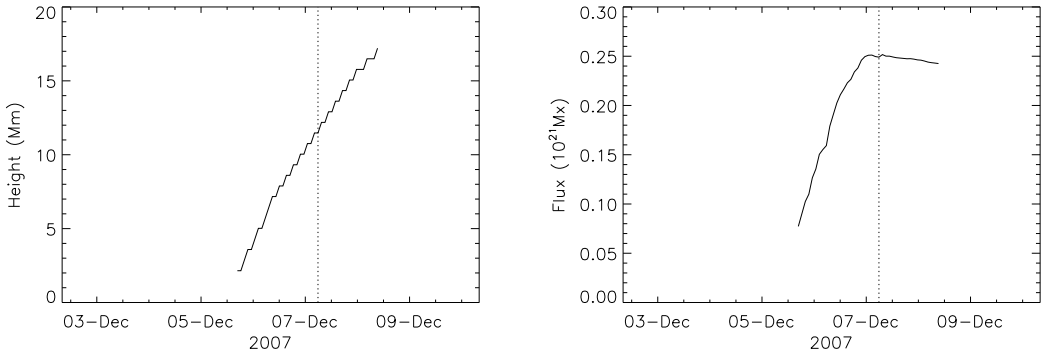

Figure 3.14: Evolution of the height (left) and flux (right) of the flux rope with time from 08:03 UT on December 2, 2007. The vertical dotted line denotes the time of the flare observed by XRT.

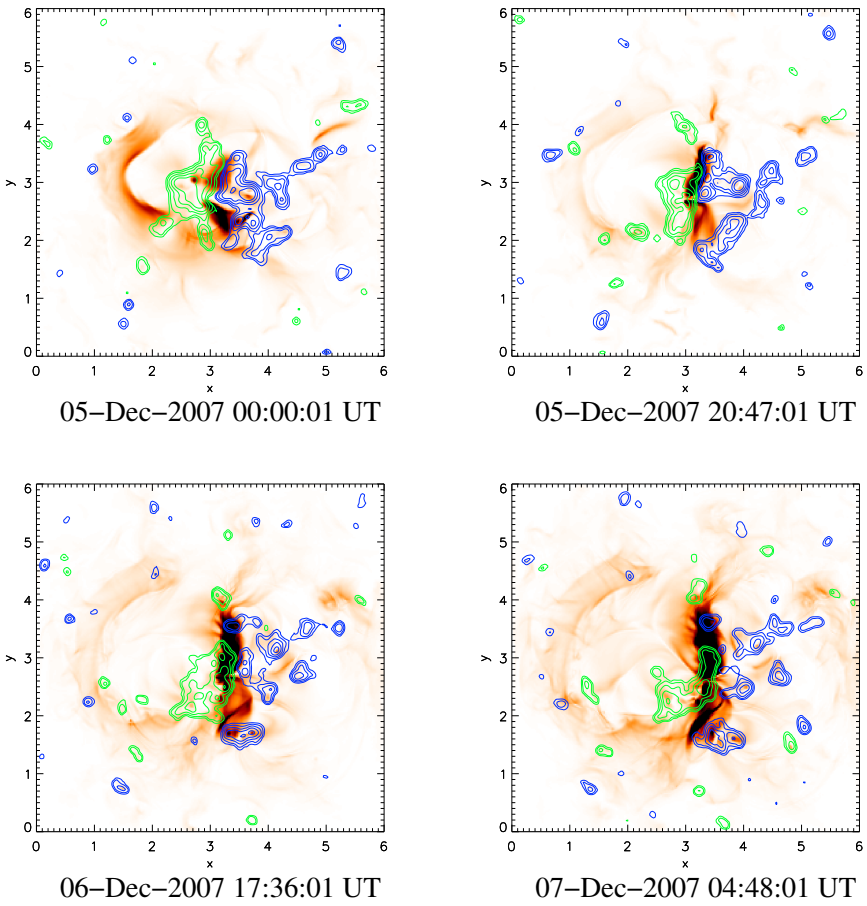

Figure 3.15: j^2 emission proxy images generated from the simulation at various times roughly corresponding to the times in Figure 3.2. The images display a strong j^2 proxy emission in the same location as the observed sigmoid. The colour scaling saturates at one-quarter of the maximum value of the LOS integrated j^2 for each image. *A movie version of this figure, 'emission_proxy.mpg', can be found in the 'chapter3' directory on the accompanying CD.*

initially increases almost linearly with time, then levels off at around 2.5×10^{20}Mx. The increase in the flux corresponds to the flux cancellation event at the centre of the active region where axial flux is built into the flux rope. It should be noted that although the flux contained within the flux rope levels off, flux cancellation still occurs in the active region. This flux cancellation, however, does not act to build additional flux into the flux rope as it occurs at a different location. At the time of the first flare (denoted by the dotted vertical lines in Figure 3.14) the flux within the flux rope is approximately 20% of the active region flux at that time.

3.6.3 Comparison to XRT images

We now compare the simulation results to the XRT images through computing a simple representation of the XRT images. This representation is achieved by assuming that the emission in the XRT images is due to Ohmic heating, which is proportional to j^2. To produce a j^2 emission proxy of XRT images, the square of the current density is

calculated at all points within the simulation and integrated along the z direction. By doing so, we calculate the emission proxy in the same manner as Meyer, Mackay, van Ballegooijen & Parnell (2013). It should be noted that Cheung & DeRosa (2012) carried out a similar approach for calculating an emission proxy, however they determined the mean current density along field lines and used this to compute the proxy image. It should also be noted that X-ray emission can only be calculated accurately from a full magnetohydrodynamical simulation, as the emission is dependent upon a number of effects, such as density, temperature and thermal conduction. This is, however, beyond the scope of the present study and therefore we use the simpler j^2 emission proxy. For a discussion on the limitations of emission proxies derived solely from the current density, please see Section 2.4 of Cheung & DeRosa (2012).

Figure 3.15 displays the LOS integrated j^2 emission proxy for times approximately equal to those of the XRT observations presented in Figure 3.2. The top left panel of Figure 3.15, corresponding to the top left panel of Figure 3.2, displays strong j^2 proxy emission in the north of the active region, the same location as strong emission observed by XRT. Strong j^2 proxy emission is also present at the south of the active region, which is not visible in the XRT image. The C-shaped feature to the west of the active region is a flux rope formed due to boundary effects, and is unphysical. This is also faintly visible in the other panels of Figure 3.15. The top right panel of Figure 3.15, corresponding to the top right panel of Figure 3.2, again possesses strong j^2 proxy emission at the north of the active region in good agreement with the XRT observations, however the j^2 emission proxy feature in the south bears little resemblance to the emission observed in the south by XRT.

The bottom left panel of Figure 3.15, corresponding to the bottom left panel of Figure 3.2, has strong j^2 proxy emission at the same location as the observed sigmoid. The j^2 emission proxy image reproduces the observed emission at the northern end of the sigmoid well, but is not so good at reproducing the emission at the south of the sigmoid as the j^2 proxy emission stops further north than that seen in the XRT observation. The arcade emission visible in the south of the XRT observation is not present in the j^2 emission proxy image. The bottom right panel of Figure 3.15, corresponding to the bottom right panel of Figure 3.2, displays a j^2 emission proxy map very similar to that of the bottom left panel. The excess j^2 proxy emission in the south of the active region visible in every panel is due to a second flux rope formed in the simulation. The flux rope has the opposite direction of twist to that found in the northern flux rope, and its origins will be discussed in Section 3.10.

3.6.4 Free Magnetic Energy

Following the methodology of Mackay et al. (2011), we now investigate the evolution of free magnetic energy in the simulation. The free magnetic energy is defined as

$$E = \frac{1}{8\pi}\int (B^2 - B_p^2) d\tau \tag{3.10}$$

where B is the magnetic flux density from the simulation, and B_p is the magnetic flux density corresponding to a potential field extrapolated from the same boundary conditions as the simulation field. The potential fields are calculated in the same way as the initial condition potential field. Figure 3.16 shows the time-evolution of the free magnetic energy for the simulation. The sharp rise of the free magnetic energy around the start of the 5^{th} Dec 2007 corresponds to the first large flux cancellation event (denoted by the dashed vertical line in Figure 3.16) and the counter-clockwise shearing motions. The flux rope was

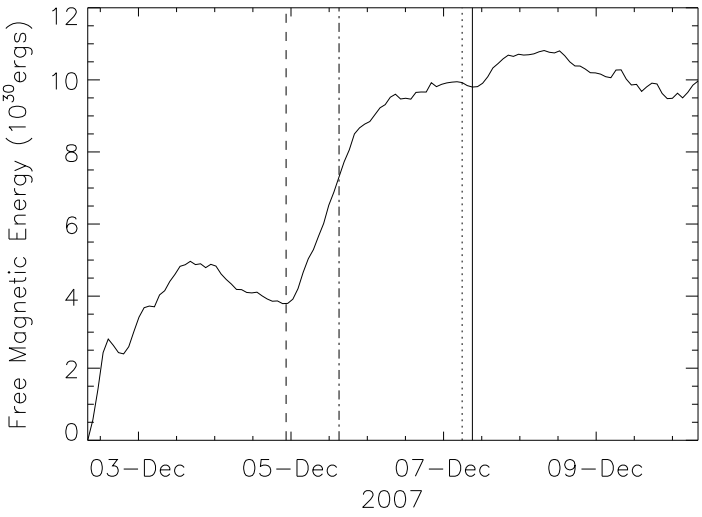

Figure 3.16: Free magnetic energy as a function of time from 08:03 UT on December 2, 2007. Note the sharp rise in free magnetic energy beginning late on the 4^{th} Dec. This corresponds to the time of the initial flux cancellation event and formation of the flux rope. The vertical dashed line denotes the time of onset of the main flux cancellation event. The dot-dashed vertical line denotes the time at which a flux rope has formed in the simulation. The dotted vertical line is the time of the observed B1.4-class GOES flare. Finally, the solid vertical line denotes the time after which we feel the magnetofrictional method can no longer be used to describe the evolution of the active region.

formed during this process (denoted by the dot-dash line in Figure 3.16). This suggests that much of the free magnetic energy is stored within the flux rope. Indeed, a plot of the free magnetic energy density integrated along the z-axis - Figure 3.17 - reveals that the majority of the free magnetic energy (white region) is stored at the location of the flux rope. The free magnetic energy contained within the flux rope is calculated at 04:48 UT on 7 Dec 2007 to be 6.1×10^{30} erg. This is more than sufficient to account for a B-class GOES flare, which is estimated to emit $\gtrsim 10^{27}$erg (Hannah et al. 2011).

3.6.5 Helicity

Motions at the photosphere inject magnetic helicity in addition to free magnetic energy into the corona. Helicity is a topological measure of the connectivity of the magnetic field, and is invariant in ideal MHD, and approximately conserved during magnetic reconnection (Berger 1999). Here we investigate the evolution of the relative helicity in our simulation in a manner consistent with Mackay et al. (2011). The relative helicity, which is gauge invariant, is calculated by

$$H_r = \int (\mathbf{A} \cdot \mathbf{B}) d\tau - \int (\mathbf{A}_p \cdot \mathbf{B}_p) d\tau \tag{3.11}$$

where $\mathbf{A}$ is the magnetic vector potential for the simulation's magnetic flux density, $\mathbf{B}$, and $\mathbf{A}_p$ is the magnetic vector potential for the potential field, $\mathbf{B}_p$, corresponding to the same photospheric field and BCs. Figure 3.18 displays the time evolution of the relative helicity for the simulation.

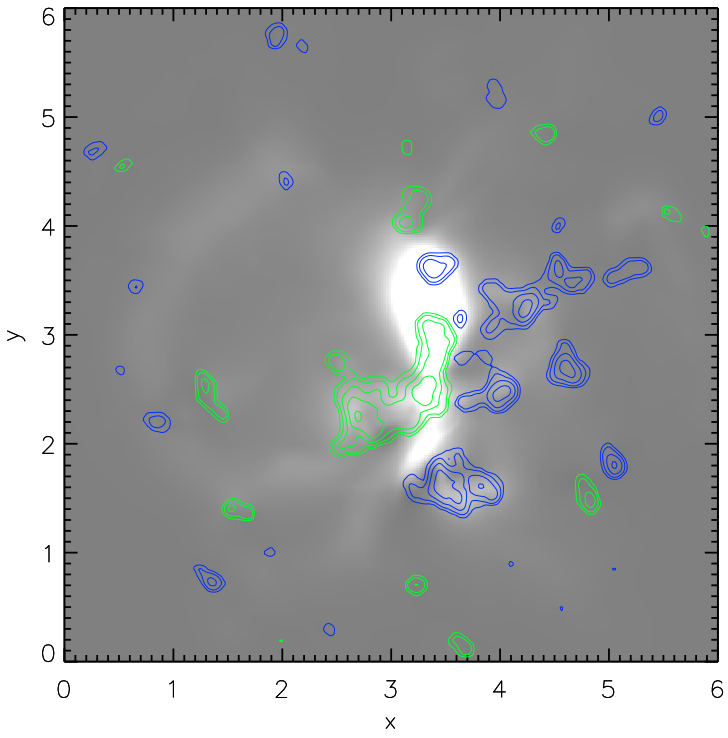

Figure 3.17: Integral of the free magnetic energy density along the z-axis at 04:48 UT on December 7, 2007, where white denotes areas of high free magnetic energy storage, and grey denote areas of low free magnetic energy storage.

In Figure 3.18 the relative helicity initially decreases until the beginning of the 4^{th} Dec, then increases almost linearly for the remainder of the simulation. This is qualitatively similar to the evolution of the tilt angle of the active region (Figure 3.7), which initially decreases until the 4^{th} Dec, remains constant for just over one day, then increases for the duration of the observations. With the exception of the first two days of the simulation, the general trend in the relative helicity is a linear increase, implying the near constant injection of positive helicity into the corona. This is in agreement with previous studies which show that the dominant sign of helicity in southern hemisphere active regions is positive (Pevtsov et al. 1995).

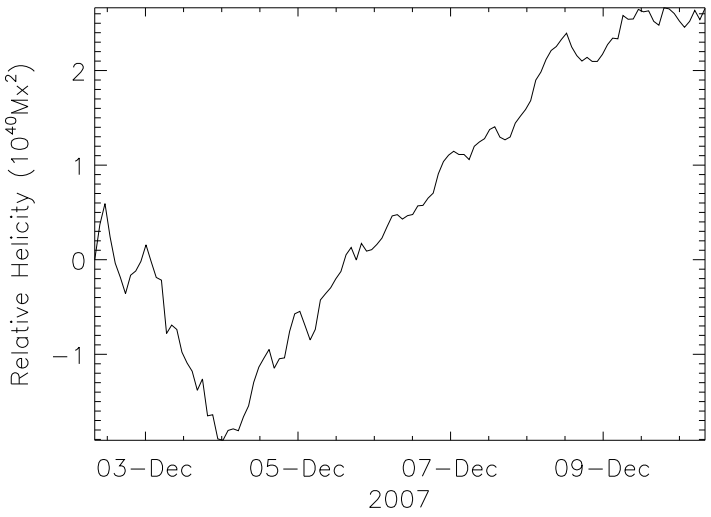

Figure 3.18: Relative helicity as a function of time from 08:03 UT on December 2, 2007.

3.7 Uncleaned Magnetograms

To determine the effect that the cleaning process has on the simulation results, a simulation was run using uncleaned magnetograms (though with the necessary flux balancing) and a potential field initial condition. Figure 3.19 displays a field line plot of the initial condition used. This section describes the results of this simulation.

3.7.1 Magnetic Field Line Evolution

Figure 3.20 displays a selection of field line plots at the same times as those corresponding to Figure 3.11, outlining the features present in the simulation corresponding to features in the X-ray observations (Figure 3.2). The field structures produced in the simulation at all times closely match the field structures in the simulation using cleaned magnetograms (Section 3.6 – Figure 3.11). This is reassuring, as the cleaning process is designed to retain the large-scale magnetic features which should dominate the large-scale evolution of the corona, whilst removing the small features which should have little effect on the large-scale evolution of the corona. Like the primary simulation, the flux rope associated with the X-ray sigmoid formed in the simulation on the 5$^{\text{th}}$ December. Also, like in the primary simulation, the field lines became strongly twisted on the fifth day of the simulation.

3.7.2 Flux Rope Properties

Figure 3.21 outlines the evolution of the northern flux rope's height and flux with time. These quantities were calculated using the techniques described in Section 3.6. Like in the primary simulation, the flux rope's height increases nearly linearly with time, and at the time of the flare has reached a height of 10Mm – 1Mm lower than the flux rope in the primary simulation. The flux rope's flux increases until the time of the flare, where it has reached a level of 2.3×10^{20} Mx – slightly lower than the flux contained within the flux rope in the primary simulation. This corresponds to roughly 18% of the active region's flux at this time.

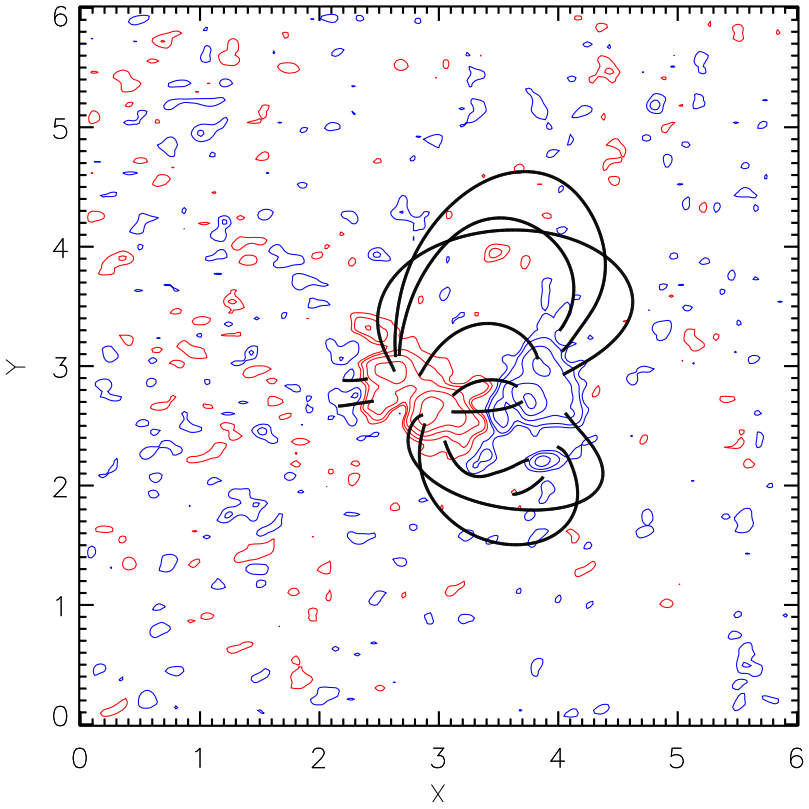

Figure 3.19: Selection of field lines (solid black lines) illustrating the potential initial condition using uncleaned magnetograms where red and blue contours denote positive and negative flux respectively.

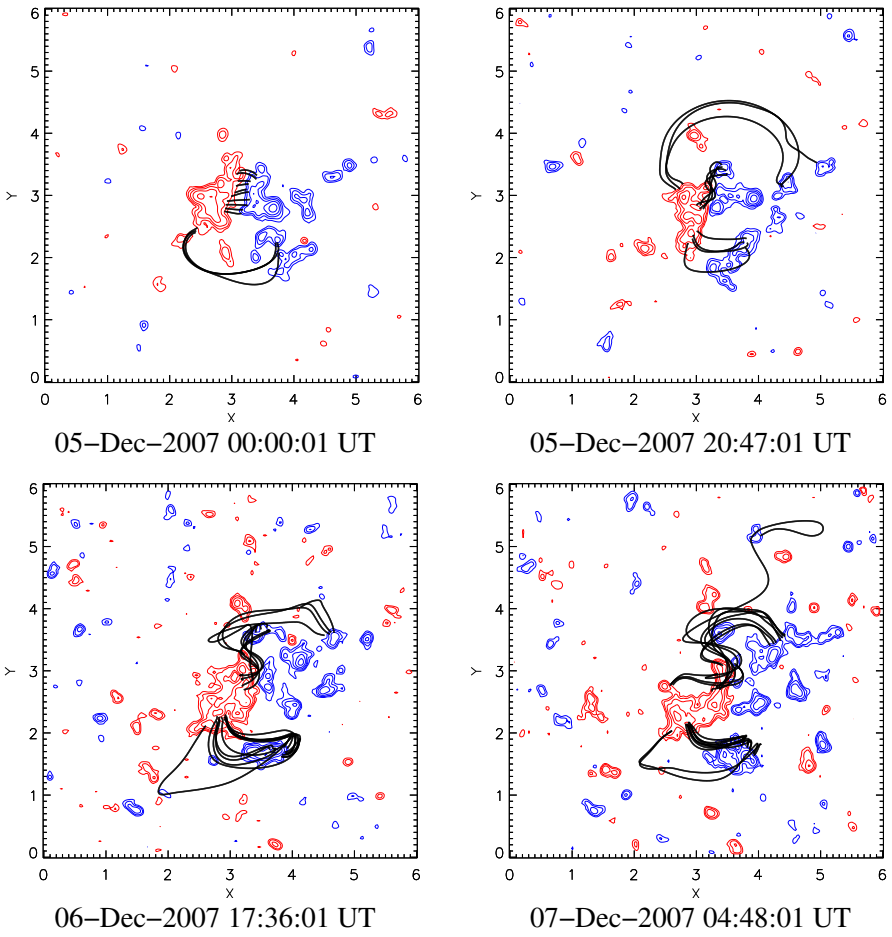

Figure 3.20: Field line plots generated from the simulation using uncleaned magnetograms at various times approximately corresponding to the times in Figure 3.2. The red and blue contours denote positive and negative photospheric flux respectively.

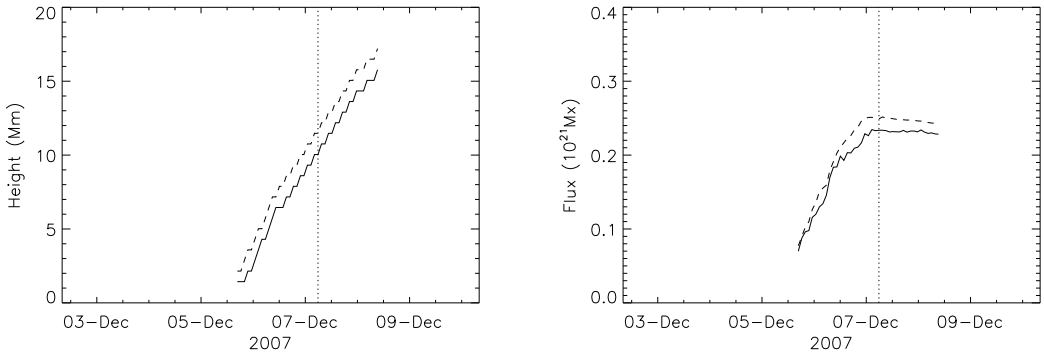

Figure 3.21: Evolution of the height (left) and flux (right) of the flux rope from the simulation using uncleaned magnetograms (solid line) and the primary simulation (dashed line) with time from 08:03 UT on December 2, 2007. The vertical dotted line denotes the time of the flare observed by XRT.

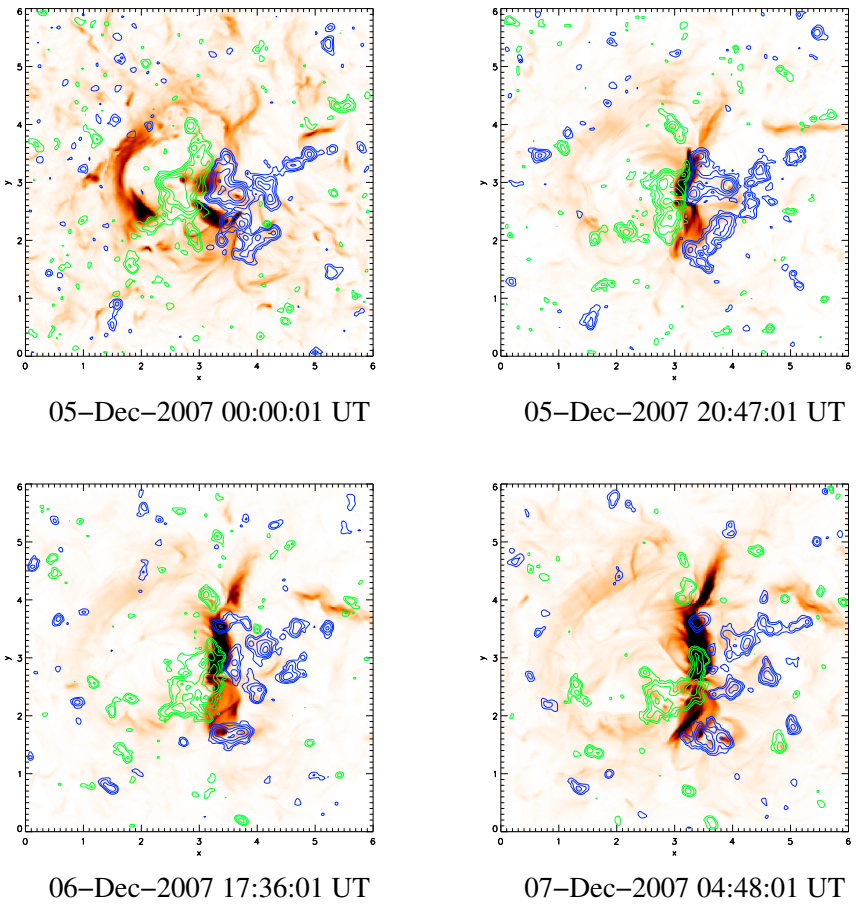

Figure 3.22: j^2 emission proxy images generated from the simulation using uncleaned magnetograms at various times roughly corresponding to the times in Figure 3.2. The colour scaling saturates at one-quarter of the maximum value of the LOS integrated j^2 for each image.

3.7.3 Comparison to XRT Images

Figure 3.22 displays the LOS integrated j^2 emission proxy for the simulation at times corresponding to those in Figure 3.15. All four panels of Figure 3.22 closely resemble those of Figure 3.15 (the emission proxy images from the primary simulation). The only significant difference between the two figures is that in Figure 3.22 there exist more proxy emission 'features' in the top left frame. These are current systems formed by the increased level of magnetogram noise present at early times due to the active region's proximity to the solar limb.

3.7.4 Free Magnetic Energy

Figure 3.23 displays the evolution of the free magnetic energy as a function of time. The free magnetic energy is calculated in the way described in Section 3.6. The free magnetic energy evolution is very similar to that of the primary simulation's (shown by the dashed line in Figure 3.23), however is much more noisy, due to the short-lived small scale magnetic features which are removed in the cleaned magntograms. Until the fifth of December, the free magnetic energy in the simulation using uncleaned magnetograms is

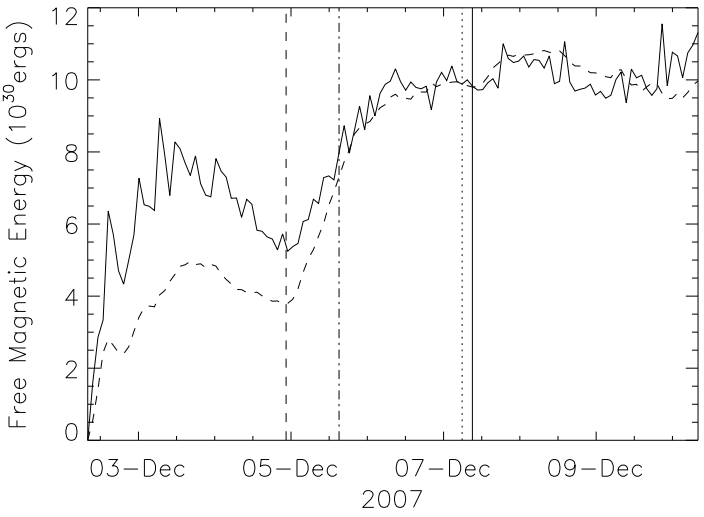

Figure 3.23: Free magnetic energy as a function of time from 08:03 UT on December 2, 2007 for the simulation with the uncleaned magnetograms (solid line) and the primary simulation (dashed line). The vertical dashed line corresponds to the time of the main flux cancellation event. The vertical dot-dashed line corresponds to the time the flux rope formed in the simulation. Finally, the vertical dotted line corresponds to the time the flare occurred and the solid line corresponds to the time the field lines became too twisted for the magnetofrictional method to follow the evolution of the simulation accurately.

higher than that of the simulation using cleaned magnetograms, though the general trend (i.e. increasing or decreasing) remains the same. This excess in free magnetic energy is attributed to the increased level of noise present in the magnetograms at earlier times due to the active region's proximity to the solar limb. This excess noise resulted in more small-scale non-potential field arising due to the fast-evolving small magnetic elements producing the current systems visible in the top left panel of Figure 3.22. The energy within the flux rope at the time of the flare was calculated to be 5.99×10^{30} erg - slightly lower than the energy contained within the flux rope in the primary simulation.

3.7.5 Helicity

Figure 3.24 displays the evolution of the relative helicity as a function of time in the simulation using uncleaned magnetograms. The relative helicity is calculated in the way described in Section 3.6. The helicity oscillates around zero until the 5th December, then rises for the duration of the simulation. Interestingly, unlike in the primary simulation, where the helicity initially decreases before rising, the helicity remains roughly zero in the simulation using uncleaned magnetograms. This may be attributed to the small-scale magnetic features adding positive helicity into the corona at a rate roughly equivalent to the rate of the large-scale field's injection of negative helicity.

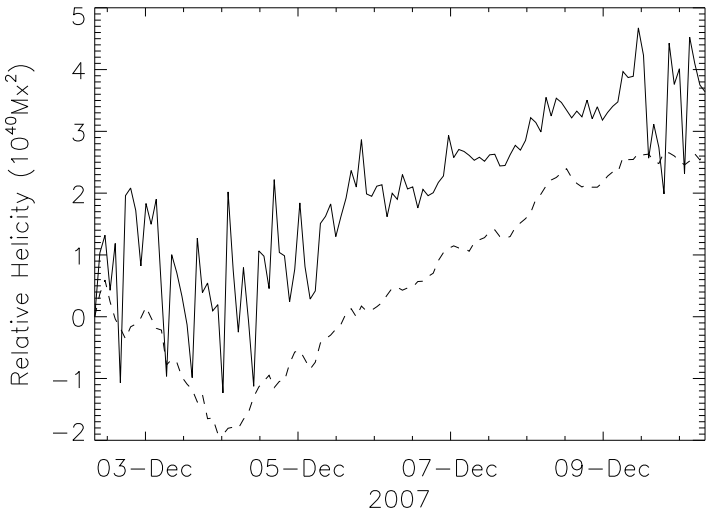

Figure 3.24: Relative helicity as a function of time from 08:03 UT on December 2, 2007 for the simulation using uncleaned magnetograms (solid line) and the primary simulation (dashed line).

3.8 Ohmic Diffusion

A simulation was run using Ohmic diffusion, where the diffusion constant was chosen to be $\eta = 440\text{km}^2\text{s}^{-1}$ ($0.01\Delta x^2/\Delta t$ in Hexa units). This was in order to determine the effects of the diffusion on the evolution of the coronal field. It is important to note that the value of η chosen here is very high (in the corona the diffusion constant is on the order of 10^{-6} km^2 s^{-1}), and therefore $440\text{km}^2\text{s}^{-1}$ is many orders of magnitude higher than the true coronal value. This section should be considered as an extreme case, and serves to demonstrate the effects of strong diffusion on the coronal evolution. The results of the simulation – which uses the same potential initial condition and photospheric evolution as the primary simulation – will be described in this section.

3.8.1 Magnetic Field Line Evolution

Figure 3.25 displays a selection of field line plots at the same times as those corresponding to Figure 3.11, outlining the main features present in the simulation corresponding to the features in the X-ray observations (Figure 3.2). In the top left panel of Figure 3.25, the arcade in the northern part of the active region possesses little to no shear, in contrast with the X-ray observations which show a sinistral shear. The simulation is able to reproduce the J-shaped emission feature visible in the south of the active region. In the top right panel of Figure 3.25 there is a strongly sheared arcade in the north of the active region corresponding to the visible emission. Unlike in the previously described simulations, a flux rope is not present here. The arcade in the south of the active region in the simulation reproduces the observed arcade in the south of the active region. In the bottom left panel of Figure 3.25 no flux rope is present. Though some J-shaped field lines are visible in the north of the active region which do match the general shape of the northern half of the observed sigmoid, the southern half of the S-shaped sigmoid emission is not reproduced at all. The arcade field highlighted in the south of the active region somewhat reproduces the emission feature visible in the south of the active region. In the bottom right panel of

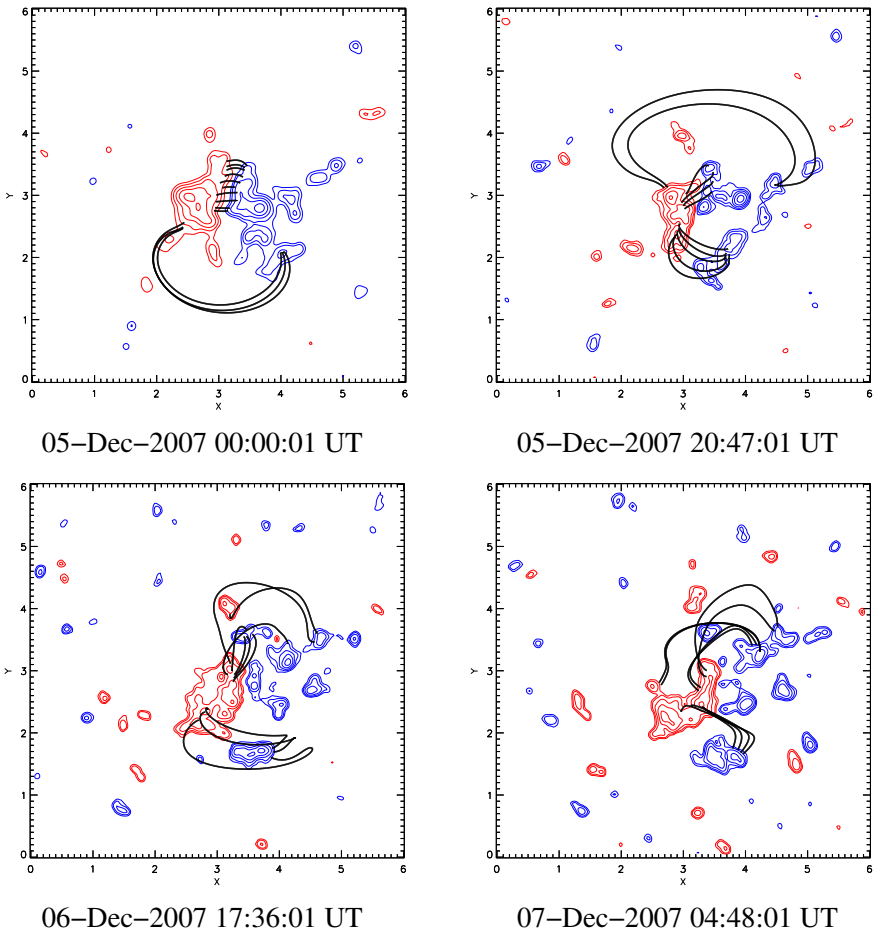

Figure 3.25: Field line plots generated from the simulation with Ohmic diffusion at various times approximately corresponding to the times in Figure 3.2. The red and blue contours denote positive and negative photospheric flux respectively.

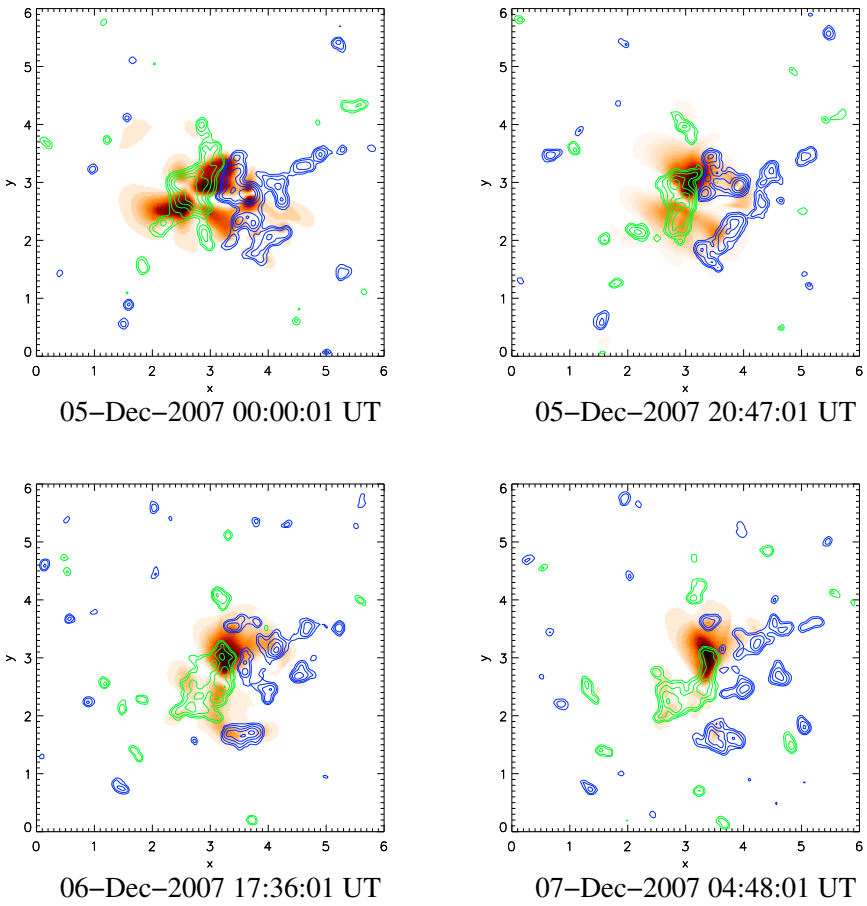

Figure 3.26: j^2 emission proxy images generated from the simulation with Ohmic diffusion at various times roughly corresponding to the times in Figure 3.2. The colour scaling saturates at one-quarter of the maximum value of the LOS integrated j^2 for each image.

Figure 3.25, still no flux rope is present. Like in the bottom left panel of Figure 3.25, J-shaped field lines are present which match the shape of the northern part of the S-Shaped sigmoid, the southern half of the sigmoid is not reproduced. Arcade field is present in the south of the active region, but it is not at the same position as the observed arcade.

3.8.2 Comparison to XRT Images

Figure 3.26 displays the LOS integrated j^2 emission proxy for the simulation at times corresponding to those in Figure 3.15. In all four panels of Figure 3.26, the emission proxy images do not provide a good match to the XRT observations.

3.8.3 Free Magnetic Energy

Figure 3.27 displays the evolution of the free magnetic energy as a function of time in the simulation. The free magnetic energy is calculated in the way described in Section 3.6. The free magnetic energy at all times is much lower than for the primary simulation, and reaches a maximum of 1.8×10^{30} erg.

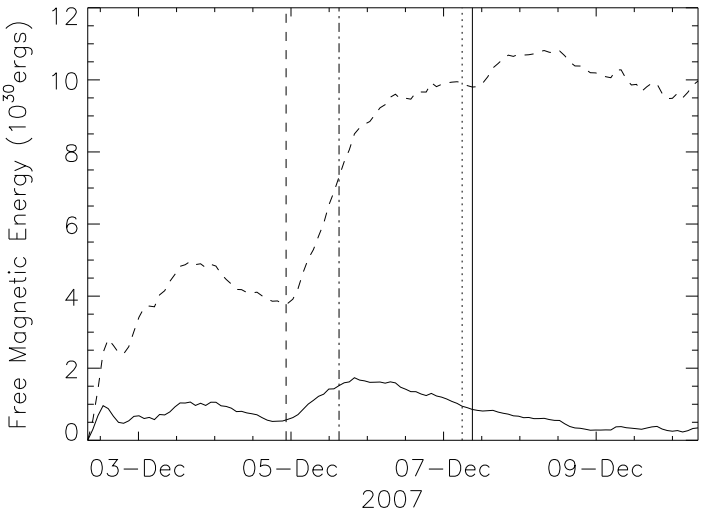

Figure 3.27: Free magnetic energy as a function of time from 08:03 UT on December 2, 2007 for the simulation with Ohmic diffusion (solid line) and the primary simulation (dashed line). The vertical dashed line corresponds to the time of the main flux cancellation event. The vertical dotted line corresponds to the time the flare occurred.

3.8.4 Helicity

Figure 3.28 displays the evolution of the relative helicity as a function of time in the simulation with Ohmic diffusion. The relative helicity is calculated in the way described in Section 3.6. The relative helicity generally decreases until the 4^{th} December, like in the primary simulation, but then, unlike the primary simulation, increases until the 5-6^{th} December, then decreases to around zero and remains at this value for the remainder of the simulation.

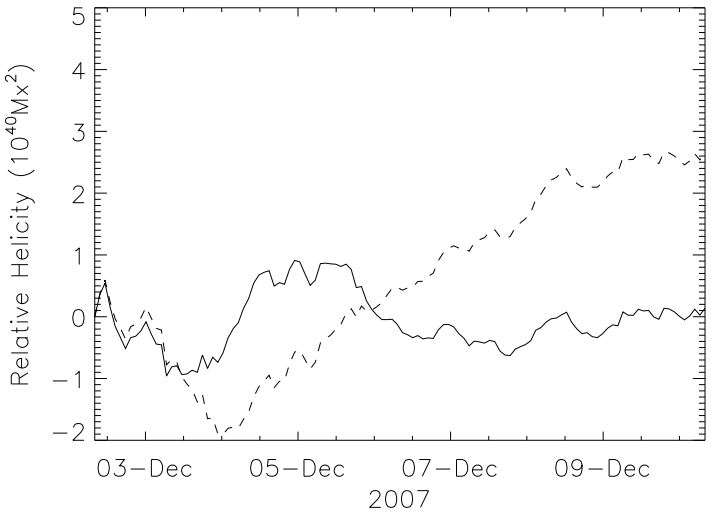

Figure 3.28: Relative helicity as a function of time from 08:03 UT on December 2, 2007 for the simulation with Ohmic diffusion (solid line) and the primary simulation (dashed line).

3.9 Hyperdiffusion

A simulation was also run using hyperdiffusion. The hyperdiffusion coefficient was chosen to be $\eta_4 = 2.2\times10^7\mathrm{km}^4\mathrm{s}^{-1}$ ($0.001\Delta x^4/\Delta t$). Like with the simulation using Ohmic diffusion (Section 3.8) this was to determine the effects of hyperdiffusion on the evolution of the coronal field.

3.9.1 Magnetic Field Line Evolution

Figure 3.29 displays a selection of field line plots at the same times as those corresponding to Figure 3.11, outlining the main features present in the simulation corresponding to features in the X-ray observations (Figure 3.2). The field structures produced in the simulation at all times closely match the field structures in the simulation using cleaned magnetograms (Section 3.6 – Figure 3.11). Like the primary simulation, the flux rope associated with the X-ray sigmoid formed in the simulation on the 5$^{\mathrm{th}}$ Dec. Also, like in the primary simulation, the field lines became strongly twisted on the fifth day of the simulation.

3.9.2 Flux Rope Properties

Figure 3.30 outlines the evolution of the northern flux rope's height and flux with time. These quantities were calculated using the techniques described in Section 3.6. Like with primary simulation (Section 3.6), the flux rope's height increases nearly linearly with time, and at the time of the flare has reached a height of 11Mm, like the primary simulation. The flux rope's flux increases until the time of the flare, where it has reached a level of 2.5×10^{20} Mx. This corresponds to roughly 20% of the active region's flux at this time, and is the same result as that from the primary simulation.

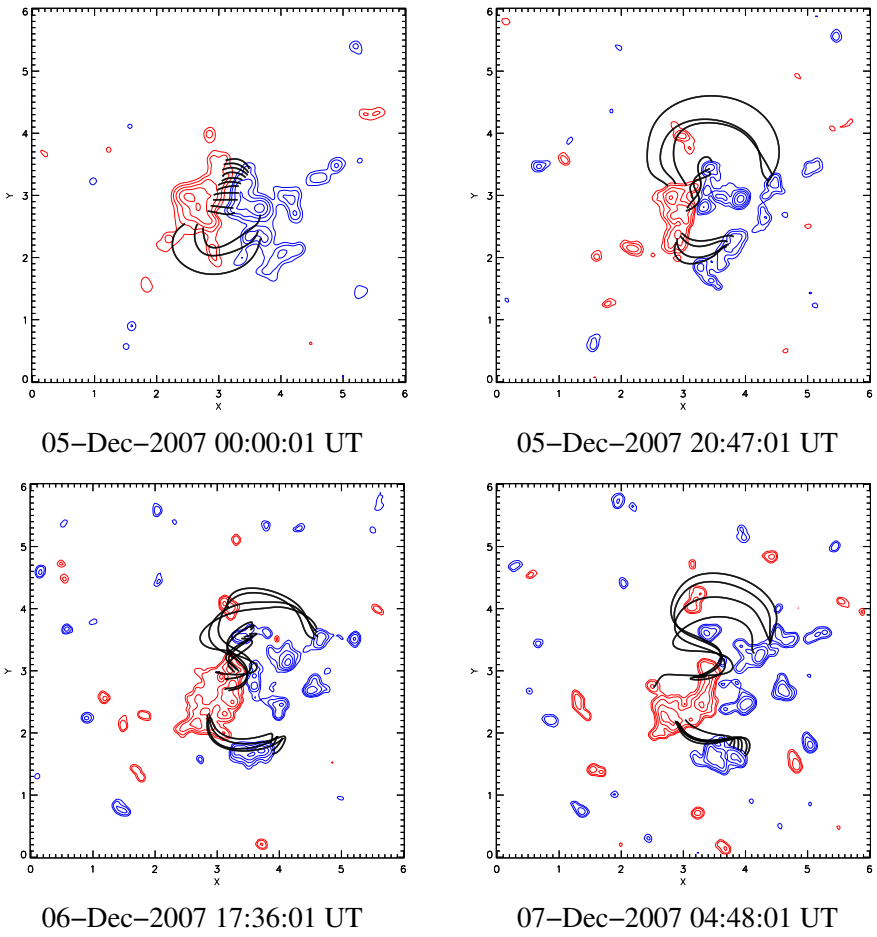

Figure 3.29: Field line plots generated from the simulation with hyperdiffusion at various times approximately corresponding to the times in Figure 3.2. The red and blue contours denote positive and negative photospheric flux respectively.

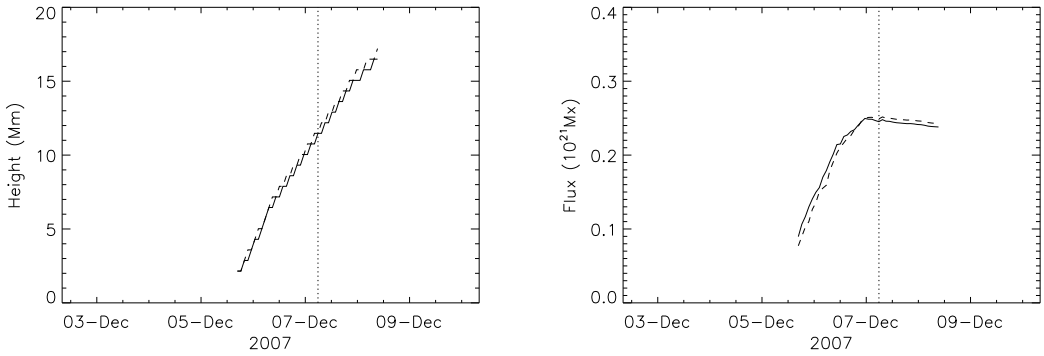

Figure 3.30: Evolution of the height (left) and flux (right) of the flux rope with time from 08:03 UT on December 2, 2007 for the simulation with hyperdiffusion (solid line) and the primary simulation (dashed line). The vertical dotted line denotes the time of the flare observed by XRT.

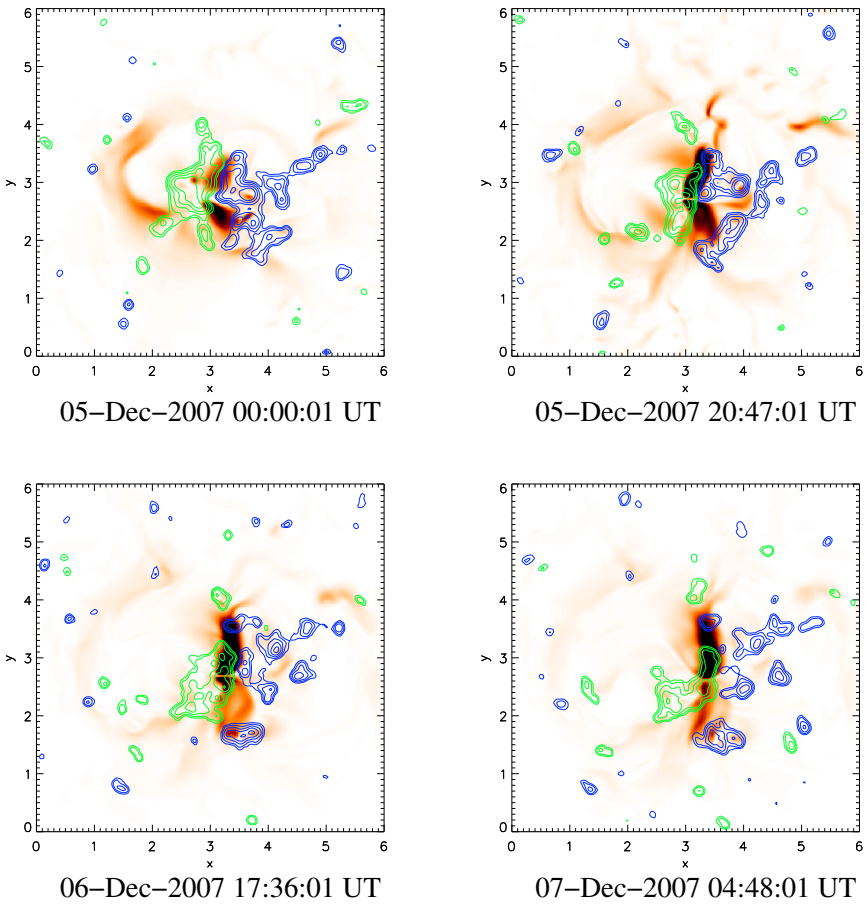

Figure 3.31: j^2 emission proxy images generated from the simulation with hyperdiffusion at various times roughly corresponding to the times in Figure 3.2. The colour scaling saturates at one-quarter of the maximum value of the LOS integrated j^2 for each image.

3.9.3 Comparison to XRT Images

Figure 3.31 displays the LOS integrated j^2 emission proxy for the simulation at times corresponding to those in Figure 3.15. All four panels of Figure 3.31 closely resemble those of Figure 3.15 (the emission proxy images from Section 3.6). The only significant difference between the two figures is that in Figure 3.31 the emission proxy images appear smoother. This is because hyperdiffusion acts to smooth gradients in the force-free parameter, α, and so as a result smooths the current distribution, producing a smoother looking emission proxy image.

3.9.4 Free Magnetic Energy

Figure 3.32 displays the evolution of the free magnetic energy as a function of time in the simulation. The free magnetic energy is calculated in the way described in Section 3.6. The free magnetic energy evolution is very similar to that of the primary simulation (dashed line in Figure 3.32), however the energy is slightly lower throughout the simulation. This is due to the hyperdiffusion removing energy from the simulation. The energy within the flux rope at the time of the flare was calculated to be 5.73×10^{30} erg - slightly less than the energy contained within the flux rope in the primary simulation.

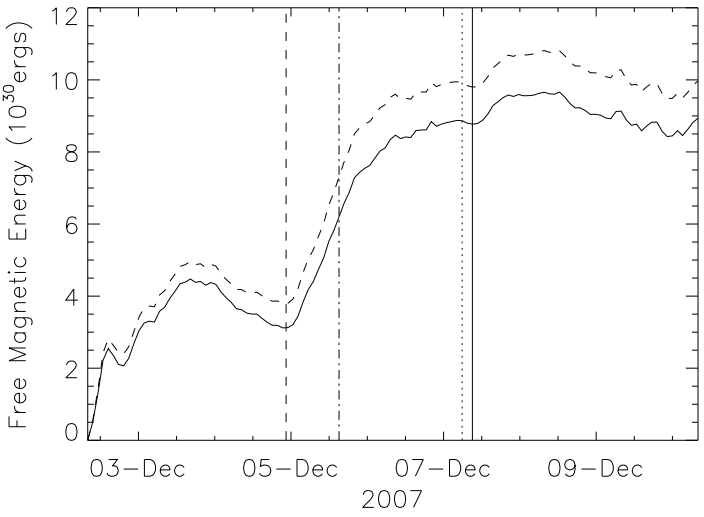

Figure 3.32: Free magnetic energy as a function of time from 08:03 UT on December 2, 2007 for the simulation with hyperdiffusion (solid line) and the primary simulation (dashed line). The vertical dashed line corresponds to the time of the main flux cancellation event. The vertical dot-dashed line corresponds to the time the flux rope formed in the simulation. The vertical dotted line corresponds to the time the flare occurred and the solid vertical line corresponds to the time the field lines became too twisted for the magnetofrictional method to follow the evolution of the simulation accurately.

3.9.5 Helicity

Figure 3.33 displays the evolution of the relative helicity as a function of time in the simulation. The relative helicity is calculated in the way described in Section 3.6. The evolution of the relative helicity is almost identical to the evolution of the helicity in the primary simulation (dashed line in Figure 3.33). This is to be expected, as hyperdiffusion is supposed to conserve magnetic helicity.

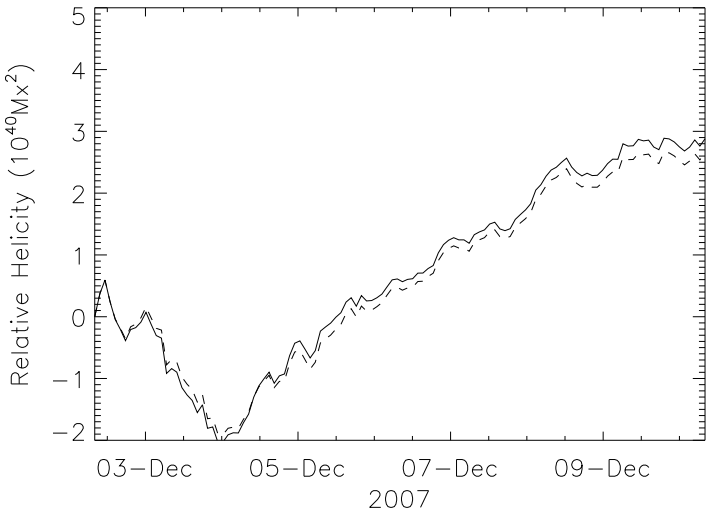

Figure 3.33: Relative helicity as a function of time from 08:03 UT on December 2, 2007 for the simulation with hyperdiffusion (solid line) and the primary simulation (dashed line).

3.10 Discussion

Within this chapter the coronal magnetic field of AR10977 has been simulated from the active region's initial emergence phase, followed by a decay phase with significant flux cancellation and counter-clockwise rotation. X-ray observations of the active region showed that a sigmoid formed during its lifetime and eventually led to an eruption from the active region. To simulate these events the coronal magnetic field of the active region was modelled using the method employed by Mackay et al. (2011), where its evolution was driven by a series of cleaned 96-minute LOS magnetograms from SOHO/MDI. These magnetograms produced an evolving lower boundary condition closely resembling the observed evolution of the active region's photospheric magnetic field on a pixel-by-pixel basis. In Section 3.10.1 the results of the primary simulation will be discussed. Sections 3.10.2 and 3.10.3 will discuss the simulations using uncleaned magnetograms and diffusive terms respectively, and compare them with the primary simulation.

3.10.1 Primary Simulation

The main features of the evolution of the active region's coronal magnetic field as observed by Hinode XRT were reproduced by the simulation. This verifies that the modelling technique of using LOS magnetograms put forward by Mackay et al. (2011), but not previously tested against coronal observations, is a valid technique to study the evolution of the coronal magnetic field. In particular in the simulation a flux rope formed on December 5 2007, whose location matched the location of a Hinode XRT sigmoid. The formation mechanism of the flux rope and its properties were determined. The flux rope formed as a result of the transformation of a sheared arcade into twisted field lines due to flux cancellation. This was in agreement with the flux rope formation method proposed by van Ballegooijen & Martens (1989). The shear of the arcade originated from the counter-clockwise rotation of the negative magnetic polarity region relative to the positive polarity region. In the XRT observations, the sigmoid was not observed until 15:51 UT on 6 Dec 2007 – roughly a day after the flux rope formed in the simulation. This indicates that

there may not be a simple relationship between the formation of a flux rope as expressed in terms of magnetic field lines and the observation of a sigmoid seen in X-rays. The difference in times between the two could also be related to the initial condition used in the simulation. The flux rope continued to increase in size until the time of the observed eruption, where analysis of the flux rope determined that it contained 2.5×10^{20}Mx of flux. This is approximately 20% of the active region flux, which is lower than the flux determined by Green et al. (2011) and Savcheva et al. (2012). The flux we found is however just greater than the critical ratio for force balance found in previous studies (Bobra et al. 2008, Su et al. 2009, Savcheva & van Ballegooijen 2009), suggesting that the flux rope was unstable at the time of the observed flare. The flux rope was also found to be rising with a constant velocity of 63m s^{-1}.

In general, comparisons of the field lines from the simulations with the XRT observations showed a good agreement, with the simulation reproducing many of the observed features. The simulations provided a very good fit for the northern half of the flux rope, however the fit was not so good for the southern end of the flux rope. The poor fit in the southern half of the flux rope could be attributed to the initial condition not being a good representation of the magnetic field in the south of the active region. In order to directly compare the simulated coronal field with XRT observations, j^2 emission proxy images were produced by integrating the square of the current density along the z direction. These images again showed that our simulations better reproduced the observed features in the north of the active region compared to the south. While the LOS integrated j^2 emission proxy images reproduced emission at the position of the sigmoid relatively well, they have been unable to reproduce the arcade seen in the observed XRT images. This may in part be due to the crude method employed. Additionally, in the j^2 emission proxy images only the centre of the flux rope can be seen. This can be explained by the field within the volume of the flux rope being twisted, and thus containing current. This would translate into more emission in our j^2 emission proxy images. In the Titov & Démoulin (1999) model, the emission responsible for sigmoids is generated in a thin current layer underneath the flux rope. In our j^2 emission proxy images, this thin layer will have the 'emission' from the current within the flux rope superimposed on top of it and will likely not be discernible in the images.

The free magnetic energy was calculated as a function of time for the simulation. Over the duration of the simulation, approximately 1×10^{31}erg of free magnetic energy was injected into the corona. There was a sharp rise in the free magnetic energy beginning early on the 5^{th} Dec 2007. This time corresponded to a large flux cancellation event and the flux rope formation, suggesting that much of the free magnetic energy input is associated with the flux rope formation. The free magnetic energy contained within the flux rope at the time of the flare was found to be 6.1×10^{30}erg. This is in good agreement with the results of Savcheva et al. (2012) who found an energy of 6×10^{30}erg.

The relative helicity, a topological measure of the connectivity of the magnetic field, was calculated as a function of time for the simulation. The relative helicity initially decreased, but later increased for the duration of the simulation. The evolution of the relative helicity with time is correlated with the evolution of the tilt angle of the active region. This suggests that the dominant source of helicity injection is the large scale rotation of the active region. This is in agreement with Mackay et al. (2011) who proposed that the increase of helicity in their simulation may be related to the evolution of the large scale properties of their active region. While the large scale evolution of the active region is one source of helicity injection, other sources may also exist. Section 4.3 of Mackay et al. (2011) presents a discussion on other possible sources of helicity injection.

In the simulation, a second flux rope formed to the south of the flux rope associated with the observed sigmoid. This additional flux rope formed when the negative polarity region in the magnetograms first began to fragment, and a portion of it moved southward (top-centre and top-right panel of Figure 3.1), producing an arcade with a strong dextral shear. This flux rope did not form due to flux cancellation in a manner consistent with that of van Ballegooijen & Martens (1989), but instead formed through reconnection of the sheared arcade in a manner similar to that observed in the simulations of DeVore & Antiochos (2000). This flux rope possessed the opposite direction of twist compared to the flux rope associated with the observed sigmoid. Due to this its soft X-ray signature would be a sigmoid with an inverted S-shape. In the XRT observations (Figure 3.2) there is no such inverted S-shaped feature present in the southern portion of the active region. The origin of this discrepancy in terms of the arbitrary choice of the initial condition will now be discussed. One possibility is that the initial condition used in the simulation was incorrect at this location. If the initial condition possessed a shear across the PIL of a sinistral type (positive relative helicity) then during the initial fragmentation of the negative polarity region no arcade with dextral shear would form at the south of the active region, preventing the formation of the southern flux rope. Such an initial condition field with sinistral shear would possess a positive relative helicity. This would result in a value of relative helicity which is closer to that found by Savcheva et al. (2012) compared to the value obtained from the potential field initial condition. In Chapter 4 simulations with LFF initial conditions are carried out to test this hypothesis.

On the morning of December 7, the simulations' field lines became too twisted for the magnetofrictional method to remain valid. This time lies within a few hours of the eruption of the sigmoid. The loss of validity of the magnetofrictional method, which evolves a field through a series of NLFF equilibria, is a suggestion that an instability, or non-equilibrium state has occurred, which the simulations cannot track. It should be noted that the choice of the magnetofrictional coefficient affects the timescale over which the coronal field can respond to changes produced by the photospheric evolution. This process and its corresponding timescales are comprehensively discussed in Section 2.1 of Cheung & DeRosa (2012). Our choice of large frictional coefficient, although ensuring that the simulated field remains close to a NLFF configuration at all times, results in long evolution timescales. In our study, the flux rope does not erupt, although the simulation breaks down soon after the time of the observed flare. This is an indication that the coronal field is attempting to evolve faster than the magnetofrictional code - with our choice of frictional coefficient - can deal with. This implies a loss of equilibrium has occurred. It is interesting that the time of the flare and the time of the breakdown in the simulation occur within a few hours of one another. This suggests that the simulation technique of using observed magnetograms to drive the evolution of the coronal field has correctly followed the dynamics of the system to the build-up of an eruption.

3.10.2 Use of Cleaned Magnetograms

The difference between using cleaned and uncleaned magnetograms is now discussed. The cleaning process is designed to remove small-scale transient features in the magnetograms such as noise and network magnetic elements, whilst retaining the large-scale magnetic features of the active region which are of interest for this study. Upon comparing the differences between a simulation using uncleaned magnetograms (Section 3.7) and cleaned magnetograms (Section 3.6), it is clear that the large-scale properties of the simulated magnetic fields in both simulations are similar. This is the desired effect, as the cleaning process is designed to retain the large-scale magnetic field of the active region. The

main difference between the two simulations is with the free magnetic energy, which is consistently higher for the simulation using uncleaned magnetograms (Figure 3.23) than for the simulation using cleaned magnetograms (Figure 3.16). The energy excess in the simulation using uncleaned magnetograms is due to the small-scale magnetic features and noise injecting energy into the corona. This energy excess is most noticeable over the first few days of the simulation, when the magnetograms are at their noisiest. The other noticeable difference between the two simulations is the magnetic helicity. Whilst in the simulation using cleaned magnetograms the helicity decreases for the first two days to almost -2×10^{40} Mx^2 then increases for the duration of the simulation to around 2.5×10^{40} Mx^2, in the simulation using uncleaned magnetograms, the relative helicity remains roughly constant for the first two days, then increases to around 4.5×10^{40} Mx^2 by the end of the simulation. This suggests that the small scale features removed by the cleaning process inject positive helicity into the corona. This is consistent with the 'helicity condensation' process described by Antiochos (2013), whereby the combined twists of small-scale flux elements can make a significant contribution to the helicity in the solar corona.

3.10.3 Effects of Diffusion

The effects of the two runs with diffusive terms (Sections 3.8 and 3.9) will now be discussed. In contrast to all the other simulations run, no flux rope was formed in the simulation with Ohmic diffusion (Section 3.8). This is due to the high diffusion acting to remove the large currents such as those present in the flux rope, or a sheared arcade. Any non-potentiality injected into the field is therefore diffused away, resulting in a coronal field which remains near potential throughout the simulation. This is evident when considering the free magnetic energy in this simulation (Figure 3.27) which at all times is considerably lower than that of any of the other simulations. The helicity evolution (Figure 3.28) is also different to the equivalent run with no diffusion (Section 3.6), with a smaller range of values. As the magnetic helicity decays on the global diffusion timescale, the reduced buildup of helicity in the simulation is probably due to the diffusion acting to diffuse away the helicity. Indeed, the global diffusion timescale is 24 days. It should be noted here that the choice of η in this study is very high, as is apparent from the significant effect it has had on the evolution of the coronal field. Use of a smaller η would reduce the effects of diffusion, and allow a flux rope to form in the north of the active region, as happened in the other simulations.

The hyperdiffusive simulation's results (Section 3.9) are very similar to those of the non-diffusive simulation (Section 3.6). The field line evolution, flux rope properties, emission proxy images and the free magnetic energy and relative helicity evolutions are qualitatively very similar. The main differences are that the emission proxy images from the hyperdiffusive simulation (Figure 3.31) appear smoother than the emission proxies from the non-diffusive simulation (Figure 3.15). This is because the hyperdiffusion acts to remove gradients in the force-free parameter, $\alpha(\mathbf{r})$, and so smooths the current distribution, which is proportional to $\alpha(\mathbf{r})\mathbf{B}$. Also, the free magnetic energy built up in the hyperdiffusive simulation (Figure 3.32) is less than that in the non-diffusive simulation (Figure 3.16). This is due to the hyperdiffusion removing energy from the simulation.

Whilst the primary simulation (Section 3.6) does not explicitly contain any diffusive terms, there is an inclusion of numerical diffusion due to the finite resolution of the simulation. This numerical diffusion permits reconnection of field lines to occur even in the absence of explicit diffusion. The numerical diffusion also has the effect of removing energy from the simulation. Numerical diffusion, which is incredibly difficult to accurately

predict, becomes important when large gradients are present on small length scales, for example current sheets, or small unresolved features. One way to reduce the strength of numerical diffusion is to run the simulation in a higher resolution, as this has the effect of increasing the number of gridpoints across any given feature, reducing in smaller gradients between adjacent gridpoints.

Chapter 4

Modelling the Coronal Field of AR10977 II: Investigating Different Initial Conditions

4.1 Introduction

In Chapter 3 the coronal magnetic field of AR10977 was simulated using the magnetofrictional method. The primary simulation employed cleaned magnetograms to drive the coronal evolution and used a potential field initial condition. No explicit diffusive terms were included in the induction equation. In the primary simulation, a flux rope formed at the location of an observed X-ray sigmoid. At the time of the sigmoid's eruption, the flux contained within the flux rope was found to be approximately 20% of the active region flux. This was less than the value of $\gtrsim 30\%$ estimated by Green et al. (2011) and $\sim 50\%$ as determined by Savcheva et al. (2012). It was found that the simulation better reproduced the northern half of the active region than the southern half. In particular a flux rope formed in the south of the active region with dextral twist. Such a flux rope would be expected to produce an inverse S-shaped sigmoid, yet no such sigmoid was visible in the XRT observations. The differences between the observations of the south of the active region and the simulation were attributed to the potential initial condition not accurately representing the coronal field at the start time. Along with the primary simulation, additional simulations were run to determine the effects the magnetogram cleaning process and the omission of Ohmic and hyper-diffusion had on the evolution of the coronal field.

In this Chapter, further simulations are carried out which use different initial conditions to the one used in Chapter 3. These include starting the simulation at a later time (Section 4.2), using linear force-free initial conditions (Section 4.3) and running the simulation at a higher resolution (Sections 4.4 and 4.5). In Section 4.6 the limitations of using line-of sight magnetograms as a lower boundary condition are investigated. Finally, in Section 4.7 the results of this chapter are discussed, and the main findings of Chapters 3 and 4 are summarised.

4.2 Later Start Time

Until the 4^{th} December the active region rotates in a clockwise fashion. During this time, negative magnetic helicity is injected into the corona (e.g. see Figure 3.18). In order to determine the effect this clockwise rotation has on the later evolution of the coronal

field, a simulation was run starting after the clockwise rotation had occurred. As such the subsequent evolution of a coronal field from this time with no negative relative helicity may be studied, and contrasted with the primary simulation. This also considers what may have happened if the active region had rotated onto the visible disk of the Sun two days later, and thus the early clockwise rotation had gone unobserved. A potential field was extrapolated from the magnetogram at 08:00 UT on 4$^{\text{th}}$ Dec 2007 – two days after the start time in the other simulations. This potential initial condition is displayed in Figure 4.1.

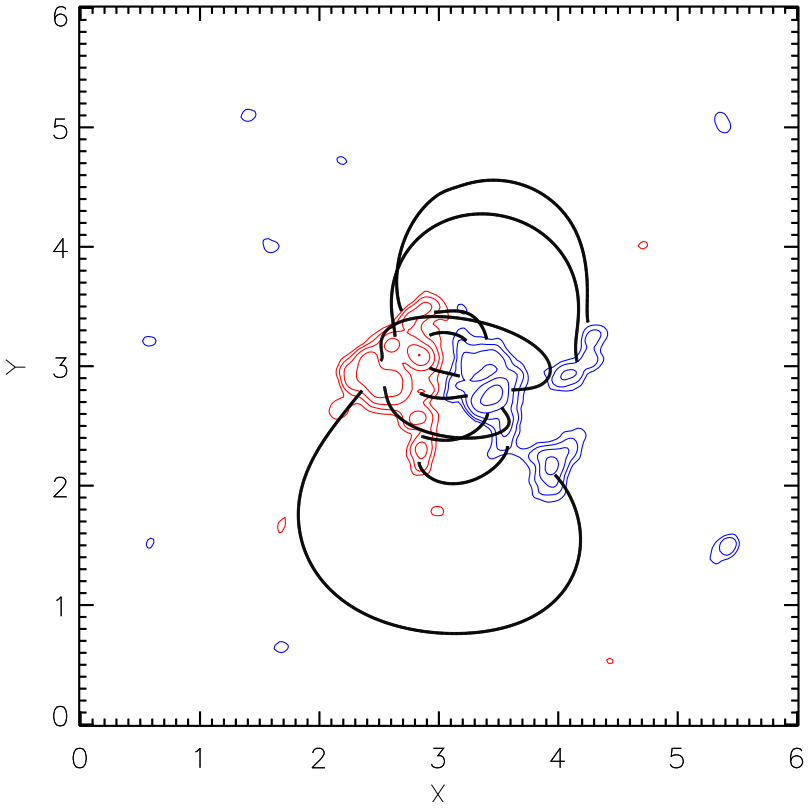

Figure 4.1: Selection of field lines (solid black lines) illustrating the potential initial condition at 08:00 UT on 4$^{\text{th}}$ Dec 2007 where red and blue contours denote positive and negative photospheric flux respectively.

4.2.1 Magnetic Field Line Evolution

Figure 4.2 displays a selection of field line plots at the same times as those corresponding to Figure 3.11, outlining the features present in the simulation corresponding to features in the X-ray observations (Figure 3.2). In the top left panel of Figure 4.2, the arcade in the northern part of the active region possesses slight sinistral shear, in agreement with the X-ray observations. This is in contrast to the primary simulation (Section 3.6) where there is no significant shear present. The J-shaped emission feature visible in the south of the active region is also reproduced. In the top right panel of Figure 4.2 the sheared structure in the north of the active region is reproduced, as well as the arcade feature in the south of the active region. In the bottom left panel of Figure 4.2 the flux rope is clearly visible, with its longer field lines possessing two turns. This is in contrast to the

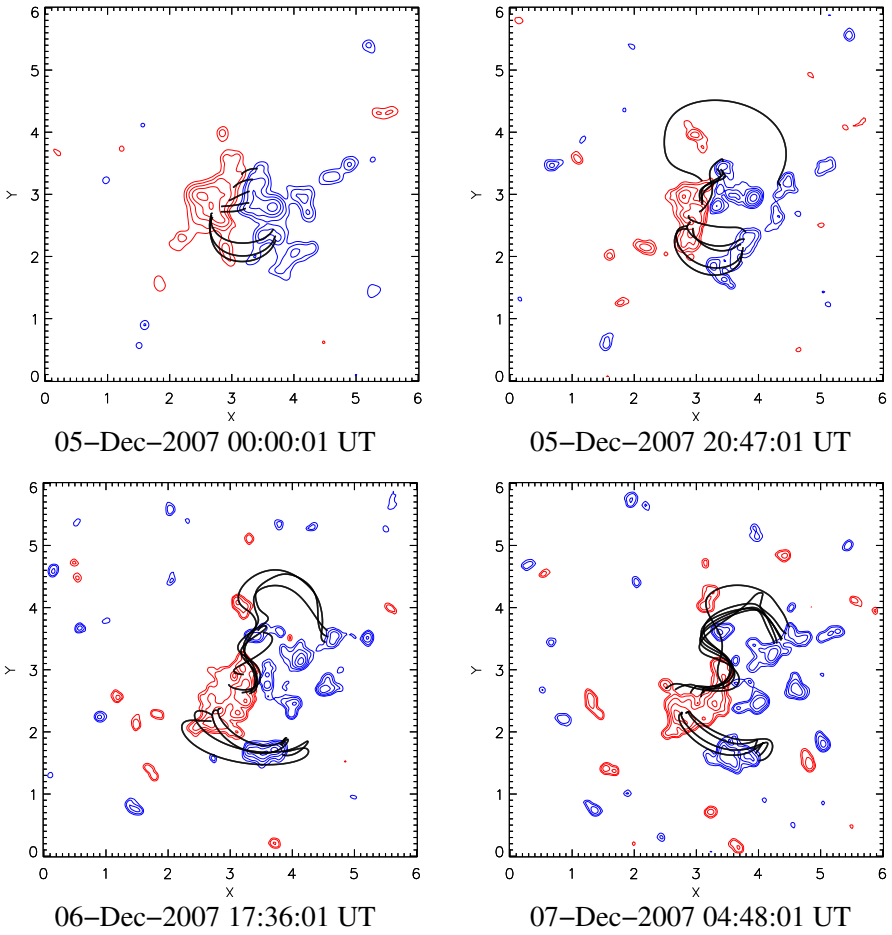

Figure 4.2: Field line plots generated from the simulation with a later starting time (08:00 UT on 4$^{\text{th}}$ Dec 2007) at the times approximately corresponding to the times in Figure 3.2. The red and blue contours denote positive and negative photospheric flux respectively.

bottom left panel of Figure 3.11 where every field line in the flux rope only possesses one turn. Like the primary simulation (Section 3.6), the northern end of the flux rope is better reproduced than its southern end, which terminates further north than the observed X-ray sigmoid. The arcade in the south of the active region reproduces the emission feature visible in the south of the active region. In the bottom right panel of Figure 4.2, the flux rope's southern footpoint has moved further east (like in the primary simulation (Section 3.6). The emission feature in the south of the active region is well reproduced by the simulation. The northern flux rope formed at 11:11 UT on the 5$^{\text{th}}$ December. Like with the primary simulation (Section 3.6) on the fifth day (09:36 UT on 7-Dec-2007) the field lines become strongly twisted and the magnetofrictional method can no longer properly describe the coronal evolution.

4.2.2 Flux Rope Properties

Figure 4.3 outlines the evolution of the northern flux rope's height and flux with time. These quantities were calculated using the techniques described in Section 3.6. Similar to the primary simulation, the flux rope's height increases nearly linearly with time, and at the time of the flare has reached a height of 13Mm. This is higher than the height of

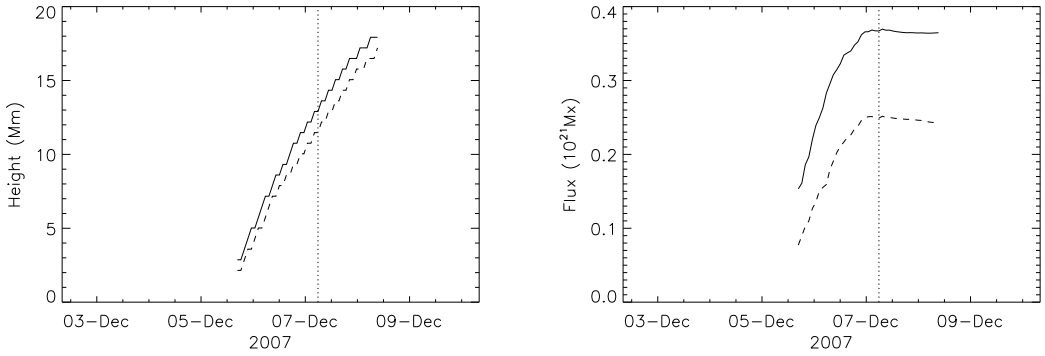

Figure 4.3: Evolution of the height (left) and flux (right) of the flux rope with time from 08:03 UT on December 2, 2007 for the simulation with a later start time (solid line) and the primary simulation (dashed line). The vertical dotted line denotes the time of the flare observed by XRT.

11Mm achieved by the flux rope in the primary simulation. The flux rope's flux increases until the time of the flare, where it has reached a level of 3.8×10^{20} Mx. This corresponds to roughly 30% of the active region's flux at this time - roughly 1.5 times the flux rope flux in the primary simulation. This value matches the minimum flux contained within the flux rope as determined by Green et al. (2011).

4.2.3 Comparison to XRT Images

Figure 4.4 displays the LOS integrated j^2 emission proxy for the simulation at times corresponding to those in Figure 3.15. In all four panels of Figure 4.4, the emission proxy reproduces the observed emission features in the north of the active region well, however as was the case with the primary simulation, the emission proxy does not reproduce the observed emission in the south of the active region. Once again, this is due to a secondary flux rope formed in the south of the active region, which dominates the j^2 emission proxy in the south of the active region.

4.2.4 Free Magnetic Energy

Figure 4.5 displays the evolution of the free magnetic energy as a function of time in the simulation. The free magnetic energy is calculated in the manner described in Section 3.6. The free magnetic energy evolution is very similar to that of the primary simulation (dashed line in Figure 4.5), though more free magnetic energy is built up during the simulation. The possible causes of this will be discussed in Section 4.7.1. The free magnetic energy within the flux rope was calculated to be 10.3×10^{30} erg at the time of the observed flare. This is higher than the energy in the flux rope in the primary simulation (6.1×10^{30} erg).

4.2.5 Helicity

Figure 4.6 displays the evolution of the relative helicity as a function of time in the simulation with a later start time (solid line) and the primary simulation (dashed line). The relative helicity is calculated in the way described in Section 3.6. The relative helicity

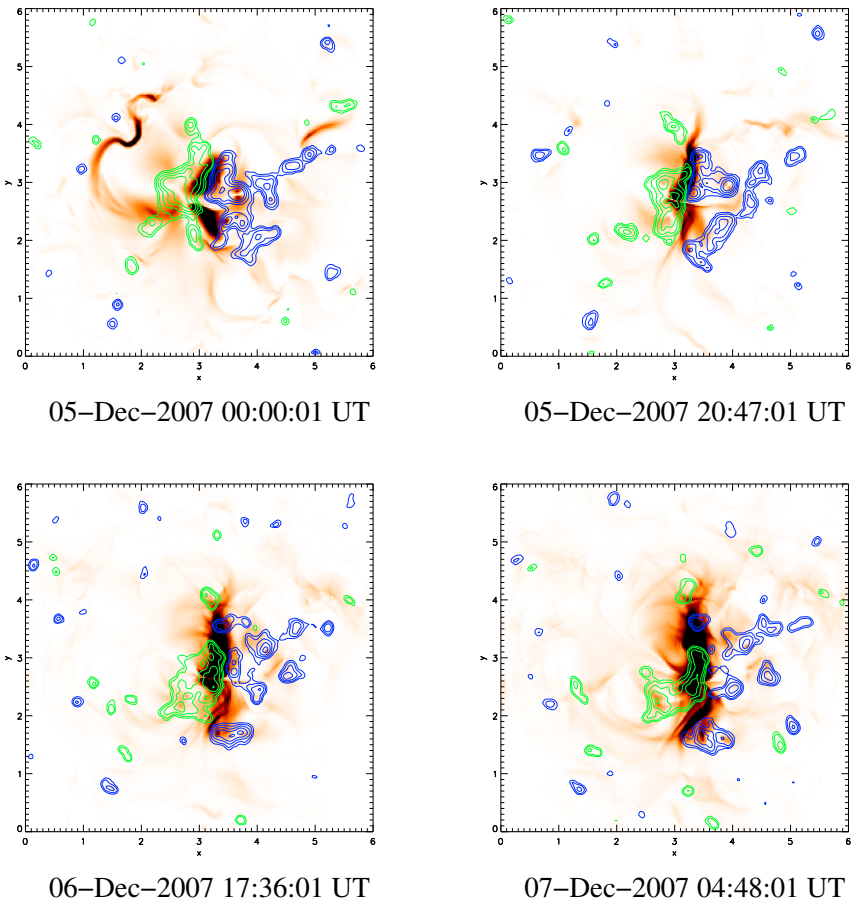

Figure 4.4: j^2 emission proxy images generated from the simulation with a later starting time at various times roughly corresponding to the times in Figure 3.2. The colour scaling saturates at one-quarter of the maximum value of the LOS integrated j^2 for each image.

remains roughly constant until the 6$^{\text{th}}$ December, then increases for the rest of the simulation. The general trend is an increase in the relative helicity. The evolutions of the relative helicity in both the primary simulation and the simulation with a later start time are very similar.

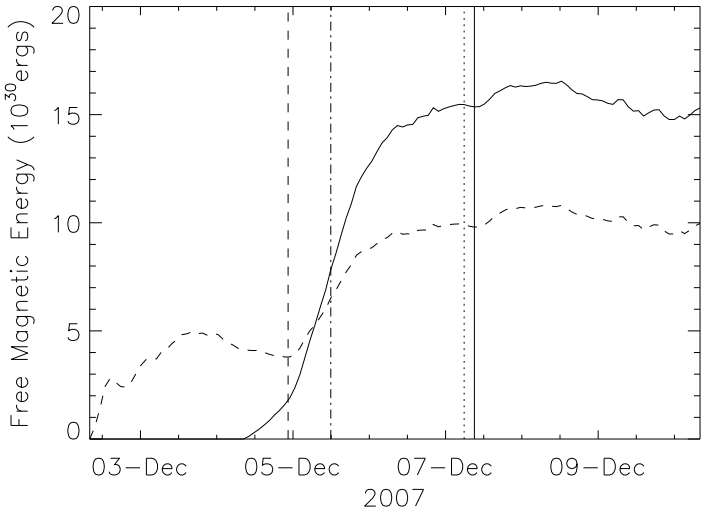

Figure 4.5: Free magnetic energy as a function of time from 08:03 UT on December 2, 2007 for the simulation with a later start time (solid line) and the primary simulation (dashed line). The vertical dashed line corresponds to the time of the main flux cancellation event. The vertical dot-dashed line corresponds to the time the flux rope formed in the simulation with a later start time. The vertical dotted line corresponds to the time the flare occurred and the solid vertical line corresponds to the time the field lines became too twisted for the magnetofrictional method to follow the evolution of the simulation accurately.

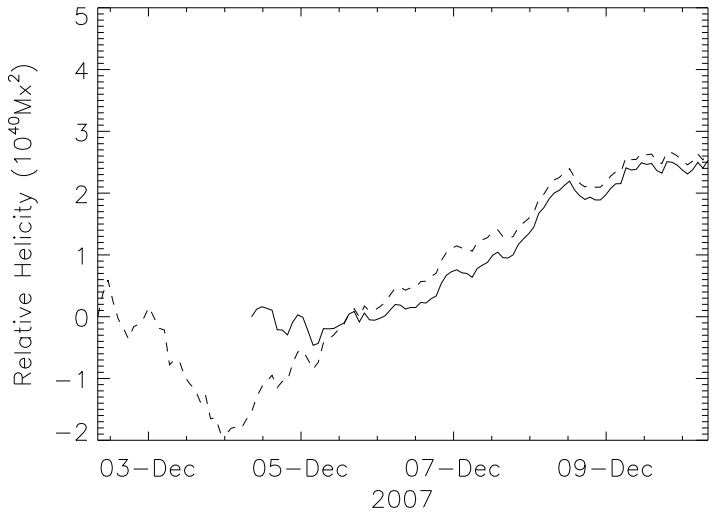

Figure 4.6: Relative helicity as a function of time from 08:03 UT on December 2, 2007 for the simulation with a later start time (solid line) and the primary simulation (dashed line).

4.3 Linear Force Free Initial Conditions

In Section 3.10.1 it is discussed that the differences in the south of the active region between the observations and the simulation could be due to the potential field initial condition not being a good representation of the coronal field at the simulation start time. In this section the results of simulations using linear force-free (LFF) initial conditions are described. In the simulations we use $\alpha = \pm 3.29 \times 10^{-8}$ m^{-1}. These fields are constructed using the method described in Section 3.5.2. Figure 4.7 displays the initial condition LFF fields used in the two simulations.

4.3.1 Magnetic Field Line Evolution

Positive-α LFF initial condition

Figure 4.8 displays a selection of field line plots at the same times as those corresponding to Figure 3.11. These outline the features present in the simulation with the positive-α LFF initial condition that correspond to features in the X-ray observations (Figure 3.2). In the top left panel of Figure 4.8, the arcade in the northern part of the active region possesses slight sinistral shear, in agreement with the X-ray observations. Similarly, the simulation also reproduces the J-shaped emission feature visible in the south of the active region. In the top right panel of Figure 4.8 the northern flux rope is visible. Its southern footpoints extend further south than the flux rope in the primary simulation (Figure 3.11). The simulation is unable to reproduce the loops to the north of the active region, however can reproduce those visible in the south of the active region. In the bottom left panel of Figure 4.8 the flux rope is clearly visible, and very closely resembles the XRT sigmoid. The southern footpoints of the flux rope extend further south than for the case of the flux rope in the primary simulation (Figure 3.11). The arcade-like structure in the XRT observations at the south of the active region is not reproduced by the simulation. In the bottom right panel of Figure 4.8 the S-shaped field lines belonging to the flux rope have increased in length, resulting in a larger S-shape, as seen in the observations. Unlike in the observations, the southern extent of the flux rope terminates near the centre of the positive polarity region, not at the southern end as is seen in the observations. The emission feature in the south of the active region is not reproduced by the simulation. The northern flux rope formed at 12:47 UT on the 5$^{\text{th}}$ December. Similar to the primary simulation (Section 3.6), on the fifth day the field lines become strongly twisted, and the magnetofrictional method can no longer properly describe the coronal evolution.

Negative-α LFF initial condition

Figure 4.9 displays a selection of field line plots at the same times as those corresponding to Figure 3.11, outlining the features present in the simulation with the negative-α LFF initial condition corresponding to features in the X-ray observations (Figure 3.2). In the top left panel of Figure 4.9, the arcade in the northern part of the active region possesses slight dextral shear, in contrast to the X-ray observations, which display a sinistral shear. The simulation is unable to reproduce the the J-shaped emission feature visible in the south of the active region. In the top right panel of Figure 4.9 a flux rope is visible in the north of the active region in the location of the observed emission. A field line structure resembling the emission in the south of the active region is present in the simulation. In the bottom left panel of Figure 4.9 the flux rope is visible, however, its field lines do not display a clear S-shape. The southern extent of the flux rope is much further north than the southern extent of the sigmoid in the X-ray observations. A field line structure

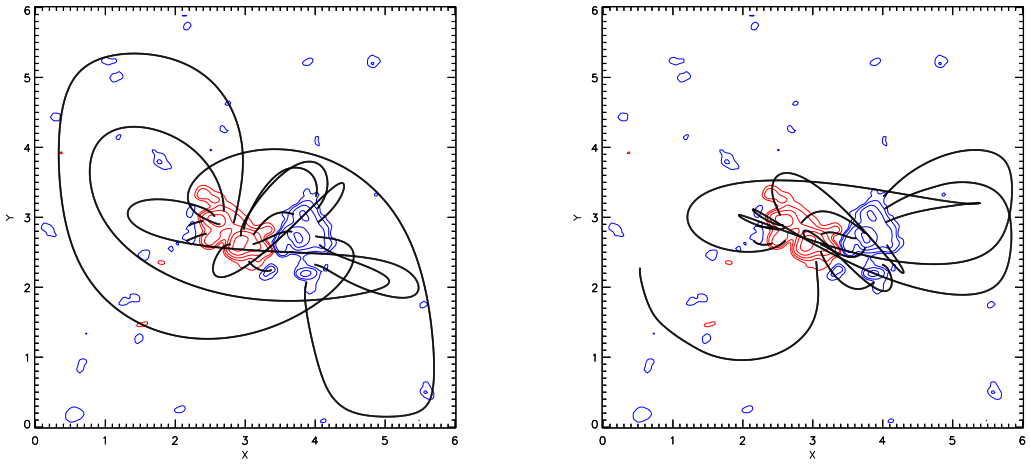

Figure 4.7: Selection of field lines (solid black lines) illustrating the positive-α (left) and negative-α (right) linear-force-free initial conditions where red and blue contours denote positive and negative photospheric flux respectively.

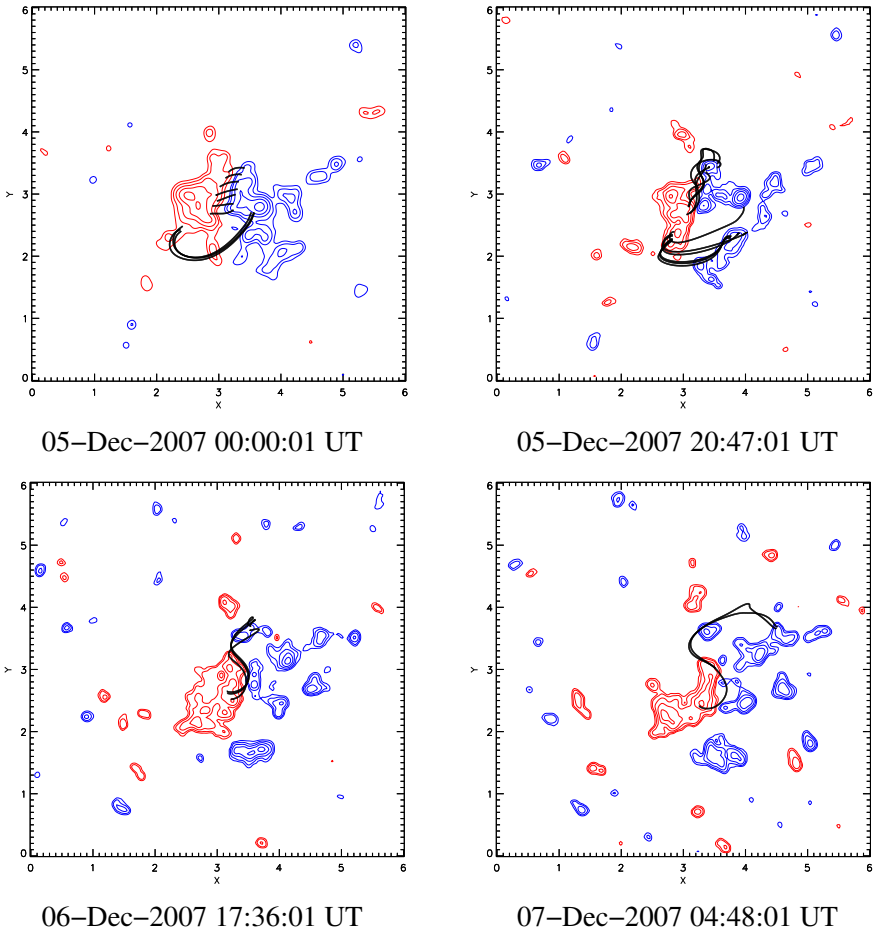

Figure 4.8: Field line plots generated from the simulation with a positive-α LFF initial condition at various times approximately corresponding to the times in Figure 3.2. The red and blue contours denote positive and negative photospheric flux respectively.

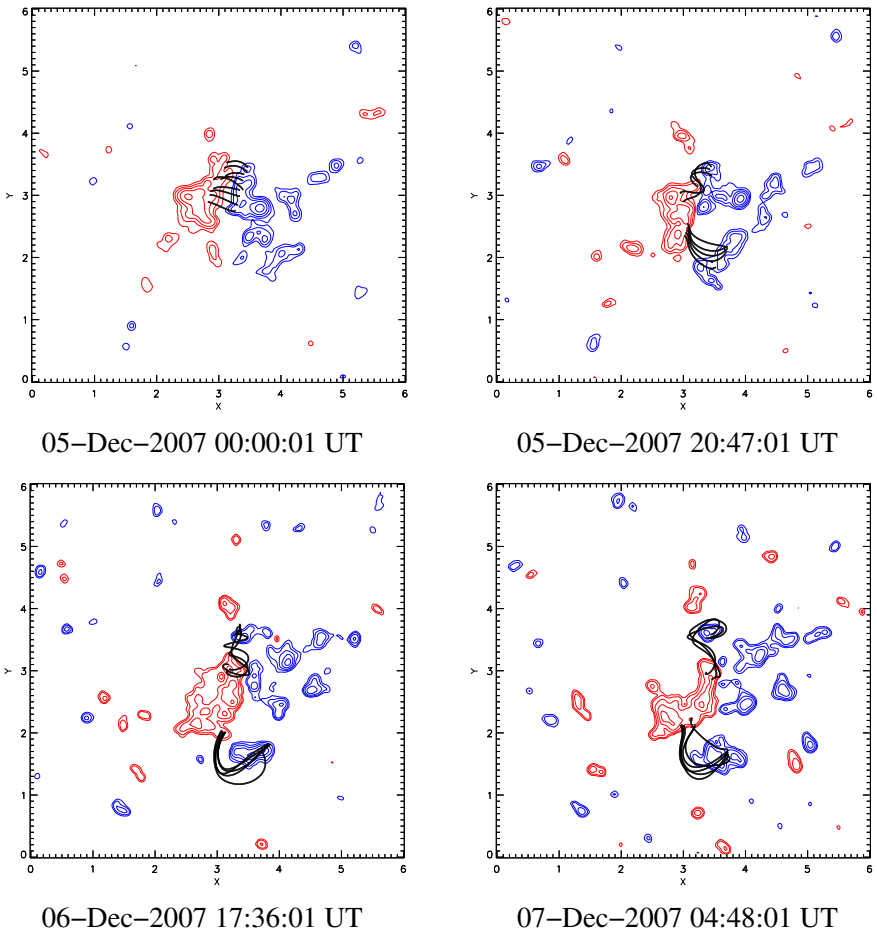

Figure 4.9: Field line plots generated from the simulation with a negative-α initial condition at various times approximately corresponding to the times in Figure 3.2. The red and blue contours denote positive and negative photospheric flux respectively.

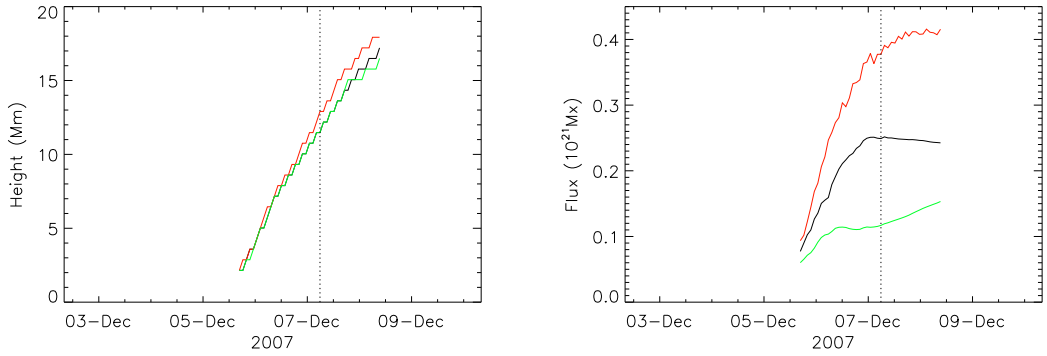

Figure 4.10: Evolution of the height (left) and flux (right) of the flux ropes in the simulations with positive-α (red line) and negative-α (green line) LFF initial conditions, along with the primary simulation (black) with time from 08:03 UT on December 2, 2007. The vertical dotted line denotes the time of the flare observed by XRT.

resembling the emission in the south of the active region is present in the simulation. In the bottom right panel of Figure 4.9, the flux rope's field lines are more S-shaped, however the southern footpoints of the flux rope are far further north in the simulation than in the observations. The emission feature in the south of the active region is well reproduced by the simulation. The northern flux rope formed at 14:23 UT on the 5^{th} December. Like the simulations with the potential and positive-α LFF field initial conditions, on the fifth day the field lines become strongly twisted, and the magnetofrictional method can no longer properly describe the coronal evolution.

4.3.2 Flux Rope Properties

Figure 4.10 outlines the evolution of the northern flux rope's height and flux with time in the simulations with positive-α (red) and negative-α (green) LFF initial conditions, along with the primary simulation (black). These quantities were calculated using the techniques described in Section 3.6. Similar to the primary simulation, the flux rope's height increases nearly linearly with time in both simulations with LFF initial conditions. The height of the flux rope in the positive-α LFF simulation at the time of the flare is 13Mm, whilst for the negative-α LFF simulation the flux rope reaches a height of 11Mm. In the simulation with the positive-α LFF initial condition, the flux rope's flux is 3.7×10^{20} Mx at the time of the flare. This corresponds to roughly 30% of the active region's flux at this time. For the simulation with the negative-α LFF initial condition, at the time of the flare the flux rope's flux is 1.2×10^{20} Mx. This is only 10% of the active region's flux at that time. For comparison, in the primary simulation the flux rope flux at the time of the flare is 20%.

4.3.3 Comparison to XRT Images

Figure 4.11 displays the LOS integrated j^2 emission proxy for the simulation with the positive-α LFF initial condition at times corresponding to those in Figure 4.8. In all four panels of Figure 4.11, the emission proxy reproduces the observed emission in the north of the active region well, however the emission proxy does not reproduce the observed emission in the south of the active region. This is due to a secondary flux rope formed

in the south of the active region, which dominates the j^2 emission proxy in the south of the active region. Similarly, Figure 4.12 displays the LOS integrated j^2 emission proxy for the simulation with the negative-α LFF initial condition at times corresponding to those in Figure 4.9. In all four panels of Figure 4.12, the emission proxy is again able to somewhat reproduce the observed emission features in the north of the active region, however is unable to reproduce the observed emission in the south of the active region. Once again, this is due to a secondary flux rope located in the south of the active region, which dominates the j^2 emission proxy in the south of the active region.

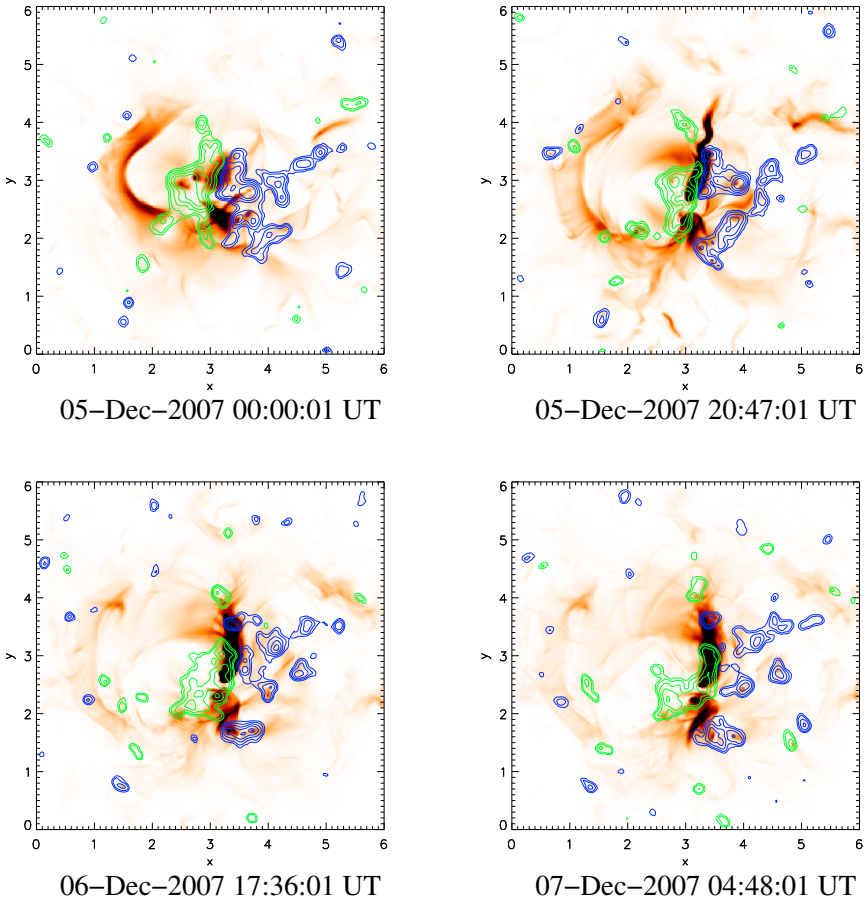

Figure 4.11: j^2 emission proxy images generated from the simulation with a positive-α initial condition at various times roughly corresponding to the times in Figure 3.2. The colour scaling saturates at one-quarter of the maximum value of the LOS integrated j^2 for each image.

4.3.4 Free Magnetic Energy

Figure 4.13 displays the evolution of the free magnetic energy as a function of time for the simulations with the positive-α (red) and negative-α (green) LFF initial conditions. Also shown for comparison is the evolution of the free magnetic energy in the primary simulation (black). The free magnetic energy is calculated in the manner described in Section 3.6. In both simulations the free magnetic energy evolution is qualitatively very similar to that of the primary simulation (Section 3.6 – Figure 3.16), however they are offset by 4×10^{30} erg

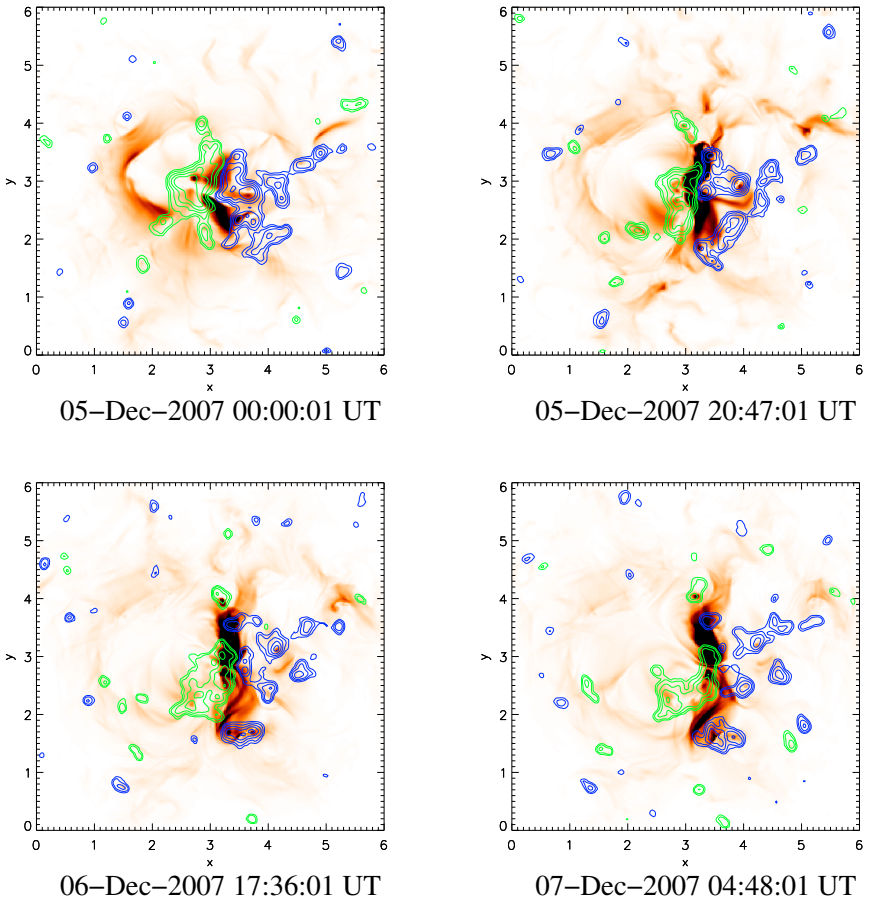

Figure 4.12: j^2 emission proxy images generated from the simulation with the negative-α initial condition at various times roughly corresponding to the times in Figure 3.2. The colour scaling saturates at one-quarter of the maximum value of the LOS integrated j^2 for each image.

due to the LFF initial conditions possessing a non-zero free magnetic energy. The energy within the flux rope at the time of the flare was calculated to be 8.39×10^{30} erg for the simulation with the positive-α LFF initial condition, and 5.94×10^{30} erg for the simulation with the negative-α LFF initial condition. For comparison, in the primary simulation the free magnetic energy within the flux rope is 6.10×10^{30} erg.

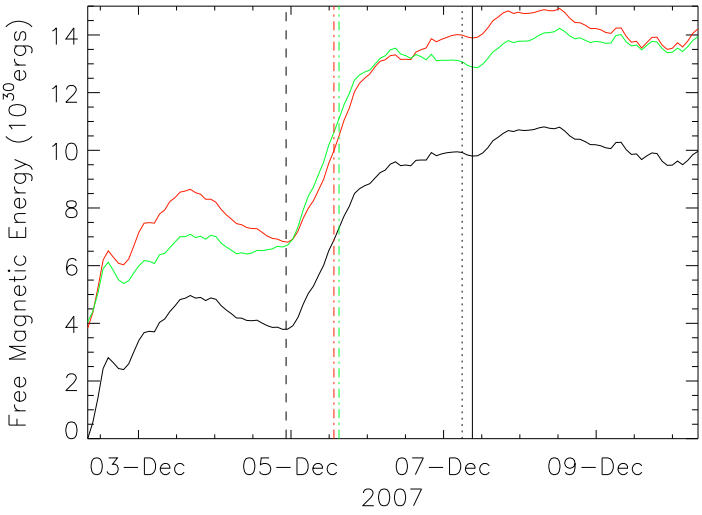

Figure 4.13: Free magnetic energy as a function of time from 08:03 UT on December 2, 2007 for the simulations with positive-α (red) and negative-α (green) LFF initial conditions. Also shown is the evolution of the free magnetic energy for the primary simulation (black line). The dashed line corresponds to the time of the main flux cancellation event. The red/green dot-dashed line corresponds to the time the flux rope formed in the simulation with the positive/negative-alpha initial condition. The dotted line corresponds to the time the flare occurred and the solid line corresponds to the time the field lines became too twisted for the magnetofrictional method to follow the evolution of the simulation accurately.

4.3.5 Helicity

Figure 4.14 displays the evolution of the relative helicity for the simulation with the positive-α LFF initial condition as a function of time. The relative helicity is calculated in the way described in Section 3.6. The relative helicity decreases sharply until the 4^{th} December, slightly increases until the 5^{th} December, decreases again until the 6^{th} December, then remains near constant for the remaining duration of the simulation. Unlike the primary simulation (Section 3.6), the helicity evolution does not qualitatively agree with the evolution of the active region's tilt angle (Figure 3.7).

Figure 4.15 displays the evolution of the relative helicity as a function of time for the simulation with the negative-α LFF initial condition. The relative helicity decreases slightly until the 4^{th} December, then increases almost linearly for the duration of the simulation. The helicity evolution qualitatively agrees with the evolution of the active region's tilt angle (Figure 3.7), however, its range over the duration of the simulation (8×10^{40} Mx^2) is far greater than the range over which the helicity varies for the primary simulation (4.5×10^{40} Mx^2).

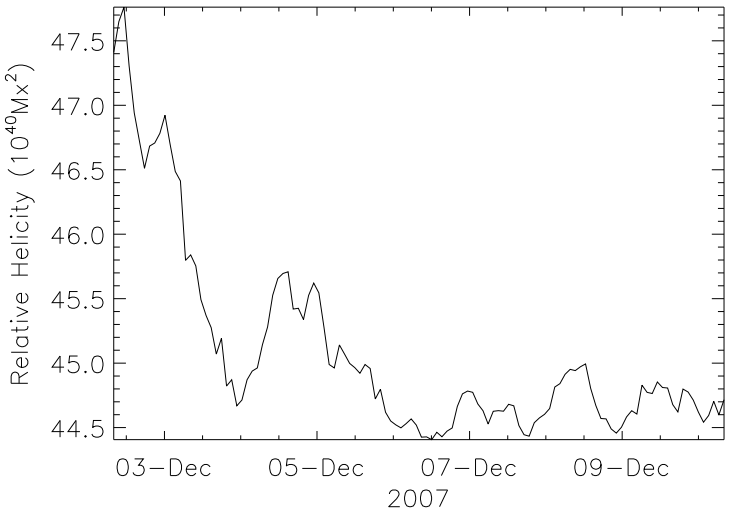

Figure 4.14: Relative helicity as a function of time from 08:03 UT on December 2, 2007 for the simulation with the positive-α LFF initial condition.

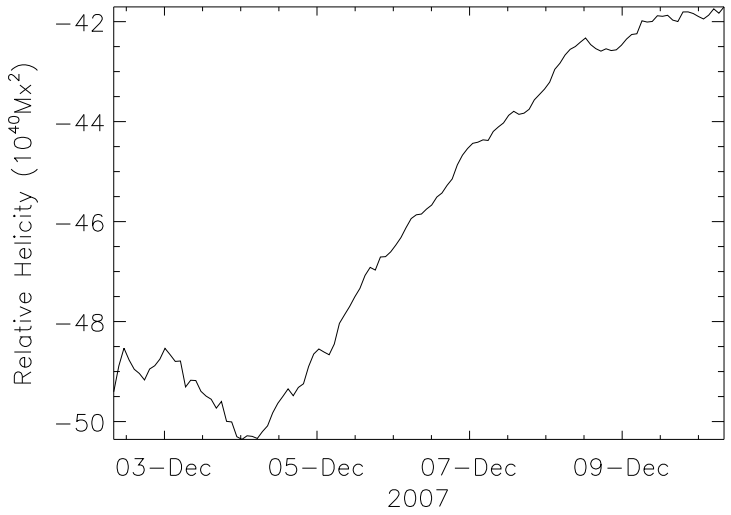

Figure 4.15: Relative helicity as a function of time from 08:03 UT on December 2, 2007 for the simulation with the negative-α LFF initial condition.

4.4 High Resolution – Potential Initial Condition

In the primary simulation and the two previous simulations using linear force-free initial conditions the evolution of the free magnetic energy was similar (save for the offset of 4×10^{30} erg in the LFF simulations due to the non-zero initial free magnetic energy). The similarity is due to the energy input into the corona being due to the surface motions injecting a Poynting flux into the corona. As the surface evolution is identical in all three simulations, the energy input should be similar. In a closed volume (in ideal MHD), the magnetic helicity is conserved. In the simulations – which have closed top and side boundaries – helicity can thus only be injected through the lower boundary, and as such can only be injected due to flux emergence, flux cancellation and photospheric motions. In all three simulations the photospheric evolution is identical, so it would be expected that the helicity evolution is similar (save for an offset due to the initial helicities being different due to the different initial conditions). As is clear from Figures 3.18, 4.14 and 4.15 this is not the case. The discrepancies between the helicity evolutions could be due to diffusive effects, which acts to reduce the relative helicity. Indeed, in the simulations with LFF initial conditions the general trend is for the helicity to increase/decrease towards zero. As these simulations do not explicitly include diffusion, the source of the diffusion must be numerical diffusion.

In order to determine the effect that the numerical diffusion has on the coronal evolution in the simulations, two simulations – one with a potential initial condition, and one with a positive-α LFF initial condition – were run at a resolution of 512^3. At a higher resolution the effects of numerical diffusion should be reduced as features in a higher resolution simulation are better resolved.

The data preparation steps for the high resolution simulations were similar to those described in Section 3.3, except that the magnetograms were resized to 508×508 instead of 254×254, and then placed in a 512×512 square. In this section, we describe the evolution of the high resolution simulation using a potential initial condition. In the following section (Section 4.5) we describe the high resolution simulation with a positive-α LFF initial condition.

4.4.1 Magnetic Field Line Evolution

Figure 4.16 displays a selection of field line plots at the same times as those corresponding to Figure 3.11, outlining the features present in the simulation corresponding to features in the X-ray observations (Figure 3.2). In the top left panel of Figure 4.16, the arcade in the northern part of the active region possesses a slight sinistral shear, in agreement with the X-ray observations. Similarly, the simulation also reproduces the the J-shaped emission feature visible in the south of the active region. In the top right panel of Figure 4.16 the northern flux rope is visible with two turns, in comparison to the flux rope in the top right panel of Figure 3.11, which only has one turn. The high resolution simulation is also able to reproduce the loops to the north of the active region, as well as those in the south of the active region. In the bottom left panel of Figure 4.16 the flux rope is clearly visible, with the inner field lines possessing two turns, whilst the outer field lines possessing only one turn. This is in contrast to the bottom left panel of Figure 3.11 where every field line in the flux rope only possesses one turn. Like the primary simulation (Section 3.6), the high resolution simulation better reproduces the northern end of the flux rope than its southern end, which terminates further north than the observed x-ray sigmoid. The arcade in the south of the active region reproduces the emission feature visible in the south of the active region. In the bottom right panel of Figure 4.16, the flux rope's southern footpoint has

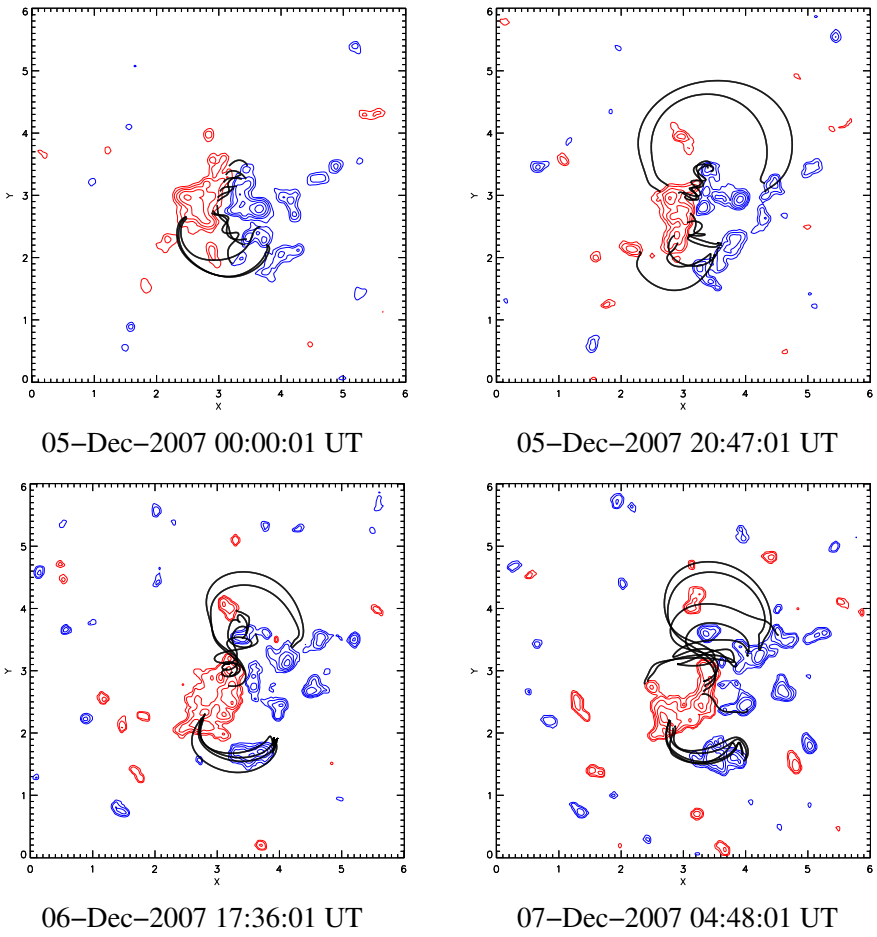

Figure 4.16: Field line plots generated from the high resolution simulation (with a potential initial condition) at various times approximately corresponding to the times in Figure 3.2. The red and blue contours denote positive and negative photospheric flux respectively.

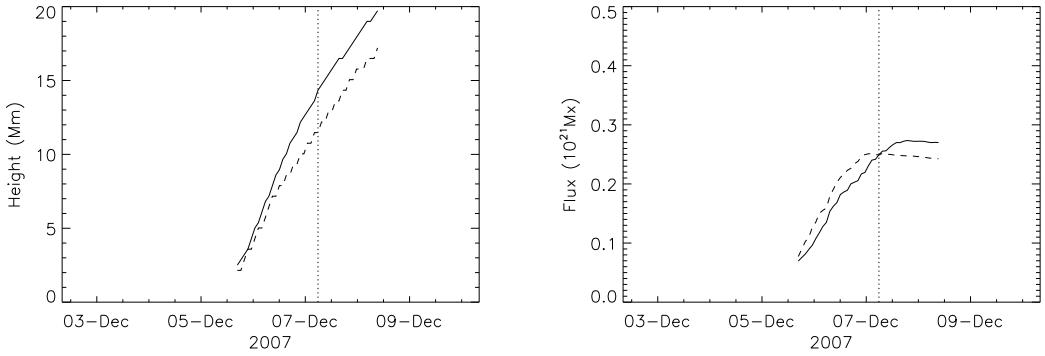

Figure 4.17: Evolution of the height (left) and flux (right) of the flux rope with time from 08:03 UT on December 2, 2007 for the high resolution simulation with a potential initial condition (solid line) and the primary simulation (dashed line). The vertical dotted line denotes the time of the flare observed by XRT.

moved further east – like in the primary simulation (Section 3.6). The emission feature in the south of the active region is well reproduced by the simulation. The northern flux rope formed at 04:47 UT on the 5$^{\text{th}}$ December. Like with the primary simulation (Section 3.6) on the fifth day the field lines become strongly twisted, and the magnetofrictional method can no longer properly describe the coronal evolution.

4.4.2 Flux Rope Properties

Figure 4.17 outlines the evolution of the northern flux rope's height and flux with time (solid line). Also shown is the evolution of the northern flux rope's height and flux in the primary simulation (dashed line). These quantities were calculated using the techniques described in Section 3.6. Like in the primary simulation, the flux rope's height increases nearly linearly with time, however at the time of the flare has reached a height of 14Mm, in contrast to the height of 11Mm achieved in the primary simulation. The flux rope's flux increases linearly until the time of the flare, where it has reached a level of 2.5×10^{20} Mx. This corresponds to roughly 20% of the active region's flux at this time, similar to the primary simulation.

4.4.3 Comparison to XRT Images

Figure 4.18 displays the LOS integrated j^2 emission proxy for the high resolution simulation at times corresponding to those in Figure 4.16. In all four panels of Figure 4.18, the emission proxy reproduces the observed emission features in the north well, however the emission proxy does not reproduce the observed emission in the south of the active region. Once again, this is due to a secondary flux rope present in the south of the active region, which dominates the j^2 emission proxy in the south of the active region.

4.4.4 Free Magnetic Energy

Figure 4.19 displays the evolution of the free magnetic energy as a function of time in the high resolution simulation (solid line). The free magnetic energy is calculated in the way described in Section 3.6. The free magnetic energy evolution is very similar to that of

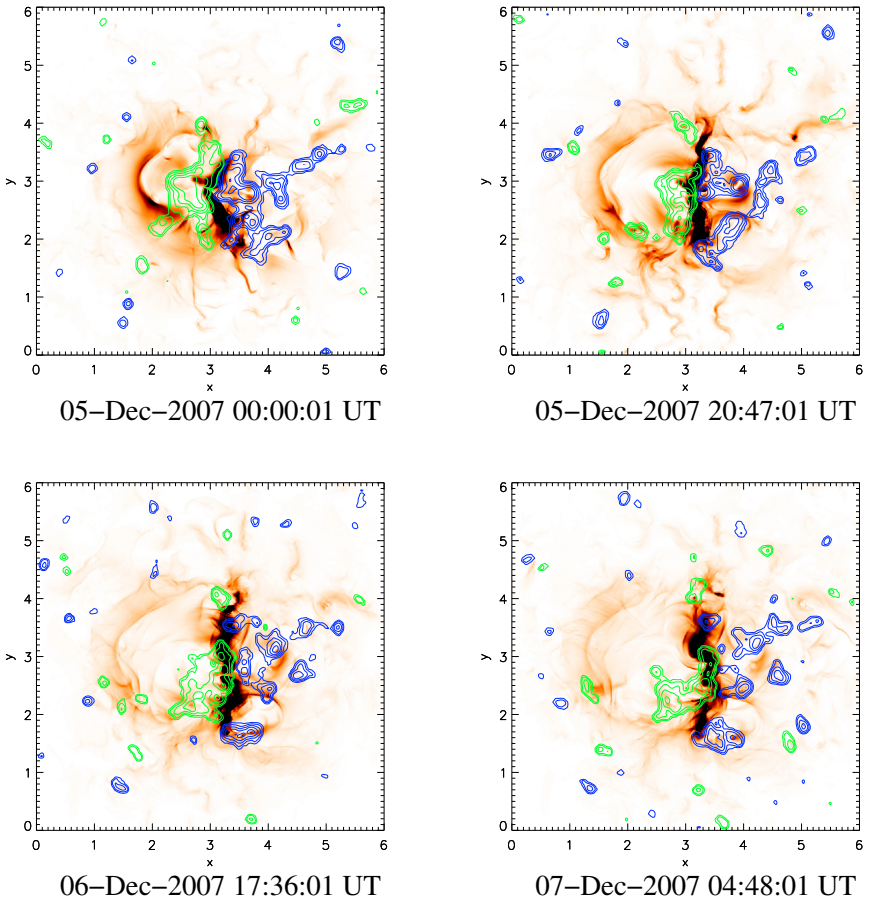

Figure 4.18: j^2 emission proxy images generated from the high resolution simulation with the potential initial condition at various times roughly corresponding to the times in Figure 3.2. The colour scaling saturates at one-quarter of the maximum value of the LOS integrated j^2 for each image.

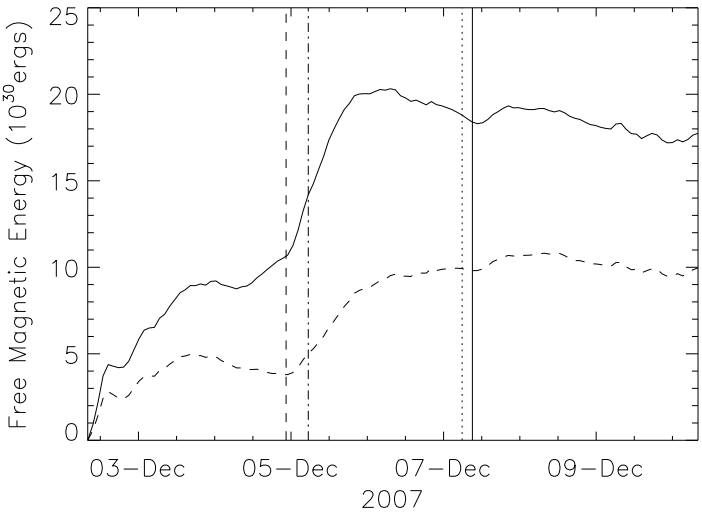

Figure 4.19: Free magnetic energy as a function of time from 08:03 UT on December 2, 2007 for the high resolution simulation with a potential initial condition (solid line) and the primary simulation (solid line). The vertical dashed line corresponds to the time of the main flux cancellation event. The vertical dot-dashed line corresponds to the time the flux rope formed in the high resolution simulation. The vertical dotted line corresponds to the time the flare occurred and the vertical solid line corresponds to the time the field lines became too twisted for the magnetofrictional method to follow the evolution of the simulation accurately.

the lower resolution primary simulation (dashed line ion Figure 4.19), however is scaled up by a factor of roughly two. The possible reasons for this discrepancy will be discussed in Section 4.7.3. The free magnetic energy within the flux rope at the time of the flare was calculated to be 10.9×10^{30} erg, just under double the free magnetic energy contained within the flux rope in the primary simulation.

4.4.5 Helicity

Figure 4.20 displays the evolution of the relative helicity as a function of time in the high resolution simulation (solid line) and the primary simulation (dashed line). The relative helicity is calculated in the way described in Section 3.6. The relative helicity decreases until the 4^{th} December, remains almost constant for a day, then increases for the rest of the simulation. The evolution of the helicity very closely matches that of the evolution of the active region's tilt angle (Figure 3.7).

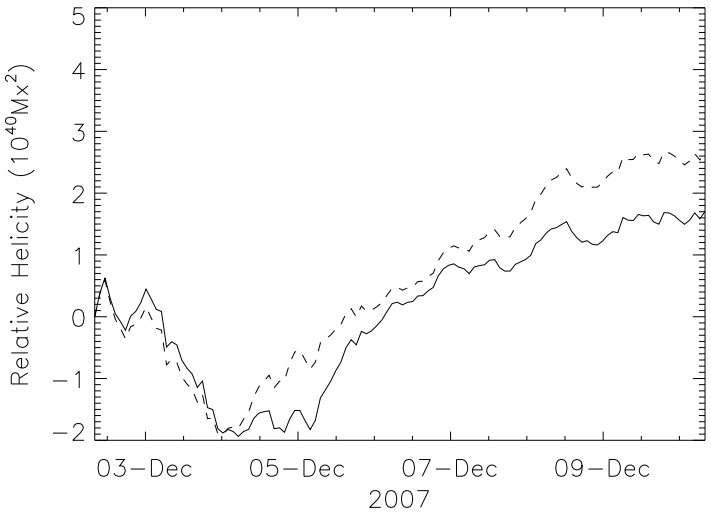

Figure 4.20: Relative helicity as a function of time from 08:03 UT on December 2, 2007 for the high resolution simulation with a potential initial condition (solid line). Also shown is the evolution of the relative helicity in the primary simulation (dashed line).

4.5 High Resolution – Positive-α Linear Force Free Initial Condition

In this section the high resolution simulation with an initial condition LFF field with $\alpha = +3.29 \times 10^{-8}$ m^{-1} is described, and contrasted to its corresponding lower resolution simulation (Section 4.3).

4.5.1 Magnetic Field Line Evolution

Figure 4.21 displays a selection of field line plots at the same times as those corresponding to Figure 3.11, outlining the features present in the simulation corresponding to features seen in the X-ray observations (Figure 3.2). In the top left panel of Figure 4.21, the arcade in the northern part of the active region possesses a sinistral shear, in agreement with the X-ray observations. Similarly, the simulation also reproduces the J-shaped emission feature visible in the south of the active region. In the top right panel of Figure 4.21 the northern flux rope is visible with two turns, in comparison to the flux rope in the top right panel of Figure 4.8, which only has one turn. The high resolution simulation is also able to reproduce the observed loops in the south of the active region. In the bottom left panel of Figure 4.21 the flux rope is clearly visible, with flux rope field lines possessing two turns. This is in contrast to the bottom left panel of Figure 4.8 where every field line in the flux rope only possesses one turn. Like the low resolution positive-α simulation (Section 4.3), the high resolution simulation better reproduces the northern end of the flux rope than its southern end, which terminates further north than the observed X-ray sigmoid. Also like the low resolution positive-α simulation, the observed arcade in the south of the flux rope is not reproduced. In the bottom right panel of Figure 4.21, the flux rope has a very similar shape to the bottom left panel. similar to the lower resolution positive-α simulation (Section 4.3), the high resolution resolution positive-α simulation is unable to reproduce the observed arcade in the south of the active region. The northern

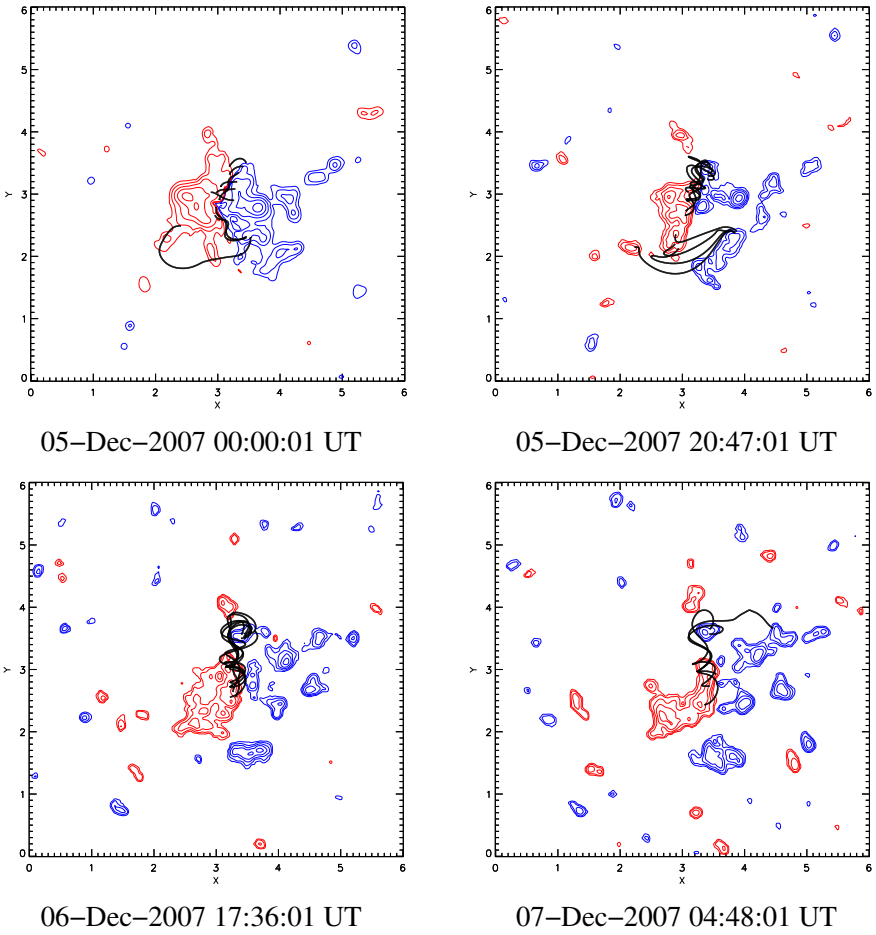

Figure 4.21: Field line plots generated from the high resolution simulation with a positive-α initial condition at various times approximately corresponding to the times in Figure 3.2. The red and blue contours denote positive and negative photospheric flux respectively.

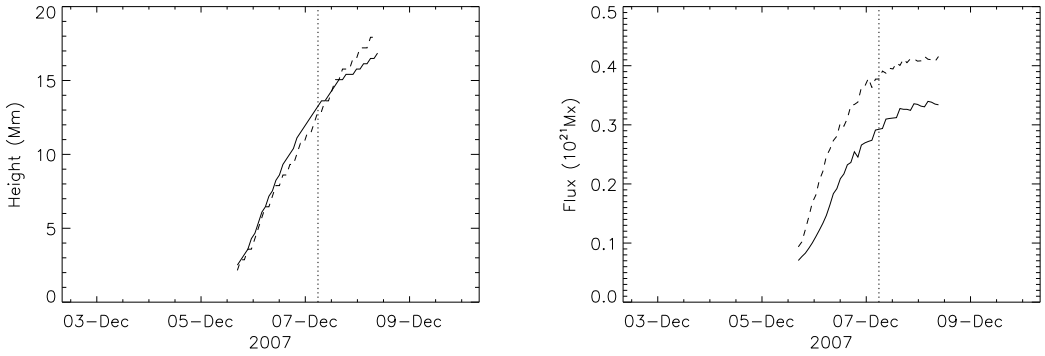

Figure 4.22: Evolution of the height (left) and flux (right) of the flux rope with time from 08:03 UT on December 2, 2007 for the high (solid line) and low (dashed line) resolution simulations with $+\alpha$ LFF initial conditions. The vertical dotted line denotes the time of the flare observed by XRT.

flux rope formed at 00:00 UT on the 5^{th} December. As with the low resolution positive-α simulation (Section 4.3) on the fifth day the field lines become strongly twisted, and the magnetofrictional method can no longer properly describe the coronal evolution.

4.5.2 Flux Rope Properties

Figure 4.22 outlines the evolution of the northern flux rope's height and flux with time in the high resolution simulation with the positive-α LFF initial condition. Also shown is the evolution of the height and flux of the flux rope in the lower resolution simulation with the positive-α LFF initial condition (see Section 4.3). These quantities were calculated using the techniques described in Section 3.6. Similar to the low resolution positive-α simulation, the flux rope's height increases nearly linearly with time, and at the time of the flare has reached a height of 13Mm. The flux rope's flux in the high resolution simulation increases until the time of the flare, where it has reached a level of 3.0×10^{20} Mx. This corresponds to roughly 24% of the active region's flux at this time. This is less than in the corresponding lower resolution simulation, where it reaches 30% of the active region's flux.

4.5.3 Comparison to XRT Images

Figure 4.23 displays the LOS integrated j^2 emission proxy for the high resolution simulation at times corresponding to those in Figure 4.21. In all four panels of Figure 4.23, the emission proxy reproduces the observed emission features in the north well, however the emission proxy does not reproduce the observed emission in the south of the active region. Once again, this is due to a secondary flux rope formed in the south of the active region, which dominates the j^2 emission proxy at this location.

4.5.4 Free Magnetic Energy

Figure 4.24 displays the evolution of the free magnetic energy as a function of time in the high resolution simulation with the positive-α LFF initial condition. Also shown is the evolution of the free magnetic energy in the lower resolution simulation with the positive-α

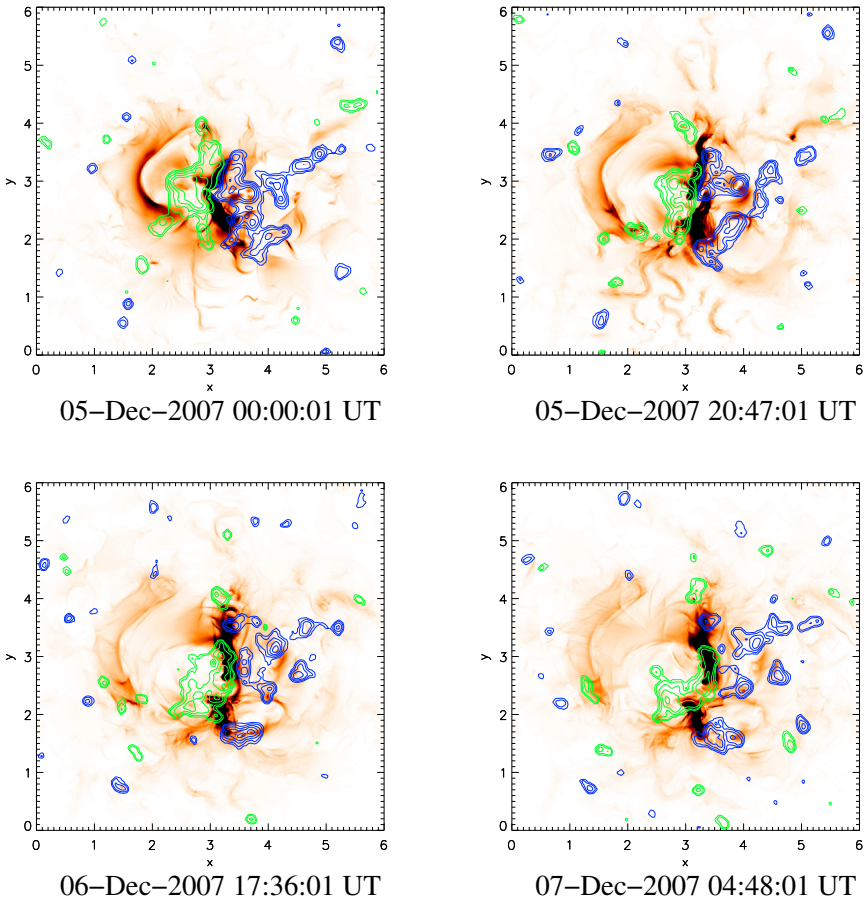

Figure 4.23: j^2 emission proxy images generated from the high resolution simulation with a positive-α initial condition at various times roughly corresponding to the times in Figure 3.2. The colour scaling saturates at one-quarter of the maximum value of the LOS integrated j^2 for each image.

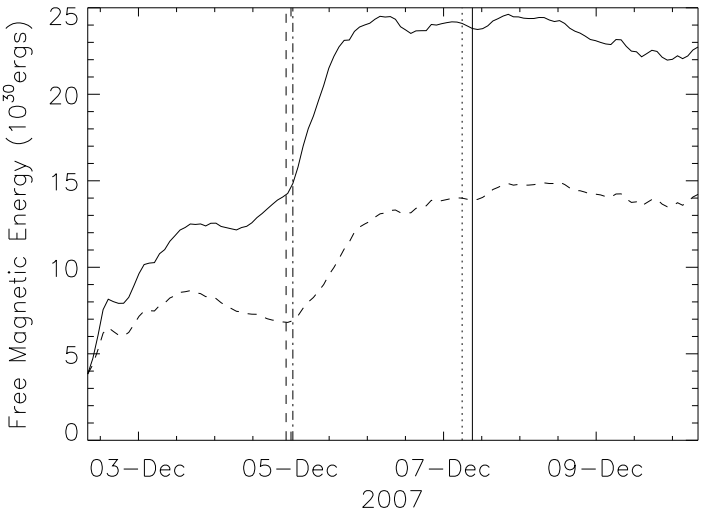

Figure 4.24: Free magnetic energy as a function of time from 08:03 UT on December 2, 2007 in the high (solid line) and low (dashed line) resolution simulations with positive-α LFF initial conditions. The vertical dashed line corresponds to the time of the main flux cancellation event. The vertical dot-dashed line corresponds to the time the flux rope formed in the high resolution simulation. The vertical dotted line corresponds to the time the flare occurred and the vertical solid line corresponds to the time the field lines became too twisted for the magnetofrictional method to follow the evolution of the simulation accurately.

LFF initial condition (see Section 4.3). The free magnetic energy is calculated in the way described in Section 3.6. The free magnetic energy evolution of the high resolution positive-α simulation is very similar to that of the low resolution positive-α simulation (Section 4.3), however the energy input is greater. The possible reasons for this discrepancy will be discussed in Section 4.7.3. The energy within the flux rope at the time of the flare in the higher resolution simulation was calculated to be 13.7×10^{30} erg. This is greater than the value of 8.39×10^{30} erg in the lower resolution simulation.

4.5.5 Helicity

Figure 4.25 displays the evolution of the relative helicity as a function of time in the high resolution simulation with the positive-α LFF initial condition (solid line). Also shown for comparison is the evolution of the relative helicity as a function of time in the low resolution simulation with the positive-α LFF initial condition (dashed line). The relative helicity is calculated in the way described in Section 3.6. The relative helicity in the high resolution simulation decreases until the 4^{th} December, remains almost constant for a day, then increases for the rest of the simulation. The evolution of the helicity very closely matches that of the evolution of the active region's tilt angle (Figure 3.7), in contrast to the low resolution positive-α simulation, whose helicity evolution does not follow the active region's tilt angle evolution.

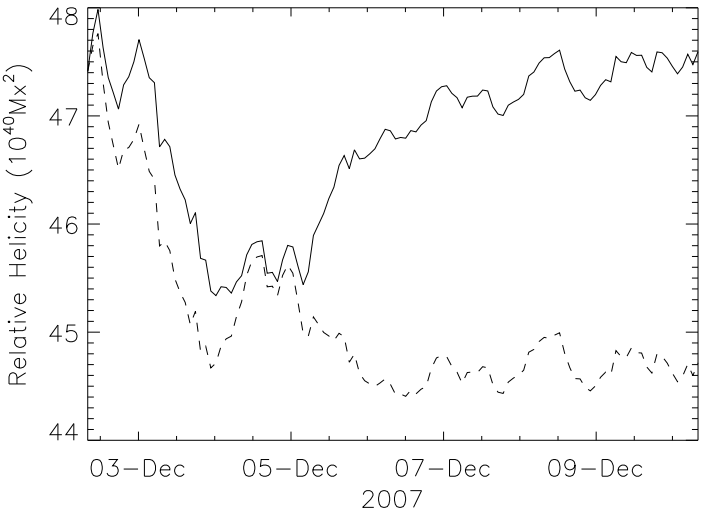

Figure 4.25: Relative helicity as a function of time from 08:03 UT on December 2, 2007 for the high (solid line) and low (dashed line) resolution simulations with positive-α LFF initial conditions.

4.6 Limitations of Using Line of Sight Magnetograms as a Lower Boundary Condition

The method used in this thesis to simulate the evolving coronal magnetic field of an active region is limited due to the use of line of sight (LOS) magnetograms. When determining B_z from the LOS magnetograms, the assumption is made that the majority of the signal along the LOS comes from the radial field. In other words, $B_{\rm LOS} \approx B_r \cos\theta_{\rm LOS}$, where $\theta_{\rm LOS}$ is the angle the line of sight makes with the normal to the photosphere. Using this assumption, no information on the horizontal field component may be recovered. Vector magnetograms (such as those available from SDO/HMI or Hinode/SOT) show that the magnetic field at the photosphere is not purely radial and can have significant horizontal components. If LOS magnetograms are used as a lower boundary condition, no information on the horizontal magnetic fields is present, and effects such as a rotational motion of the photospheric field cannot be recovered by the simulation.

In order to demonstrate this, two simulations were set up with a photospheric flux distribution, B_z, chosen to be:

$$B_z(x,y) = B_0 \left[\exp\left(-\frac{r_0^2}{\Delta r^2}\right) - \exp\left(-\frac{r_1^2}{\Delta r^2}\right) \right] \tag{4.1}$$

where B_0 is the peak magnetic flux density, $r_0^2 = (x-x_0)^2 + (y-y_0)^2$, $r_1^2 = (x-x_1)^2 + (y-y_1)^2$, (x_0, y_0) is the centre of the positive flux, (x_1, y_1) is the centre of the negative flux and Δr is the width of the gaussian profiles used for the positive and negative flux concentrations. This flux distribution is displayed in Figure 4.26, along with the velocity

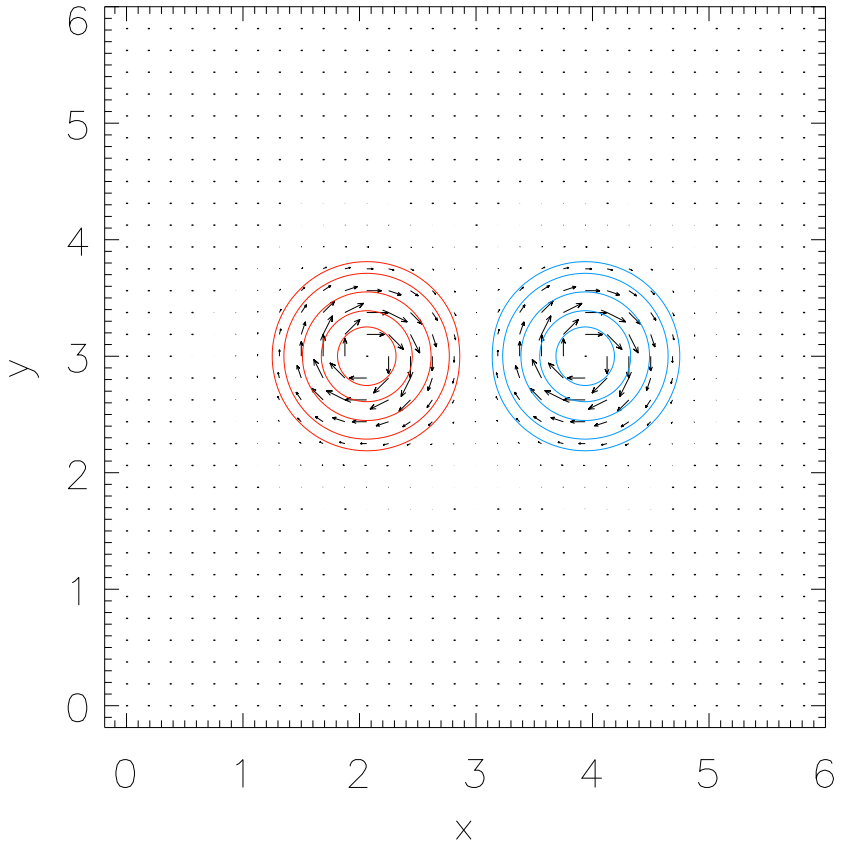

Figure 4.26: The magnetic field distribution on the photosphere (red and blue contours representing positive and negative magnetic flux respectively) and the velocity field applied to the photospheric field (vectors).

field it is evolved according to,

$$v_x(x,y) = \Omega_0 \left[\frac{r_0}{\Delta r} \exp\left(-\frac{r_0^2}{\Delta r^2} \right) \sin\theta_0 + \frac{r_1}{\Delta r} \exp\left(-\frac{r_1^2}{\Delta r^2} \right) \sin\theta_1 \right] \tag{4.2}$$

$$v_y(x,y) = -\Omega_0 \left[\frac{r_0}{\Delta r} \exp\left(-\frac{r_0^2}{\Delta r^2} \right) \cos\theta_0 + \frac{r_1}{\Delta r} \exp\left(-\frac{r_1^2}{\Delta r^2} \right) \cos\theta_1 \right] \tag{4.3}$$

where Ω_0 is the angular velocity of rotation and

$$\theta_{0/1} = \arctan\left(\frac{y - y_{0/1}}{x - x_{0/1}} \right). \tag{4.4}$$

The velocity field acts to rotate each polarity about its centre of flux. This rotation keeps B_z unchanged with time.

In the first simulation (hereby Simulation 1) the photospheric magnetic potentials are prescribed according to B_z using the method described in Section 3.5. As the B_z profile remains unchanged, due to the method employed the values of A_{xb} and A_{yb} are identical for every time. In the second simulation (hereby Simulation 2) the photospheric magnetic

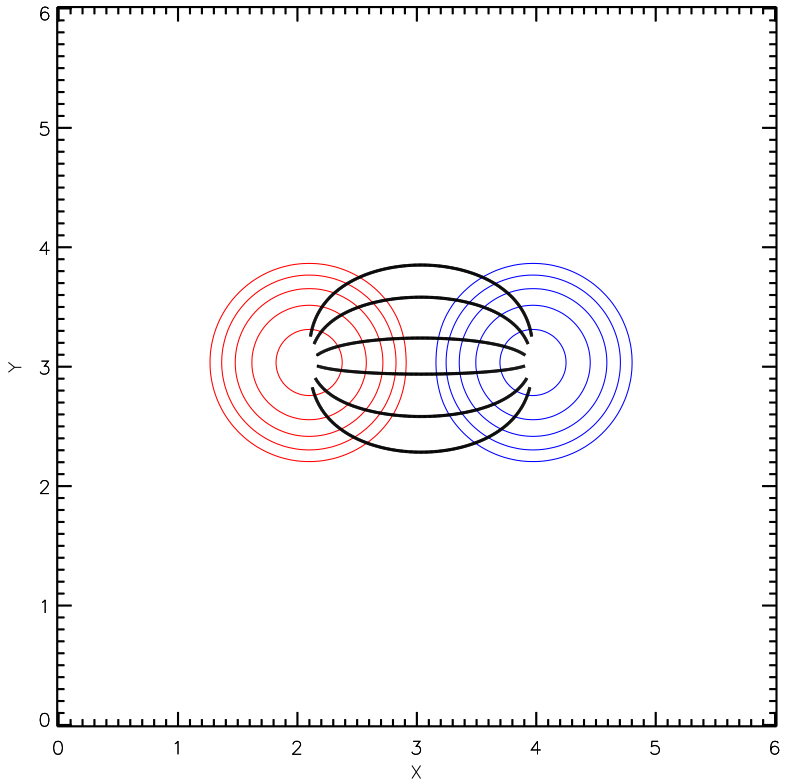

Figure 4.27: Potential initial condition coronal field for Simulations 1 and 2.

potentials are evolved according to the equations of surface flux transport:

$$\frac{\partial A_{xb}}{\partial t} = v_y B_z \tag{4.5}$$

$$\frac{\partial A_{yb}}{\partial t} = -v_x B_z. \tag{4.6}$$

and are thus time evolving as $v_y B_z$ and $v_x B_z$ are nonzero. It is important to emphasise that in both simulations the time evolution of B_z is identical and only the time evolution of A_{xb} and A_{yb} differ. Whilst the A_{xb} and A_{yb} in Simulation 2 produce the same B_z distribution as in Simulation 1, they do not result in the same horizontal (B_x and B_y) component on the photosphere. This is because B_x and B_y are dependent upon vertical gradients in A_{yb} and A_{xb} respectively, which differ between Simulations 1 and 2.

The simulations were run with 256^3 resolution using Hexa, with the initial potential coronal field calculated in the same manner as described in Section 3.5.2. The initial coronal field is displayed in Figure 4.27. Figure 4.28 displays field line plots from Simulations 1 and 2 when $\Omega_0 t = 2\pi$. It is clear that in Simulation 1 – which solely uses B_z to reconstruct A_{xb} and A_{yb} – that the coronal field has not changed from the initial condition. In Simulation 2, which uses the surface transport equation to derive the evolution of A_{xb} and A_{yb} according to the applied velocity, it is clear that the coronal field has become twisted due to the rotational motions applied at the base.

The above results demonstrate that the horizontal fields, which cannot be obtained from LOS magnetograms, can have a large effect to the evolution of the coronal magnetic field. It is important to note that since the LOS magnetograms do not provide the

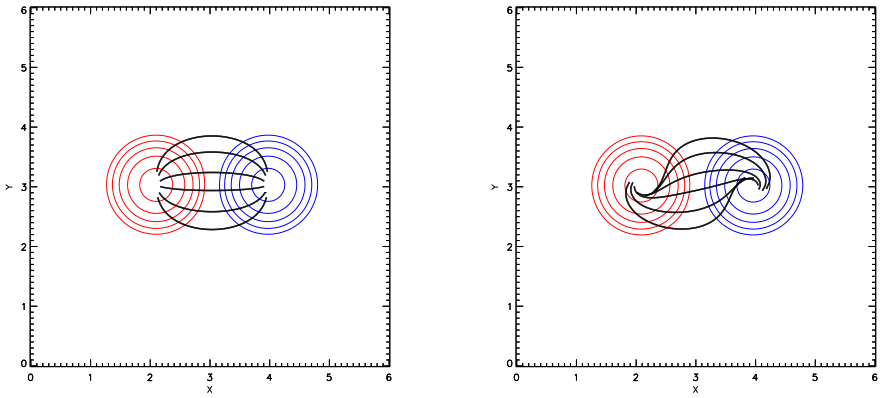

Figure 4.28: Field line plots from Simulations 1 (left) and 2 (right) after $\Omega_0 t = 2\pi$. It is clear that whilst the field lines in Simulation 1 look identical to those in the potential initial condition (Figure 4.27), in Simulation 2 the field has become twisted.

horizontal magnetic fields at the photosphere, some assumption of their nature must be made when constructing A_{xb} and A_{yb}. In this thesis, the vector potential on the base is calculated independently for each time using Equation 3.4. The continuous time evolution is achieved through linearly interpolating A_{xb} and A_{yb} from one time to another. As such, the horizontal fields induced in our simulations are driven by the the linear transformation of A_{xb} and A_{yb} from one observation to another. In a previous study, Cheung & DeRosa (2012) model AR11158 using the magnetofrictional method in a manner very similar to that of Mackay et al. (2011) and the work on AR10977 described in this thesis. In their study, they are able to form a flux rope in the active region by imposing an unobserved spatially uniform twisting motion to their lower boundary conditions. Interestingly, in this thesis' study on AR10977 twisting motions do not need to be applied in order to form the flux rope at the location of the XRT sigmoid. It is unclear why the model used in this thesis does not require the extra twisting motions. Two possible explanations are that either:

1. The evolution of the magnetic field of the active region considered here is fundamentally different compared to the one studied by Cheung & DeRosa (2012). A detailed study of the magnetic evolution of the two active regions would be required to determine if this is the case.

2. The boundary treatments of Cheung & DeRosa (2012) and Mackay et al. (2011) may inject different non-potential fields into the corona. It is possible that the technique used in the present study captures a horizontal non-potential component that builds up the axial flux of the flux rope. In contrast Cheung & DeRosa (2012) may require the inclusion of twisting motions if their technique injects a weaker non-potential horizontal component.

Resolving these issues is beyond the scope of this thesis.

4.7 Discussion

In this section, the results of the above simulations are summarised, compared with each other, and the differences between then discussed. Table 4.1 outlines the southern extent

Resolution	α	Diffusion	Other	Flux (10^{20} Mx)	Energy (10^{30} erg)	S Footpoint
256	0	-	-	0.25	6.10	2.7
256	+	-	-	0.37	8.39	2.4
256	−	-	-	0.17	5.94	2.9
256	0	Hyper	-	0.25	5.73	2.7
256	0	Ohmic	-	-	-	-
256	0	-	No cleaning	0.23	5.99	2.7
256	0	-	Later start time	0.38	10.3	2.6
512	0	-	-	0.25	10.9	2.7
512	+	-	-	0.29	13.7	2.2
Observations / previous studies				≤ 0.4[1]	6 [2]	2.0 [3]

Table 4.1: A table summarising the properties of the northern flux ropes in each simulation.

of the flux rope (in Hexa units), the flux within the flux rope and the free magnetic energy at the time of the flare for the different simulations, observations and previous studies.

4.7.1 Starting Time

One simulation with a potential initial condition was run starting two days after the other simulations (Section 4.2). The start time of this simulation was after the initial clockwise rotation of the active region, where negative helicity was injected into the corona (e.g. Figure 3.18). Through comparing the results of this simulation with the primary simulation (Section 3.6) the effect that the initial clockwise rotation of the active region had on the subsequent evolution of the corona may be inferred. Upon inspection of the field line plots (Figures 3.11 and 4.2) the main difference which can be seen is in the top left panel of each figure, where the arcade field (which is transformed into the flux rope during the flux cancellation event) possesses sinistral shear in the simulation starting after the clockwise rotation, and no shear in the simulation that started before the clockwise rotation. The field line plots in the other panels of Figures 3.11 and 4.2 look qualitatively similar. Due to the greater shear present in the simulation that started at the later time, during the flux cancellation event more axial flux is built into the flux rope than in the primary simulation. Also, the flux rope in the simulation that started at a later time formed three hours earlier than the flux rope in the primary simulation.

Upon considering the evolution of the free magnetic energy between the simulations started before and after the clockwise rotation, it is clear that in the simulation that started after the clockwise rotation more free magnetic energy is built up during the simulation. One possible explanation for this is that during the clockwise rotation the active region's coronal field is wound up, injecting negative magnetic helicity and free magnetic energy. At the beginning of the counter-clockwise rotation, the active region's coronal field is then unwound (increasing the magnetic helicity towards zero and decreasing the free magnetic energy) before being wound back up with positive helicity and having free magnetic energy added. This is evident in the energy plot (Figure 3.16) where the free magnetic energy decreases slightly between the fourth and fifth of December. In the simulation that started after the clockwise rotation ended, the onset of counter-clockwise rotation begins to shear

[1] Green et al. (2011)
[2] Savcheva et al. (2012)
[3] Observations

up the coronal field and build up free magnetic energy. No unwinding of the field takes place, and thus no energy is removed from the coronal magnetic field. The free magnetic energy built up in this simulation is thus higher than that built up in the simulation starting before the clockwise rotation. Similarly the flux rope in the simulation which started after the clockwise rotation of the active region contains more free magnetic energy than the simulation that started before the clockwise rotation. This is because the sheared arcade from which the flux rope forms is more sheared in the simulation starting after the clockwise rotation and so more axial flux and thus free magnetic energy is built into the flux rope during its formation.

It can be concluded that the effect of the clockwise rotation on the subsequent evolution of the active region's magnetic field was to reduce the flux (and free magnetic energy) in the flux rope by injecting negative magnetic helicity into the corona, which reduced the efficiency of the counter-clockwise rotation forming the flux rope. Whilst the clockwise rotation resulted in less flux and energy in the flux rope, the initial clockwise rotation had no significant effect on the shape of the flux rope's field lines.

4.7.2 Choice of α

Several differences between the results of the simulations using potential and linear force-free initial conditions are apparent. By considering the flux rope formed in the simulations, and comparing it to the observed sigmoid, the simulation with a positive-α initial condition provided the best fit, followed by the simulation with the initial potential field. The worst fit was the simulation with the negative-α initial condition. This is not surprising, as active regions in the southern hemisphere of the Sun tend to possess positive helicity, corresponding to a positive value of α. The choice of an initial condition with negative-α is therefore in contradiction to observations, and so is unlikely to be a plausible initial condition. Considering the flux rope flux at the time of the flare, once again it is found that the simulation which produces the best match with the findings of Green et al. (2011) and Savcheva et al. (2012) is that with the positive-α initial condition, followed by the potential initial condition, and finally the negative-α initial condition. The free magnetic energy contained within the flux rope that best matches the findings of Savcheva et al. (2012) is the low-resolution simulation with an initial potential field (the primary simulation).

The northern flux ropes in the high and low resolution simulations with a positive-α initial condition formed earlier than those in their corresponding simulations with a potential initial condition. The formation time for the northern flux rope was the same in the simulations with the potential and negative-α initial conditions.

Whilst the simulation with a positve-α initial condition provides the best fit for the flux rope, it is unable to reproduce the arcade in the south of the active region. The simulations with the potential and negative-α initial conditions, which do not provide the best fit for the northern flux rope, can however reproduce the south of the active region better. This implies that the likely magnetic field configuration of the active region at the beginning of the observations is a NLFF with a predominantly positive α in the northern half of the active region, and zero or negative α in the south of the active region. These findings contrast with the suggestion in Section 3.10.1 that a simulation with a positive α in the south of the active region may result in a better fit. It is also suggested in Section 3.10.1 that the flux rope in the south of the active region may not form in a simulation with a $+\alpha$ LFF initial condition, however for the relatively large value of α chosen in this thesis, the souther flux rope still formed.

An important thing to note about linear force-free fields is that the degree of twist a field line has is proportional to its length. Therefore, even in linear force-free fields with

relatively large values of $|\alpha|$, short field lines are relatively untwisted. This is evident in Figure 4.7 where the short field lines in the inside of the active region that cross the polarity inversion line are relatively untwisted, whilst the long field lines towards the outside of the active region are highly twisted. The flux rope forms from the arcade across the PIL, whose field lines are relatively short, and therefore relatively insensitive to the choice of α. In order to significantly alter the formation and properties of the flux rope, a large value of $|\alpha|$ must be chosen in order to produce an initial strong shear across the PIL. Such a large $|\alpha|$ would result in highly twisted field lines towards the edge of the active region, which are unphysical. A non-linear force-free initial condition would overcome this problem, however the construction of such a field is non-trivial.

4.7.3 Simulation Resolution

Now the differences between the high resolution simulations (Sections 4.4 and 4.5) and their corresponding low resolution simulations (Sections 3.6 and 4.3) will be discussed. The high resolution simulations produce the same field line structures (Figures 4.16 and 4.21) as the low resolution simulations (Figures 3.11 and 4.8), however, in the high resolution simulations the flux rope formed contains two turns, compared to the low resolution simulations where the flux ropes contain only one turn. This effect is due to the numerical diffusion, which is weaker in the high resolution simulation due to the smaller grid spacing. The lower numerical diffusion results in less diffusion of the flux rope field lines, permitting a more twisted structure. In the lower resolution simulations the flux rope possesses fewer turns as numerical diffusion acts to diffuse some of the poloidal flux of the flux rope, resulting in a less twisted structure. Additionally, the northern flux rope in the high resolution simulations forms at earlier times than in the low resolution simulations.

The effect of the lessened numerical diffusion in the high resolution simulations is also apparent when considering the evolution of the free magnetic energy. In the high resolution simulations (Figures 4.19 and 4.24), roughly twice the amount of free magnetic energy is built up during the simulations compared to the low resolution simulations (Figures 3.16 and 4.13). This is attributed to the smaller numerical diffusion in the high resolution simulations removing less energy from the system. Additionally, the free magnetic energy within the flux ropes is found to be higher in the high-resolution simulations than in the low-resolution simulations. This is due to the flux ropes in the high-resolution simulations containing more twist, and thus more free magnetic energy.

The differences between the high and low resolution simulations are most apparent when considering the evolution of the relative magnetic helicity (Figures 3.18, 4.14, 4.20 and 4.25). In both high resolution simulations the relative helicity evolution very closely matches the evolution of the active region's tilt angle. Whilst this is true for the low resolution simulation with a potential initial condition (the primary simulation), it is not the case for the low resolution simulation with a positive-α initial condition, where the general trend is for the helicity to decrease throughout the duration of the simulation. This could be attributed to the numerical diffusion diffusing away the high amount of helicity present in the positive-α initial condition simulation. A similar effect is seen in the simulation with a negative-α initial condition (Figure 4.15), where the helicity increases steeply for the duration of the simulation. Since in both the high resolution simulations the evolution of the relative helicity is qualitatively the same (save for the offset of 47.5×10^{40} Mx^2 due to the different initial conditions) it is reasonable to assume that the relative helicity it well conserved in both these simulations, and that the injection of the helicity is due to the evolution of the tilt angle of the active region.

4.7.4 Summary

In all the simulations (save for the one with Ohmic diffusion) a flux rope formed at the location of the observed X-ray sigmoid. The flux rope in the simulations formed roughly one day before the sigmoid was visible in XRT observations. In all the simulations the field lines become strongly twisted (implying a non-equilibrium event has occurred) on the fifth day, at a time corresponding to the observed flare and eruption of the sigmoid. This implies that the state of the flux rope in the simulations by this time had become almost independent of the initial condition, as its loss of equilibrium occurred at the same time in each simulation. The simulations were better at simulating the northern half of the active region than the southern half. In all the simulations (save for the one with Ohmic diffusion) a second flux rope formed in the south of the active region. In the XRT images no evidence of this flux rope is present. It was proposed that using a positive-α linear force-free initial condition may prevent this flux rope from forming, however this was found to not be the case. The positive-α simulations did however provide the best fit with the XRT observations of the sigmoid, insofar as the southern footpoint of the northern flux rope was located closest to the southern footpoint of the sigmoid.

Simulations with Ohmic diffusion and hyperdiffusion were carried out. In the simulation with Ohmic diffusion no flux ropes formed. This was due to the value of η that was used in the simulation being rather high, causing any strongly sheared field to diffuse away. The results of the simulation with hyperdiffusion were very similar to the simulations that did not use hyperdiffusion. The principal difference was that the emission proxy images produced from the simulation with hyperdiffusion were smoother looking than the images produced from the simulations without hyperdiffusion. It was found that the cleaning process applied to the magnetograms reduced the noise in the simulations without affecting the large-scale properties of the active region.

The flux contained within the flux rope was found to be 20% of the active region flux in the primary simulation. In the simulations with positive- and negative-α LFF initial conditions the flux rope flux was found to be 24-30% and 10% respectively. Green et al. (2011) and Savcheva et al. (2012) estimated the flux rope flux to be $\geq$ 30% and 50% respectively. The simulations with $+\alpha$ initial conditions thus provide the best match with the flux. A simulation was run at a later start time, after the active region's clockwise rotation phase. The flux in the flux rope in this simulation was found to also be 30% of the active region's flux.

The evolution of the free magnetic energy in the simulations were qualitatively similar. This is not surprising, as since the computational box has closed top and side boundaries, the free magnetic energy must be injected into the simulation through the photospheric evolution, which is identical in each simulation. In the high resolution simulations the free magnetic energy injection was roughly a factor of two higher than in the lower resolution simulations. This is because numerical diffusion is weaker in the higher resolution simulations, so less energy is lost due to this. The free magnetic energy contained within the flux rope was highest for the simulations with a positive-α initial condition. The simulation with negative-α produced the flux rope with the lowest free magnetic energy content.

It was found that the helicity evolution throughout the simulations very closely matched the evolution of the tilt angle of the active region. This implies that the large-scale motions of the active region are the primary source of magnetic helicity in the corona around active regions. From the results of the simulation using uncleaned magnetograms it was suggested that the smale-scale magnetic features inject positive helicity into the simulation. This is consistent with the helicity condensation model of Antiochos (2013).

In this thesis, we have tested the modelling technique of Mackay et al. (2011), which

uses a time series of MDI magnetograms and a magnetofrictional relaxation technique. The test, which produces results consistent with a previous observational study (Green et al. 2011) and static models (Savcheva et al. 2012) is also able to successfully reproduce the time-evolution of the active region as observed by Hinode XRT. These included the formation of a sigmoidal flux rope through flux cancellation and the development of the flux rope towards eruption. It is important to emphasise that although the simulations described in the previous two chapters use different initial conditions and resolutions, the qualitative evolution of the active region and its flux rope's properties are similar in each simulation. In particular, it is found that twisting motions such as those employed by Cheung & DeRosa (2012) to match coronal images were not required to produce a flux rope. In addition, the technique we applied shows that solely surface motions deduced from observed magnetograms can be sufficient to explain the energy required to satisfy the observed flare. This study shows that magnetofrictional techniques driven by observed LOS magnetograms – such as those of Mackay et al. (2011) – are a very useful tool with which to study the evolution of the solar corona.

Chapter 5

Constructing Proxy SOLIS Synoptic Magnetograms Using SDO/HMI or SOHO/MDI Magnetograms

5.1 Introduction

Synoptic magnetograms (a.k.a. Carrington rotation magnetograms) are a global representation of the Sun's magnetic field over a Carrington rotation (a period of 27.2753 days). At present the only instruments capable of producing magnetograms are on the Earth (e.g. SOLIS, Kitt Peak, GONG), in its orbit (e.g. SDO/HMI, Hinode/SOT) or at the L1 Lagrangian point (SOHO/MDI). Due to this only the magnetic field lying on the visible hemisphere of the Sun (from Earth) may be measured at any one time. In order to construct a representation of the Sun's global magnetic field, a series of magnetograms must be taken at different times (corresponding to different solar longitudes due to the Sun's rotation) and stitched together to form a synoptic magnetogram. It is important to note that since a synoptic magnetogram is constructed from a series of magnetograms taken at different times, every line of longitude in the synoptic magnetogram corresponds to a different date and time. A synoptic magnetogram therefore does not represent a snapshot of the global solar magnetic field at any one instant of time. Rather it represents the magnetic field of the central meridian of the Sun as a function of time over the Carrington Rotation. Figure 5.1 displays a synoptic magnetogram from SOLIS (Synoptic Optical Long-term Investigations of the Sun) for Carrington rotation 2138, corresponding to the date range 11-Jun-13 05:25 UTC to 8-Jul-2013 10:10 UTC. On the image, both the longitude (lower horizontal axis) and the dates corresponding to each line of longitude (upper horizontal axis) are displayed.

Synoptic magnetograms are of great interest to solar physics as they provide a global representation of the Sun's photospheric magnetic field. They may be used to construct potential field extrapolations of the Sun's coronal magnetic field (Altschuler & Newkirk 1969). Such extrapolations can then, for example, be used to study the structure of the solar wind (e.g. Arge et al. (2004), Crooker et al. (2012)), the formation of filament channels (van Ballegooijen et al. 1998) or to study the variation of the corona's magnetic topology over time (Platten et al. 2014). In another application, the ongoing work started in Yeates et al. (2007) uses synoptic magnetograms from Kitt Peak, and latterly SOLIS

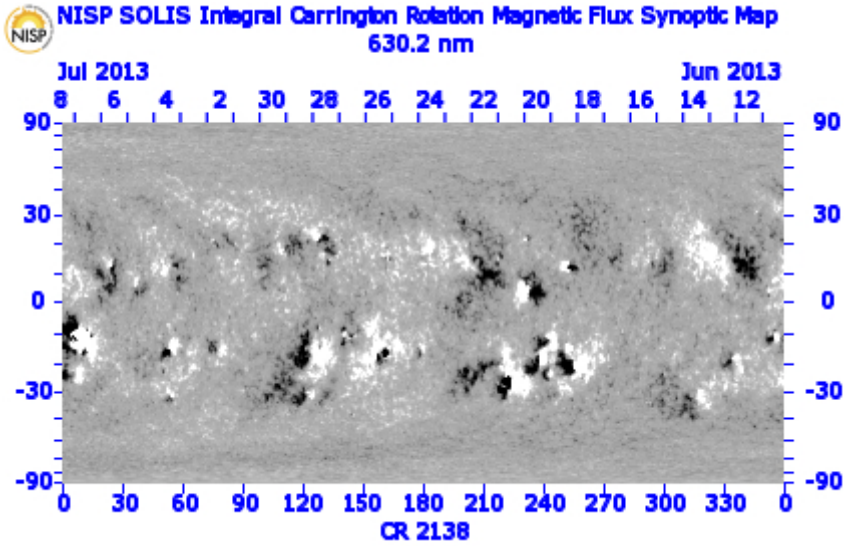

Figure 5.1: A synoptic magnetogram for Carrington Rotation 2138 from SOLIS. The vertical axis denotes the latitude (in degrees), the lower horizontal axis denotes the Carrington longitude (in degrees) and the upper horizontal axis denotes the date the lines of longitude refer to. White and black correspond to positive and negative magnetic flux density respectively. (Source: http://solis.nso.edu)

to determine where new active regions emerge on the Sun. These active regions are then approximated as magnetic bipoles and emerged into a global 3D magnetic flux transport magnetofrictional model of the Sun's corona (Yeates et al. 2007, Mackay & van Ballegooijen 2006). Through this they are able to produce a continuously evolving NLFF representation of the Sun's coronal field. To date their longest simulations have simulated the global non-potential field of the Sun from March 1996 to May 2014 (See Yeates & Mackay (2012)).

As of July 2014, the telescope that provides data for SOLIS has been dismantled, and is being relocated from Kitt Peak NSO to a new site – yet to be announced – in late 2015. As such, until it has been relocated it will not be in operation and therefore no SOLIS synoptic magnetograms will be produced. As the work of Yeates et al. (2007) makes use of SOLIS' data and the 3D magnetifrictional model's parameters are calibrated for NSO/Kitt Peak and SOLIS data, the continuity of this study will suffer from the lack of such magnetograms. In order to avoid this problem, in this chapter the production and calibration of synoptic magnetograms using either SDO/HMI or SOHO/MDI magnetograms is investigated. The calibration of the bipole properties derived from either the SDO/HMI or SOHO/MDI synoptic magnetograms to those derived from NSO/SOLIS is important for the continuity of the simulations. These SDO/HMI or SOHO/MDI synoptic magnetograms will then be used to replace the SOLIS magnetograms for periods where SOLIS data is unavailable.

This chapter is structured as follows. In Section 5.2 the methods used to construct SOLIS synoptic magnetograms are investigated and reproduced. Section 5.3 outlines the methods used to construct synoptic magnetograms from HMI and MDI magnetograms. The HMI and MDI synoptic magnetograms are compared with SOLIS synoptic magnetograms in Section 5.4. In Section 5.5 a set of properties of bipoles to be emerged into the magnetofrictional simulation of Yeates et al. (2007) as determined by HMI synoptic magnetograms is presented. Finally, in Section 5.6 the findings of this chapter are discussed.

5.2 Construction of SOLIS Synoptic Magnetograms

Before attempting to produce synoptic magnetograms from HMI or MDI magnetograms, it is important to be able to reproduce the procedure applied by SOLIS to produce the SOLIS synoptic magnetograms from their own daily magnetograms. This is to ensure that the method used to construct the HMI or MDI magnetograms is as close as possible to that used to construct the SOLIS magnetograms. There are two types of SOLIS synoptic magnetograms available: high resolution (0.2° per pixel resulting in a 1800×900 image) and low resolution (1° per pixel resulting in a 360×180 image). The code by Yeates et al. (2007) makes use of low resolution SOLIS magnetograms, however in this chapter the production of both high and low resolution synoptic magnetograms is investigated along with the relationships between them.

5.2.1 Daily Magnetograms

The SOLIS project supplies daily magnetograms of the Sun (weather permitting). The magnetograms are taken by the Vector Spectromagnetograph (VSM) instrument. Although VSM is capable of producing vector magnetograms, in this study we were only interested in the line-of-sight magnetograms it produces. Two different types of magnetogram are made by VSM. One uses the Fe I line at 6301.5 Å which measures the photospheric magnetic field, and the other uses the Ca II line at 8542 Å which measures the chromospheric magnetic field. In this work we are only interested in the photospheric magnetic field, therefore we only consider the Fe I magnetograms.

In constructing the SOLIS synoptic magnetograms, we do not use the raw daily magnetograms, but rather the provided 'Daily Heliographic Magnetograms.' These have first been converted from line of sight magnetic field to normal component, and then have been remapped from image coordinates to heliographic coordinates (longitude and sin(latitude)). They are therefore already in the correct format to be used in the construction of the synoptic magnetogram, which is a map of the normal component magnetic field with coordinates of longitude and sin(latitude). The longitude in each map is the longitude relative to the Sun's central meridian, so in each map the longitude ranges from $-90°$ to $+90°$.

Figure 5.2 displays a low resolution (left) and high resolution (right) daily heliographic magnetogram from 03/06/2013. First, the process to convert a high resolution daily heliographic magnetogram to a low resolution daily heliographic magnetogram is investigated. This is needed as the high resolution HMI and MDI images must be degraded to a lower resolution in order to make synoptic magnetograms equivalent to the low resolution SOLIS synoptic magnetograms. For consistency a similar technique applied to degrade the high resolution SOLIS magnetograms to low resolution should be applied to the HMI or MDI magnetograms. The following methods are investigated:

- Sampling: Take every fifth pixel from the high resolution magnetogtam (in the longitude and sin(latitude) direction) and use these to construct the low resolution magnetogram. E.g. `lowres(i,j) = highres(5i,5j)`

- Averaging: Average the values of the 5×5 pixel region in the high resolution magnetogram corresponding to a pixel in the low resolution magnetogram. This method conserves the total flux, and since each pixel in a magnetogram merely measures the mean field in that pixel, this essentially simulates using a camera with a lower resolution.

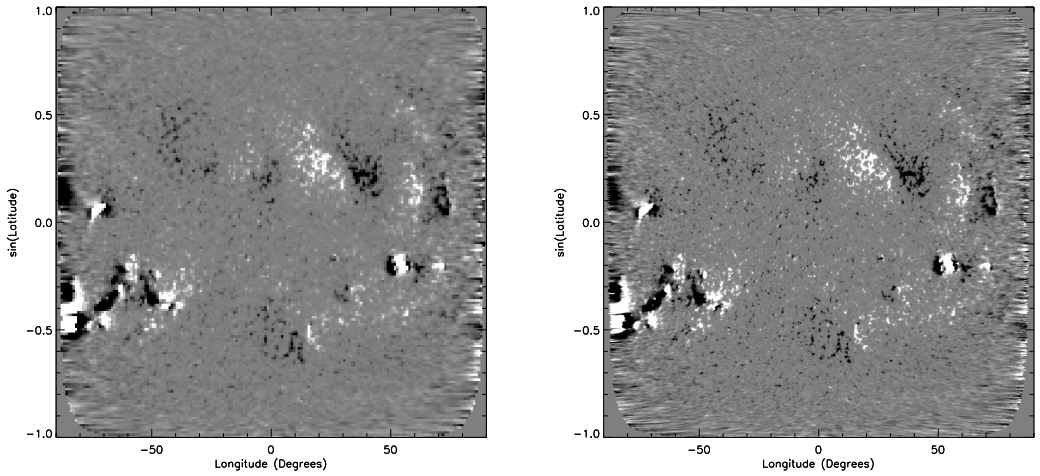

Figure 5.2: Low resolution (left) and high resolution (right) SOLIS daily heliographic magnetogram from 03/06/2013 where white and black represent positive and negative flux densities respectively, and the fields are saturated at ±100 G.

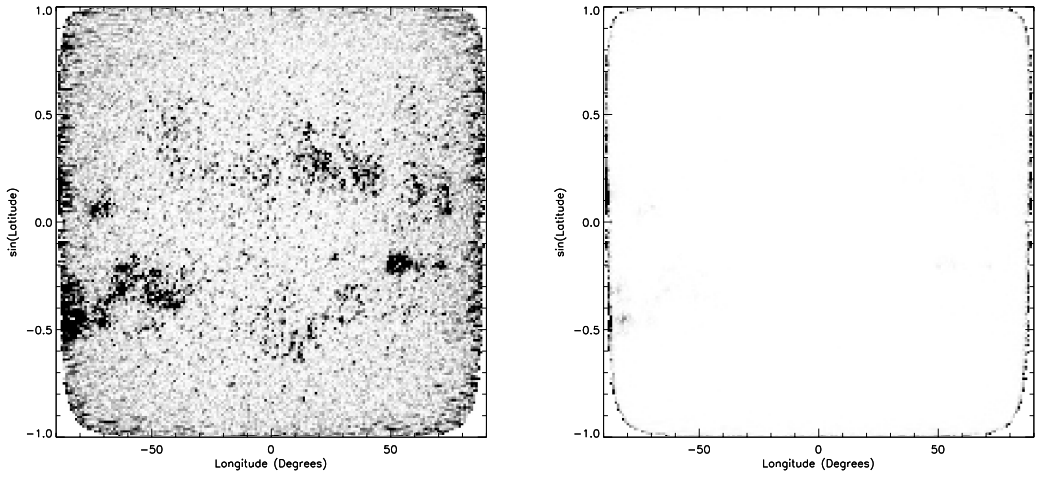

Figure 5.3: Absolute difference images between the low resolution daily heliographic magnetogram and the degraded (by sampling (left) and averaging (right)) high resolution magnetograms. The image is saturated at 50 G.

Figure 5.3 displays the difference images between the low resolution SOLIS daily magnetogram and the degraded high resolution SOLIS magnetograms. It is clear that the sampling method (left panel) does not accurately reproduce the low resolution SOLIS image as there are many differences between the two images. The averaging method (right panel) however reproduces the low resolution image almost exactly in the centre of the image but only fails to reproduce the low resolution image towards the solar limb. We speculate that the differences at the limb are most likely due to the VSM images being degraded before being mapped onto a heliographic projection, whilst we degrade the image after it is in a heliographic projection. Whilst degrading the image before changing its projection will have little effect on pixels near the disk centre - which are not affected significantly by the remapping - pixels towards the solar limb may be changed significantly if the image is degraded before remapping compared to if the image is degraded after remapping.

To summarise, we find that the averaging process better reproduces the low resolution daily heliographic magnetograms. This will therefore be the method that will be used in later sections to degrade MDI or HMI magnetograms such that they can produce low (1°) resolution magnetograms.

5.2.2 Synoptic Magnetogram Construction

As mentioned above, a synoptic magnetogram is constructed from a series of (typically) daily magnetograms stitched together. This stitching process is achieved by taking a weighted average of the individual daily magnetograms, where the weighting is a function of longitude. According to the SOLIS website (http://solis/nso/edu/0/vsm/aboutmaps.html and http://solis.nso.edu/vsm/map_info.html), the low resolution synoptic maps are constructed using a weighting factor of the form

$$w_{\text{low}}(l) = \cos^4(l), \tag{5.1}$$

where l is the longitude relative to the central meridian. The high resolution maps use a Gaussian weighting of

$$w_{\text{high}}(l) = \exp\left[-\left(\frac{l}{\Delta l}\right)^2\right]. \tag{5.2}$$

With regard to the width of the Gaussian profile, http://solis/nso/edu/0/vsm/aboutmaps.html states that $\Delta l = 7°$, whilst http://solis.nso.edu/vsm/map_info.html states that the FWHM of the profile is 14°, corresponding to $\Delta l = 8.40°$. As two different values for Δl are quoted, we will investigate both and will determine which produces a better fit to the SOLIS synoptic magnetograms. The full synoptic map is constructed by taking the sum of the weighted daily maps (placed at the correct longitude) and dividing this by the total weighting. Mathematically this is

$$\text{Map}[\phi, \sin(\lambda)] = \left(\sum_{i=0}^{N+1} w(l + l_{0i})\text{Daily}_i[l + l_{0i}, \sin(\lambda)]\right)\left(\sum_{i=0}^{N+1} w(l + l_{0i})\right)^{-1}, \tag{5.3}$$

where N is the number of daily magnetograms used from that rotation, Daily_i is the i^{th} daily magnetogram, l_{0i} is the Carrington longitude corresponding to the central meridian of the i^{th} daily magnetogram, w is the weighting function (Equations 5.1 and 5.2), ϕ is the Carrington longitude and λ is the latitude. In constructing the synoptic map, the final daily magnetogram from the preceding Carrington Rotation (with index number 0) and

the first daily magnetogram from the following Carrington Rotation (with index number $N + 1$) are also used and are placed at longitudes $> 360°$ and $< 0°$ respectively. The inclusion of these magnetograms ensures the magnetic field at the longitudinal boundaries of the map (0° and 360°) is made up from a similar time average of daily magnetograms.

High resolution synoptic map

High resolution synoptic maps with both $\Delta l = 7°$ and 8.40° were constructed and compared with the SOLIS synoptic maps. Figure 5.4 displays the SOLIS high resolution synoptic map for CR2138 (top) and the reconstructed maps using $\Delta l = 7°$ (centre) and $\Delta l = 8.40°$ (bottom). By eye, all three maps look identical. It is therefore pertinent to construct difference maps between the SOLIS and reconstructed maps in order to highlight the differences between them (Figure 5.5). It is clear that the reconstructed map using $\Delta l = 7°$ is a far closer match with the SOLIS map than the reconstructed map using $\Delta l = 8.40°$. In the $\Delta l = 7°$ map however, there are two vertical bands which show a greater difference. Upon close inspection, magnetic features within these bands have slightly different shapes in the SOLIS and reconstructed magnetograms. SOLIS typically publishes one daily heliographic magnetogram per day, although it is entirely possible that more than one are produced. We hypothesise that the two longitutinal bands where the SOLIS and reconstructed synoptic magnetograms do not agree identically in the $\Delta l = 7°$ case arise from parts of the SOLIS synoptic magnetogram that have been produced from unpublished daily magnetograms, corresponding to slightly different times than the published magnetograms used in the reconstruction. Such a feature does not affect the studies of Yeates et al. (2007) who are only interested in the large-scale properties of the magnetograms, not the pixel by pixel values.

Low resolution synoptic map

Low resolution maps were constructed from the daily heliographic magnetograms. Figure 5.6 displays the low resolution SOLIS (left) and reconstructed (right) maps for Carrington Rotation 2138. To the eye, they are indistinguishable. In order to highlight the differences between them, a difference image is produced (Figure 5.7). At a glance, it is clear that the reconstruction does not completely match the original SOLIS map. Whilst they do not completely match, in order to demonstrate that they are very similar, a scatter plot between the magnetic flux densities of each pixel from original low resolution map and the reconstructed map is produced, and is displayed in Figure 5.8. A scaling factor of 0.973 was found between the SOLIS synoptic magnetogram and the reconstructed magnetogram, and is denoted by the solid line in Figure 5.8. Since the scale factor is almost unity (dashed line in Figure 5.8) and there is not a great deal of scatter, the reconstructed low resolution synoptic magnetogram is a good representation of the low resolution SOLIS synoptic magnetogram. We speculate that the differences between our reconstructed SOLIS map and the original could be due to the SOLIS pipeline applying the weighting function (Equation 5.1) to the daily magnetograms before the magnetogram's resolution is degraded down to 1°. In our method, we apply the weighting function after the daily magnetogram has had its resolution degraded. Since when applying pixel-to-pixel comparisons (Figure 5.8) we find that our reconstructed synoptic magnetograms have an almost 1:1 match with the SOLIS synoptic magnetograms, we may deduce that the method we have used to construct the low and high resolution synoptic magnetograms is consistent with that applied by SOLIS. We may now use this method to construct synoptic images from HMI and MDI magnetograms.

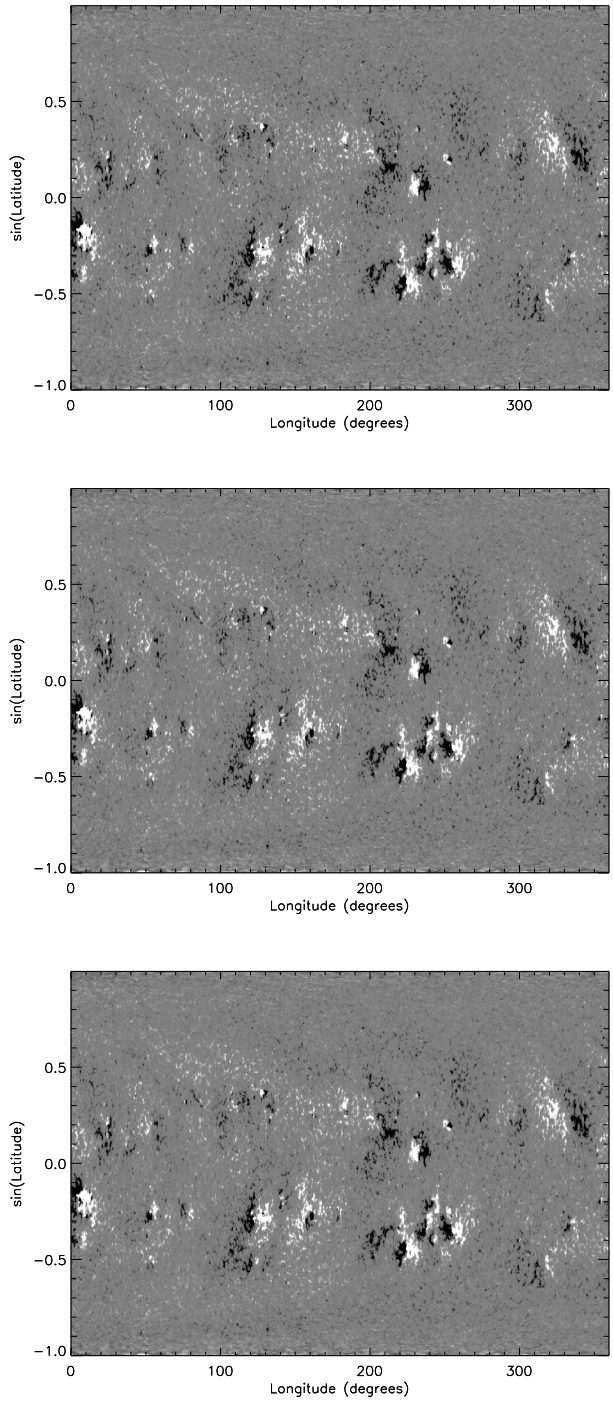

Figure 5.4: Synoptic maps from CR2138. Top: the SOLIS map. Centre: the reconstructed SOLIS magnetogram using $\Delta l = 7°$. Bottom: The reconstructed SOLIS magnetogram using $\Delta l = 8.40°$.

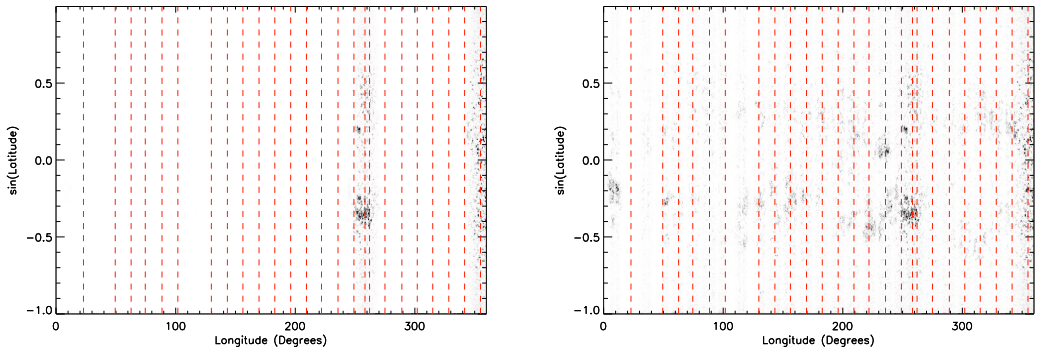

Figure 5.5: Absolute difference maps between the SOLIS synoptic magnetogram and the reconstructed synoptic magnetogram with $\Delta l = 7°$ (left) and $\Delta l = 8.40°$ (right). The red dashed vertical lines denote the central meridian longitudes of the daily magnetograms used to reconstruct the synoptic magnetograms. The images are saturated at 50 G.

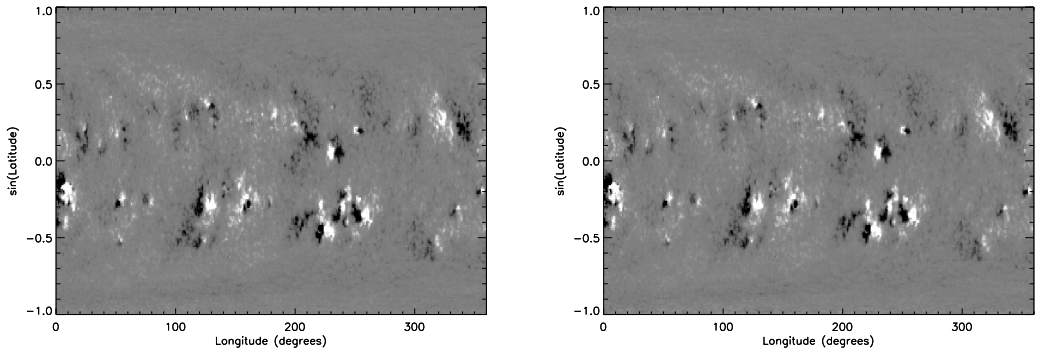

Figure 5.6: Low resolution SOLIS (left) and reconstructed (right) synoptic magnetograms from Carrington Rotation 2138.

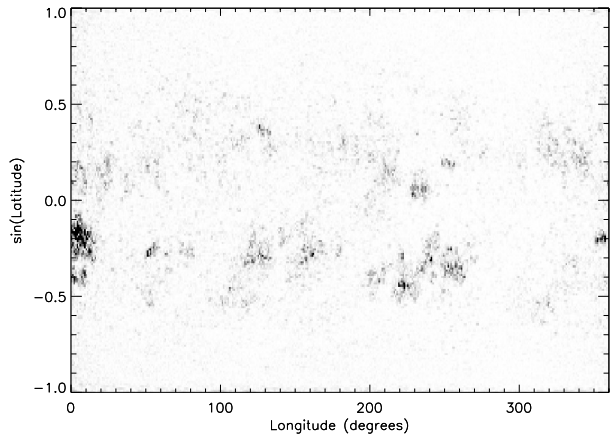

Figure 5.7: Absolute difference map between the low resolution SOLIS synoptic map and our reconstruction. The image has been saturated at 50 G.

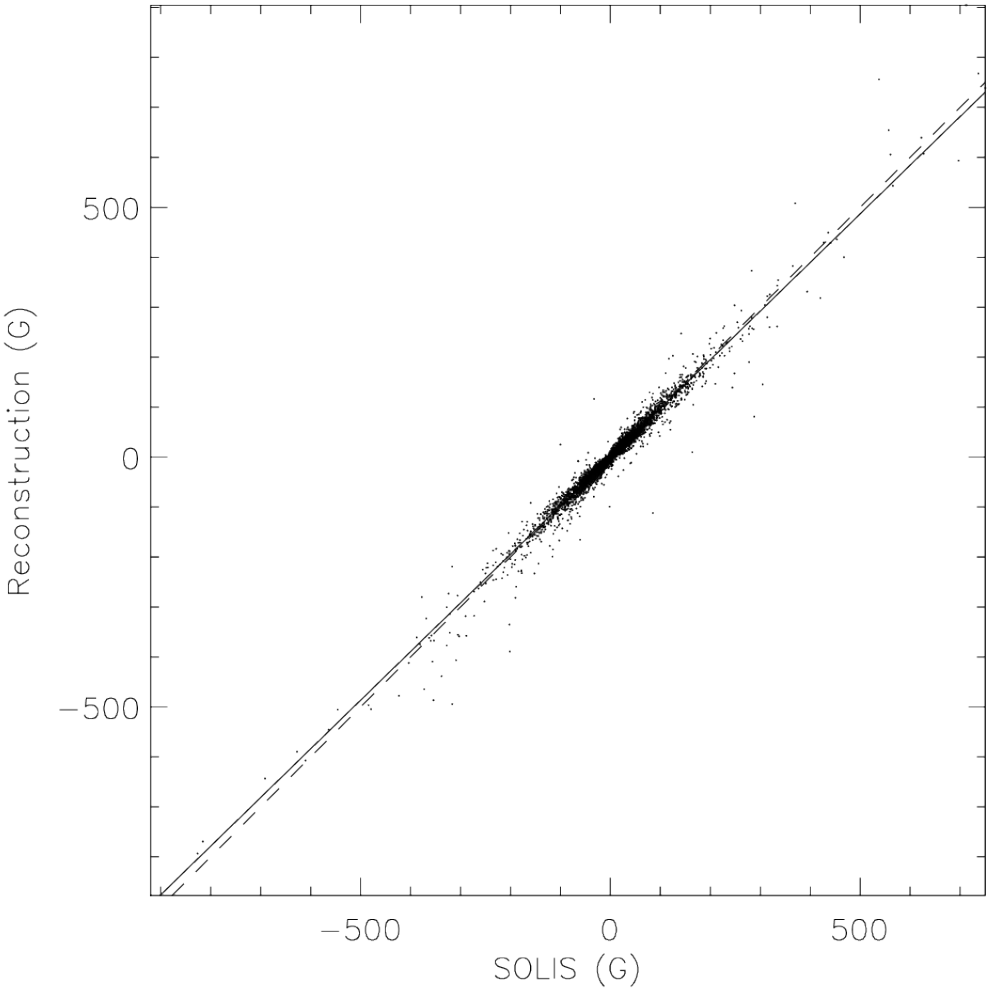

Figure 5.8: Scatter plot of the magnetic flux densities per pixel between the low resolution SOLIS synoptic map and its reconstruction. The dashed line corresponds to a 1:1 correlation between the values, and the solid line is the fitted relation, with a gradient of 0.973.

5.3 Construction of HMI and MDI Synoptic Magnetograms

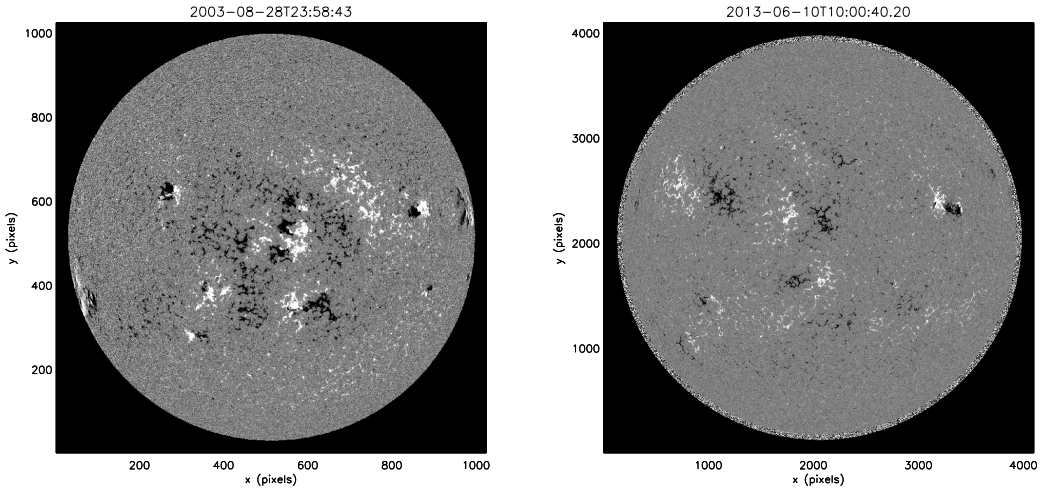

Figure 5.9: Examples of the MDI (left) and HMI (right) line of sight magnetograms that are used to produce the synoptic magnetograms.

In this section the construction of synoptic magnetograms from SDO/HMI and SOHO/MDI are described. In particular we describe the method used to select the magnetograms and convert them to a heliographic projection, so that they resemble the SOLIS daily heliographic projection magnetograms (see Figure 5.2). Once the magnetograms are in the heliographic projection, the construction of the synoptic magnetograms is carried out using the method described in Section 5.2.2.

5.3.1 HMI and MDI Magnetograms

MDI produces full disk line of sight magnetograms, with images of 1024×1024 pixels and a resolution of 1.98" per pixel. MDI uses the Ni I absorption line at 6768Å. In this chapter we make use of MDI magnetograms with a 96 minute cadence. Figure 5.9 (left) displays a MDI magnetogram from August 2003. HMI produces line of sight full disk magnetograms with images of 4096×4096 pixels, corresponding to an angular resolution of 0.5". HMI uses a Fe I absorption line at 6173Å. In this chapter, we use HMI magnetograms with a 45s cadence. Figure 5.9 (right) displays a HMI magnetogram from June 2013.

5.3.2 Selection of Magnetograms

Whilst SOLIS typically publishes one magnetogram per day, HMI and MDI produce many per day. Although in principle it is possible to produce a synoptic magnetogram using every 45 second (for the case of HMI) or 96 minute (for the case of MDI) magnetogram, this would be computationally expensive and would require vast amounts of data storage. Since SOLIS produces synoptic magnetograms from single daily images, we select one MDI and HMI magnetogram per day to use to construct our synoptic magnetograms. The selection process for magnetograms is as follows:

1. For a given Carrington rotation, N, determine its start date and time, d_1.
2. Determine the time 24 hours before the start of the rotation, $d_0 = d_1 - 1$.

3. Select a series of 29 magnetograms at times spaced approximately 24 hours apart beginning at d_0.

This series of 29 magnetograms will include a magnetogram from the final day of Carrington rotation $N-1$, 27 magnetograms belonging to days within Carrington rotation N and a magnetogram from the first day of Carrington rotation $N+1$. These 29 magnetograms are used to construct the synoptic magnetogram for Carrington rotation N.

5.3.3 Converting Line of Sight Full Disk Magnetograms to Normal-Component Heliographic Magnetograms

Before constructing the synoptic magnetogram in the same manner as in Section 5.2.2 the HMI and MDI magnetograms must first be converted to normal-component heliographic-projection magnetograms of the correct resolution. This is carried out in three steps. Firstly the magnetograms must be converted from line of sight to normal component. This is achieved by assuming that the magnetic field at the photosphere is approximately radial, so that the line of sight magnetogram therefore approximately measures $B_r\cos(\psi)$, where ψ is the angle the normal to the photosphere makes to the line of sight. For every pixel in the magnetogram, ψ is calculated by

$$\psi = \arcsin\left(\frac{r}{R_\odot}\right) \tag{5.4}$$

where r is the distance between that pixel and the disk centre and $R_\odot$ is the solar radius. Each pixel is then divided by $\cos\psi$ to convert the line of sight magnetic field into the normal component. Now the magnetogram must be transformed into a heliographic projection. To achieve this, evenly spaced grids of longitude, and sin(latitude) are produced, ranging from $-90°$ to $+90°$ in longitude and -1 to $+1$ in sin(latitude). For HMI these grids contain 3600×3600 elements (to compensate for its very high 4096×4096 resolution), and for MDI the grids contain 900×900 elements. Using the IDL SolarSoftWare commands `wcs_convert_to_coord` and `wcs_get_pixel` arrays of pixel coordinates corresponding to the longitude and latitude grids are produced. The magnetograms are then interpolated onto these points, producing heliographic projection magnetograms. Finally, the magnetograms must be resized to 900×900 and 180×180 to be used for the high and low resolution synoptic magnetograms respectively. This resizing is achieved by using the averaging procedure described in Section 5.2.1. Examples of the high resolution (900×900) heliographic projection maps are displayed in Figure 5.10 for the full-disk images shown in Figure 5.9. The construction of the synoptic magnetograms is then carried out as described in Section 5.2.2. Figures 5.11 and 5.12 display examples of high and low resolution synoptic magnetograms produced from HMI and MDI respectively.

5.4 Comparison Between MDI, HMI and SOLIS Synoptic Magnetograms

In this section the high and low resolution HMI and MDI synoptic magnetograms that have been constructed are compared to the high and low resolution SOLIS magnetograms. This comparison is carried out as the three sets of magnetograms use different absorption lines and have different instrumental features. For continuity with the simulations of Yeates & Mackay (2012) the relations between the fluxes and bipole properties determined by each instrument need to be determined.

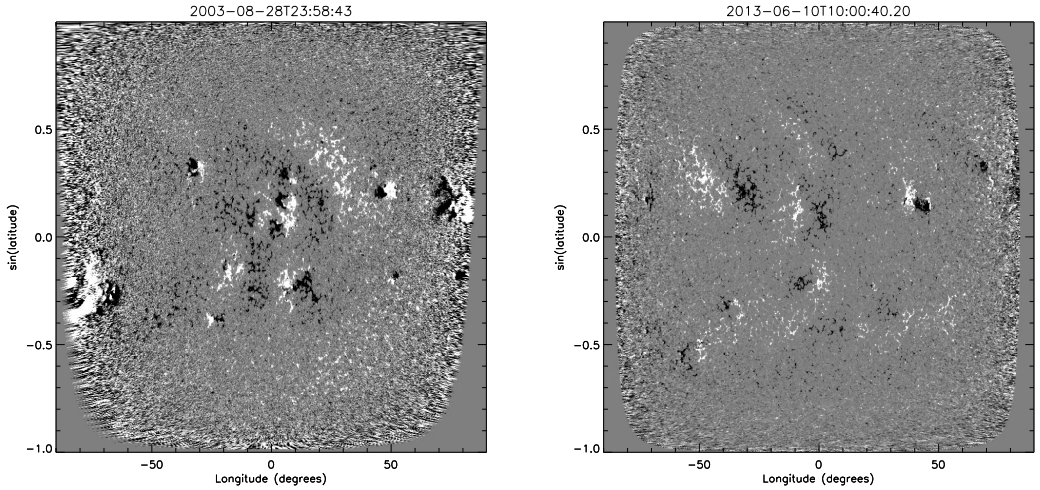

Figure 5.10: Examples of the heliographic projection normal component MDI (left) and HMI (right) magnetograms. These images resemble the SOLIS daily heliographic magnetograms (Figure 5.2).

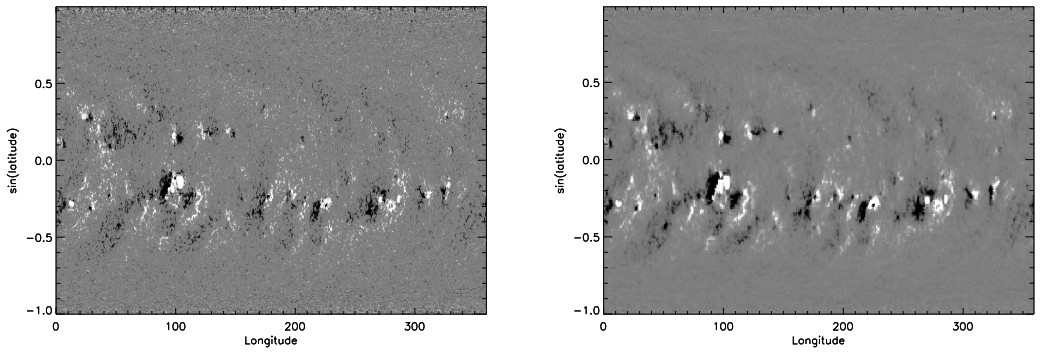

Figure 5.11: Examples of the high (left) and low (right) HMI synoptic magnetograms from Carrington Rotation 2145.

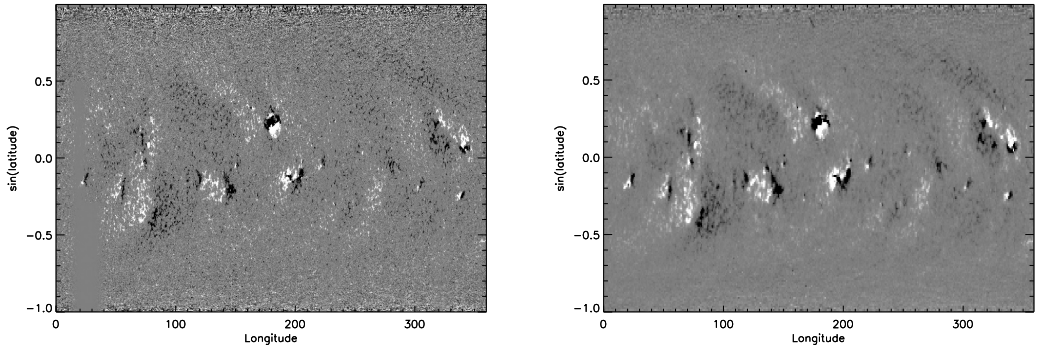

Figure 5.12: Examples of the high (left) and low (right) MDI synoptic magnetograms from Carrington Rotation 2025.

Flux Range (G)	MDI	HMI
0–50	1.2	0.70
25–200	0.97	0.94
100–500	1.1	1.1
100+	1.2	1.3
500+	1.2	1.5

Table 5.1: SOLIS to MDI and SOLIS to HMI scaling factors found by Pietarila et al. (2013). For high field strengths, both MDI and HMI measure higher flux densities than SOLIS.

Flux Range (G)	MDI	HMI
0–50	0.39	0.39
25–200	0.85	0.79
100–500	1.04	0.97
100+	1.19	1.12
500+	1.33	1.25
all	1.03	0.88
50+	1.15	1.06

Table 5.2: SOLIS to MDI and SOLIS to HMI scaling factors for the high resolution synoptic magnetograms.

5.4.1 Pixel-to-Pixel Comparisons

To begin with we carry out pixel-to-pixel comparisons between the low and high resolution synoptic magnetograms. We draw comparisons with the work of Pietarila et al. (2013), who compared SOLIS daily longitudinal magnetograms with MDI and HMI longitudinal magnetograms. The resulting scale factors from their pixel-to-pixel comparisons between HMI and SOLIS and MDI and SOLIS are displayed in Table 5.1. They find that for pixels with high field strengths (e.g $>$ 100G) both HMI and MDI measure larger flux densities than SOLIS by factors of approximately 1.3 and 1.2 respectively. For pixels with low field strengths ($<$ 50G), HMI measures lower flux densities than SOLIS, whilst MDI measures similar or slightly higher flux densities. Within the range of 25–200G similar values are found from each instrument.

In order to carry out the comparisons, we take a series of 10 Carrington Rotations (2140-2149 – corresponding to the date range of Aug 2013 to April 2014 – for HMI and 2020-2029 – corresponding to the date range Aug 2004 to April 2005 – for MDI) and construct a scatter plot comparing each pixel from the HMI or MDI synoptic magnetograms with their corresponding pixels from the SOLIS synoptic magnetograms as obtained from the SOLIS archives. Scaling relations are then fitted to the scatter plots using the same flux density ranges as those in Table 5.1. Figures 5.13 and 5.14 display the scatter plots from the high resolution and low resolution synoptic magnetograms respectively

High resolution

We first consider the high resolution synoptic maps. These findings may best be compared with those of Pietarila et al. (2013) as their comparisons use the high resolution SOLIS daily heliographic magnetograms. In Table 5.2 the scaling relations found in the present

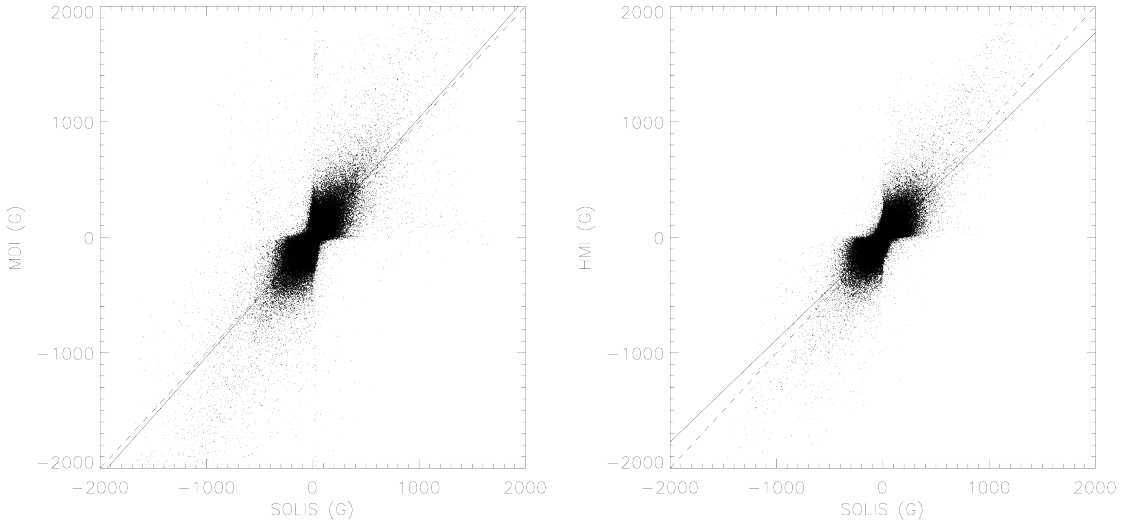

Figure 5.13: Scatter plots of the pixel values of the high resolution MDI (left) and HMI (right) synoptic magnetograms against their corresponding SOLIS synoptic magnetograms. The solid line is the scaling relation derived for all fluxes. The dashed line represents a 1:1 scaling.

study for the high resolution synoptic magnetograms are displayed over the same flux ranges as displayed in Table 5.1. We also include the scaling relation for all flux densities greater than 50G. For low field strengths (25–200G), SOLIS measures stronger flux densities than either HMI or MDI. For high field strengths ($>$ 100G), both MDI and HMI measure stronger flux densities than SOLIS. This is a similar trend to that found by Pietarila et al. (2013). For low field strengths however, we find SOLIS measures much higher flux densities compared to those determined by Pietarila et al. (2013). Whilst Pietarila et al. (2013) finds that for high field strengths HMI measures flux densities roughly 1.5 times those of SOLIS, we find this factor is at most 1.25. Similarly, whilst Pietarila et al. (2013) finds that for high field strengths MDI measures flux densities roughly 1.2 times those of SOLIS, we find the larger factor of 1.33. In contrast to Pietarila et al. (2013), for high field strengths we find MDI measures higher flux densities than HMI. For flux densities that are greater than 50G we find that both HMI and MDI measure greater flux densities that SOLIS. Over this range, MDI measures higher flux densities than HMI. The possible reasons for the differences between SOLIS, HMI and MDI flux density measurements will be discussed in Section 5.6

Low resolution

We now carry out the same analysis on the low resolution magnetograms. Table 5.3 displays the scaling relations found for the low resolution synoptic magnetograms. The scaling relations are similar to those for the high resolution magnetograms, although the scale factors are closer to unity. Crucially, the same trends are found, namely that for high field strengths both HMI and MDI measure higher flux densities than SOLIS. For flux densities greater than 50G, like in the high resolution case, MDI measures higher flux densities than HMI. For this flux density range, both HMI and MDI measure higher flux densities than SOLIS.

To summarise, for high and low resolution synoptic magnetograms we find that both

Flux Range (G)	MDI	HMI
0–50	0.78	0.72
25–200	0.96	0.83
100–500	1.05	0.94
100+	1.16	1.06
500+	1.29	1.21
all	1.06	0.97
50+	1.12	1.02

Table 5.3: SOLIS to MDI and SOLIS to HMI scaling factors found for the low resolution synoptic magnetograms.

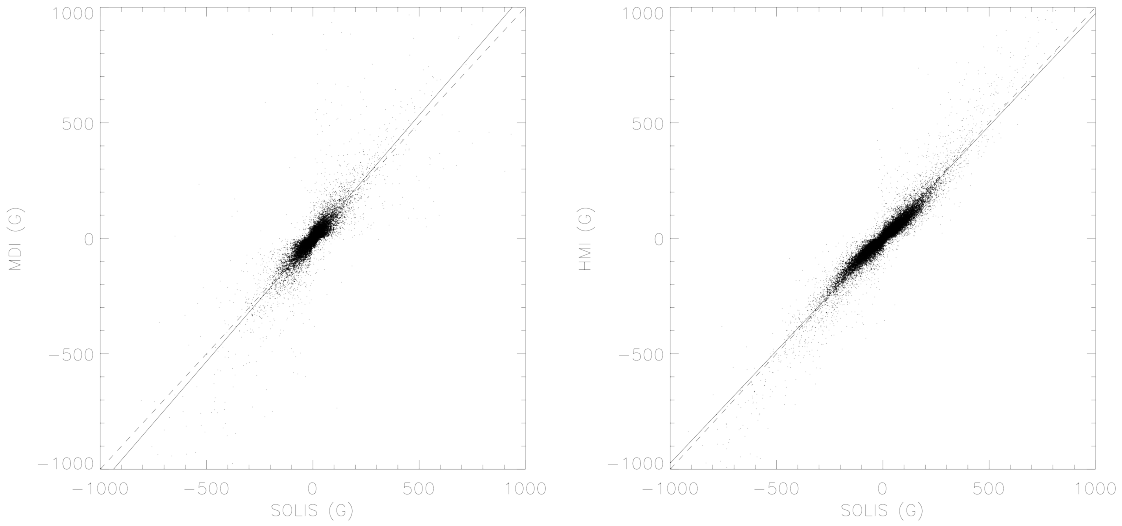

Figure 5.14: Scatter plots of the pixel values of the low resolution MDI (left) and HMI (right) synoptic magnetograms against their corresponding SOLIS synoptic magnetograms. The solid line is the scaling relation derived for all fluxes. The dashed line represents a 1:1 scaling.

HMI and MDI measure lower flux densities than SOLIS for weak (< 100 G) field regions, and they measure higher flux densities for strong field (> 100 G) regions. Taking all flux density values into account, HMI and MDI both measure simular flux densities to SOLIS.

5.4.2 Derived Active Region Properties

The low resolution HMI and MDI synoptic magnetograms are to be used to replace low resolution SOLIS synoptic magnetograms in determining the properties (location, flux, tilt angle and separation) of newly emerged active regions to be input into the global magnetofrictional simulation described by Yeates et al. (2007). It is important for consistency therefore that the same active region properties are determined from the HMI and MDI magnetograms as to those deduced from the SOLIS magnetograms. We thus compare the properties of emerged active regions as determined from the SOLIS synoptic magnetograms with those determined from the HMI and MDI synoptic magnetograms. If the properties differ between SOLIS and HMI or SOLIS and MDI then appropriate scaling relations must be found so that the differences can be corrected, to ensure the continuity of possible future simulations.

Semi-Automated Active Region Detection Procedure

We use the same semi-automated procedure as used by Yeates et al. (2007) to determine the properties of the newly emerged active regions. The code is described in great detail in Yeates et al. (2007) and Yeates (2008), however, it will briefly be described here. The code compares the synoptic magnetogram for a given Carrington rotation to the synoptic magnetogram (corrected for differential rotation) from the previous rotation. In order to apply the differential rotation correction to the magnetogram from the previous rotation, the magnetogram from the rotation preceding it is also required. Thus, in order to determine the newly emerged bipoles from Carrington rotation N, synoptic magnetograms are required from three Carrington rotations: N, $N-1$ and $N-2$. In order for the semi-automated routine to locate new active regions, the following steps are carried out:

1. In the synoptic magnetogram for Carrington rotation N, and the map from rotation $N-1$ (corrected for differential rotation), active region flux is defined as locations where the absolute magnetic flux density is greater than 50G. Any field weaker than this is set to zero.

2. A difference map is then constructed between the two magnetograms. Pixels on the difference map with positive values correspond to new flux, whilst pixels with negative values correspond to old flux.

3. Bipolar regions with predominantly positive-valued pixels in the difference map (new flux) are defined as new active regions, and their centre of flux, tilt angle, separation and flux are calculated.

In addition to these automatically determined active regions, the user may manually select other regions to be classified as newly emerged active regions. This is useful if there is, for example, a complex multipolar region which the automated code cannot properly identify, or an old region with an unusually large flux – implying that new flux has emerged within it.

This procedure is carried out for the HMI and MDI synoptic magnetograms, and their corresponding SOLIS synoptic magnetograms. The output of the procedure is a list of active region positions, separations, tilt angles and fluxes. The lists of new active regions

identified from the HMI or MDI and SOLIS magnetograms must then be compared with each other to find the active regions common to each list. To determine if an active region identified from a SOLIS magnetogram corresponds to an active region identified from the corresponding HMI or MDI magnetogram, the longitudes and latitudes of the two active regions are compared and if they agree to within 5° they are identified as being the same active region. Active regions identified from one magnetogram, but not from another (e.g. an active region determined from a SOLIS magnetogram but not determined from the corresponding MDI magnetogram) are discarded. The origins of these active regions are discussed in Section 5.6.

5.4.3 HMI

Figure 5.15 displays scatter plots of the tilt angles, separations and fluxes of active regions determined from HMI and SOLIS magnetograms between Carrington Rotations 2140 and 2149. The semi-automated procedure determined 153 active regions from the SOLIS magnetograms, and 159 from the HMI magnetograms. Of these, 126 active regions were found to be common to both magnetograms. It is clear from Figure 5.15 that the tilt angles and separations have nearly a 1:1 relation with each other, so SOLIS and HMI synoptic magnetograms produce consistent tilt angles and separations. There is, however a difference between the fluxes, which are lower from HMI than from SOLIS. Fitting a scaling relation, it is found that the fluxes determined from SOLIS magnetograms are 1.10 times higher than those from HMI. In conclusion the active region fluxes as determined from HMI magnetograms must be multiplied by a factor of 1.10 in order to make them match those from SOLIS magnetograms, however the tilt angles and separations do not need to be altered.

5.4.4 MDI

Figure 5.16 displays scatter plots of the tilt angles, separations and fluxes of active regions determined from MDI and SOLIS magnetograms between Carrington rotations 2020 and 2029. The semi-automated procedure determined 109 active regions from the SOLIS magnetograms, and 139 from the MDI magnetograms. Of these, 82 active regions were found to be common to both magnetograms. It is clear from figure 5.16 that the tilt angles and separations have a nearly 1:1 relation with each other, so the tilt angles and separations determined from SOLIS and MDI are comparable. There is, however a difference between the fluxes, which are higher for MDI than for SOLIS. Fitting a scaling relation, it is found that the fluxes determined from SOLIS magnetograms are 0.80 times lower than those from MDI. In conclusion the active region fluxes as determined from MDI magnetograms must be multiplied by a factor of 0.8 in order to make them match those from SOLIS magnetograms. As with the properties determined from the HMI synoptic magnetograms, the tilt angles and separations do not need to be corrected for.

5.5 Bipoles to be emerged during Carrington rotation 2152

The HMI synoptic magnetograms can now be used to produce sets of bipole properties for Carrington rotations where there are no SOLIS synoptic magnetograms available. In order to demonstrate the use of HMI magnetograms, we present the set of bipoles and their properties that were determined to have emerged during Carrington rotation 2152 – the first rotation where there is incomplete SOLIS data – using HMI synoptic magnetograms. In order to do this, synoptic magnetograms are constructed using HMI observations for

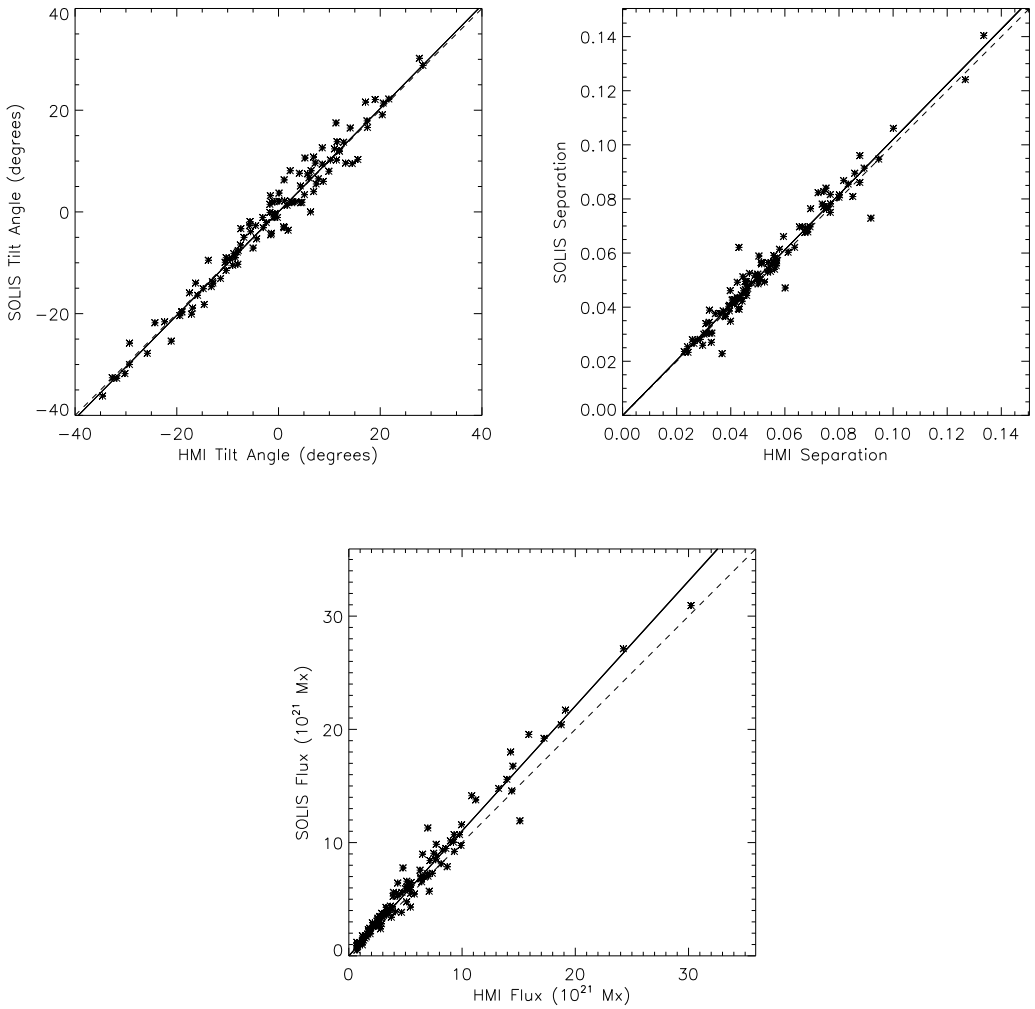

Figure 5.15: Scatter plots of the tilt angles (top left), separations (top right) and fluxes (bottom) of 126 active regions as determined from HMI and SOLIS synoptic magnetograms. The solid lines on the plots are the scaling relation between the quantities, and the dashed lines denote a 1:1 scaling.

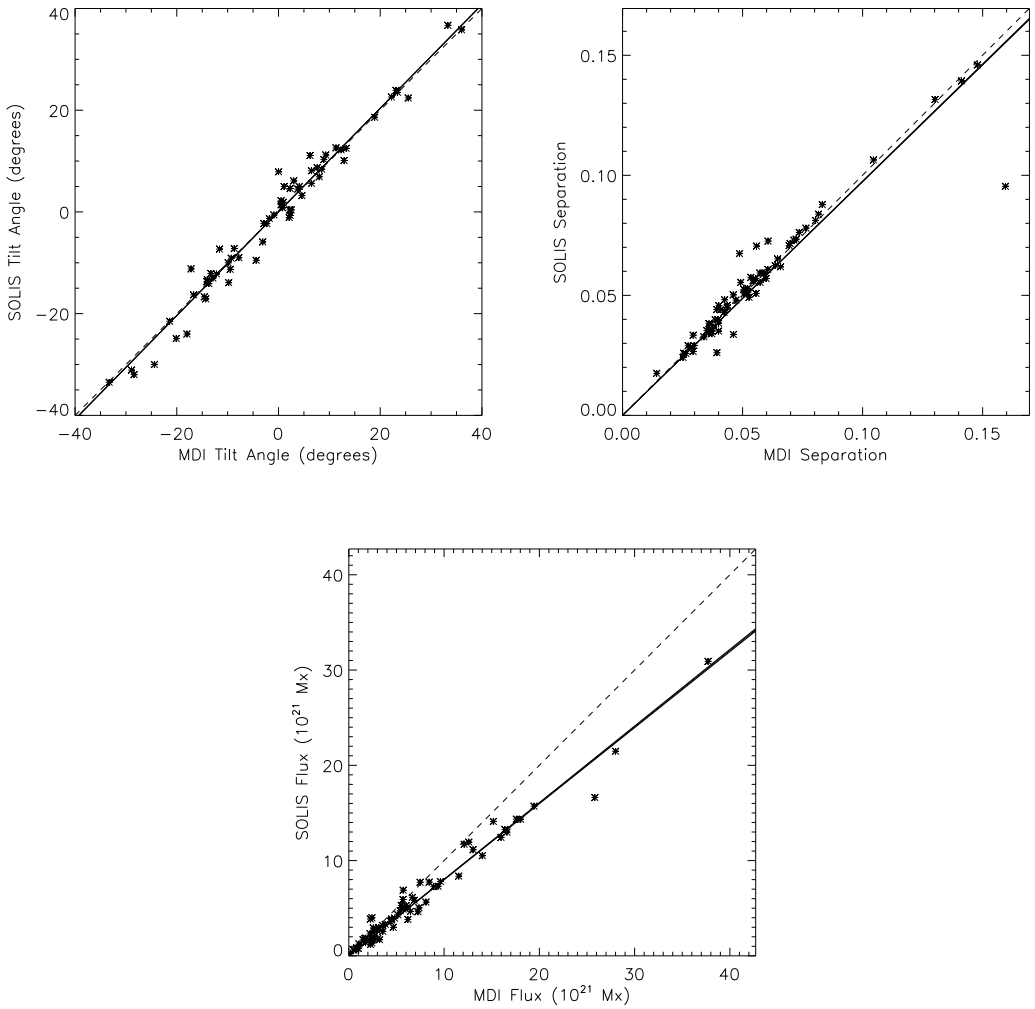

Figure 5.16: Scatter plots of the tilt angles (top left), separations (top right) and fluxes (bottom) of 82 active regions as determined from MDI and SOLIS synoptic magnetograms. The solid lines on the plots are the scaling relation between the quantities, and the dashed lines denote a 1:1 scaling.

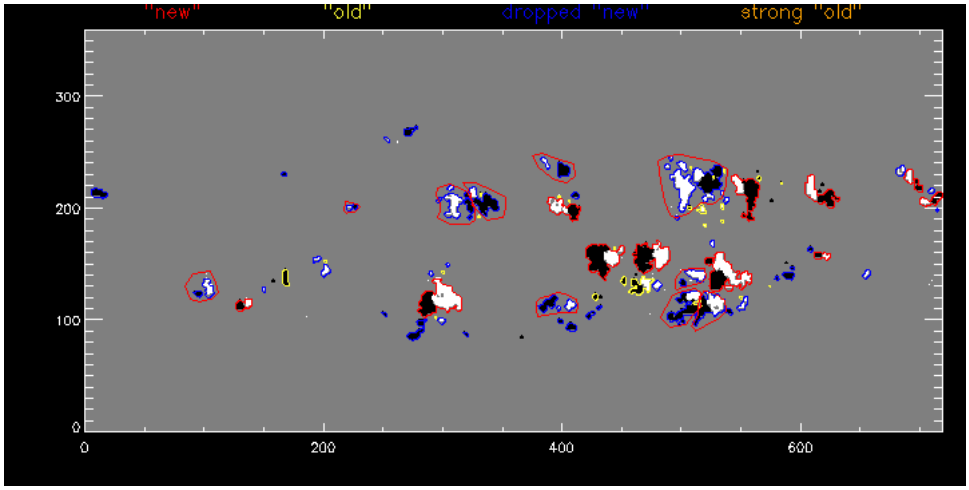

Figure 5.17: The active regions present in Carrington rotation 2152 as determined by the semi-automated procedure. Active regions contoured in red were identified by the procedure as being newly emerged active regions. Active regions contoured in yellow were identified as old active regions which were present in the previous Carrington rotation. Active regions contoured in blue are 'new' active regions that the procedure is unable to automatically characterise. The user must manually select or deselect these as appropriate.

Carrington rotations 2150–2152 (as outlined in Section 5.3) and these are inputted into the semi-automated procedure (Section 5.4.2 and Yeates et al. (2007)). The bipole fluxes as determined from the semi-automated procedure are then multiplied by a factor of 1.1 (Section 5.4.3) in order to be made consistent with the fluxes that SOLIS would have measured. Figure 5.17 displays the active regions as characterised by the semi-automated code. In total 21 new active regions were determined. Table 5.4 displays the properties of these bipoles to be emerged into the global magnetofrictional simulation during Carrington rotation 2152 as determined by the semi-automated code from the HMI synoptic magnetogram.

5.6 Discussion

In this chapter we have developed a method to produce synoptic magnetograms from SDO/HMI and SOHO/MDI magnetograms. The aim was to be able to find a temporary replacement for SOLIS synoptic magnetograms whilst the instrument that produces the data from which they are constructed is being relocated to a new site. These HMI or MDI magnetograms would be used to determine the properties of newly emerged active regions to be included in the global magnetofrictional simulation described by Yeates et al. (2007) to ensure the work may be continued beyond July 2014.

To begin with, the construction of SOLIS synoptic magnetograms from SOLIS daily magnetograms was investigated in order to ensure that the future MDI and HMI synoptic magnetograms were constructed in a similar manner for consistency. We were able to almost perfectly reproduce the high resolution SOLIS magnetograms, however the low resolution synoptic magnetograms we produced were not identical to the SOLIS magnetograms. Although the reconstructed low resolution magnetograms were not an exact match, a pixel by pixel comparison showed that the magnetograms were correlated to a high degree, and therefore the reconstruction represented the original reasonably well.

Day of year	Longitude	Latitude	Tilt Angle	Separation	Flux
195	147.7	-20.5	-15.9	0.0673	-8.529e+21
186	267.5	-12.4	-29.0	0.0392	-1.207e+22
190	218.3	-8.1	-2.7	0.0509	-1.510e+22
188	238.4	-7.5	-0.6	0.0591	-1.321e+22
185	276.6	11.7	29.4	0.0486	+4.984e+21
183	308.2	10.3	22.0	0.0612	+3.829e+21
191	201.5	6.1	8.2	0.0572	+2.829e+21
180	347.6	13.8	36.8	0.0426	+1.187e+21
179	354.7	8.5	-13.8	0.0418	+1.470e+21
201	66.9	-21.6	-14.6	0.0307	-1.192e+21
183	309.1	-7.4	3.2	0.0292	-4.653e+20
194	165.9	9.2	31.6	0.0505	+3.822e+21
194	157.7	7.1	7.7	0.0603	+4.080e+21
187	256.8	13.7	-8.7	0.0837	+1.393e+22
203	49.4	-17.1	-18.9	0.0456	-1.594e+21
198	111.9	6.6	-5.8	0.0200	+2.473e+20
191	196.6	18.4	16.9	0.0654	+1.879e+21
191	198.4	-21.7	4.6	0.0631	-2.165e+21
187	253.0	-21.0	-45.3	0.0523	-6.686e+21
186	261.7	-22.3	-22.9	0.0425	-4.259e+21
187	253.6	-14.0	-23.4	0.0506	-1.960e+21

Table 5.4: Table of the properties of bipoles from Carrington rotation 2152 to be emerged into the global simulation. The sign of the flux denotes the sign of the trailing polarity in the bipole.

High and low resolution HMI and MDI synoptic magnetograms were then produced, and pixel by pixel comparisons with their corresponding SOLIS synoptic magnetograms were carried out. For low magnetic field strengths, both the MDI and HMI synoptic magnetograms measured lower magnetic flux densities than the SOLIS synoptic magnetograms. For high field strengths the trend was reversed, and the HMI and MDI synoptic magnetograms measured higher flux densities than the SOLIS synoptic magnetograms. MDI consistently measured higher magnetic flux densities than HMI. The possible causes of the different flux density measurements from the three instruments will now be discussed. Firstly, HMI, MDI and SOLIS/VSM use different absorption lines to measure the magnetic field. These lines need not necessarily be formed at the same height in the photosphere, and therefore effectively measure the magnetic field at different locations. Secondly, all three observatories have a different resolution. HMI has 0.5" per pixel, MDI has 2" per pixel and VSM has 1" per pixel. All three instruments will therefore measure different magnetic flux densities and will have different instrumental responses. Even though when comparing the flux densities the magnetograms from all three observatories had been degraded to the same resolution, the detectors' original resolutions may still have an effect on the resultant magnetic flux densities at the degraded resolutions. Another significant difference between SOLIS and MDI or HMI is that SOLIS is ground based, whilst MDI and HMI are space based. SOLIS' images are therefore hindered by atmospheric seeing, which has the effect of smearing out the image, and effectively degrading its resolution. SOLIS may therefore measure weaker strong magnetic flux densities than the space based instruments as the atmosphere has smeared out the strong field regions, diluting their strength. The same argument could be applied to why SOLIS measures stronger weak field than the space based observatories, as the weak field regions could be contaminated by flux from strong field regions due to the atmospheric seeing.

The properties of newly emerged active regions (tilt angle, separation and flux) were then determined by a semi-automated detection code (Yeates et al. 2007). The properties from active regions determined from the MDI and HMI synoptic magnetograms were compared with the properties as determined from the corresponding SOLIS synoptic magnetograms. The tilt angles and separations showed good agreement between MDI or HMI and SOLIS, however the fluxes measured were different. The fluxes of active regions measured from MDI were found to be 1.25 times the flux of the same active regions as determined from SOLIS, whilst for HMI the fluxes were found to be 0.9 times smaller than those from SOLIS. In order to ensure that SOLIS and MDI or HMI gave consistent active region properties, the fluxes of active regions determined from MDI have to be multiplied by a factor of 0.8, whilst the fluxes of active regions from HMI have to be multiplied by a factor of 1.1. This is consistent with the results from the pixel to pixel comparisons, which showed that the MDI synoptic magnetograms measured higher flux densities than the HMI synoptic magnetograms. Whilst the fluxes determined from HMI and MDI required to be scaled, the tilt angles and separations did not. Table 5.5 outlines the scaling relations that needed to be applied.

	Tilt Angle	Separation	Flux
HMI	1	1	1.1
MDI	1	1	0.8

Table 5.5: Scaling factors required to convert the bipole properties as determined from HMI or MDI to those of SOLIS.

There were a number of newly emerged active regions that were identified from the

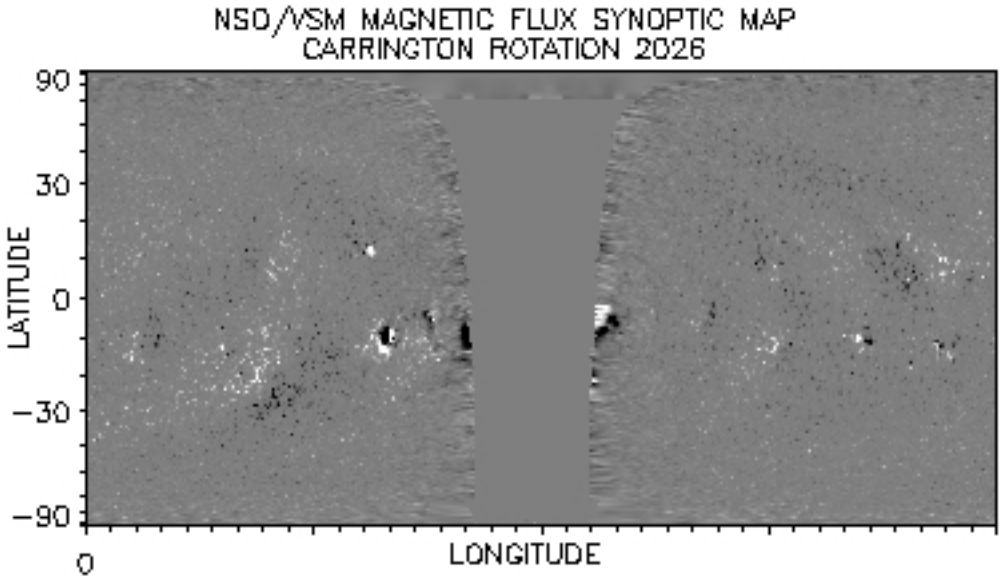

Figure 5.18: An example of a SOLIS synoptic magnetogram from Carrington Rotation 2026 with a data gap. (Source: http://solis.nso.edu)

SOLIS synoptic magnetograms, but not from MDI or HMI and vice versa. Their origins will now be discussed. Firstly, since SOLIS is ground based it is at the mercy of the weather conditions, and so on cloudy days no observations can be taken and therefore there are gaps in the SOLIS data. Due to the averaging process used to stitch the daily magnetograms together to create a synoptic magnetogram, these gaps in the observations do not usually result in a gap in the synoptic magnetogram. The longitude corresponding to the missing observation is constructed from data from the following and preceding days. If there is a gap of several days (due to weather) then the longitudes corresponding to these times may not accurately represent the magnetic field of the Sun on these days. As a consequence, the properties of a newly emerged active region at this location may be incorrect. Both HMI and MDI, which are unhindered by bad weather, provide magnetograms every day so there are no gaps. The magnetic field at longitudes corresponding to gaps in the SOLIS data therefore may be quite different on the SOLIS map compared to the HMI or MDI maps. Active regions in this longitudinal band may therefore be detected in one map, but not the other. Additionally if there is a sufficiently large contiguous set of days with no data, then a gap may be present in the synoptic SOLIS magnetogram (for an example of this, see Figure 5.18). There is no data within this gap, so no active region may be classified here. At the edge of the gap, which consists of noisy field from the solar limb, the automated detection routine may classify some noise as active regions. These false active regions are not present on the HMI or MDI active regions. The automated routine may also identify a reasonably complex active region as two active regions in one map, but as one in another.

In conclusion, HMI and MDI synoptic magnetograms may now be used in place of SOLIS magnetograms to determine the properties of emerged active regions for use in the global magnetogrictional simulation of Yeates et al. (2007). Indeed, HMI synoptic magnetograms may be a more accurate source than SOLIS as they do not possess data gaps due to bad weather and therefore better represent a true synoptic representation of the Sun's magnetic field.

Chapter 6

Investigating the Effects of Stellar Surface Transport on Coronal Dynamics

6.1 Introduction

The coronae of stars respond dynamically to the emergence and surface flux transport of their star's magnetic field. The surface transport has a number of associated timescales, from the relatively short timescales of flux emergence and differential rotation to the long timescales of stellar cycles. The corona's response to the surface dynamics manifests itself as the star's X-ray luminosity, stellar wind, coronal mass ejections and flares. All of these responses may actively impact on planets orbiting the star. For example, the stellar wind and CMEs apply a torque on the star, causing it to lose angular momentum and spin down (Weber & Davis 1967, Collier Cameron & Robinson 1989). On the Sun, the relations between the surface dynamics and the coronal response are well studied (for a review please see Mackay & Yeates (2012)), however the way in which these relations translate to other stars is not well understood. Previous studies that have considered the stellar coronal responses have found relations between the magnetic flux and the X-ray luminosity (Pevtsov et al. 2003), the magnetic flux and the energy available for driving stellar winds (Schwadron et al. 2006) and the relations between stellar flares and CMEs (Aarnio et al. 2011, Drake et al. 2013).

For the Sun, a series of studies has been carried out into the effects of photospheric magnetic flux transport on its large scale coronal field (van Ballegooijen et al. 1998, 2000, Mackay & van Ballegooijen 2006, Yeates et al. 2008, Yeates & Mackay 2012). In a stellar context, the evolution of the coronal field of the K0 star AB Doradus was modelled by Pointer et al. (2002) using the coronal modelling method of van Ballegooijen et al. (1998). Further to this, Cohen et al. (2010) ran a magnetohydrodynamical simulation of the corona of AB Doradus in order to determine the loss rates of the star's mass and angular momentum. Mackay et al. (2004) investigated the photospheric magnetic flux transport on active stars in order to investigate the formation of the observed polar spot caps. This study considered only the evolution of the photospheric magnetic field, and did not investigate the coronal magnetic field evolution.

With evidence that some stars have higher levels of differential rotation than the Sun, it is useful to understand how the enhanced differential rotation affects the dynamics of the stellar corona. In order to address this, in this chapter scaling relations for the formation time and lifetime of flux ropes with differential rotation are determined. This is achieved

by simulating the formation (and subsequent eruptions) of flux ropes formed in a simple isolated decaying bipolar active region. To carry out the study, a magnetic flux transport model is used to determine the evolution of the stellar photospheric field. This evolving photospheric field is then used to drive the evolution of the coronal magnetic field by applying a magnetofrictional technique. The FFF3 code (Chapter 2) is used to simulate the stellar corona. Work from this chapter is published in Gibb, Jardine & Mackay (2014).

6.2 The Model

6.2.1 Surface Flux Transport Model

In order to model the evolution of the coronal magnetic field with the magnetofrictional method, we require a description of the evolution of the photospheric magnetic field. The photospheric evolution is determined using the flux transport model described in Mackay & van Ballegooijen (2006). This model assumes the radial photospheric magnetic field, B_r, is influenced solely through the effects of differential rotation, meridional flow and surface diffusion. The surface diffusion represents the effects of small scale flows such as supergranulation on the large scale field. The radial magnetic field at the photosphere is expressed by the vector magnetic potentials $A_{\theta b}$ and $A_{\phi b}$ through

$$B_r = \frac{1}{R_* \sin\theta}\left[\frac{\partial}{\partial\theta}(\sin\theta A_{\phi b}) - \frac{\partial A_{\theta b}}{\partial\phi}\right]. \tag{6.1}$$

The magnetic vector potentials are evolved by solving the two dimensional flux transport equation:

$$\begin{aligned}\frac{\partial A_{\theta b}}{\partial t} &= u_\phi B_r - \frac{D}{R_* \sin\theta}\frac{\partial B_r}{\partial\phi},\\ \frac{\partial A_{\phi b}}{\partial t} &= -u_\theta B_r + \frac{D}{R_*}\frac{\partial B_r}{\partial\theta},\end{aligned} \tag{6.2}$$

where u_ϕ is the azimuthal velocity, u_θ is the meridional flow velocity, R_* is the stellar radius and D is the photospheric diffusion constant. It should be noted that we use θ to denote the co-latitude (angle measured from the north pole), and λ to denote the latitude (angle measured from the equator), where $\theta = 90^\circ - \lambda$.

Azimuthal velocity

The azimuthal velocity is of the form

$$u_\phi = \Omega(\theta) R_* \sin\theta, \tag{6.3}$$

where $\Omega(\theta)$ is the differential rotation profile, taken to be the stellar rotation profile (see Section 1.2.3),

$$\Omega_*(\theta) = \Omega_0 - d\Omega \cos^2\theta, \tag{6.4}$$

Where Ω_0 is the star's equatorial angular velocity and $d\Omega$ is a parameter representing the degree of differential rotation. It is desirable to be able to directly compare the stellar differential rotation profile to the solar rotation profile:

$$\Omega_\odot(\theta) = 14.71 - 2.30\cos^2\theta - 1.62\cos^4\theta \text{ deg day}^{-1}, \tag{6.5}$$

(see Section 1.1.5). To do this, a value of $d\Omega$ is determined which best represents the solar profile. This is achieved by minimising the quantity

$$\delta = \int_0^\pi \left(\Omega_\odot(\theta) - \Omega_*(\theta)\right)^2 d\theta = \int_0^\pi \left(d\Omega \cos^2\theta - 2.30\cos^2\theta - 1.62\cos^4\theta\right)^2 d\theta, \tag{6.6}$$

which represents the difference between the solar and stellar differential rotation models, with respect to $d\Omega$. The value of $d\Omega$ which minimises δ is

$$d\Omega_\odot = \frac{\int_0^\pi (2.30\cos^2\theta + 1.62\cos^4\theta)\cos^2\theta d\theta}{\int_0^\pi \cos^4\theta d\theta} = 3.65 \text{ deg day}^{-1}. \tag{6.7}$$

In this study, $\Omega(\theta)$ is chosen to be

$$\Omega(\theta) = K\left(\Omega_0 - d\Omega_\odot \cos^2\theta\right), \tag{6.8}$$

where Ω_0 is chosen to be 0.9215 deg day^{-1} such that $\Omega(\theta)$ is zero at 30° latitude. In other words, Equation 6.8 is expressed in a reference frame that co-rotates with 30° latitude. The constant K acts to scale the profile to stars with higher differential rotation rates. Thus we can express the stellar differential rotation rate, $d\Omega_*$, as

$$d\Omega_* = K d\Omega_\odot. \tag{6.9}$$

The above differential rotation profile (Equation 6.8) and the azimuthal velocity (Equation 6.3) are plotted for several different values of K in Figure 6.1.

Meridional velocity

The meridional velocity is prescribed by

$$u_\theta = u_y = C\cos\left[\frac{\pi(\theta_{\max} + \theta_{\min} - 2\theta)}{2(\theta_{\max} - \theta_{\min})}\right], \tag{6.10}$$

where $C = 15$ ms^{-1} is chosen to be the peak meridional flow velocity of the Sun. The profile is chosen such that the meridional flow vanishes at the latitudinal boundaries $(\theta_{\min}, \theta_{\max})$ of the simulation. We adopt the solar meridional flow profile as we have no knowledge of the meridional flow profiles of other stars. In Section 6.3.3 the effects of the meridional flow on the formation and lifetime of flux ropes are discussed. Figure 6.2 displays the meridional velocity profile used in the simulations in this study, where $\theta_{\min} = 25°$ and $\theta_{\max} = 94.5°$.

Numerical implementation of the surface transport

FFF3 uses the coordinates x, y and z, related to r, θ and ϕ by

$$x(\phi) = \frac{\phi}{\Delta}, \tag{6.11}$$

$$y(\theta) = \frac{-\ln\left(\tan\frac{\theta}{2}\right)}{\Delta}, \tag{6.12}$$

$$z(r) = \frac{\ln\left(\frac{r}{R_*}\right)}{\Delta}, \tag{6.13}$$

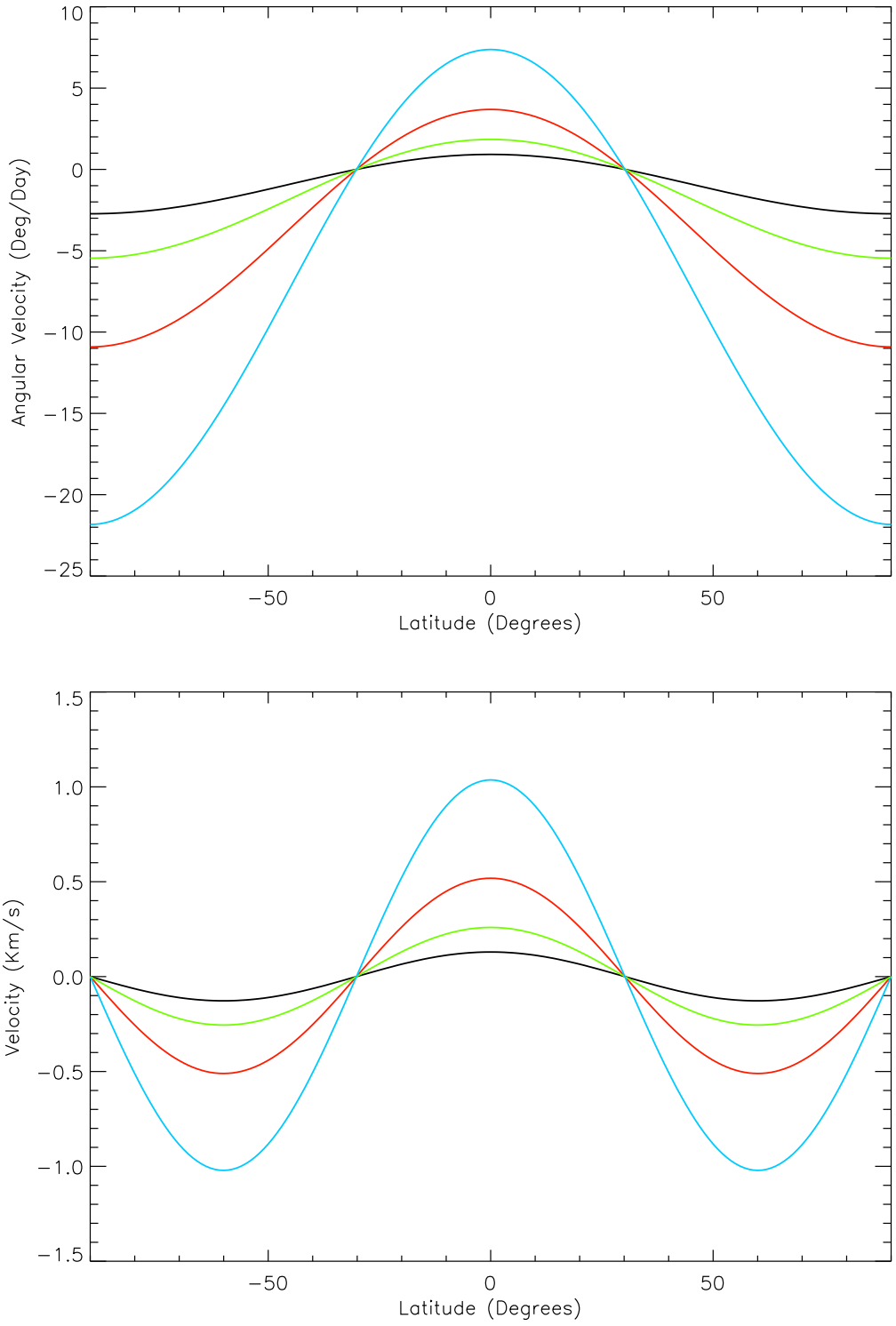

Figure 6.1: Top: The angular velocity of differential rotation (Equation 6.8) for K=1 (black), 2 (green), 4 (red) and 8 (blue). Bottom: The azimuthal velocity (Equation 6.3) for K=1,2,4 and 8.

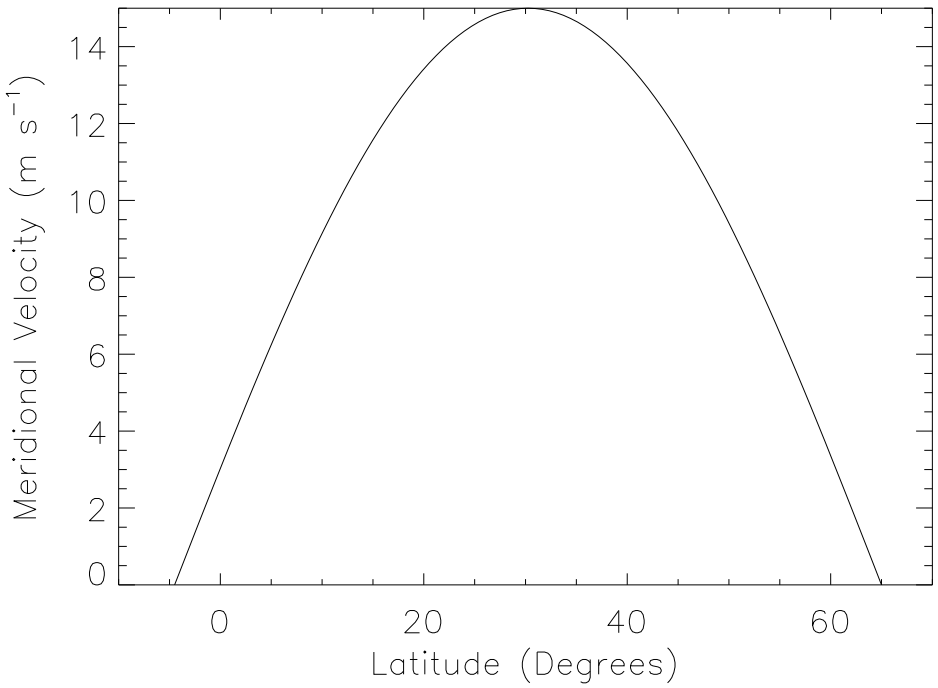

Figure 6.2: The meridional velocity profile used in the simulations. Note that the meridional flow goes to zero at $-4.5°$ and $65°$ latitude – the latitudinal boundaries of the simulations.

where Δ is the longitudinal grid spacing. For more detail, please refer to Chapter 2 Section 2.3 and Appendix A Section A.2. In FFF3, the surface flux transport equation (Equation 6.2) is thus given by

$$\begin{aligned}\frac{\partial A_{yb}}{\partial t} &= -u_x B_z + D\frac{\partial B_z}{\partial x},\\ \frac{\partial A_{xb}}{\partial t} &= u_y B_z - D\frac{\partial B_z}{\partial y}.\end{aligned} \tag{6.14}$$

In order to solve this, firstly B_z is calculated on the cell centres using the Stoke's theorem method (Equation 2.34) by calculating

$$B_z(i+\tfrac{1}{2}, j+\tfrac{1}{2}) = \frac{[A_{yb}h_{y_{A_y}}](i+1,j+\frac{1}{2}) - [A_{xb}h_{x_{A_x}}](i+\frac{1}{2},j+1) - [A_{yb}h_{y_{A_y}}](i,j+\frac{1}{2}) + [A_{xb}h_{x_{A_x}}](i+\frac{1}{2},j)}{[h_{x_{B_z}}h_{y_{B_z}}](i+\frac{1}{2},j+\frac{1}{2})} \tag{6.15}$$

for $i = 1, N_x$ and $j = 1, N_y$. The same boundary conditions are applied to B_z as described in Section A.2.2 of Appendix A. B_z is then averaged onto cell corners. The quantities $u_x B_z$ and $u_y B_z$ are calculated at the cell corners and then averaged onto the cell ribs. The diffusive terms are calculated on cell ribs. Numerically, the surface transport equations (Equation 6.14) are integrated by

$$A_{yb}(i, j+\tfrac{1}{2})[t+\Delta t] = A_{yb}(i, j+\tfrac{1}{2})[t] - \left(u_x B_z(i, j+\tfrac{1}{2}) + D\frac{B_z(i+\frac{1}{2}, j+\frac{1}{2}) - B_z(i+\frac{1}{2}, j+\frac{1}{2})}{h_{x_{A_y}}(i, j+\frac{1}{2})}\right)\Delta t \tag{6.16}$$

$$A_{xb}(i+\tfrac{1}{2}, j)[t+\Delta t] = A_{xb}(i+\tfrac{1}{2}, j)[t] + \left(u_x B_z(i+\tfrac{1}{2}, j) - D\frac{B_z(i+\frac{1}{2}, j+\frac{1}{2}) - B_z(i+\frac{1}{2}, j-\frac{1}{2})}{h_{y_{A_x}}(i+\frac{1}{2}, j)}\right)\Delta t \tag{6.17}$$

where the derivatives to calculate the diffusive term use cell face values for B_z. The A_{xb} and A_{yb} variables are then used as the lower boundary condition for FFF3 such that

$$A_x(i+\tfrac{1}{2}, j, 0) = A_{xb}(i+\tfrac{1}{2}, j), \tag{6.18}$$

$$A_y(i, j+\tfrac{1}{2}, 0) = A_{yb}(i, j+\tfrac{1}{2}). \tag{6.19}$$

6.2.2 Coronal Evolution Model

FFF3 evolves the coronal magnetic field using the ideal induction equation,

$$\frac{\partial \mathbf{A}}{\partial t} = \mathbf{v} \times \mathbf{B}, \tag{6.20}$$

where $\mathbf{v} = \mathbf{v}_{\mathrm{MF}} + \mathbf{v}_{\mathrm{out}}$ contains contributions from the magnetofrictional velocity ($\mathbf{v}_{\mathrm{MF}}$) and an outflow velocity ($\mathbf{v}_{\mathrm{out}}$). The magnetofrictional velocity is

$$\mathbf{v}_{\mathrm{MF}} = \frac{1}{\nu}\frac{\mathbf{j} \times \mathbf{B}}{B^2}. \tag{6.21}$$

The changing photospheric magnetic field – as specified by the flux transport model – induces a Lorentz force above the photosphere. The magnetofrictional velocity, which is

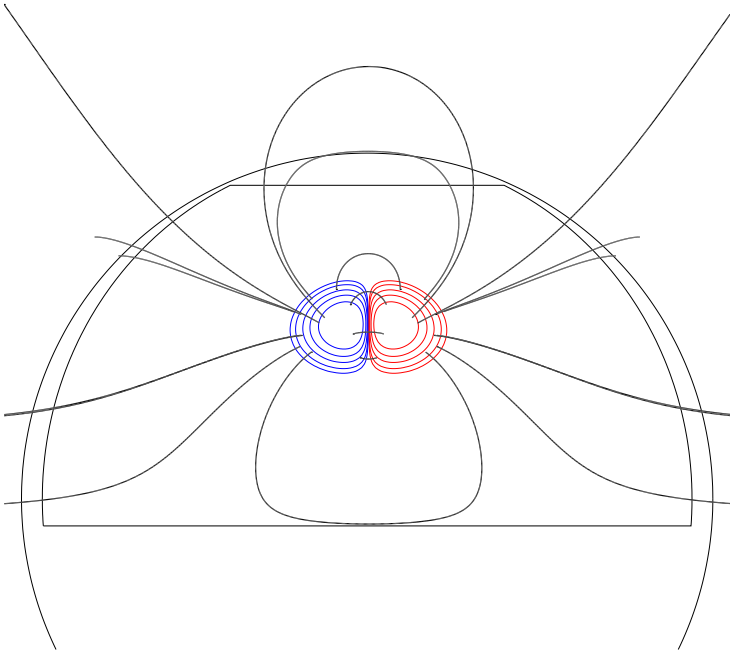

Figure 6.3: A field line plot of the potential initial condition used in this study where red and blue contours represent positive and negative surface flux respectively.

aligned in the direction of the Lorentz force, acts to advect the coronal field towards a new non-linear force-free equilibrium. The changing photospheric field thus drives the evolution of the coronal field through a series of force-free equilibria.

In addition to the magnetofrictional velocity we also apply a radial outflow velocity of the form

$$\mathbf{v}_{\text{out}} = v_0 \exp\left(\frac{z - z_{\max}}{z_w}\right)\hat{\mathbf{z}}, \tag{6.22}$$

where $v_0 = 100$ km s^{-1} and z_w is the width over which the radial velocity falls off at the outer boundary. This outflow velocity is chosen to ensure that the coronal magnetic field at the upper boundary is radial, and also allows any flux ropes that have lifted off from the photosphere to be removed from the computational box. The outflow velocity is negligible in the low-down corona. Note that once the field lines become radial near the outer boundary the outflow velocity has no effect on the evolution of the magnetic field.

For more details on the coronal evolution model, see Chapter 2 Section 2.3 and Appendix A Section A.2.

6.2.3 Simulation Set-Up

We simulate a stellar corona between 0° and 140° longitude, −4.5° and 65° latitude (25° and 94.5° co-latitude), and between radii of $1R_*$ and $2.5R_*$. The grid spacing, Δ, is set to be 0.5°. This results in a grid containing $280 \times 182 \times 105$ cells.

In order to model the photospheric and coronal evolution of the active region, we first must prescribe an initial state. The initial state we choose is a simple bipole whose centre point has latitudinal and longitudinal coordinates of $(\lambda_0, \phi_0) = (30°, 70°)$. The half separation between the peaks of positive and negative flux on the photosphere is

chosen to be $\rho_0 = 4.5°$. The bipole's peak flux density at the photosphere is chosen to be $B_0 = -100$ G, resulting in a flux of 1.5×10^{22} Mx – in agreement with the typical flux of a solar active region. Finally, the bipole's tilt angle (the angle between the east-west line and the line between the peaks of the positive and negative flux) is chosen to be $\gamma = 0°$. We prescribe the radial photospheric field, $B_z(x, y, 0)$ according to

$$B_z(x, y, 0) = \frac{B_0 x'}{\rho_0} \exp\left(-\frac{x'^2/2 + y'^2}{2\rho_0^2}\right), \tag{6.23}$$

where

$$x' = (\phi - \phi_0)\cos(-\gamma) + (\lambda - \lambda_0)\sin(-\gamma) \tag{6.24}$$

$$y' = (\lambda - \lambda_0)\cos(-\gamma) - (\phi - \phi_0)\sin(-\gamma). \tag{6.25}$$

A potential field in the corona is then calculated from the photospheric field, using the method described by van Ballegooijen et al. (2000). The potential field computed assumes that the magnetic field is radial at the upper ($r = 2.5R_*$) boundary. Figure 6.3 displays the initial condition field we use. Note that in all simulations we assume that $R_* = R_\odot$. In Section 6.3.4 we investigate the effects of varying γ.

Figure 6.4 shows field lines from the potential initial condition in a cut in the x-z plane before and after the outflow velocity in FFF3 (Equation 6.22) has been applied. As can be seen, the outflow velocity has little to no effect on the field below a height of z=50 which is equivalent to 1.54 stellar radii.

6.3 Results

In this section we consider the effects of varying the differential rotation and surface diffusion coefficient on the formation time and lifetime of flux ropes on solar-like stars. We investigate a range of differential rotations between $d\Omega_*/d\Omega_\odot = 1$ (lap time of 98.6 days) and $d\Omega_*/d\Omega_\odot = 10$ (lap time of 9.86 days). This choice approximately covers the range of differential rotation rates greater than the Sun's that have been measured to date. As we have no knowledge of the values of the surface diffusion coefficients on different stars, we also investigate four different surface diffusion constants, namely $D = 225, 450, 900$ and 1800 km^{2}s^{-1} (global surface diffusion timescales ranging from 68–8.5 years).

In our simulations, flux ropes are formed above the polarity inversion line within the active region. The flux ropes form when the arcade field between the two magnetic polarities becomes sheared due to the differential rotation shearing the photospheric flux distribution. Surface diffusion acts to bring the footpoints of the sheared field lines towards each other. The footpoints cancel and reconnect, producing a long field line which is strongly aligned with the polarity inversion line. The surface diffusion continues to bring the footpoints of sheared arcades toward each other. Subsequent cancellation and reconnection of these footpoints lead to field lines that wrap around the long loop aligned with the polarity inversion line, forming a flux rope. The above formation mechanism is that proposed by van Ballegooijen & Martens (1989). It is clear from the above description that both shear and flux cancellation are required to form a flux rope. In our simulations, the shear is generated through the effect of differential rotation, whilst the flux cancellation is achieved by the surface diffusion.

Figure 6.5 shows a selection of snapshots from a simulation with $d\Omega_*/d\Omega_\odot = 3$ (corresponding to a lap time of 32.8 days) and $D = 450$ km^{2}s^{-1} which highlight the typical evolution of the coronal field in all of the simulations. Firstly, the differential rotation

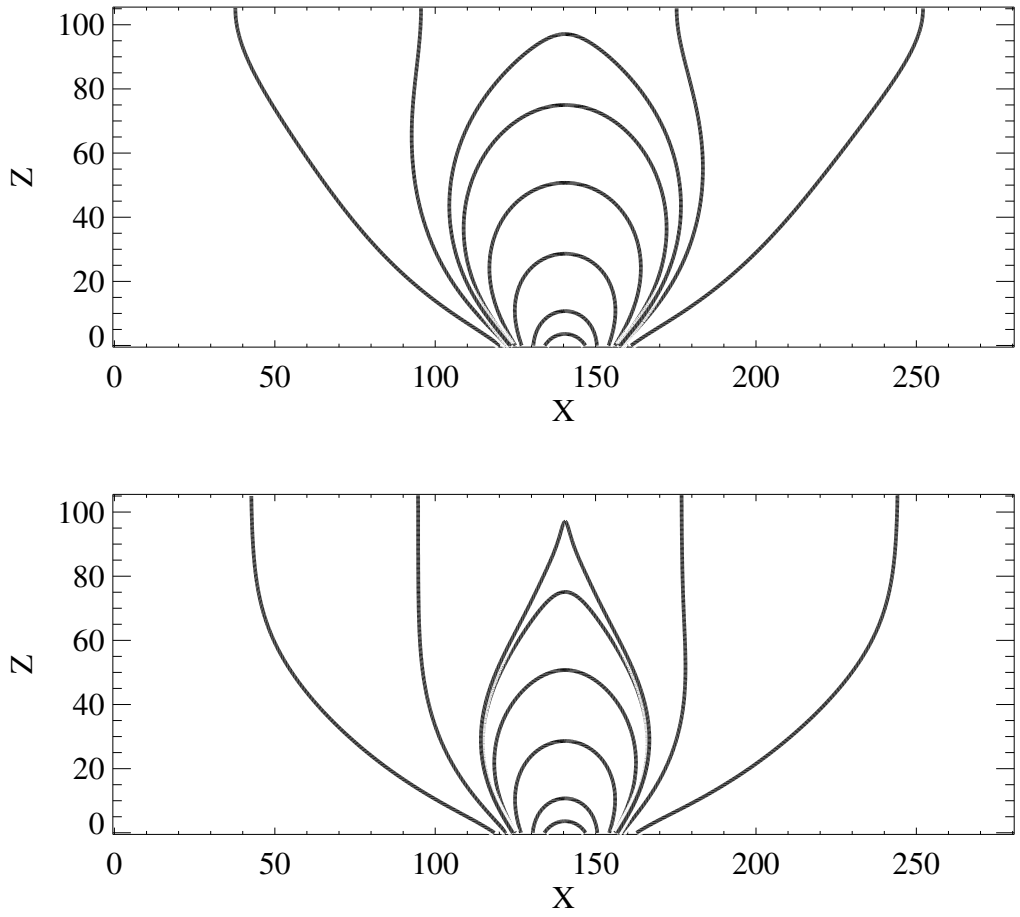

Figure 6.4: Field line plots of the initial condition field before (top) and after (bottom) the outflow velocity has been applied. The axes are scaled according to the coordinates described in Equations 6.11 and 6.13.

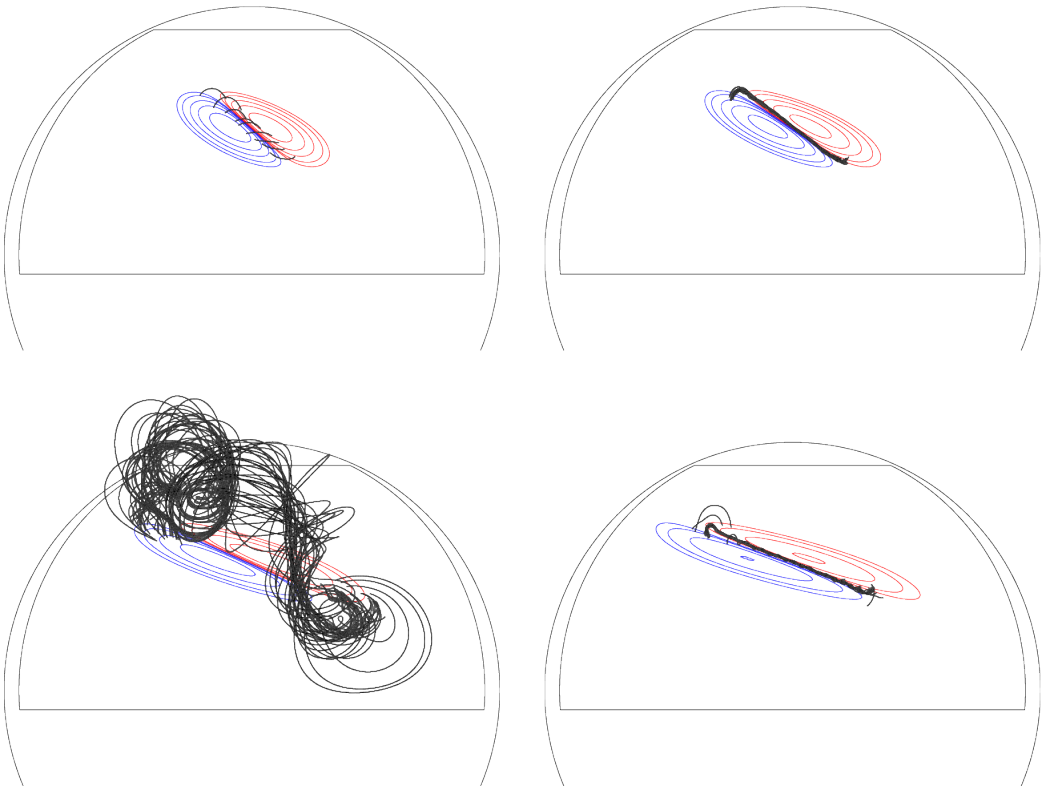

Figure 6.5: Snapshots from the simulation with $d\Omega_*/d\Omega_\odot = 3$ and $D = 450$ km^{2}s^{-1} outlining the sheared arcade (top left) transforming into a flux rope (top right), the eruption of the flux rope (bottom left) then the formation of a second flux rope (bottom right). Red and blue contours represent positive and negative surface flux respectively. In each panel the contour levels are the same. *A movie version of this figure, 'eruption.mp4', can be found in the 'chapter6' directory on the accompanying CD.*

shears the photospheric flux distribution, which results in a sheared arcade field (top left panel of Figure 6.5). Flux cancellation transforms the sheared arcade into a flux rope (top right of Figure 6.5). The continued shearing and cancellation increases the size of the flux rope which eventually leads to the flux rope becoming unstable and lifting off from the photosphere (bottom left panel of Figure 6.5), leaving a sheared arcade. This sheared arcade may form into a second flux rope due to the ongoing differential rotation and flux cancellation (bottom right Figure 6.5). In this study we consider two timescales; the timescale for a flux rope to form and the length of time that it may remain stable before eruption - its lifetime.

6.3.1 Formation Timescale

First, we consider the formation timescale as a function of differential rotation for the four different surface diffusion constants. In order to do this, the earliest time in the simulation at which a flux rope is detected must be determined. As is described in Chapter 2, there are two methods used in this thesis to detect and characterise flux ropes – by considering the Lorentz forces or by considering the horizontal field crossing the PIL. The FRfinder routine (Section 2.5) is run on the output from the simulation, and the earliest time a flux rope is detected is defined as the flux rope formation time. Figure 6.6 displays the points belonging to the flux rope axis (blue crosses) determined by FRfinder overlaid on a contour plot of the photospheric flux distribution for t=1, 4, 8 and 10 days in the simulation with $d\Omega_*/d\Omega_\odot = 3$ and $D = 450$ km^{2}s^{-1}. In the figure, it is clear that the flux rope is only present on the tenth day.

Using PILfinder (Section 2.6), the variation of the shear angle θ_s (Equation 2.50) at every time in the simulation can be determined. Using this method, the formation time for the flux rope is defined as the time it takes from the beginning of the simulation for the shear angle across the PIL to become $> 90°$. Figure 6.7 displays plots of the shear angle as a function of latitude at the same times as Figure 6.6. As time progresses into the simulation the tilt angle increases towards 90° and exceeds 90° sometime between the eighth and tenth days of the simulation.

Table 6.1 outlines for each run the formation time as determined by the FRfinder and PILfinder codes. Upon inspection, it is immediately clear that the formation times found by FRfinder are consistently greater than (or equal to) those found by PILfinder for a given simulation. This is attributed to the FRfinder code requiring to have a well-defined flux rope structure before it can find a point along the axis, whilst PILfinder only needs the shear angle to exceed 90° at one point in order to determine a flux rope has been formed. Therefore PILfinder will always detect a flux rope before FRfinder can. For the remainder of this thesis, the formation time is taken to be the formation time as determined by PILfinder. FFF3 only outputs snapshots of the simulation with a certain frequency, the output frequency, which in this study is either one day, or 0.25 days. As such, if a flux rope is not present in snapshot number n, but is present in snapshot number $n + 1$, then we know that it formed sometime between these two snapshots. We take the error in the formation time, $\Delta\tau_{\text{Form}}$, to be the output frequency, as we cannot be certain of the formation time to an accuracy greater than the output frequency of the simulation.

Figure 6.8 displays the evolution of formation times as a function of differential rotation scaling for various surface diffusion coefficients. It is clear from the plots that for all surface diffusion coefficients investigated, the formation time decreases with increasing differential rotation scaling. Increasing the surface diffusion coefficient has the effect of decreasing the formation times. In order to determine the relation between formation time and

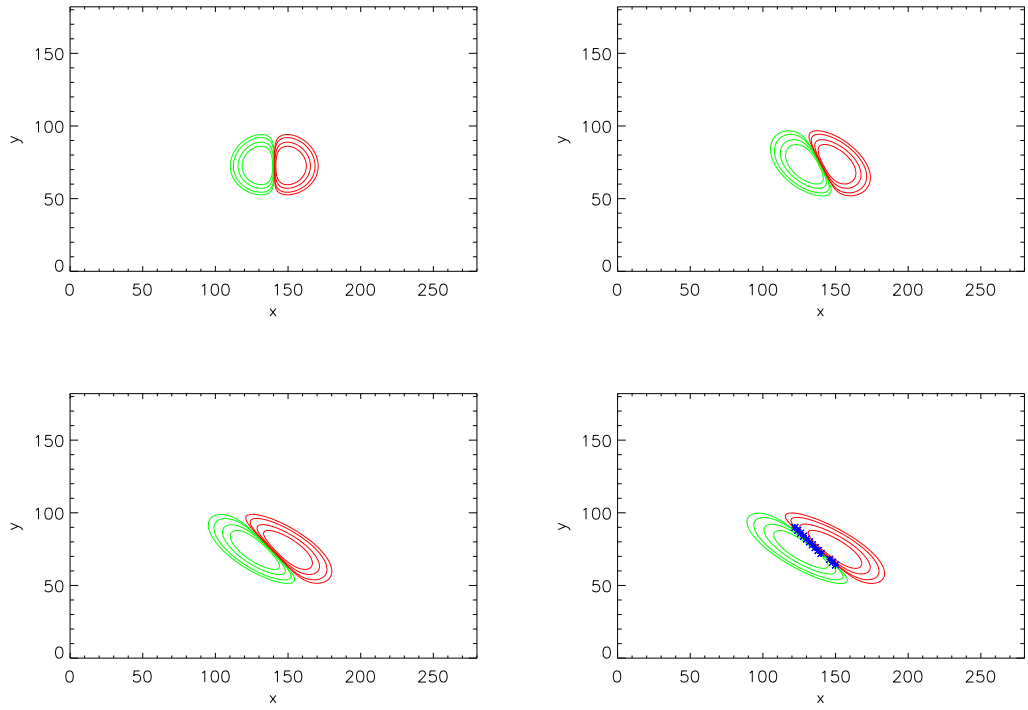

Figure 6.6: Flux rope axis locations (blue crosses) as determined by FRfinder on days 0 (top left), 4 (top right), 8 (bottom left) and 10 (bottom right) of the simulation with $d\Omega_*/d\Omega_\odot = 3$ and $D = 450\ \mathrm{km^2 s^{-1}}$. The red and green contours denote positive and negative photospheric magnetic field respectively. Note that no flux rope is detected on days 0, 4 and 8.

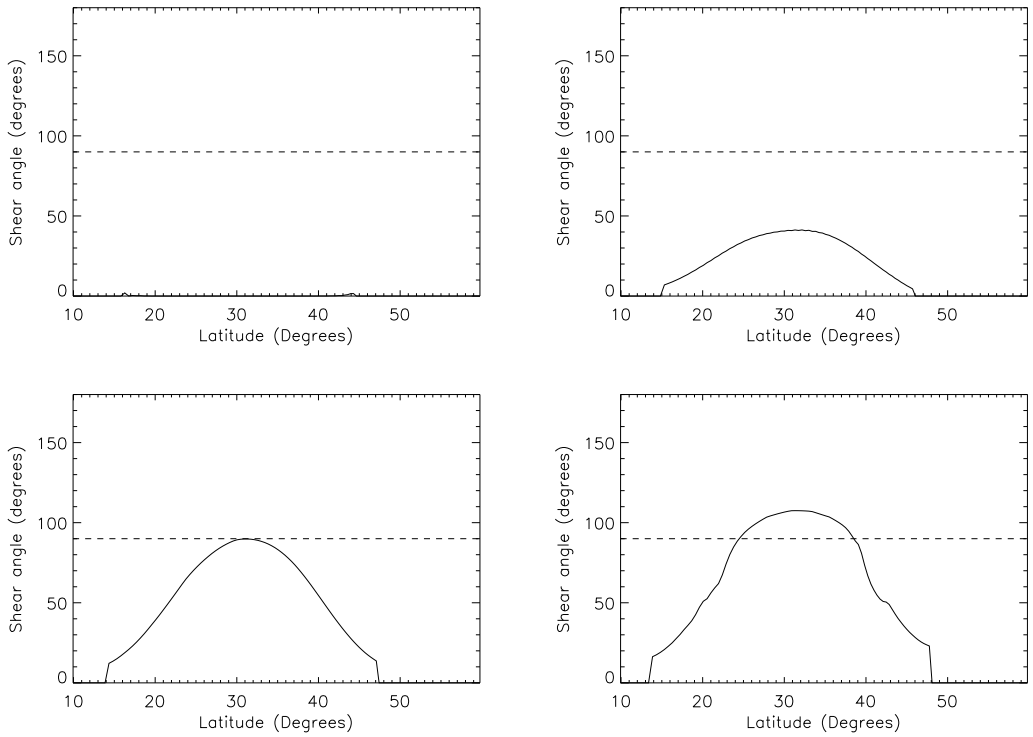

Figure 6.7: The evolution of the shear angle across the PIL as a function of latitude on days 0 (top left), 4 (top right), 8 (bottom left) and 10 (bottom right) for the simulation with $d\Omega_*/d\Omega_\odot = 3$ and $D = 450$ km^{2}s^{-1}. The horizontal dashed line denotes a shear angle of 90°. Note that the shear angle does not exceed 90° on days 0, 4 and 8. Only on day 10 does the shear angle exceed 90°, implying that a flux rope is present above the PIL at this time.

K	η (km^2s^{-1})	Output Frequency (days)	τ_{Form} (FRfinder)	τ_{Form} (PILfinder)
1	225	1	22	21
2	225	0.25	14	13.5
4	225	0.25	9	8.75
6	225	0.25	7	6.75
8	225	0.25	5.5	5.5
10	225	0.25	4.75	4.75
1	450	1	17	16
2	450	1	12	11
3	450	1	8.75	8.25
4	450	1	7	6.75
5	450	0.25	6.25	6
6	450	0.25	5.5	5.25
7	450	0.25	5.0	4.75
8	450	0.25	4.5	4.5
9	450	0.25	4.25	4.25
10	450	0.25	4	4
1	900	1	12	11
2	900	0.25	8	7.5
3	900	0.25	6.75	6.25
4	900	0.25	5.25	5
6	900	0.25	4.25	4
8	900	0.25	3.5	3.5
10	900	0.25	3	3
1	1800	0.25	7.75	7.25
2	1800	0.25	5.75	5.5
4	1800	0.25	4	3.75
6	1800	0.25	3	3
8	1800	0.25	2.75	2.75
10	1800	0.25	2.25	2.25

Table 6.1: Formation times for the simulations carried out as determined by the FRfinder and PILfinder codes.

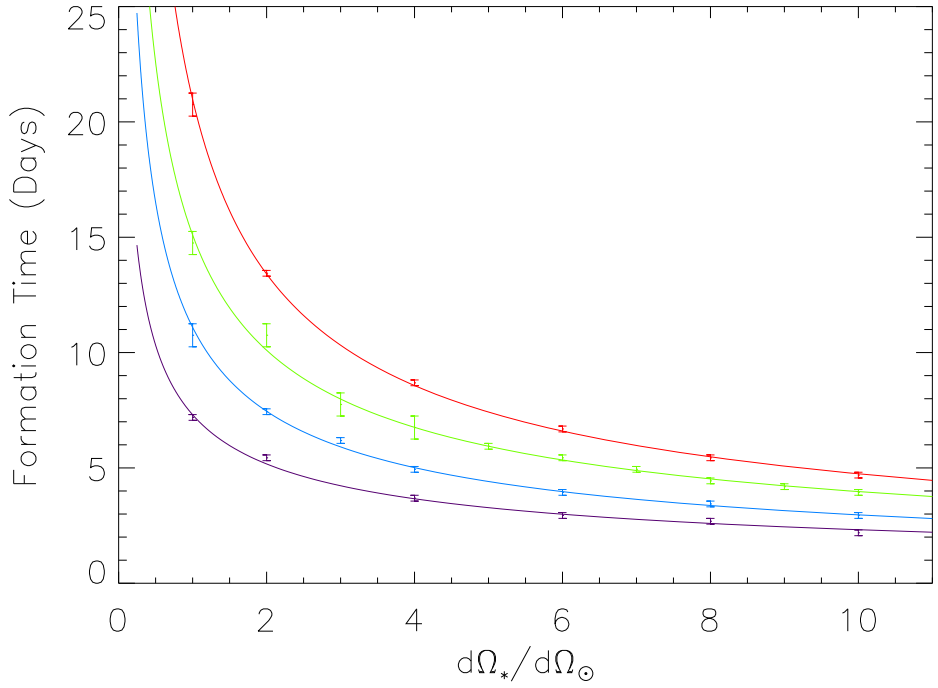

Figure 6.8: Formation timescales as a function of differential rotation for diffusion constants of 250 km^2s^{-1} (red), 450 km^2s^{-1} (green), 900 km^2s^{-1} (blue) and 1800 km^2s^{-1} (purple). The curves are the power laws fitted to the data as described in Table 6.2.

D ($\mathrm{km^2 s^{-1}}$)	m_{ML}	A_{ML}
225	0.646 ± 0.009	1.08 ± 0.01
450	0.580 ± 0.015	1.05 ± 0.01
900	0.573 ± 0.017	0.80 ± 0.01
1800	0.498 ± 0.011	0.74 ± 0.01

Table 6.2: The maximum likelihood estimates of the power law index, m, and the scaling constant, A, from Equation 6.26 and their errors for different surface diffusion constants.

differential rotation scaling, we fit a scaling law of the form

$$\tau_{\mathrm{Form}} = A(\tau_{\mathrm{Lap}})^m, \tag{6.26}$$

to the data, where τ_{Form} is the formation time, τ_{Lap} is the lap time, A is a scaling constant and m is the power law index. In order to fit the parameters to the scaling law, firstly the logarithm of the scaling law is taken to give

$$y = mx + c, \tag{6.27}$$

where $y = \ln(\tau_{\mathrm{Form}})$, $x = \ln(\tau_{\mathrm{Lap}})$ and $c = \ln A$. The error, Δy, was calculated by

$$\Delta y = \frac{\ln(\tau_{\mathrm{Form}} + \Delta\tau_{\mathrm{Form}}) - \ln(\tau_{\mathrm{Form}} - \Delta\tau_{\mathrm{Form}})}{2}. \tag{6.28}$$

The parameters m and c are then determined using the maximum likelihood method, described in Appendix B.

Table 6.2 displays the maximum likelihood estimators for the power law index, m, and the scaling constant, A, and their errors for the different surface diffusion constants chosen. From the table, it is clear that m is roughly one half for all the surface diffusion constants investigated, and that A decreases with increasing surface diffusion. Upon increasing the surface diffusion constant by a factor of eight, the power law index decreases by $\approx 25\%$. We thus conclude that the the power law index has a weak dependence on the surface diffusion. We find the mean power law index to be 0.574 with a standard deviation of 0.06.

Increasing the surface diffusion constant decreases the scaling constant, A. In order to investigate the dependence of the scaling constant on the surface diffusion, we assume that the power law index, m, is independent of the surface diffusion. This assumption is made so that we can directly compare the scaling constants obtained from all four surface diffusion constants investigated. We determine the scaling constant assuming that $m = 0.574$ – the mean value of the power law index found in this study. To do this, we solve Equation B.14 for each diffusion coefficient, whilst keeping m fixed at 0.574. From the values of c determined for each diffusion coefficient, it is found that

$$c \propto -(0.44 \pm 0.01) \ln D \tag{6.29}$$

and so

$$A \propto D^{(-0.44 \pm 0.01)}. \tag{6.30}$$

We therefore tentatively conclude that the formation timescale is approximately determined by

$$\tau_{\mathrm{Form}} \propto D^{-0.44} (\tau_{\mathrm{Lap}})^{0.57}. \tag{6.31}$$

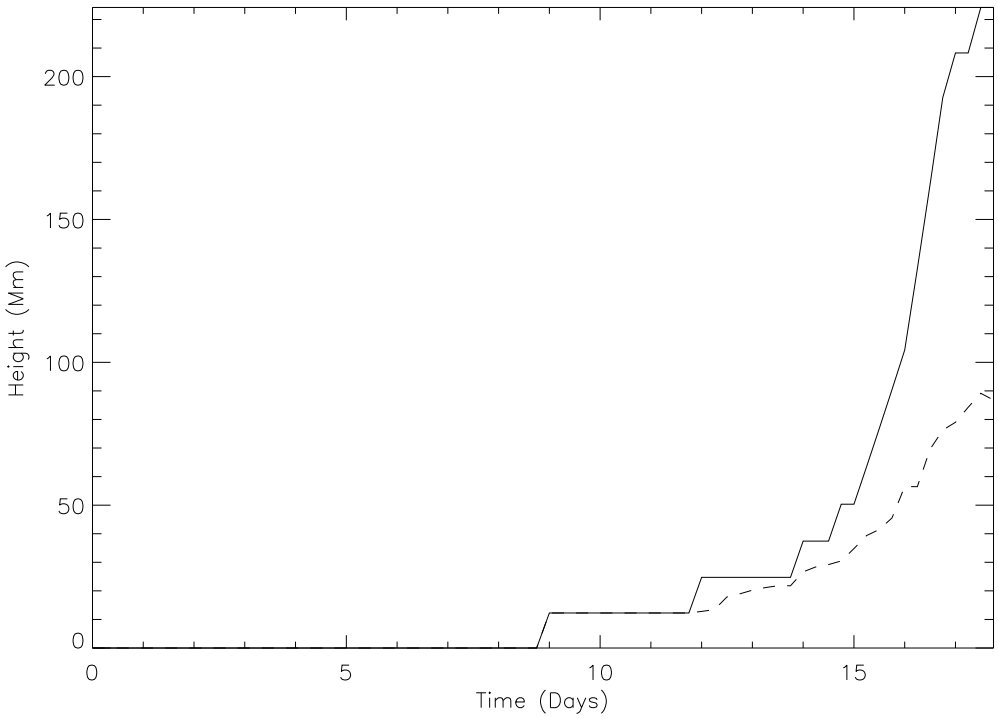

Figure 6.9: The evolution of the maximum (solid line) and mean (dashed line) height of points belonging to flux rope axes as a function of time in the simulation with $d\Omega_*/d\Omega_\odot = 3$ and $D = 450$ km^{2}s^{-1}. Note that both the mean and maximum heights begin to increase at around 12-15 days.

Further to this, if we note that the diffusion time can be expressed as $\tau_{\text{Diff}} \approx L^2/D$ then we find that approximately,

$$\tau_{\text{Form}} \propto \sqrt{\tau_{\text{Lap}}\tau_{\text{Diff}}}. \tag{6.32}$$

It is very important to note that the scalings determined here are obtained from a range of under one decade in both lap time and surface diffusion constant. The scalings derived must therefore be regarded with caution.

6.3.2 Lifetime

Another important timescale to investigate is the lifetime of a flux rope. We define this as the length of time between its formation and the onset of its eruption. There are several methods used in this thesis to define the onset times of eruption, using both FRfinder and PILfinder.

- When a flux rope becomes unstable, it lifts off from the photosphere and rises upwards. Therefore by considering the height of its axis (as determined by FRfinder), its eruption time may be inferred by when the height begins to increase. In Figure 6.9, the evolution of the mean (dashed line) and maximum (solid line) heights of points belonging to the flux rope's axis as a function of time is plotted for the simulation with $d\Omega_*/d\Omega_\odot = 3$ and $D = 450$ km^{2}s^{-1}.

- A sharp increase in the mean velocity of the flux rope axis may indicate the onset of an eruption. The velocity is determined by calculating the magnetofrictional

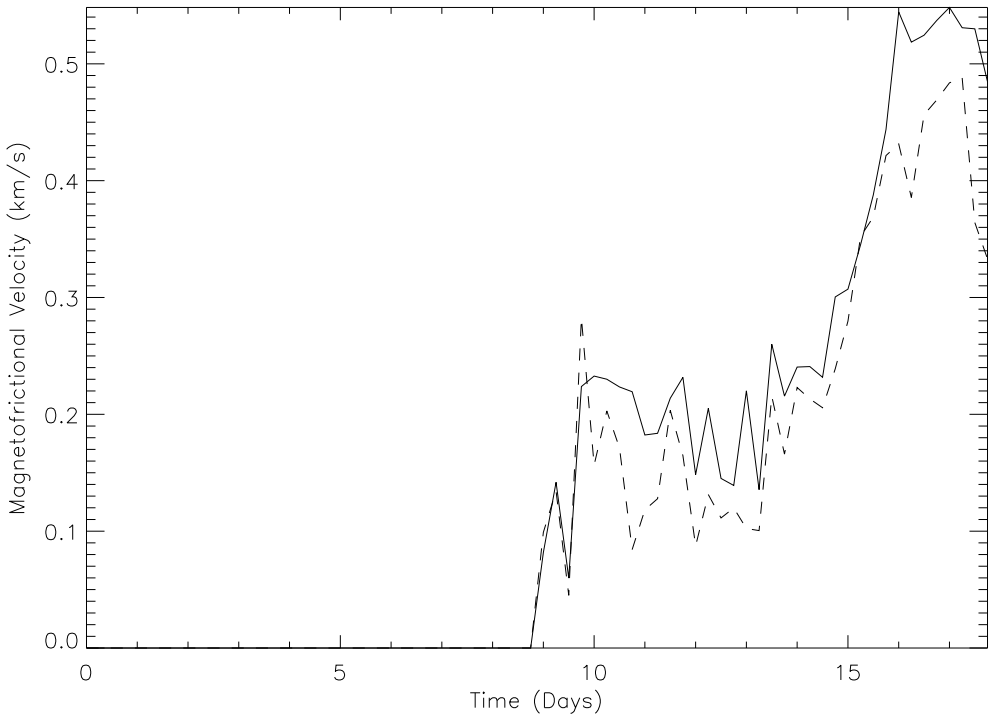

Figure 6.10: The median (solid line) and mean (dashed line) velocities of points belonging to the flux rope axis as a function of time for the simulation with $d\Omega_*/d\Omega_\odot = 3$ and $D = 450$ km^{2}s^{-1}. Note that the velocities exhibit a sharp increase between days 14 and 15.

velocity – Equation 2.4 – at points belonging to the flux rope's axis as determined by FRfinder. Figure 6.10 displays the mean (dashed line) and median (solid line) velocity of the points belonging to the flux rope axis as a function of time for the simulation with $d\Omega_*/d\Omega_\odot = 3$ and $D = 450$ km^{2}s^{-1}.

- When the flux rope forms, its axis appears as a straight line in the $x-y$ plane. As it becomes unstable its axis deforms, and is no longer well described by a straight line (Figure 6.11). Measuring its deviation from a straight line can be used to indicate when the flux rope begins to erupt. In order to do this, at each time we fit a straight line to the flux rope axis, and determine the reduced chi-squared (see Appendix B). When the reduced chi-squared becomes $\gg 1$ the axis is no longer well described by a straight line, and the flux rope may have become unstable. Figure 6.12 displays the evolution of the reduced chi-squared for the simulation with $d\Omega_*/d\Omega_\odot = 3$ and $D = 450$ km^{2}s^{-1}. *Please note that the errors in the y coordinate of the flux rope axis (which are required to determine the chi-squared) are taken to be the grid spacing in the y direction (h_y).*

- Using PILfinder, the time the flux rope begins to lift off from the photosphere may be determined. This may be done by measuring the evolution of the length of the region with shear angle greater than 90° with time (e.g. see Figure 6.13). An indication of the onset of an eruption is when this region begins to shrink, or disappears altogether. Alternatively, by considering the evolution of the mean/median/maximum shear angle along the PIL with time, the onset of the eruption may be inferred from when

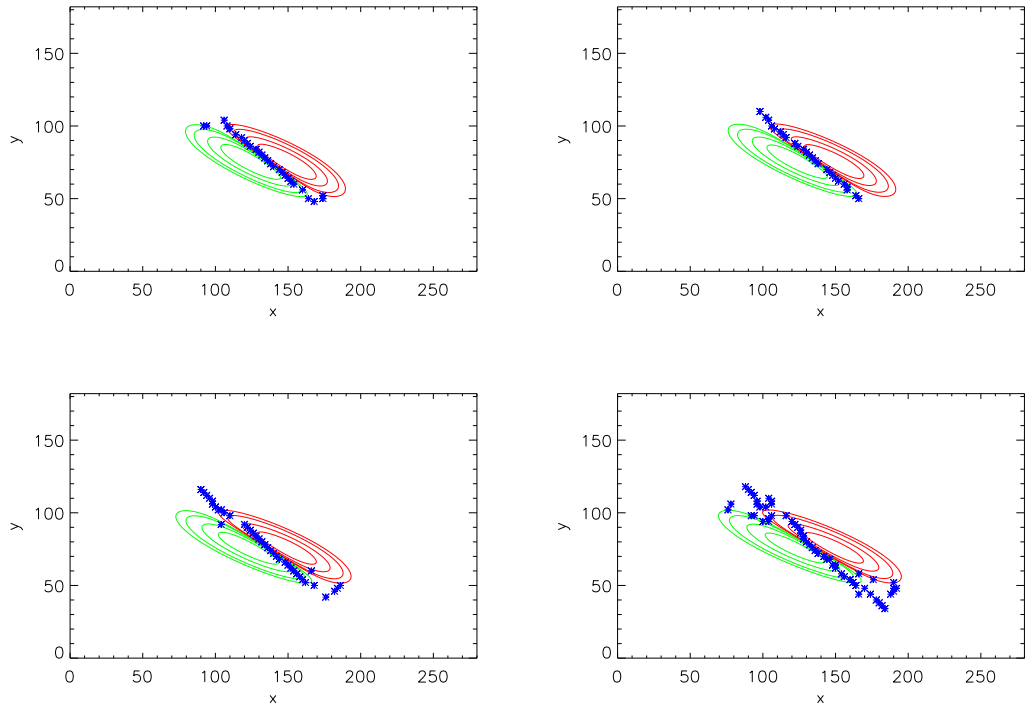

Figure 6.11: The points belonging to the flux rope axis as determined by FRfinder (blue crosses) for days 13 (top left) 14 (top right) 15 (bottom left) and 16 (bottom right) in the simulation with $d\Omega_*/d\Omega_\odot = 3$ and $D = 450$ km^{2}s^{-1}. Note that whilst on days 13 and 14 the flux rope axis is well described by a straight line, on days 15 and 16 the flux rope axis begins to deviate from a straight line.

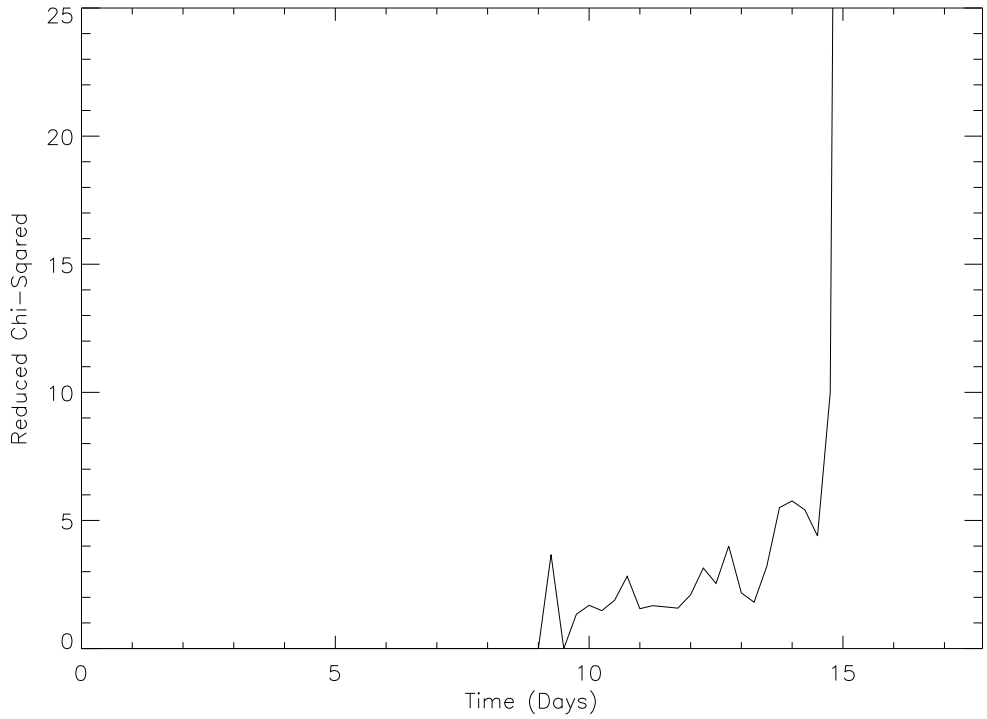

Figure 6.12: The evolution of the reduced chi-squared (of the flux rope axis points to a straight line) with time for the simulation with $d\Omega_*/d\Omega_\odot = 3$ and $D = 450$ km^{2}s^{-1}. Note that the reduced chi-squared increases sharply between days 13 and 15. Although not shown on the graph, the reduced chi-squared reaches a value of 250 on day 16.

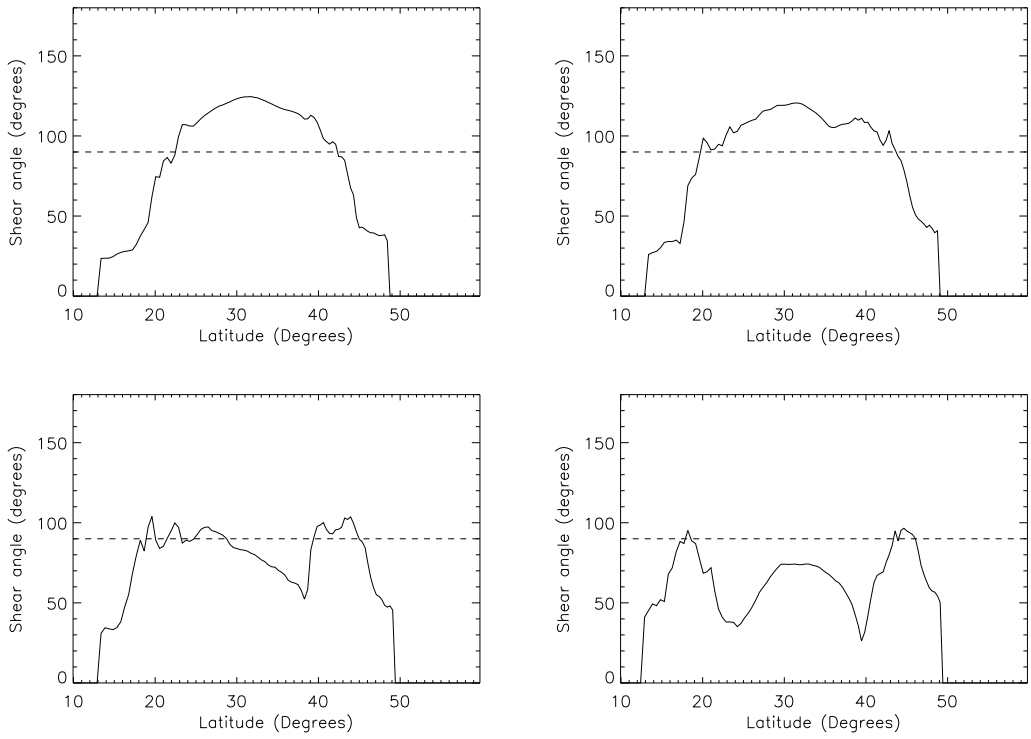

Figure 6.13: The evolution of the shear angle along the PIL with latitude for days 13 (top left) 14 (top right) 15 (bottom left) and 16 (bottom right) in the simulation with $d\Omega_*/d\Omega_\odot = 3$ and $D = 450$ km^{2}s^{-1}. The horizontal dashed line highlights a shear angle of 90°. Note that on days 13 and 14 a large region along of the PIL has a shear angle greater than 90°, corresponding to a flux rope above the PIL at this point. On days 15 and 16 the shear angle is $< 90°$ along most of the PIL, implying the majority of the flux rope has lifted off from the PIL.

the mean/median/maximum shear angle begins to decrease (e.g. see Figure 6.14).

Figures 6.9 to 6.14 display the graphs for the above methods of determining the eruption times for the simulation with $d\Omega_*/d\Omega_\odot = 3$ and $D = 450$ km^{2}s^{-1}. Figure 6.15 displays field line plots highlighting the flux rope on days 13-16. Using all the methods combined, the figures suggest an eruption time of around 13-15 days for this simulation. The eruption time is taken to be 14 ± 1 days. The same analysis is applied for every simulation. Generally, the times derived from each method agree with each other to within two days for low differential rotation stars ($d\Omega_*/d\Omega_\odot < 3$), and within 0.5 days for high differential rotation stars ($d\Omega_*/d\Omega_\odot > 3$).

Figure 6.16 displays the evolution of the flux rope's lifetime as a function of differential rotation scaling for the four surface diffusion coefficients investigated. From the plots, it can be seen that for all surface diffusion coefficients investigated the lifetime is inversely proportional to the differential rotation scaling. We find that for stars with differential rotation rates greater than approximately three times the solar value (lap times less than 32 days - highlighted by a vertical dotted line in Figure 6.16) the lifetime is independent of the surface diffusion. This may be interpreted as the lifetime being solely dependent upon the shearing caused by the differential rotation. In order to demonstrate this, we may consider the shear timescale. We define this as the time required for the differential

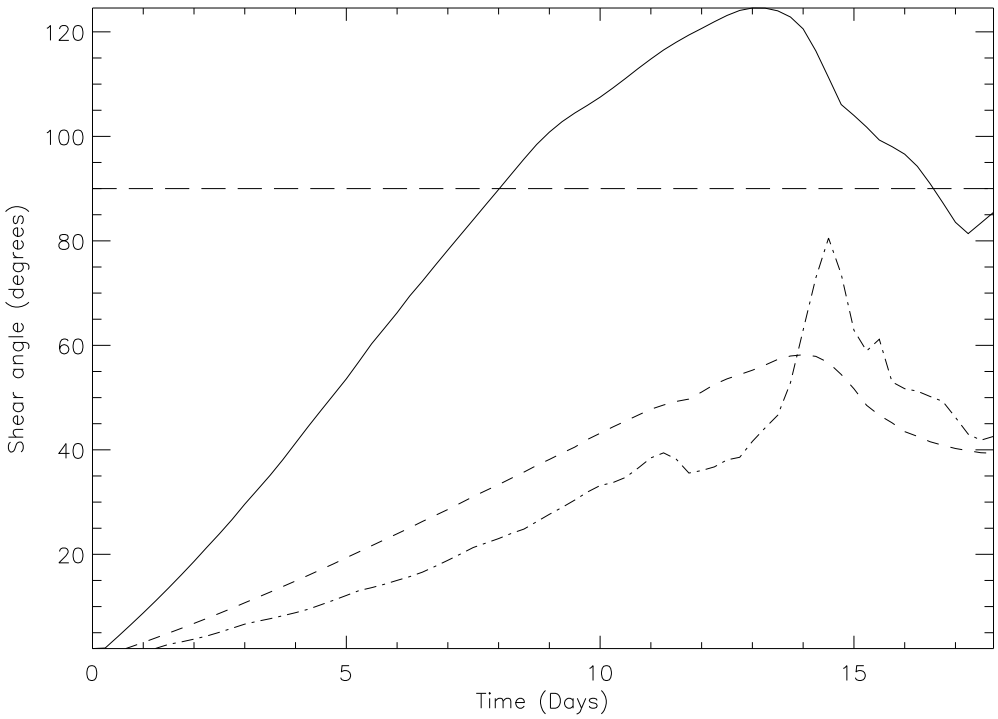

Figure 6.14: The evolution of the maximum (solid line) mean (dashed line) and median (dotted line) shear angle across the PIL as a function of time for the simulation with $d\Omega_*/d\Omega_\odot = 3$ and $D = 450$ km^{2}s^{-1}. Note that the maximum, mean and median shear angles both have a maximum around days 13-15.

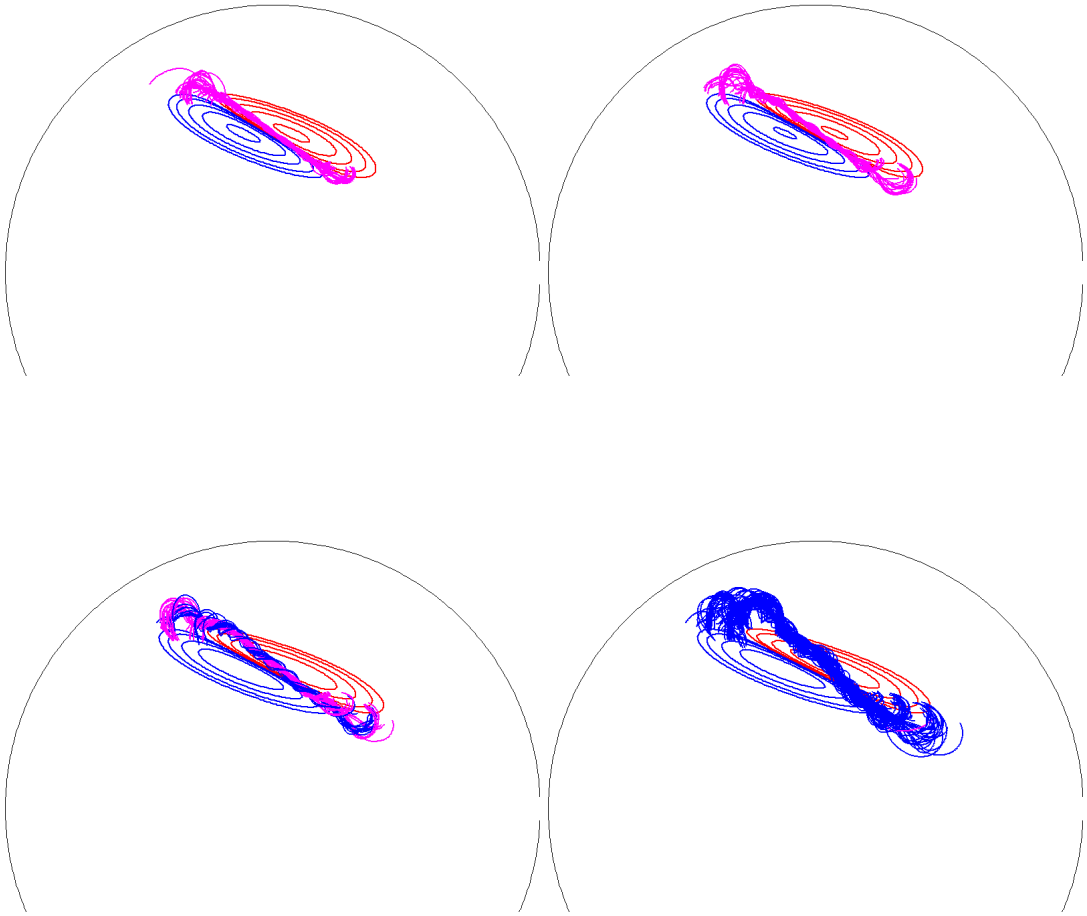

Figure 6.15: Field line plots highlighting the flux rope for days 13 (top left) 14 (top right) 15 (bottom left) and 16 (bottom right) in the simulation with $d\Omega_*/d\Omega_\odot = 3$ and $D = 450$ km^{2}s^{-1}. On days 15 and 16 it can be seen that the flux rope has lifted off from the photosphere and has begun to rise.

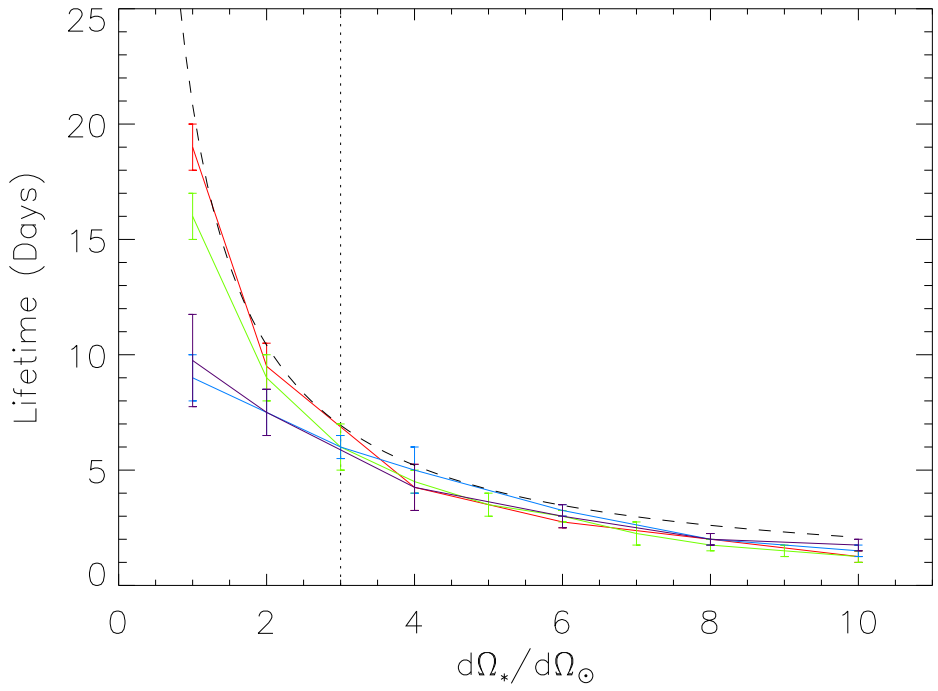

Figure 6.16: Flux rope lifetime as a function differential rotation for diffusion constants of 250 km^2s^{-1} (red), 450 km^2s^{-1} (green), 900 km^2s^{-1} (blue) and 1800 km^2s^{-1} (purple). The dashed line is the shear timescale (Equation 6.38).

rotation to re-orient a PIL initially aligned in the north-south direction to an angle of 45° from the north-south line.

To calculate this timescale, consider a PIL initially oriented in the north-south direction. Take two points along the PIL, one at co-latitude θ_1 and one at co-latitude $\theta_1 + \delta\theta$, where $\delta\theta \ll \theta_1$. The longitude of a point belonging to the PIL as a function of time is

$$\phi(\theta, t) = \Omega(\theta)t. \tag{6.33}$$

The PIL will have reached an angle of 45° with the north-south direction when

$$R[\phi(\theta_1 + \delta\theta, t) - \phi(\theta_1, t)] \sin\theta_1 = R\delta\phi \sin\theta_1 = R\delta\theta. \tag{6.34}$$

(see Figure 6.17). Taking a Taylor expansion of $\Omega(\theta)$ (Equation 6.8) about θ_1 we get

$$\Omega(\theta_1 + \delta\theta) = \Omega(\theta_1) + \delta\theta \left.\frac{\partial\Omega}{\partial\theta}\right|_{\theta_1}. \tag{6.35}$$

Substituting Equations 6.33 and 6.35 into Equation 6.34,

$$\delta\theta \frac{\partial\Omega}{\partial\theta} t = \frac{\delta\theta}{\sin\theta_1}, \tag{6.36}$$

and therefore we find the shear timescale to be

$$\tau_{\text{Shear}} = \frac{1}{\frac{\partial\Omega}{\partial\theta}\sin\theta_1} = \frac{1}{Kd\Omega_\odot \sin^2\theta_1 \cos\theta_1}. \tag{6.37}$$

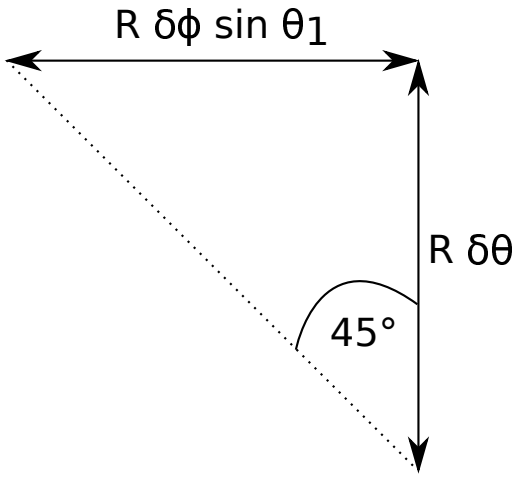

Figure 6.17: A graphic explaining the derivation of the shear timescale (Equation 6.37). The PIL (dotted line) reaches an angle of 45° to the north-south line when the poloidal displacement ($R\delta\theta$) is equal to the toroidal displacement ($R\delta\phi \sin\theta_1$).

For a latitude of 30° the shear timescale is

$$\tau_{\text{Shear}} = 20.93 \frac{d\Omega_\odot}{d\Omega_*} \text{ days}, \tag{6.38}$$

and is represented in Figure 6.16 by the black dashed curve. It can be seen that the curves for all four diffusion constants investigated are situated below the shear timescale's curve, but generally follow it. For differential rotation scalings lower than three (lap times greater than 32 days) we find that the lifetime is dependent on the surface diffusion. In this regime, higher surface diffusion decreases the lifetime. Taking the length scale for diffusion to be three grid cells at 30° latitude (the minimum diameter a flux rope must possess to be resolved in the simulation) the diffusion timescale is

$$\tau_{\text{Diff}} \approx \frac{L^2}{D} = \left(\frac{450 \text{ km}^2\text{s}^{-1}}{D} \right) 6.34 \text{ days}. \tag{6.39}$$

For $d\Omega_*/d\Omega_\odot < 3$ the diffusion timescale for larger surface diffusion constants is much shorter than the shear timescale. We interpret the decrease in the lifetime in this regime to be due to the stronger surface diffusion acting to weaken the arcade above the flux rope, reducing its ability to counter the upwards force from the flux rope with its downwards tension force.

We now summarise the above findings. The lifetime of the flux rope is proportional to the shear timescale, which itself is proportional to the lap time. Thus

$$\tau_{\text{Life}} \approx \tau_{\text{Shear}} \propto \tau_{\text{Lap}}. \tag{6.40}$$

The above relation holds unless $\tau_{\text{Shear}} \gg \tau_{\text{Diff}}$, whereby the enhanced surface diffusion decreases the lifetime such that

$$\tau_{\text{Life}} < \tau_{\text{Shear}}. \tag{6.41}$$

6.3.3 Effects of the Meridional Flow

Whilst the effects of varying the meridional flow have not been investigated through simulation, from the results in the previous sections it is possible to infer the effects that the

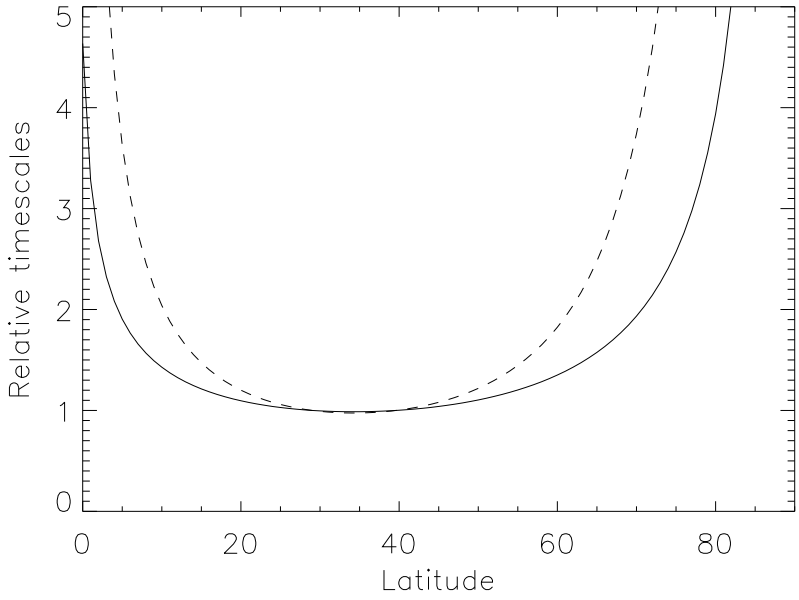

Figure 6.18: The formation time (solid line) and lifetime (dashed line) as a function of latitude relative to the the formation/life times at 30° latitude.

meridional flow would have on the formation and lifetime of flux ropes. The meridional flow acts to transport magnetic flux towards the poles. As the differential rotation is a function of latitude, a bipole experiences a different amount of shear due to the differential rotation as it is carried northwards by the meridional flow. The shear induced by the differential rotation is

$$\sin\theta \frac{d\Omega(\theta)}{d\theta} = 2d\Omega_* \sin^2\theta\cos\theta = 2Kd\Omega_\odot \sin^2\theta\cos\theta, \tag{6.42}$$

and its maximum occurs at ±35.26° latitude. Noting that the shear timescale (Equation 6.37) is the reciprocal of the shear, and that the formation time is roughly proportional to the square root of the shear timescale, we can express the lifetime and formation times of flux ropes as a function of latitude. This is displayed in Figure 6.18. It can be seen that though the maximum shear (minimum formation time and lifetime) occurs at 35.26° latitude, in the approximate range of 20° to 50° latitude the formation times and lifetimes are roughly independent of latitude.

In order for the formation time of a flux rope to be significantly affected by the meridional flow, it must be transported northward – away from the strong shear – in a timescale less than or equal to its formation time at 30° latitude. Upon inspection of Figure 6.18, for the formation time to be twice the value it is at 30° latitude – the initial latitude of the bipoles in the simulations – a bipole would have to be situated at roughly 70° latitude. On the Sun, with $v_{\rm merid} = 15{\rm m\ s}^{-1}$, it would take approximately a year to transport a bipole from 30° to 70° latitude. This is much longer than any formation time found in our simulations. Indeed, in the simulation with the greatest formation time (21 days) the meridional flow would have only transported the bipole 2° northwards in this time. On a star with ten times the meridional flow of the Sun, in 21 days a bipole could be transported 20° northwards. However even at this higher latitude, the formation time is only fractionally higher than it is at 30°. In order to at most double the formation time of the

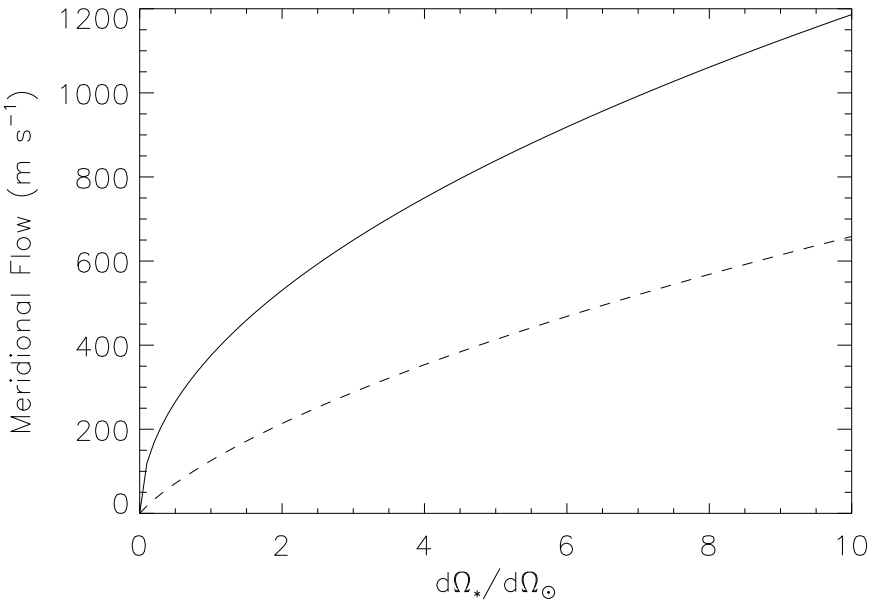

Figure 6.19: The minimum meridional flow velocity required to significantly lengthen (approximately double) the formation time (solid line) and lifetime (dashed line) of a flux rope as a function of differential rotation. As can be seen, for solar differential rotation the meridional velocity must be at least $\geq$ 250 m s^{-1} in order to significantly lengthen the formation time, and $\geq$ 150 m s^{-1} to significantly lengthen the lifetime. For stars with enhanced surface differential rotation, the meridional velocity has to be even faster.

slowest forming flux rope in our simulations, the meridional flow must be able to transport the bipole 40° north (to 70° latitude) in 21 days. This would require a meridional flow of 270m s^{-1}. It is important to note that this case is for the longest formation time (at 30° latitude) that we obtained in our simulations. For stars with shorter formation timescales, the meridional flow would have to be even faster in order for it to have a significant effect on the formation of flux ropes.

Let us now consider the lifetimes of the flux ropes. For the meridional flow to have a significant effect on the lifetime of a flux rope it must be transported northward away from the strong shear in a timescale less than or equal to the eruption time – the sum of the formation time and lifetime – evaluated at 30° latitude. Upon inspection of Figure 6.18, for the lifetime to be twice the value it is at 30° latitude, a flux rope would have to be situated at roughly 62° latitude. On the Sun it would take approximately 300 days to transport a bipole from 30° to 62° latitude. This is much longer than the longest eruption time (40 days) in the simulations. If the meridional flow were $\geq$ 110m s^{-1} then a flux rope would be able to be transported to 62° in this time.

Figure 6.19 summarises the above findings. It plots the minimum meridional flow velocity required to roughly double the formation time (solid line) and lifetime (dashed line) as a function of stellar differential rotation. The plot is made assuming a surface diffusion of 450 km^{2}s^{-1}. For stars with solar differential rotation, it is clear that large meridional velocities (at least ten times the solar meridional velocity) are required in order for the meridional flow to have a significant effect on the lifetimes of flux ropes. Unless the meridional velocity is very large ($\geq$ 300 m s^{-1}) the meridional flow is unlikely to have a

significant effect on the formation of flux ropes. On stars with stronger differential rotation than the Sun, the meridional velocity must be even greater to affect the formation and lifetimes. In conclusion, the meridional flow has a negligible effect on the formation and lifetimes of flux ropes on high differential rotation stars. For low differential rotation stars, the meridional flow can have an effect on the lifetimes of flux ropes provided that it much faster than it is on the Sun.

6.3.4 Tilt Angle

In the previous subsections of Section 6.3 we have considered bipoles with initial tilt angles of 0°. We now investigate the effect that changing the initial tilt angle has on the formation of flux ropes. To achieve this, we ran a set of simulations with $d\Omega_*/d\Omega_\odot = 2$ and $D = 450$ km^{2}s^{-1} but varying the tilt angle between 0° and +90°. The range of tilt angles chosen are consistent with Joy's law, i.e. the leading polarity is closer to the equator than the following polarity. Figure 6.20 displays the evolution of the formation time as a function of tilt angle as determined from the simulations. Also included in Figure 6.20 is an indication of the length of the flux rope formed, represented by the size of the plot symbols used. For tilt angles less than approximately 30° the tilt angle has little effect on the formation time, save for a slight increase with increasing tilt angle. The length of the flux rope is found to slightly decrease as the tilt angle is increased. For tilt angles greater than 30° the formation time increases sharply and the flux rope's length decreases slightly with increasing tilt angle until a tilt angle of approximately 60-75°. These effects are caused by the initial bipole tilt angle effectively shortening the length of region where flux cancellation may occur to form the flux rope (region between dotted lines in Figure 6.21), as the differential rotation acts to draw the northern edge of the negative polarity region, and the southern edge of the positive polarity region away from the polarity inversion line (arrows in Figure 6.21). This results in a flux rope that forms more slowly as diffusion is less able to bring opposite polarity fields together for cancellation. For tilt angles above 60-75° and up to 90° the formation time decreases and approaches the formation time for a bipole with initial tilt angle of 0°. The length of the flux rope remains short, however. This behaviour is different to the behaviour exhibited for tilt angles of less than 60-75°. We attribute this to the tilt angle being sufficiently large that the differential rotation acts to slide the two polarities past each other, resulting in a more efficient shearing of the field. This efficient shearing allows the flux rope to form relatively quickly, however the resultant flux rope is short as the polarities sliding past each other shorten the length of the region where the flux cancellation, and hence flux rope formation may occur. The flux rope formation mechanism for high initial tilt angles is somewhat different to the formation mechanism for tilt angles less than 60-75° as the shear is driven by the polarities sliding past each other, rather than deformation of the active region by the differential rotation.

6.4 Discussion

In this study we have considered the effects of differential rotation and surface diffusion on the formation and stability of flux ropes formed in a decaying active region. In order to do this we ran a series of simulations with different surface diffusion coefficients and differential rotation scalings. The simulations consisted of a surface flux transport model to prescribe the evolution of the photospheric magnetic field, coupled with a magnetofrictional technique to determine the evolution of the coronal magnetic field due to the evolving photospheric field.

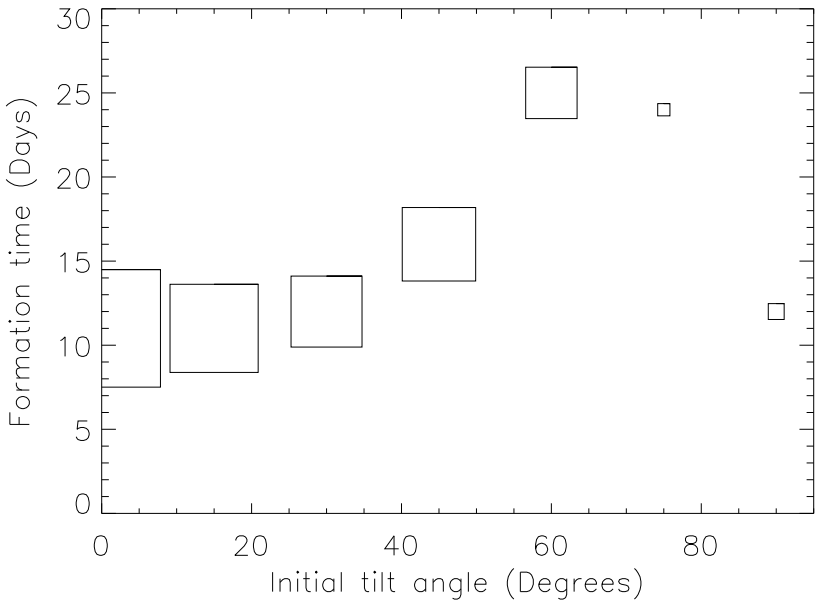

Figure 6.20: Evolution of flux rope formation timescale as a function of initial bipole tilt angle. The symbol size is proportional to the maximum length of the flux rope formed, with the largest and smallest symbols corresponding to flux rope lengths of 48° and 5° respectively.

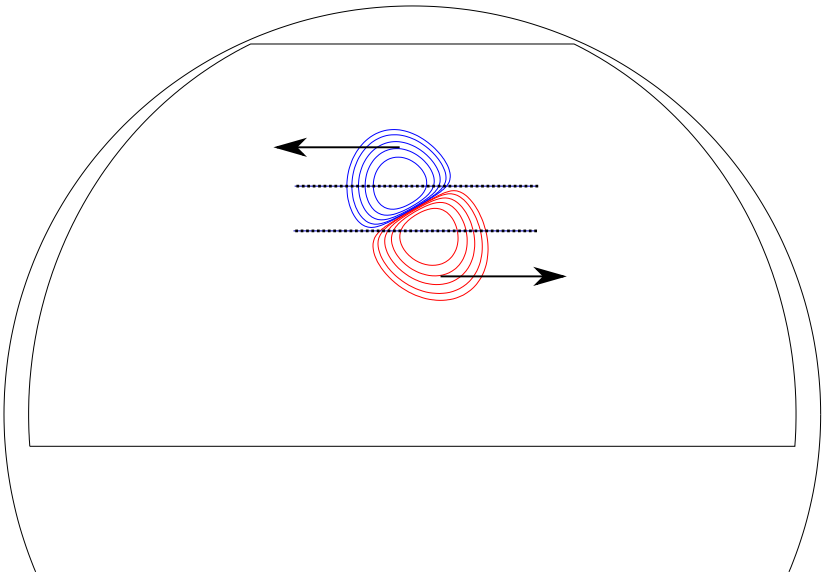

Figure 6.21: Initial condition bipole with tilt angle of 60°. The region between the dotted lines indicates where a flux rope will form at a later time. The arrows denote the direction the differential rotation advects the surface flux relative to the centre of the bipole.

We found that the formation timescale of a flux rope is approximately proportional to the geometric mean of the equator-pole lap time and the surface diffusion timescale. The lifetimes of the flux ropes are strongly dependent upon the shearing of the coronal field due to differential rotation. We find that the lifetimes are approximately equal to the shear timescale (Eqn 6.38), unless the diffusion timescale is much shorter than the shear timescale, whereby the lifetime is decreased. We interpret this shortened lifetime as being due to the enhanced diffusion adding more flux to the flux rope and weakening the arcade field that holds down the flux rope below it.

The meridional flow, which acts to transport surface magnetic flux polewards, has a negligible effect on the formation and lifetime of flux ropes. The exception to this is when the differential rotation is relatively low ($d\Omega_*/d\Omega_\odot \approx 1$) and the meridional flow is at least a factor of ten greater than the solar value. In this case, the lifetime of flux ropes may be lengthened as the meridional flow is able to transport the flux rope northward away from the strong surface shear induced by differential rotation. The meridional flow can only lengthen the formation time if it is on the order of twenty times the solar value.

Flux ropes formed from active regions with tilt angles ranging from 0-30° have similar formation times and lengths. For tilt angles above this the lengths of the flux ropes decrease with increasing tilt angle. For tilt angles between 30° and 60-75° the formation times increase due to a decreased efficiency of diffusion bringing opposite polarity field in to be cancelled. Between 60-75° and 90° the formation time decreases with increasing tilt angle. This is because the increasing tilt results in a more east-west aligned polarity inversion line, which maximises the efficiency of differential rotation to shear the field across it.

Using the results of Collier Cameron (2007), who find that the differential rotation of a star is proportional to its effective temperature according to the power law

$$d\Omega_* = 3.03\left(\frac{T_{\rm eff}}{5130\ {\rm K}}\right)^{8.6}\ {\rm deg\ day}^{-1}, \tag{6.43}$$

we may express our results from Sections 6.3.1 and 6.3.2 in terms of the stellar effective temperature. Figure 6.22 displays the formation time and lifetimes of flux ropes as a function of stellar effective temperature, with $D = 450\ {\rm km^2 s^{-1}}$. It can be seen that by increasing the stellar effective temperature from 5000 K to 7000 K the formation time for the flux rope decreases by a factor of ~ 5 and the lifetime decreases by a factor of ~ 18. This strongly implies that as we move up the main sequence, the evolution timescales of stellar coronae decrease dramatically. It is important to note that Barnes et al. (2005) and Küker & Rüdiger (2011) find a different scaling between the differential rotation and effective temperature of stars. Whilst the scalings differ quantitatively, qualitatively they are similar, insofar that as the stellar effective temperature increases the differential rotation increases.

The lifetimes of flux ropes on stars with high differential rotation are considerably shorter than on the Sun. For stars with differential rotation rates greater than four times the solar value, the lifetimes are less than five days. Similarly, for stars with differential rotation greater than eight times the solar value, the lifetime is found to be two days or fewer. For such high differential rotation stars, where the lifetime of flux ropes is likely to be less than a few days, we propose that prominences are unlikely to be observed as they are only present on the star for a very short period of time. Once a flux rope has formed, a finite amount of time is required for its magnetic dips to be populated with a sufficient amount of cool plasma for the prominence to be visible. Due to the time required to fill the flux rope with prominence plasma, the prominence may well be present on the star for

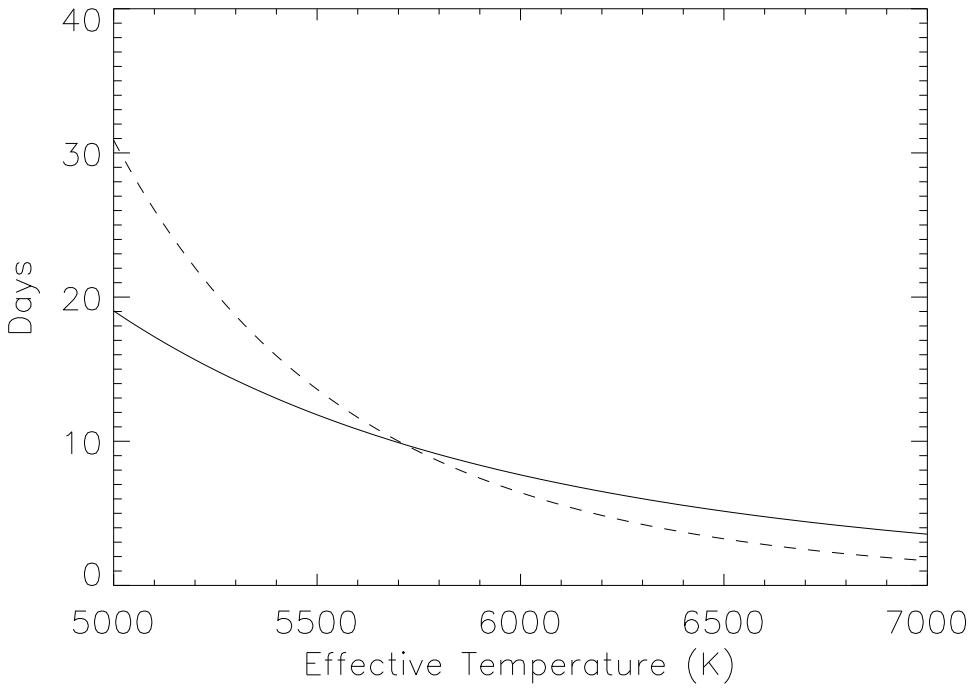

Figure 6.22: Formation time (solid line) and lifetime (dashed line) as a function of stellar effective temperature for a surface diffusion coefficient of 450 km^2s^{-1}.

a shorter period of time than the flux rope's lifetime. Therefore the lifetime we calculate is the maximum amount of time that the prominence may be visible for.

On stars with high differential rotation, the formation times and lifetimes of flux ropes are significantly shorter than they are on the Sun. We propose that such high differential rotation stars will have far more dynamic coronae, with magnetic structures evolving on much shorter timescales. In each simulation, a series of flux ropes were formed then ejected. On high differential rotation stars, the frequency of eruptions thus may be higher than on low differential rotation stars. An increase in the eruption frequency could result in an increased mass and angular momentum loss from the star. For a star with a high meridional flow, which is able to transport an active region to high latitudes in a timescale comparable to the eruption time, CMEs from erupting flux ropes may not make a significant contribution on the angular momentum loss from the star as the material will be ejected from a radius close to the star's angular momentum axis, and will therefore not contain much angular momentum. Such high-latitude eruptions would also be unlikely to have an impact on the magnetospheres of planets orbiting in the star's equatorial plane as the CMEs will be launched out of the equatorial plane.

It is important to note that in the present study we have modelled the decay and shearing of a single, isolated, bipolar active region. No external coronal fields have been included, such as those from other active regions or polar field. Polar field may play a very important role on such stars, as many ZDI observations of stars show polar spots and strong fields (Donati & Collier Cameron 1997, Donati et al. 1999, 2003). The interaction of the active region's magnetic field with an external coronal field may have a significant effect on the formation and stability of the flux rope. In the following chapter, the work in this chapter is expanded to global simulations of a stellar corona with multiple, interacting

active regions. Namely the coronal response to differential rotation and flux emergence is investigated.

It has long been known that on the Sun active regions tend to possess shear even at the time of emergence (Leka et al. 1996), with active regions in the northern/southern hemisphere generally containing negative/positive magnetic helicity (Pevtsov et al. 1995). In the present study, however, we use a potential field initial condition which possesses no shear. In our simulations, it will therefore take longer to form a flux rope from the potential bipole than for the case with an initially sheared bipole. Whilst the flux rope formation time will be decreased for an initially sheared bipole compared to a potential bipole, we believe that the scaling found in this study will remain the same, namely $\tau_{\rm Form} \propto \sqrt{\tau_{\rm Lap}\tau_{\rm Diff}}$. The lifetime, which is determined by the amount of shear being applied to the flux rope by the differential rotation, should remain unchanged. In the following chapter, bipoles with an initial shear are included in the modelling.

We finally summarise the main findings of this chapter:

- We find the formation time of a flux rope scales with the differential rotation lap time and surface diffusion timescale as $\tau_{\rm Form} \propto \sqrt{\tau_{\rm Lap}\tau_{\rm Diff}}$
- The lifetime of a flux rope scales with the shearing timescale as $\tau_{\rm Life} \approx \tau_{\rm Shear} \propto \tau_{\rm Lap}$
- For stars with very high differential rotation the lifetime of flux ropes becomes increasingly short. We propose that prominences may be difficult to observe on such stars as they will only be present for a short time.

Chapter 7

Global Long-Term Simulations of Stellar Coronae: Investigating the Effects of Flux Emergence and Differential Rotation

7.1 Introduction

In Chapter 6 we considered the formation timescale and lifetime of flux ropes on stars, in response to the flux transport effects of differential rotation and surface diffusion. The flux ropes were formed in a single isolated magnetic bipole. Whilst this simple flux distribution is ideal to gain a basic understanding into the processes involved, on a global scale it is not realistic. On the Sun, bipoles are rarely isolated and frequently emerge in groups and interact with each other. Therefore, in order to gain a deeper insight into stellar coronal dynamics, it is desirable to include a more complex photospheric field distribution than that used in Chapter 6.

For a star with solar differential rotation, it was found that the formation time and lifetime of a flux rope was 15 and 16 days respectively. It therefore took approximately one month for a flux rope to form and then erupt. On the Sun, new magnetic flux emerges from the solar interior into the corona. As such the photospheric magnetic field evolution is not just driven through surface flux transport, but includes the emergence of new bipoles. In order to simulate the corona over a long period of time (months to years) flux emergence must be included in the model.

In this chapter we build upon the work of Chapter 6 and carry out long-term global simulations of stellar coronae. These simulations include flux emergence, in addition to differential rotation, meridional flow and surface diffusion. The inclusion of flux emergence allows us to run the simulations for a long period of time (1 year) and therefore study the steady state properties of stellar coronae. In particular, we investigate the effects of the rate of flux emergence and differential rotation on the spatial distribution of flux ropes, the open magnetic flux and the free magnetic energy. We also speculate upon the coronal X-ray luminosity.

This chapter is structured as follows. In Section 7.2 we describe the construction of the bipole emergence model employed in this chapter. In Section 7.3 we outline the flux transport and coronal evolution models. In Sections 7.4 and 7.5 we present the effects of varying the flux emergence and differential rotation rates on the corona. Finally, in Section

7.6 we discuss the results of the chapter. This chapter presents a preliminary discussion of the results, which will be considered in more detail at a later date.

7.2 Flux Emergence Profile

At the present time stellar flux emergence profiles are not known, however, the nature of stellar emergence profiles has been speculated (Mackay et al. 2004) and methods have been developed that may be able to constrain them (Llama et al. 2012). As there is very little information available on the flux emergence profiles on stars, we base our stellar flux emergence profile on the well known solar flux emergence profile. On the Sun the flux emergence profile is time dependent. The butterfly diagram (see Figure 1.3) is a manifestation of this time dependence. Although stellar cycles have been observed (Wilson 1978, Donati et al. 2008, Fares et al. 2009), in this chapter we are interested in the steady state corona, and so we wish to construct a flux emergence profile whose parameters do not vary significantly in time. In other words, we wish to simulate a time period sufficiently shorter than the stellar cycle's period so that the emergence profile's parameters are nearly independent with time.

To construct our flux emergence profile, we consider the emergence of flux on the Sun between January 2000 and January 2001. During this time the distribution of the properties of emerged flux is approximately time-independent. We use the properties of flux that was determined to have emerged during this time period by Yeates (2014). The properties are derived from synoptic magnetograms of the Sun, and determine the locations of newly emerged flux. The newly emerged flux regions were approximated to be bipoles, whose fluxes, latitudes, longitudes, tilt angles, emergence times and half separations were chosen to best represent the observed emerged flux. For further details on how these values were obtained, see Yeates et al. (2007) and Chapter 5 of this Thesis. In the year between January 2000 and January 2001, Yeates (2014) determined that 227 bipoles had emerged. In this section, we describe the development of a bipole emergence model that is able to reproduce the distribution of the bipoles as found by Yeates (2014). We chose to develop a model rather than just reuse the values obtained by Yeates (2014) so that we can vary the parameters of the model to change the flux emergence rate. In addition to the above mentioned properties (latitude, longitude, flux, tilt angle and half separation), we can also specify the parameter, beta, (see Yeates et al. (2010) for details) which is a measure of the twist of a bipole's coronal magnetic field.

7.2.1 Observed Solar Profile

In this Section we consider the properties of the bipoles determined by Yeates (2014) between January 2000 and January 2001. Figures 7.1, 7.2 and 7.3 display scatter plots of all the bipoles' properties against each other. Using these scatter plots, we can determine a series of empirical relations between the different properties, allowing us to develop a bipole emergence model.

First, let us consider the relationships between the bipoles' flux, tilt angle, separation and beta against the latitude of emergence. Upon inspection of the scatter plot of flux against latitude (top left panel of Figure 7.1), it is clear that in the vast majority of cases, the flux is negative in the northern hemisphere, and positive in the southern hemisphere. The sign of the flux denotes the sign of the trailing polarity in the bipole, and thus denotes Hale's law (Hale et al. 1919). There are 6 exceptions which do not obey Hale's law. This corresponds to 2.64% of all the bipoles. Now, let us consider the relationship between the

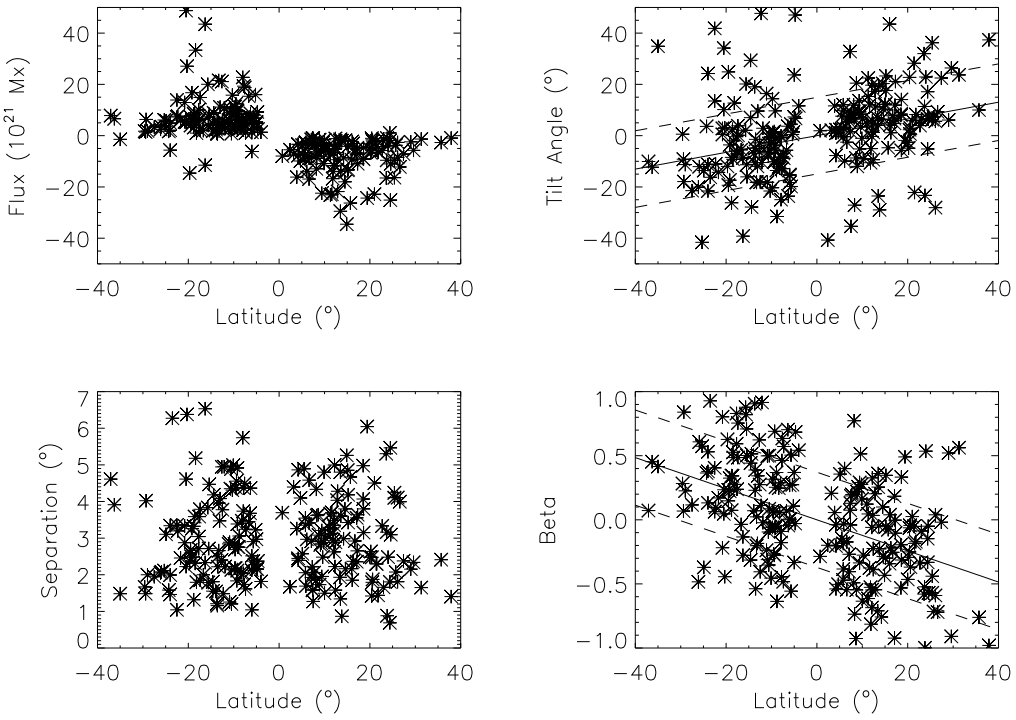

Figure 7.1: Scatter plots of the observed bipoles' flux (top left), tilt angle (top right), separation (bottom left) and beta (bottom right) against the latitude of emergence.

tilt angle and the latitude of emergence (top right panel of Figure 7.1). Upon inspection, a slight trend is visible, where the tilt angle is proportional to the latitude of emergence, however there is a great deal of scatter. We fit a scaling relation of the form

$$\gamma \propto m\lambda \tag{7.1}$$

where γ is the tilt angle, λ is the latitude and m is a scaling constant. We find that m is equal to 0.32. The standard deviation of the data about this scaling relation is 14.93°. The scaling relation and standard deviation are denoted by the solid and dashed lines in the top right panel of Figure 7.1 respectively. Upon inspecting the scatter plot of the separation against the latitude (bottom left panel of Figure 7.1) no apparent relation is present. The separation and latitude appear to be uncorrelated. Finally, upon considering the scatter plot between beta and the latitude (bottom right panel of Figure 7.1) beta and latitude appear to be anti-correlated. We fit the scaling relation

$$\beta \propto m\lambda \tag{7.2}$$

to the data and find that $m = -0.012$. The standard deviation from the scaling relationship is 0.37. The scaling relation and standard deviation are denoted by the solid and dashed lines in the bottom right panel of Figure 7.1 respectively.

Now let us consider the relations between the tilt angle, beta and separation against the flux. The tilt angle appears to be anti-correlated with the flux (top left panel of Figure 7.2). This is unsurprising given that the tilt angle is correlated with the latitude, which is anticorrelated with the flux. We fit a scaling relation of the form

$$\gamma \propto m\Phi \tag{7.3}$$

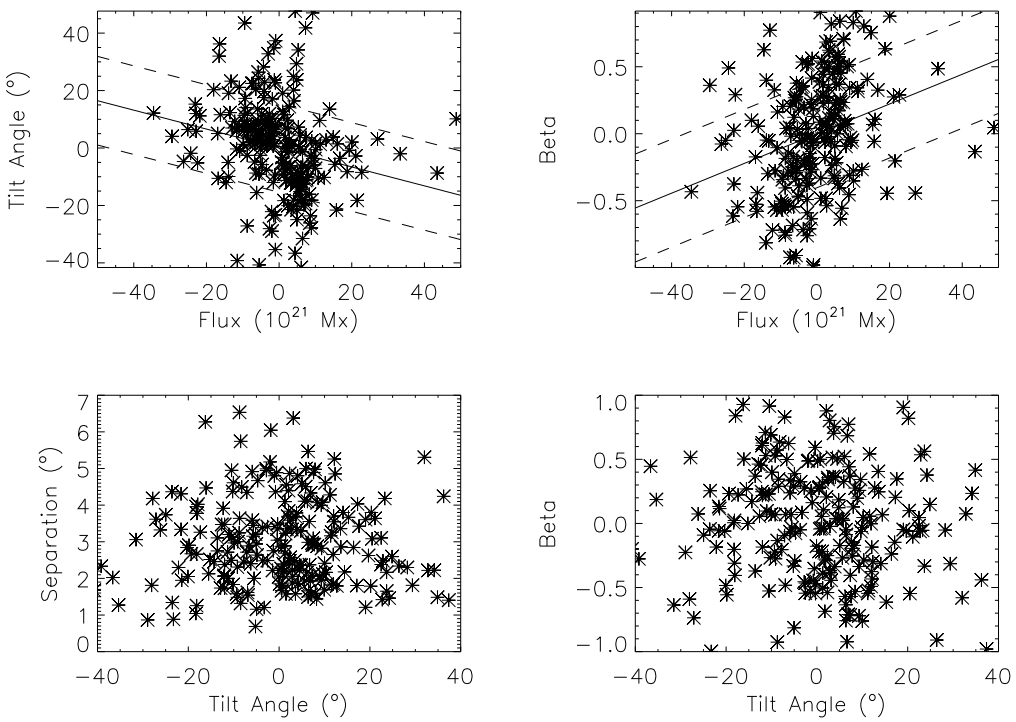

Figure 7.2: Scatter plots of the observed bipoles' tilt angle (top left) and beta (top right) against their flux and the separation (bottom left) and beta (bottom right) against tilt angle.

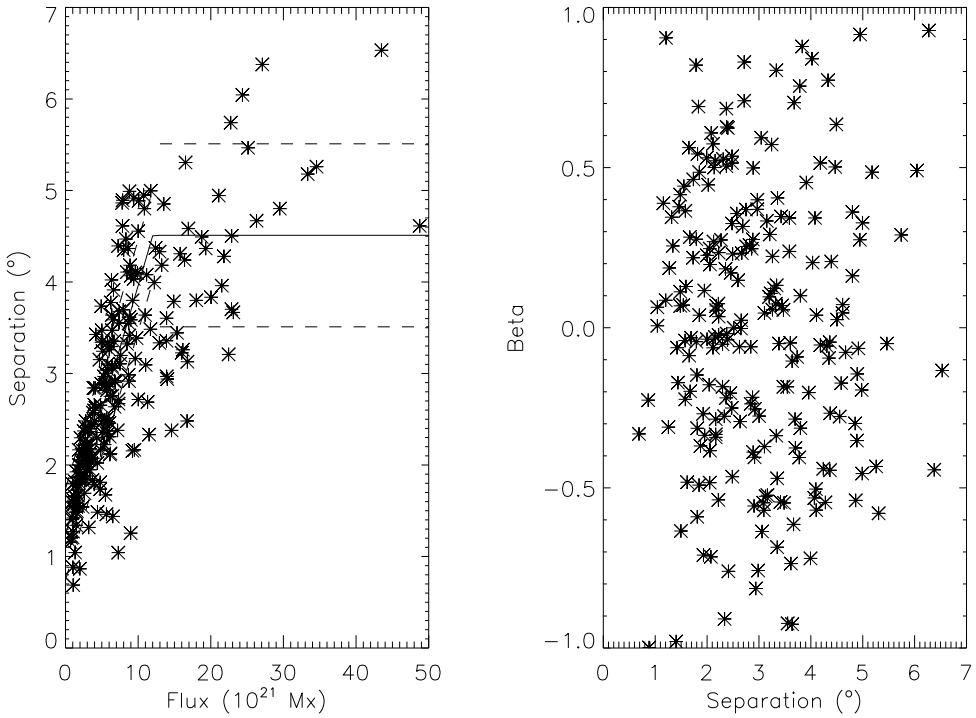

Figure 7.3: Scatter plots of the observed bipoles' separation against flux (left) and the beta against separation (right).

where Φ is the flux in 10^{21} Mx. We find $m = -0.32$ and the standard deviation from the scaling relation is 15°. The scaling relation and standard deviation are denoted by the solid and dashed lines in the top left panel of Figure 7.2 respectively. The beta and the flux appear to be correlated (top right panel of Figure 7.2). Once again, this is unsurprising as the beta is anticorrelated with latitude, which is anticorrelated with the flux. We fit a scaling relation of the form

$$\beta \propto m\Phi \tag{7.4}$$

where Φ is the flux. We find $m = 0.011$ and the standard deviation from the scaling relation is 0.4. The scaling relation and standard deviation are denoted by the solid and dashed lines in the top right panel of Figure 7.2 respectively. We note that although we determine the scaling relations between the tilt angle and the flux, and the beta and the flux, we do not use them to construct the bipole emergence model as the relations do not look very well constrained. Instead, we use the latitude of emergence to specify the tilt angle and the beta.

Upon considering the scatter plot between the flux and separation (left panel of Figure 7.3) it is clear that the flux and separation are tightly correlated. Up to a flux of $\sim 10^{22}$ Mx the separation appears to be linearly dependent upon the flux. Beyond this there is a less apparent correlation. We approximate this relation by the piecewise function

$$\rho = \begin{cases} 1.24 + 0.272\Phi \pm 0.5 & 0 < \Phi \leq 12 \times 10^{21} \text{ Mx} \\ 4.51 \pm 1 & \Phi > 12 \times 10^{21} \text{ Mx} \end{cases} \tag{7.5}$$

Where the number after the $\pm$ denotes the standard deviation. This model is shown by the solid and dashed lines in the left panel of Figure 7.3.

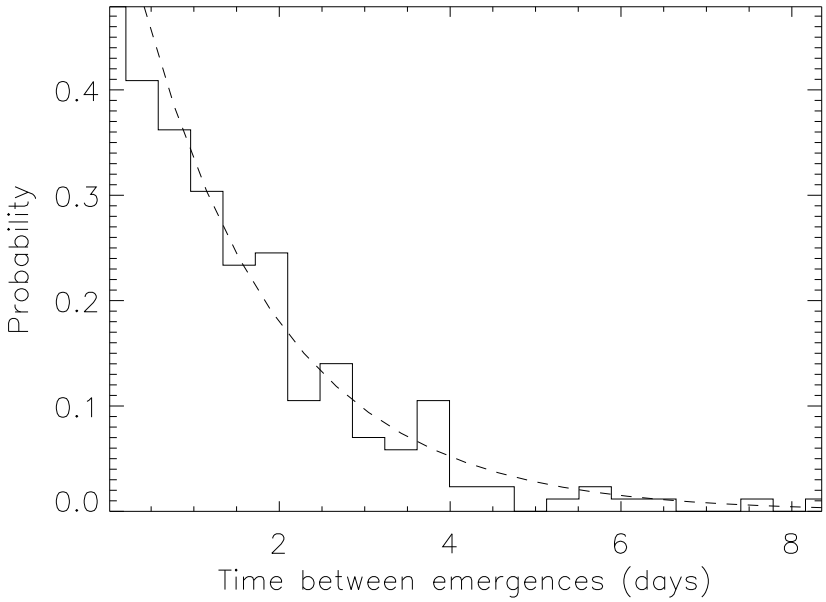

Figure 7.4: A (normalised) histogram of the times between subsequent bipole emergences with the exponential distribution with $\tau = 1.61$ days overplotted (dashed line). The exponential distribution provides a very good fit to the times between emergences.

Lastly, the separations and tilt angles (bottom left panel of Figure 7.2), the betas and tilt angles (bottom right panel of Figure 7.2) and the betas and separations (right panel of Figure 7.3) all show no signs of correlation.

Flux emergence rate

The distribution governing when a flux emergence event will occur must now be determined. Crudely, given that 227 bipoles emerged in a year, we can say that on average 0.62 bipoles emerge per day, or that a bipole emerges every 1.61 days. The exponential distribution (see Appendix C) describes the time between events which occur independently of each other at a constant average rate (τ), and therefore should be able to describe the emergence profile. Indeed, plotting a histogram of the time between emergences for the 227 bipoles and overplotting the exponential distribution with $\tau = 1.61$ days we find a good agreement. This is shown in Figure 7.4. We can construct a reduced chi-squared (see Appendix B) to compare the exponential distribution with the observed distribution. The errors are defined to be the square root of the number of occurrences in each histogram bin. We find a reduced chi-squared of 0.78, which implies the exponential distribution is a good model for the observed distribution.

Latitudinal distribution of bipoles

We must now determine the latitudinal distribution of bipoles. Upon plotting a histogram of the latitudes of emergence, it is clear that the distribution is not symmetric about the equator (Figure 7.5). In our simulations, for simplicity we use a latitudinal distribution that is symmetric about the equator. In order to obtain such a distribution, but one which is also based upon the solar distribution, we consider the histogram for the unsigned

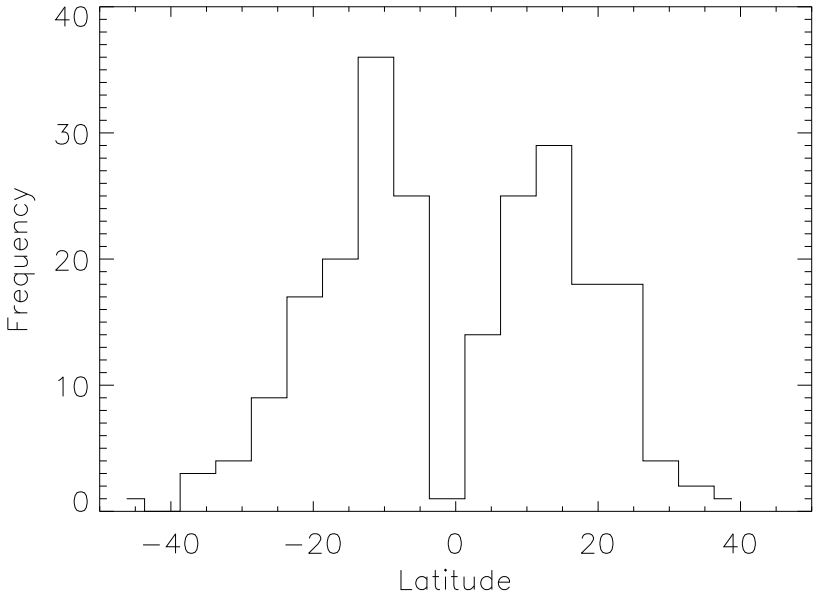

Figure 7.5: Histogram of the latitudes of emergence. Note that the histogram is not symmetric about the equator.

latitudes (Figure 7.6). The cumulative distribution function of this histogram (Figure 7.7) can be used to produce a distribution of latitudes for our bipole emergence model (Section 7.2.2) which closely matches the observed solar profile (see Appendix C for details on the method employed).

Flux distribution of bipoles

The flux distribution of bipoles must also be considered. Figure 7.8 displays the histogram of fluxes. Speculatively we overplotted an exponential distribution with $\tau = 8.40 \times 10^{20}$ Mx (the mean flux) and it appears to describe the distribution of fluxes well. The reduced chi-squared for the exponential distribution with the data is found to be 0.57, confirming the exponential distribution provides a good fit to the fluxes.

7.2.2 Bipole Emergence Model

In Section 7.2.1 we have determined a series of relationships between the various bipole properties, as well as determined the temporal, latitudinal and flux distributions of the bipoles. With this information, we can construct a bipole emergence model to represent the observed solar flux emergence profile between the years 2000 and 2001. This model can be used to consider stars with different flux emergence rates to the Sun, by altering the parameters of the model. Below we outline the procedure used to obtain the bipole properties from the bipole emergence model. The procedure uses a random number generator where we use the shorthand $U[a, b]$ for a number drawn from the uniform distribution between a and b, $N[\mu, \sigma]$ for a number drawn from a normal distribution with mean, μ, and standard deviation, σ. Finally, we use $E[\tau]$ to denote a number drawn from an exponential distribution with expected value, τ. For a description on probability distributions and obtaining random numbers that obey these distributions, please see Appendix C. Starting

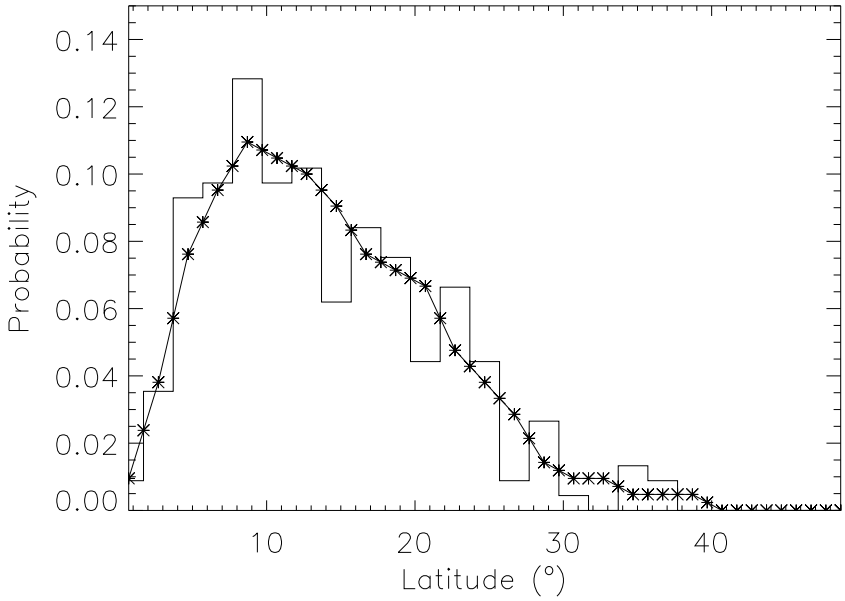

Figure 7.6: Normalised histogram of the observed distribution of the unsigned latitudes of emergence. Also shown is the smoothed normalised histogram which has been resampled to a higher resolution (crosses and solid line) for use in constructing a synthetic distribution of latitudes based on the observed solar distribution.

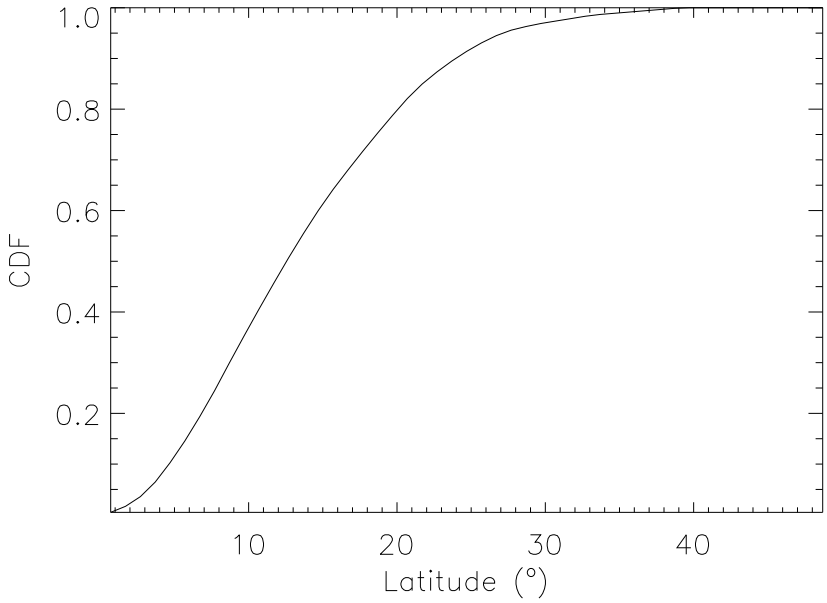

Figure 7.7: The cumulative distribution function (CDF) of the histogram shown in Figure 7.6. This is used to construct the latitude distribution used in Section 7.2.2.

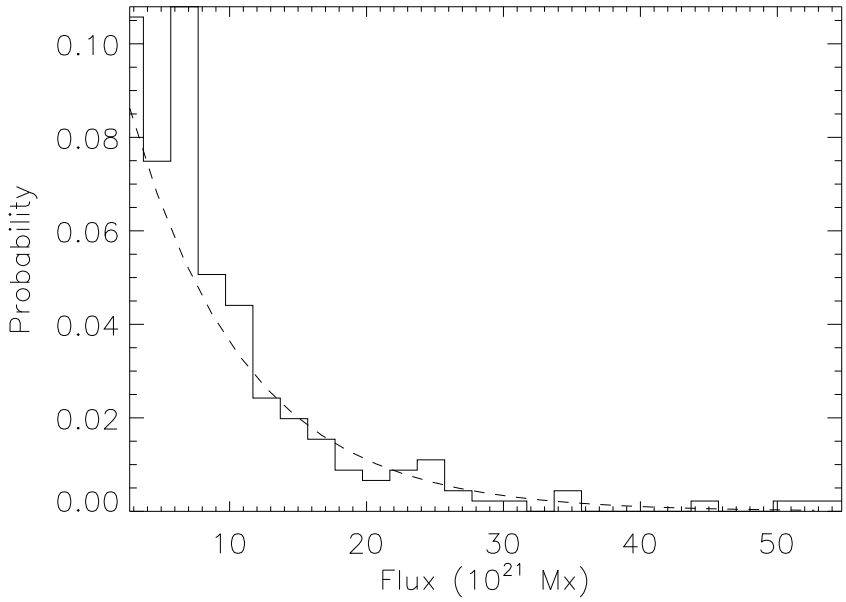

Figure 7.8: A (normalised) histogram of the bipole fluxes. Also shown is an exponential distribution (dashed line) with $\tau = 8.40 \times 10^{20}$ Mx.

at $t = 0$ days, the following procedure is carried out:

1. Determine the time for the next emergence, δt from $E[1.61/D$ days$]$, where D is a scaling parameter to scale the flux emergence rate to be lower or higher than the Sun's. Set the time, t, to $t + \delta t$.

2. Fix the longitude of emergence from $U[0°, 360°]$

3. Select the latitude of emergence from the distribution shown in Figure 7.6 using the technique described in Section C.3 of Appendix C.

4. With a 50% probability, choose the sign of the latitude to be negative.

5. Determine the bipole flux from $E[8.40 \times 10^{20}$ Mx$]$.

6. With a probability of 2.64%, set the flux to have the same sign as the latitude. Otherwise set the flux to have the opposite sign.

7. Set the tilt angle to be $0.32\lambda + N[0, 15°]$. The purpose of the normally distributed term is to add scatter to the tilt angles.

8. Set the beta to be $-0.012\lambda + N[0, 0.40]$. Once again, the purpose of the normally distributed term is to add scatter to the betas.

9. If the flux is less than 12×10^{20} Mx then set the separation to be $1.24 + 0.272\Phi + U[-0.5, 0.5]$, else set the separation to be $4.51 + N[0, 1]$. As above, the uniform and normally distributed random numbers are included to add scatter to the separations.

10. Repeat the procedure until $t \geq 365$ days.

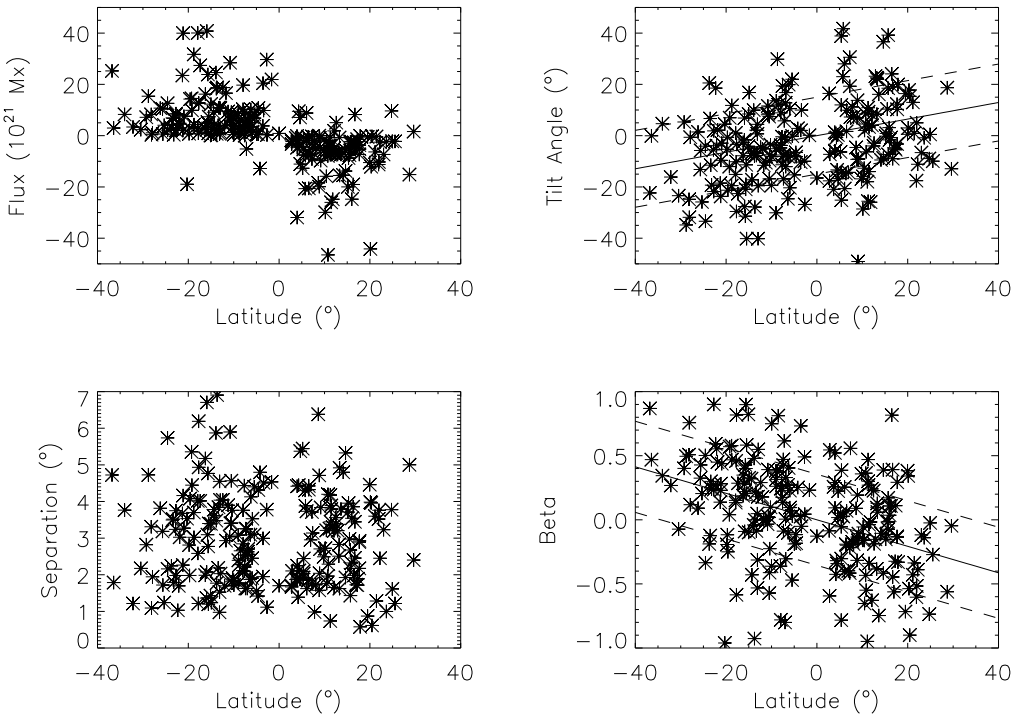

Figure 7.9: Scatter plots of the bipole emergence model's bipoles' flux (top left), tilt angle (top right), separation (bottom left) and beta (bottom right) against the latitude of emergence.

Figures 7.9, 7.10 and 7.11 display scatter plots of the properties of 222 bipoles derived from the bipole emergence model. Qualitatively they are very similar to the scatter plots of bipole quantities derived from the observations (Figures 7.1, 7.2 and 7.3). Similar to the observed bipoles, the separation and latitude, separation and tilt angle, beta and tilt angle and beta and separation show no obvious correlation. Most interestingly, as with the observed bipoles, the tilt angle and flux, and the beta and flux show anti-correlation and correlation respectively. The tilt angles and betas are specified according to the latitude (Equations 7.1 and 7.2), and the separations are specified according to the flux (Equation 7.5). The other relations (e.g. between the flux and the tilt angle) are not explicitly specified by the bipole emergence model, yet the model is able to reproduce similar relations to those in the observed bipoles. This demonstrates that our simple empirical bipole emergence model is able to reproduce a solar-like emergence profile with a minimal number of explicitly specified parameters.

7.3 Numerical Model

The numerical model applied to simulate the stellar corona is very similar to that described in Chapter 6, however there are some differences, which will be described in this section. The main difference is that a modified version of FFF3 is used, which has a variable grid

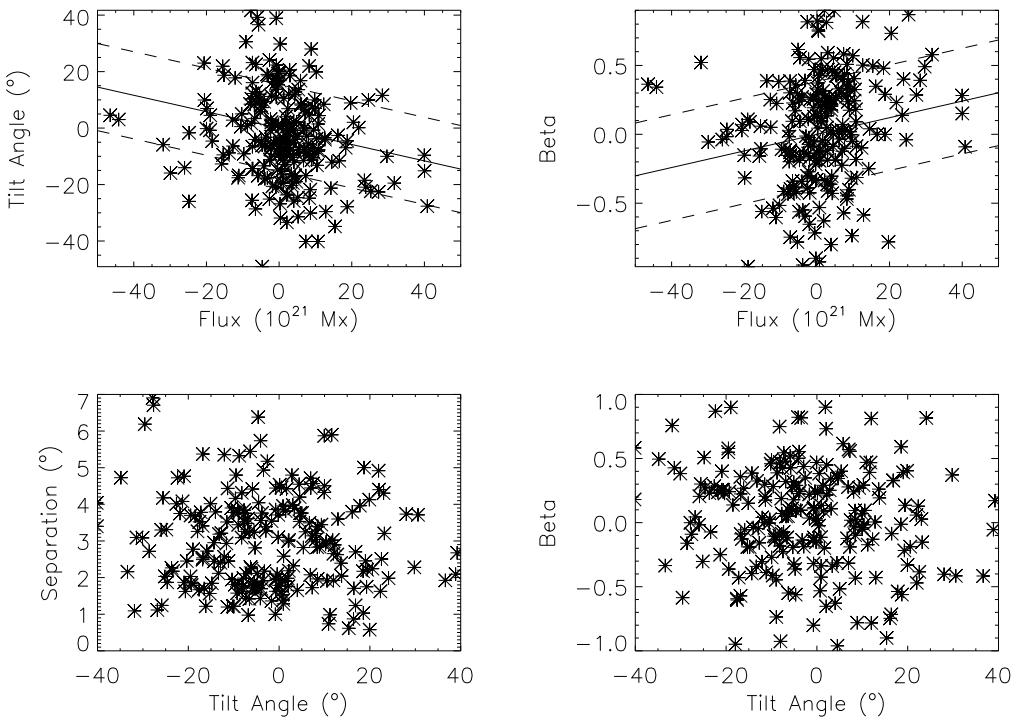

Figure 7.10: Scatter plots of the bipole emergence model's bipoles' tilt angle (top left) and beta (top right) against their flux and the separation (bottom left) and beta (bottom right) against tilt angle.

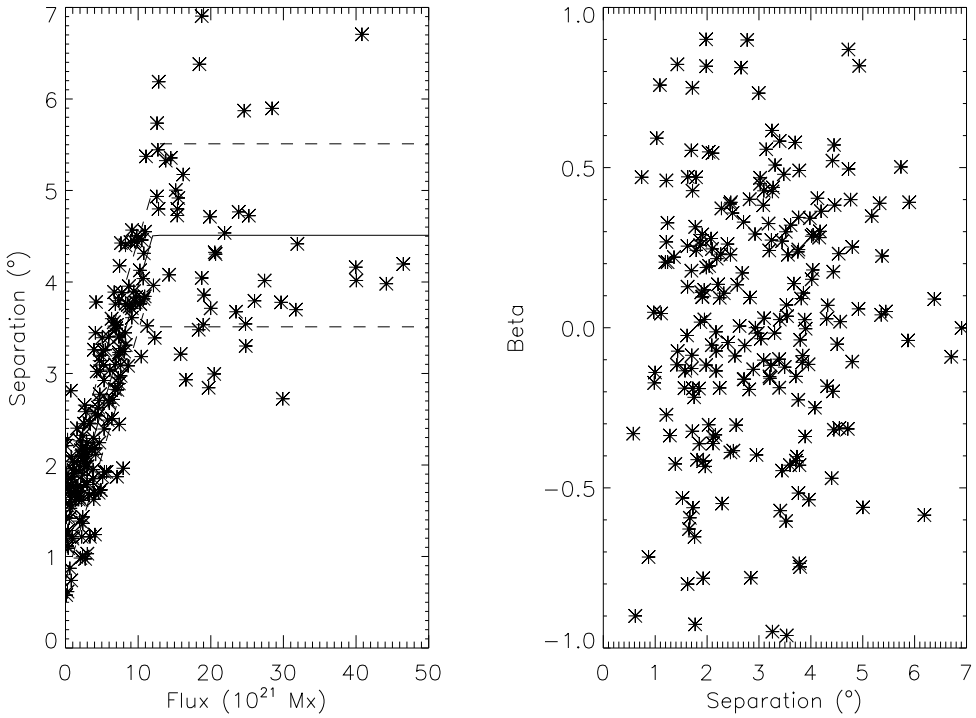

Figure 7.11: Scatter plots of the bipole emergence model's bipoles' separation against flux (left) and the beta against separation (right).

resolution. The grid in FFF3 uses the coordinates x, y and z, related to ϕ, θ and r by

$$x(\phi) = \frac{\phi}{\Delta}, \tag{7.6}$$

$$y(\theta) = \frac{-\ln\left(\tan\frac{\theta}{2}\right)}{\Delta}, \tag{7.7}$$

$$z(r) = \frac{\ln\left(\frac{r}{R_*}\right)}{\Delta}, \tag{7.8}$$

where Δ is the grid spacing in longitude. The use of a variable resolution grid – whose resolution decreases towards the poles – is motivated when considering the cell sizes. In FFF3 the cell sizes, h_x and h_y are dependent upon $r\Delta\sin\theta$, and so for a fixed grid spacing, Δ, the cell size shrinks towards the poles. As a result, the closer to the pole one wishes to simulate, the more grid cells are required. This is illustrated in Figure 7.12 where the number of grid cells in the y direction required to simulate the corona from 0° latitude to a given latitude (with $\Delta = 1°$) is displayed. For latitudes above $\sim 60°$ the number of grid cells increases dramatically and becomes asymptotically large at 90° latitude. The extra grid cells result in larger data files, and significantly more computer time required to carry out the simulations along with reducing the CFL condition. Additionally, in this study, we are most interested in the regions of the star between ±40° latitude where the bipoles are situated, and therefore do not require a high resolution at the poles. It is therefore advantageous to use a variable resolution grid, whose resolution decreases towards the pole. This reduces the total number of grid points needed to simulate the global corona, and thus decreases the amount of computational time and data storage required for the

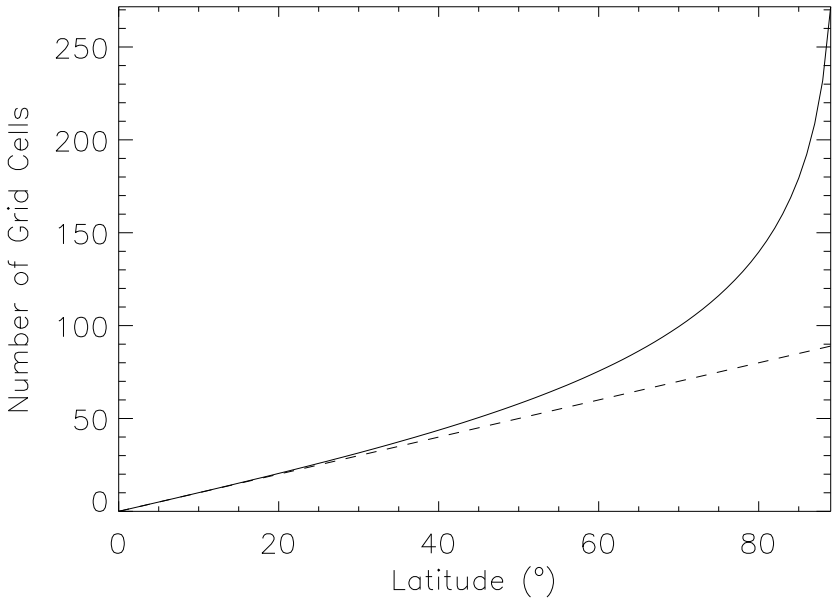

Figure 7.12: The number of grid cells in the y direction required to simulate the corona from 0° latitude to a given latitude (with $\Delta = 1°$). The number of grid cells required increases dramatically towards the pole. The dashed line denotes a 1:1 scaling between the latitude and the number of grid cells required.

simulations. The induction equation is solved in the same manner as that described in Chapter 2, however the grid spacing Δ increases by factors of two towards the pole. For more details on the variable grid code, please see Appendix A of Yeates (2014). In our simulations, the corona is simulated between $\pm 89.5°$ latitude. The grid spacing varies from 0.937° at the equator to 30° at the poles. Thus, the number of grid cells in the longitudinal direction, N_x, decreases from 384 at the equator to 12 at the poles.

The second difference is that the inclusion of flux emergence requires additional steps both in the surface flux transport model, and in the coronal evolution model. The method used to achieve the flux emergence is the method described by Yeates et al. (2008). In the subsections below, the surface flux transport and coronal evolution models will be described, along with the modifications required for flux emergence.

7.3.1 Surface Flux Transport Model

The surface transport model evolves the photospheric magnetic field, B_r according to the effects of differential rotation, meridional flow, surface diffusion and flux emergence. The radial magnetic field at the photosphere is expressed by the vector magnetic potentials $A_{\theta b}$ and $A_{\phi b}$ through

$$B_r = \frac{1}{R_* \sin\theta}\left[\frac{\partial}{\partial\theta}(\sin\theta A_{\phi b}) - \frac{\partial A_{\theta b}}{\partial\phi}\right]. \tag{7.9}$$

The magnetic vector potentials are evolved by solving the two dimensional flux transport equation:

$$\begin{aligned}\frac{\partial A_{\theta b}}{\partial t} &= u_\phi B_r - \frac{D}{R_* \sin\theta}\frac{\partial B_r}{\partial \phi} \\ \frac{\partial A_{\phi b}}{\partial t} &= -u_\theta B_r + \frac{D}{R_*}\frac{\partial B_r}{\partial \theta}\end{aligned} \tag{7.10}$$

where u_ϕ is the azimuthal velocity, u_θ is the meridional flow velocity, R_* is the stellar radius and $D = 450$ km^2 s^{-1} is the photospheric diffusion constant.

The azimuthal velocity is

$$u_\phi = K\left(\Omega_0 - d\Omega_\odot \cos^2\theta\right) R_* \sin\theta, \tag{7.11}$$

where $\Omega_0 = 0.9215$ deg day^{-1} and $d\Omega_\odot = 3.65$ deg day^{-1}. The constant K acts to scale the profile to stars with higher differential rotation rates. $K = 1$ approximately represents solar differential rotation. The azimuthal velocity is plotted for several values of K in the bottom panel of Figure 6.1.

The meridional velocity is prescribed by

$$u_\theta = C\cos\left[\frac{\pi(\theta_{\max} + \theta_{\min} - 2\theta)}{2(\theta_{\max} - \theta_{\min})}\right], \tag{7.12}$$

where $C = 15$ ms^{-1}, the peak meridional flow velocity of the Sun. We adopt the solar peak meridional flow velocity as we have no knowledge of the meridional flow profiles of other stars.

7.3.2 Coronal Evolution Model

The coronal magnetic field is evolved using the ideal induction equation,

$$\frac{\partial \mathbf{A}}{\partial t} = \mathbf{v} \times \mathbf{B}, \tag{7.13}$$

where $\mathbf{v} = \mathbf{v}_{\rm MF} + \mathbf{v}_{\rm out}$ contains contributions from the magnetofrictional velocity ($\mathbf{v}_{\rm MF}$) and an outflow velocity ($\mathbf{v}_{\rm out}$). The magnetofrictional velocity is

$$\mathbf{v}_{\rm MF} = \frac{1}{\nu}\frac{\mathbf{j} \times \mathbf{B}}{B^2}. \tag{7.14}$$

and the radial outflow velocity is

$$\mathbf{v}_{\rm out} = v_0 \exp\left(\frac{z - z_{\max}}{z_w}\right)\hat{\mathbf{z}}, \tag{7.15}$$

where $v_0 = 100$ km s^{-1} and z_w is the width over which the radial velocity falls off at the outer boundary. For more details on the coronal evolution model, see Chapter 2, Section 2.3 and Appendix A, Section A.2.

7.3.3 Implementation of Flux Emergence

Within the simulation, when a bipole is to be emerged (as determined by the bipole emergence model in Section 7.2.2), an idealised 3D bipole is added into the coronal and photospheric field. The inserted bipole's vector potentials take on the following form:

$$A_x = \beta B_0 e^{0.5} z \exp(-2\xi) \tag{7.16}$$

$$A_y = B_0 e^{0.5} \rho \exp(-\xi) \tag{7.17}$$

$$A_z = -\beta B_0 e^{0.5} x' \exp(-2\xi) \tag{7.18}$$

where

$$\xi = \frac{(x'^2 + z^2)/2 + y'^2}{\rho^2}, \tag{7.19}$$

$$x' = (x - x_0)\cos(-\gamma) + (y - y_0)\sin(-\gamma) \tag{7.20}$$

$$y' = (y - y_0)\cos(-\gamma) - (x - x_0)\sin(-\gamma), \tag{7.21}$$

$$B_0 = \frac{\Phi}{\sqrt{\pi e}\rho^2}, \tag{7.22}$$

x_0 and y_0 are the x and y locations of the bipole's centre corresponding to its latitude and longitude, ρ is the bipole's half separation, Φ is the bipole's flux and γ is the bipole's tilt angle. The parameter β is the beta described in the bipole emergence model.

Before the bipole is inserted, the pre-existing coronal (and photospheric) field within the volume the bipole is to be inserted into must be swept away. This is to ensure that the addition of the new field does not lead to any disconnected flux in the corona. It also mimics the distortion of pre-existing coronal field by the newly emerging flux, as has been observed in simulations of flux emergence (Yokoyama & Shibata 1996, Krall et al. 1998). In order to carry out the bipole insertion, the following steps are carried out:

1. The simulation's time is 'frozen' by switching off the surface flows, surface diffusivity and the magntofrictional and outflow velocities.

2. An outward velocity is applied in a dome centred upon the new bipole's position to sweep the existing coronal/photospheric field away.

3. The bipole is inserted into the corona by adding the bipole's vector potential (Equations 7.16 to 7.18) to the pre-existing coronal vector potentials.

4. The magnetofrictional and radial outflow velocities are switched on, and the new bipole is allowed to reach an equilibrium with its surroundings for 50 timesteps.

5. Time is restarted by turning on the photospheric flows and diffusion.

For further details on the flux emergence method applied, please see Yeates et al. (2008) and Yeates (2008).

7.3.4 Initial Condition

Rather than emerging the bipoles into an initially empty corona, we use a smoothed synoptic magnetogram of the solar photospheric field to construct a potential field initial condition. The synoptic magnetogram is from Carrington Rotation 1970, corresponding to the date range 24th Nov 2000 to 21st Dec 2000. This date range is from within the range of dates that the bipole emergences used to construct the bipole emergence model were taken from. The magnetogram's photospheric field distribution therefore has a spatial distribution of field consistent with our empirical flux emergence profile. In Figure 7.13 the synoptic magnetogram from Carrington rotation 1970, used to construct the initial coronal field, is displayed.

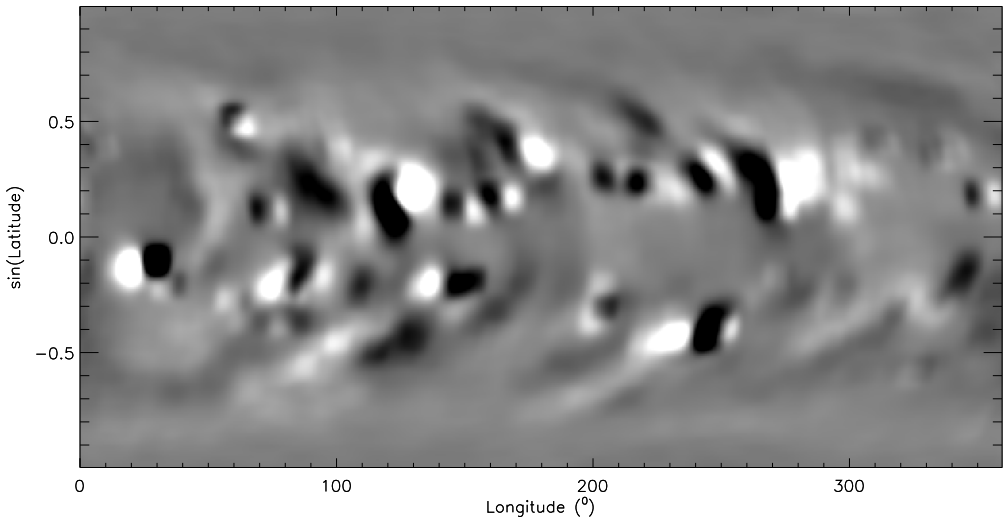

Figure 7.13: The synoptic magnetogram used to construct the potential initial condition used in the simulations. The image is saturated at ±50 G.

7.4 Varying the Flux Emergence Rate

In this section we describe simulations where we have varied the flux emergence rate (i.e. the number of bipoles emerging per day). We investigate $D = 1$, 3 and 5 times the solar flux emergence rate of 0.62 bipoles per day. The simulations were run with solar differential rotation ($K = 1$) and consider the coronal evolution over one year. In particular we investigate the effects of flux emergence on 'global' quantities, such as the open and surface flux, magnetic energy and currents. We also investigate the distribution of flux ropes on the stars, and present j^2 emission proxy images of the stellar coronae, comparing them to field line plots.

7.4.1 Flux

First, let us consider the evolution of surface flux and open flux in the simulations. Figures 7.14 to 7.16 display the surface flux, open flux, and the ratio of the surface flux to the open flux respectively. In all three figures, it is apparent that the surface flux, open flux and the ratio of fluxes reach approximate steady states. For the surface flux, all three emergence rates investigated have reached a steady state after approximately 100 days. For 1, 3 and 5 times the solar flux emergence rate, the steady state fluxes are 64×10^{22} Mx, 126×10^{22} Mx, and 175×10^{22} Mx respectively. For the open flux, it is apparent that for flux emergence rates of 3 and 5 times the solar emergence rate the open flux does not reach a steady state until roughly 150 and 200 days respectively. Once they have reached steady states, the open fluxes are 9.3×10^{22} Mx, 20.2×10^{22} Mx, and 30.4×10^{22} Mx for 1, 3 and 5 times the solar flux emergence rate respectively. Interestingly, the ratio of open to surface flux for all three emergence rates investigated is roughly 0.15. This suggests that as the flux emergence rate increases, although the corona contains more flux, its general configuration is similar.

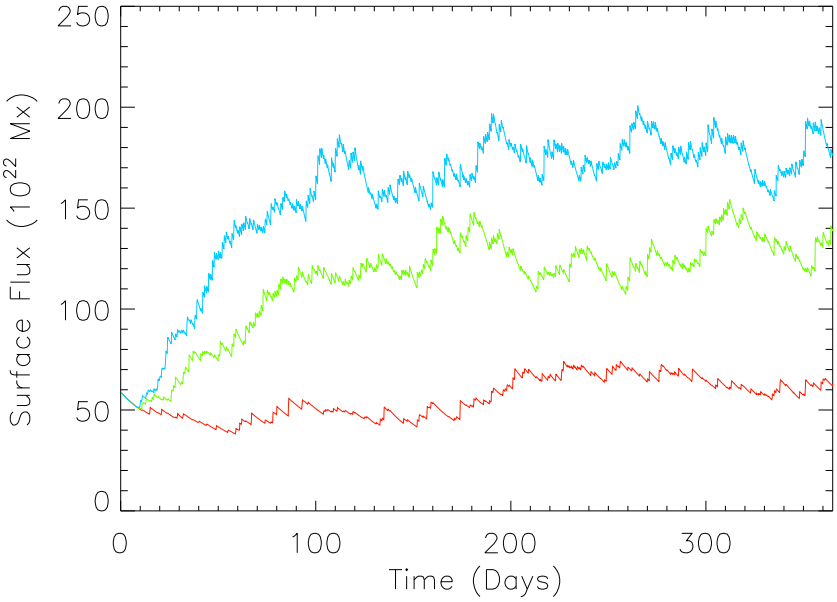

Figure 7.14: Evolution of the surface flux ($\oint |B| \cdot d\mathbf{a}$ at $R = R_*$) as a function of time for the simulations with 1 (red), 3 (green) and 5 (blue) times the solar flux emergence rate.

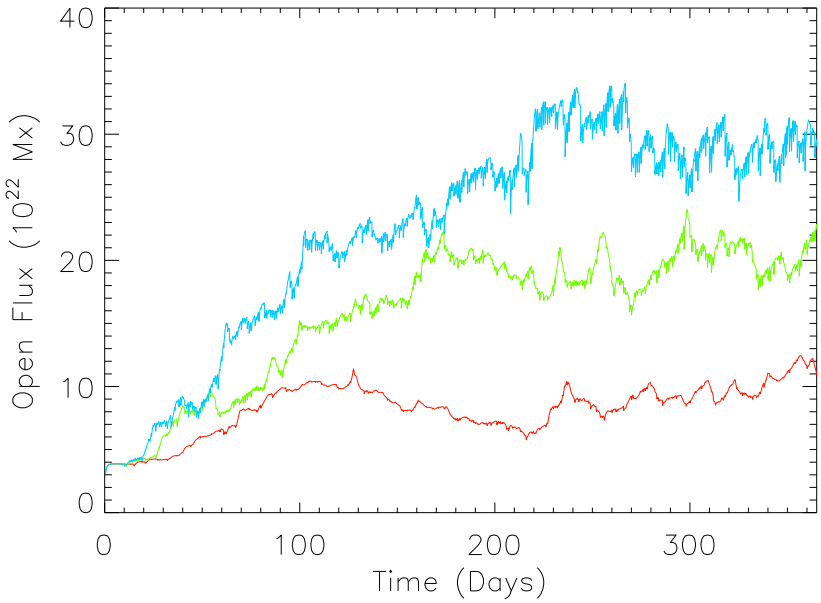

Figure 7.15: Evolution of the open flux ($\oint |B| \cdot d\mathbf{a}$ at $R = 2.5R_*$) as a function of time for the simulations with 1 (red), 3 (green) and 5 (blue) times the solar flux emergence rate.

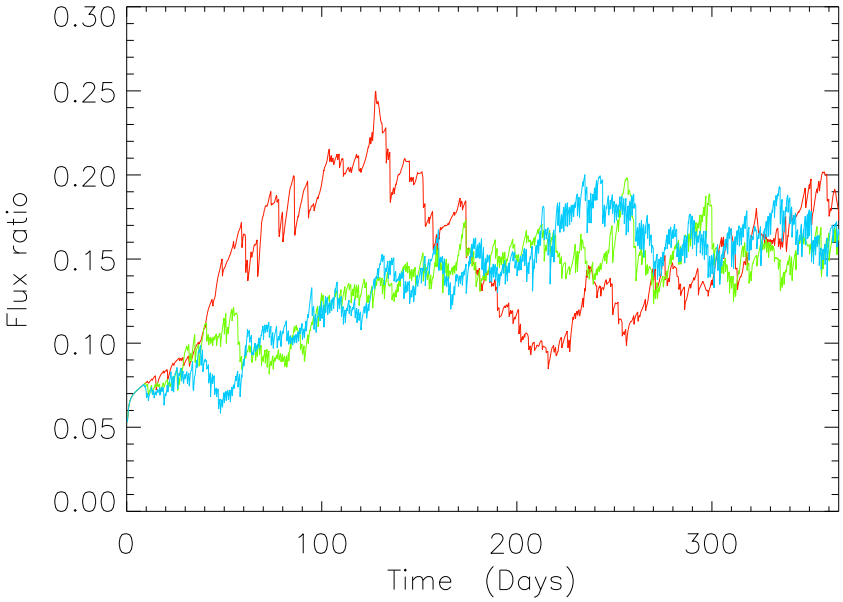

Figure 7.16: Ratio of the open flux to the surface flux as a function of time for the simulations with 1 (red), 3 (green) and 5 (blue) times the solar flux emergence rate.

7.4.2 Surface Magnetic Fields

Next we consider the surface magnetic fields. This is of interest observationally, as ZDI can measure the mean surface field. First, we consider the appearance of the surface magnetic fields. In Figure 7.17 we display maps of the photospheric magnetic field on day 193 of the simulations. These maps are representative of the typical configuration of photospheric fields in the simulations. Upon inspection of Figure 7.17, it is clear that as the flux emergence rate increases, the stellar surface becomes more and more filled with magnetic field. Also large unipolar, longitudinal 'stripes' are present in the simulations with high flux emergence rates.

We can quantify the increased coverage of the stellar surface by magnetic fields through considering the mean magnetic field. This is determined by calculating

$$\langle B \rangle = \frac{\oint B_r dA}{\oint dA}. \tag{7.23}$$

This is plotted as a function of time for each simulation in Figure 7.18. Similar to the fluxes, the mean field reaches an approximate steady state. For 1, 3 and 5 times the solar emergence rate, the mean surface fields are 9.5G, 20G and 28G. We can also determine the area of the surface of the star covered by magnetic flux. In order to do this, we define a threshold field strength of 10G, and determine the area of the stellar surface covered by field greater than 10G. This allows us to determine the 'filling factor' of the surface – the proportion of the surface covered by magnetic fields. The filling factor is displayed in Figure 7.19 for the whole stellar surface and Figure 7.20 for latitudes between $\pm 40^\circ$ - corresponding to the latitudinal range where magnetic flux emerges. For all emergence rates investigated, the filling factor over the whole surface increases with time, and in the year does not reach a steady state. This is due to the meridional flow transporting the emerged magnetic fields poleward, essentially increasing the size of the region where large

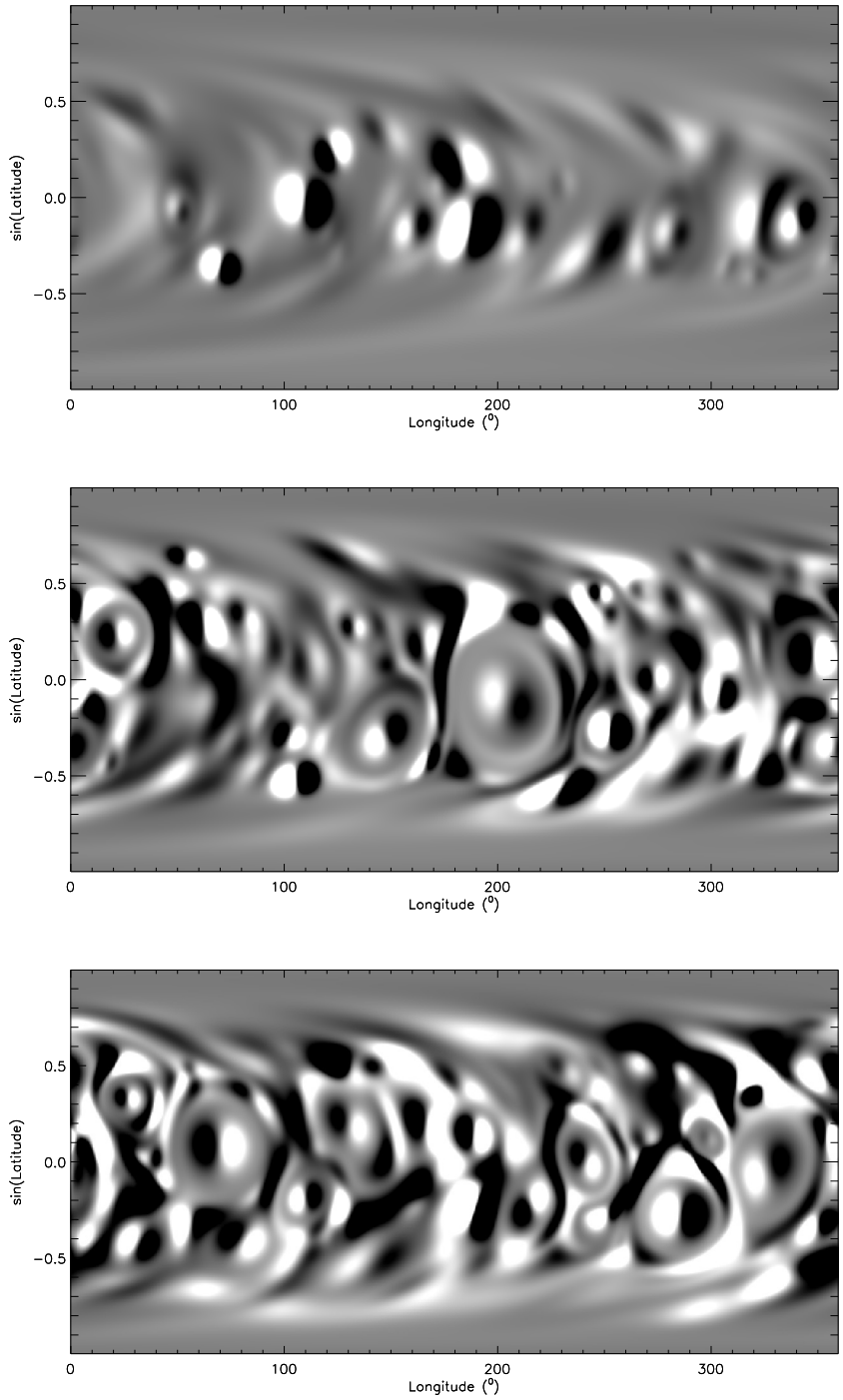

Figure 7.17: Surface maps of the photospheric magnetic field for the simulations with 1 (top), 3 (middle) and 5 (bottom) times the solar flux emergence rate on day 193 of the simulations. The images saturate at ±50 G.

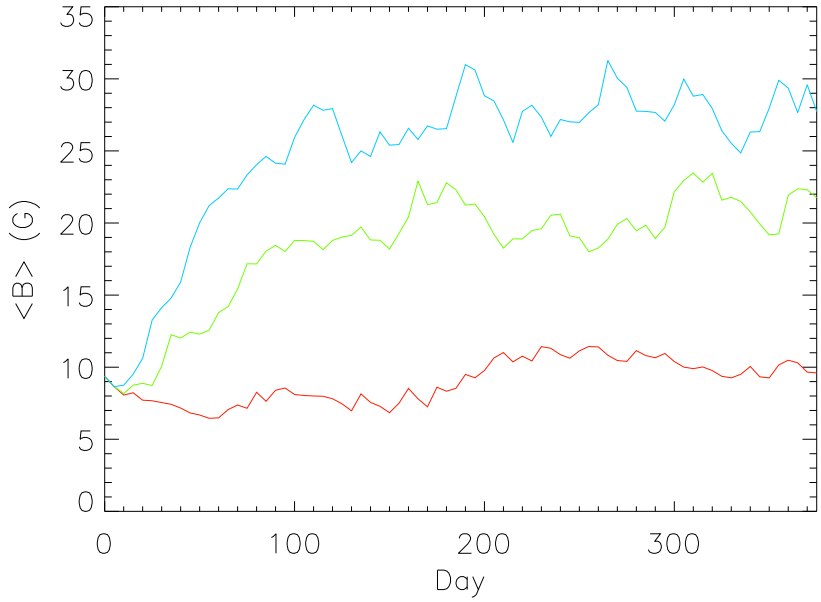

Figure 7.18: Mean surface magnetic field as a function of time for the simulations with 1 (red), 3 (green) and 5 (blue) times the solar flux emergence rate.

magnetic fields are present. Unlike the global filling factor, the filling factor between $\pm 40°$ latitude does level off and reach a steady state. This steady state is 0.39, 0.70 and 0.78 for 1, 3 and 5 times the solar flux emergence rate respectively. Interestingly, at 3 and 5 times the solar flux emergence rate, the filling factors are very similar (0.7 and 0.78). This suggests that the photosphere is becoming saturated with magnetic fields. As such when new field emerges, it emerges into pre-existing field and does not contribute to the filing factor.

7.4.3 Free Magnetic Energy

We now consider the free magnetic energy contained within the corona. In order to calculate the free magnetic energy, we must construct potential fields at each time. As the construction of these potential fields is computationally intensive, to save computer time we only calculate the free magnetic energy every five days. Figure 7.21 displays the free magnetic energy built up within the simulations. After $\sim$ 200 days the free magnetic energy reaches a steady state of approximately 1.9×10^{33} erg, 5.9×10^{33} erg and 10.5×10^{33} erg for 1, 3 and 5 times the solar flux emergence rate respectively. We also plot the ratio of the free magnetic energy to the total magnetic energy in Figure 7.22. The plot shows that the ratio of the free to total magnetic energy is roughly the same for each flux emergence rate. This, similar to the ratio of open to surface flux, implies that the general configuration of the coronal field is independent of the flux emergence rate.

7.4.4 Global Currents

One of the sources of heating in the solar corona is Ohmic heating, which is proportional to j^2. Although in our simulations we do not explicitly have any Ohmic diffusion, by calculating the volume integrated j^2 we may obtain a proxy for the heating present in

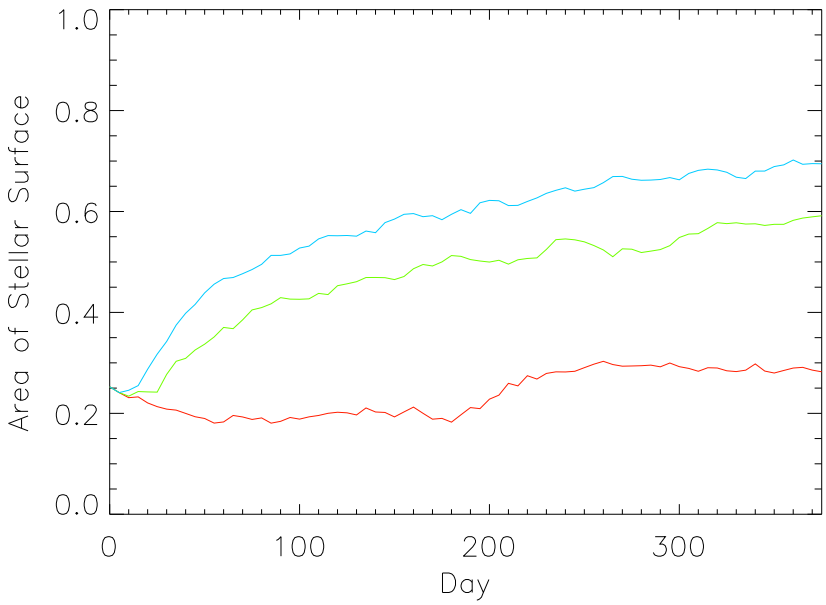

Figure 7.19: Fraction of the stellar surface covered by magnetic fields greater than 10G for the simulations with 1 (red), 3 (green) and 5 (blue) times the solar flux emergence rate.

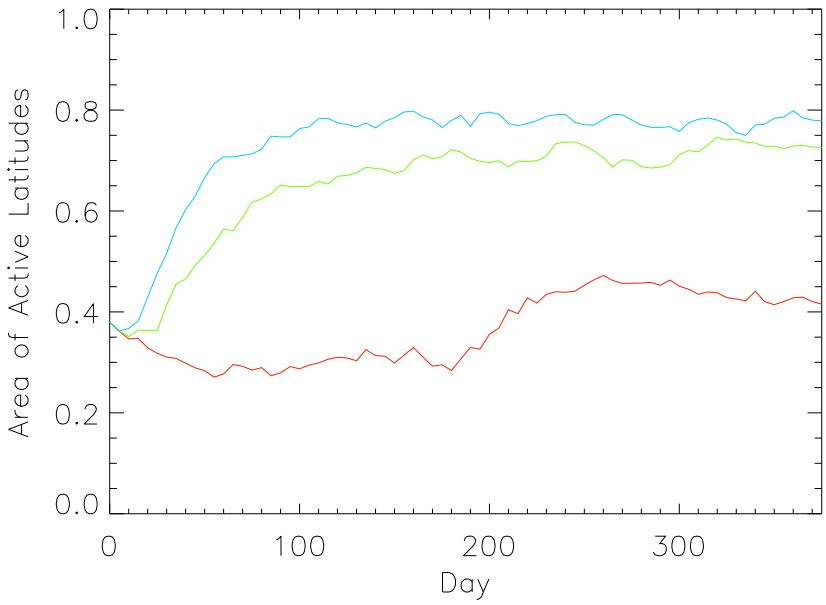

Figure 7.20: Fraction of the area between ±40° latitude covered by magnetic fields greater than 10G for the simulations with 1 (red), 3 (green) and 5 (blue) times the solar flux emergence rate.

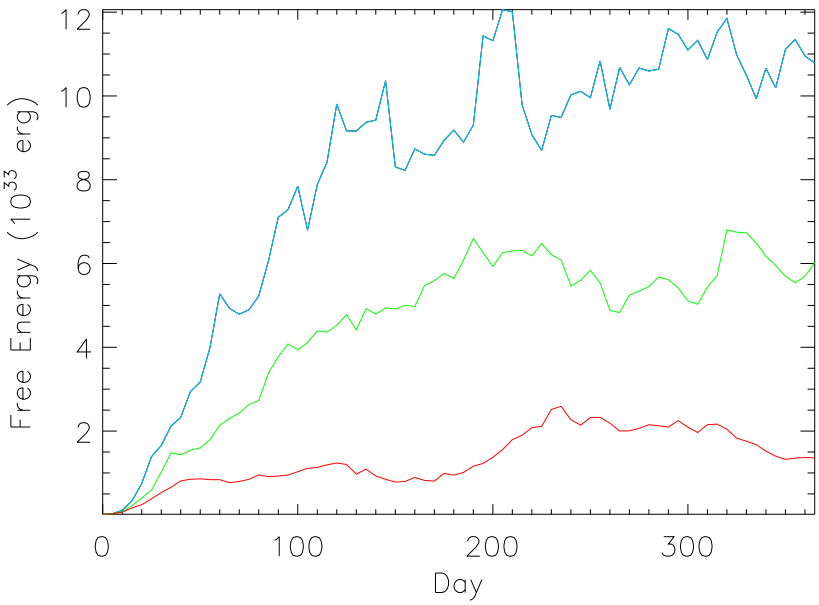

Figure 7.21: Evolution of the free magnetic energy with time in the simulations with 1 (red), 3 (green) and 5 (blue) times the solar flux emergence rate.

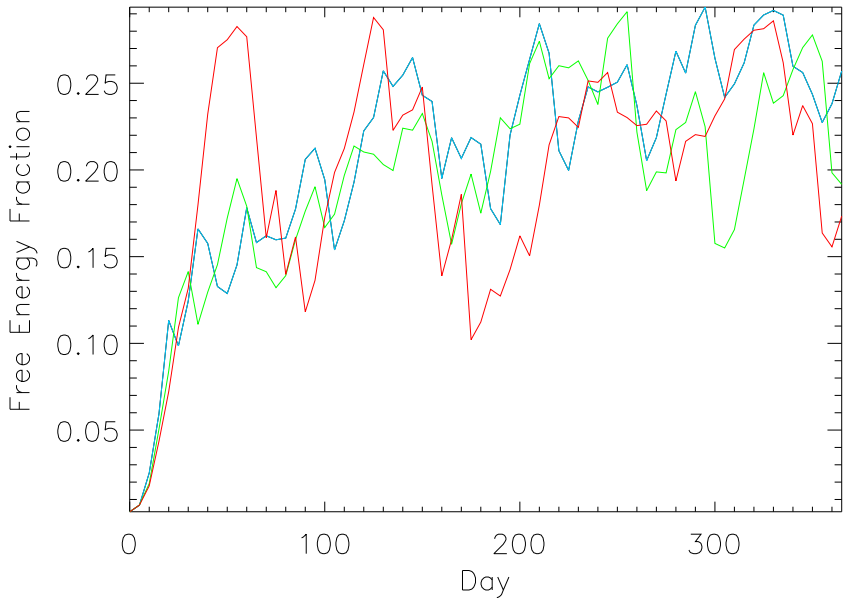

Figure 7.22: Evolution of the ratio of the free magnetic energy to the total magnetic energy in the simulations with 1 (red), 3 (green) and 5 (blue) times the solar flux emergence rate. Interestingly in all three simulations the ratio is similar.

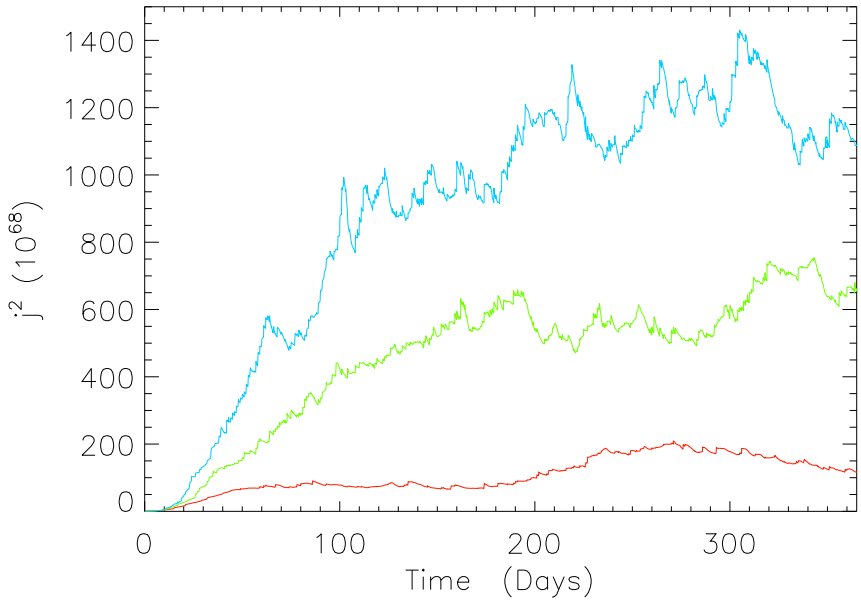

Figure 7.23: Volume-integrated j^2 heating proxy for the simulations with 1 (red), 3 (green) and 5 (blue) times the solar flux emergence rate.

the corona. Figure 7.23 displays the volume integrated j^2 as a function of time in the simulations. Similar to the flux, free magnetic energy and mean surface fields, the heating proxy reaches a steady state after 100-200 days. The mean heating proxies for 1, 3 and 5 times the solar emergence rate are 155, 589 and 1175 in dimensionless units respectively. Stars with a greater emergence rate therefore have more current in their coronae, and thus may have more heating in their coronae. Assuming a link between the heating and X-ray emission, it is a possibility that stars with high flux emergence rates may have higher X-ray luminosities.

7.4.5 Emission Proxy Images of the Stellar Corona

In Chapters 3 and 4, we produced j^2 emission proxy images of an active region in order to try to reproduce X-ray observations of the active region. We now apply a similar technique to visualise stellar coronae. Similar to the previous chapters, we assume that the emission at each point in the corona is proportional to the ohmic heating (j^2), however we also include a simple description of the plasma density. Where the corona is denser, it will emit more radiation as there are more particles present. This is reflected in the radiative loss term in the loss function (Equation 1.15) which is dependent upon ρ^2. By assuming an isothermal corona, we may obtain a crude description of the density as a function of height as

$$\rho(h) \propto \exp\left(-\frac{h}{\Lambda}\right), \tag{7.24}$$

where $h = r - R_*$ is the height above the photosphere and Λ is the pressure scale height, given by

$$\Lambda = \frac{k_B T}{\bar{\mu} g}, \tag{7.25}$$

where g is the surface gravity of the Sun, Choosing $T = 2$ MK and $\bar{\mu} = 0.5m_p$ (where m_p is the proton mass) we find $\Lambda = 120$ Mm. It is very important to note that our simulations do not include any plasma, so the density described in Equation 7.24 is unrelated to the coronal model and is only used to construct the emission proxy.

To construct our emission proxy images, we calculate $\rho^2(h)j^2$ within the coronal volume, and then integrate it along a line of sight to produce the image. This method does not represent the physical processes of radiative emission, which must include the temperature of the plasma. As we do not have any information on the coronal plasma from the simulations, we cannot address the emission problem properly, and must instead use a proxy such as the one we have developed. In Figure 7.24 (left column) we display emission proxy images constructed on day 193 for the three simulations. The images display the logarithm of the emission proxy. Figure 7.24 (right column) also displays the field line plots corresponding to the emission proxy images. The emission proxy images display many features found in coronal images of the Sun, such as coronal holes (e.g. top right of stellar disk in the top left panel of Figure 7.24) and sigmoids (e.g. top of stellar disk in the middle left panel of Figure 7.24). Upon inspection of the corresponding field line plots, it is clear that the coronal holes are associated with large unipolar regions on the photosphere, and are open field regions (e.g. see the field lines at the location of the coronal hole). Similarly, the sigmoids are associated with flux ropes, and generally obey the hemispheric rule observed by Rust & Kumar (1996), whereby the majority of sigmoids in the northern hemisphere are inverse S-shaped, and the majority of sigmoids in the southern hemisphere are S-shaped. These features (coronal holes and sigmoids) in the emission proxy images are therefore associated with the same magnetic structures that produce the observed coronal features. The emission proxy images, despite their simplicity, thus are a reasonably effective method to visualise the corona. Whilst the locations of flux ropes (determined by PILfinder) are associated with bright regions in the emission proxy images, there are many bright regions in the emission proxy images that are not associated with flux ropes. These bright regions are centred around polarity inversion lines, however, and are associated with non-potential sheared arcades. *The files 'solar_evolution.mp4', '3em_evolution.mp4' and '5em_evolution.mp4' in the 'chapter7' directory of the accompanying CD display movies of the emission proxy images for the simulations with 1, 3 and 5 times the solar flux emergence rate respectively.*

7.4.6 Flux Ropes

We now investigate the flux ropes in the stellar coronae. First, we consider the number of non-erupting flux ropes present. In Chapter 6 we found that a proxy for the onset of a flux rope eruption was the sudden disappearance of the length along a PIL where the shear angle is greater than 90°. Due to the magnetofrictional method, which cannot follow the eruptions correctly, an erupting flux rope slowly rises through the corona until it leaves the simulation though the upper boundary. The time between the onset of the eruption and the flux rope exiting the computational domain can be several days. During this time, though the erupting flux rope cannot be detected by PILfinder, as it is no longer in contact with the photosphere, it can still be detected by FRfinder. Therefore, if we were to use FRfinder to count the flux ropes in the corona, we would obtain the total number of erupting and non-erupting flux ropes. We thus use PILfinder to count the non-erupting flux ropes, as PILfinder is unable to detect erupting flux ropes.

Figure 7.25 displays the flux rope locations determined by PILfider for the simulations with 1 (top), 3 (centre) and 5 (bottom) times the solar flux emergence rate on day 193 of the simulations. As can be seen, in each simulation there are many flux ropes present.

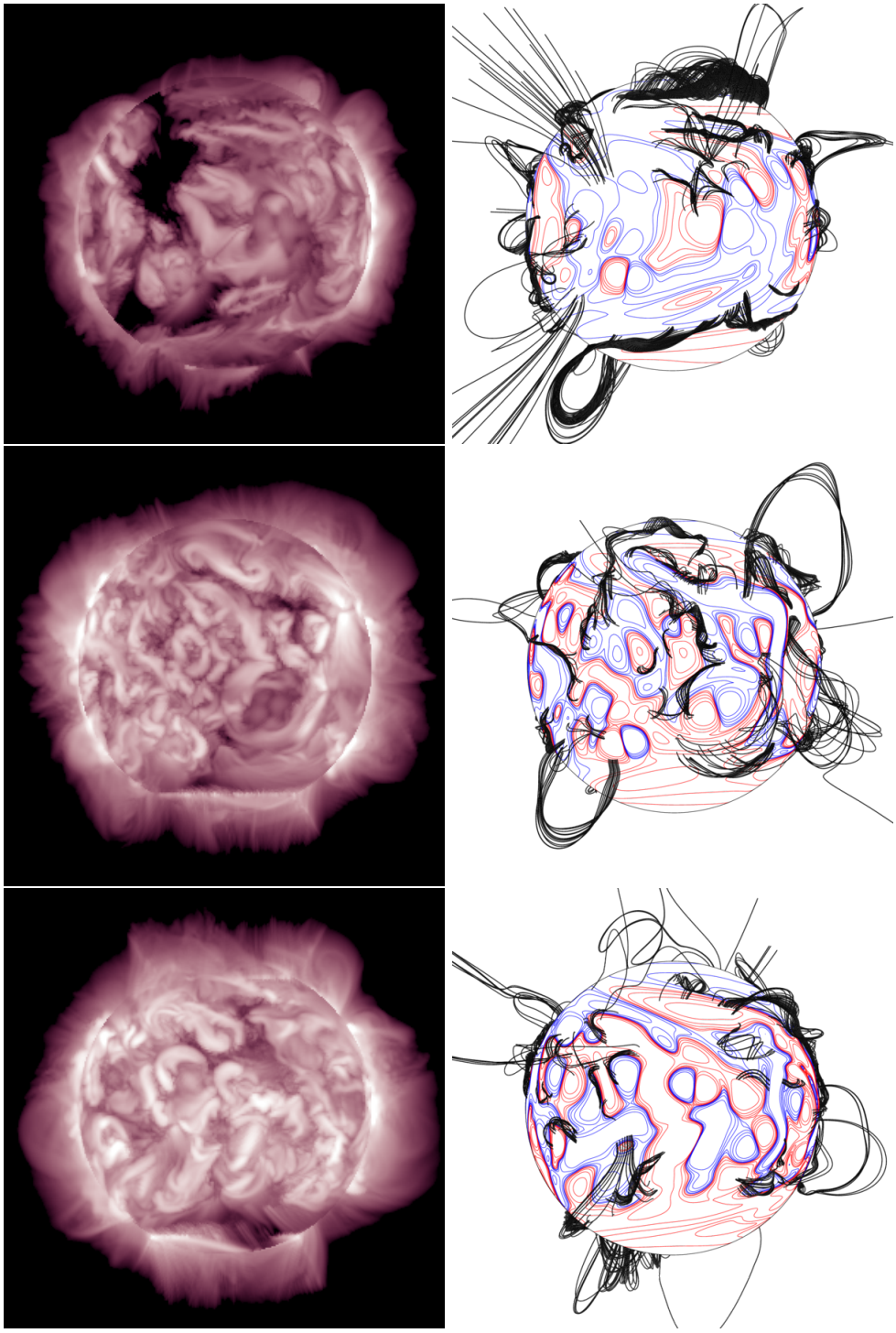

Figure 7.24: Emission proxy images (left) and the corresponding field line plots (right) of the stars with 1 (top), 3 (centre) and 5 (bottom) times the solar flux emergence rate on day 193 of the simulations. The emission proxy images display the natural logarithm of the line-of-sight integrated emission proxy, and the colour scalings are identical in each image. On the field line plots, red and blue contours denote positive and negative magnetic field respectively, and the black lines are field lines.

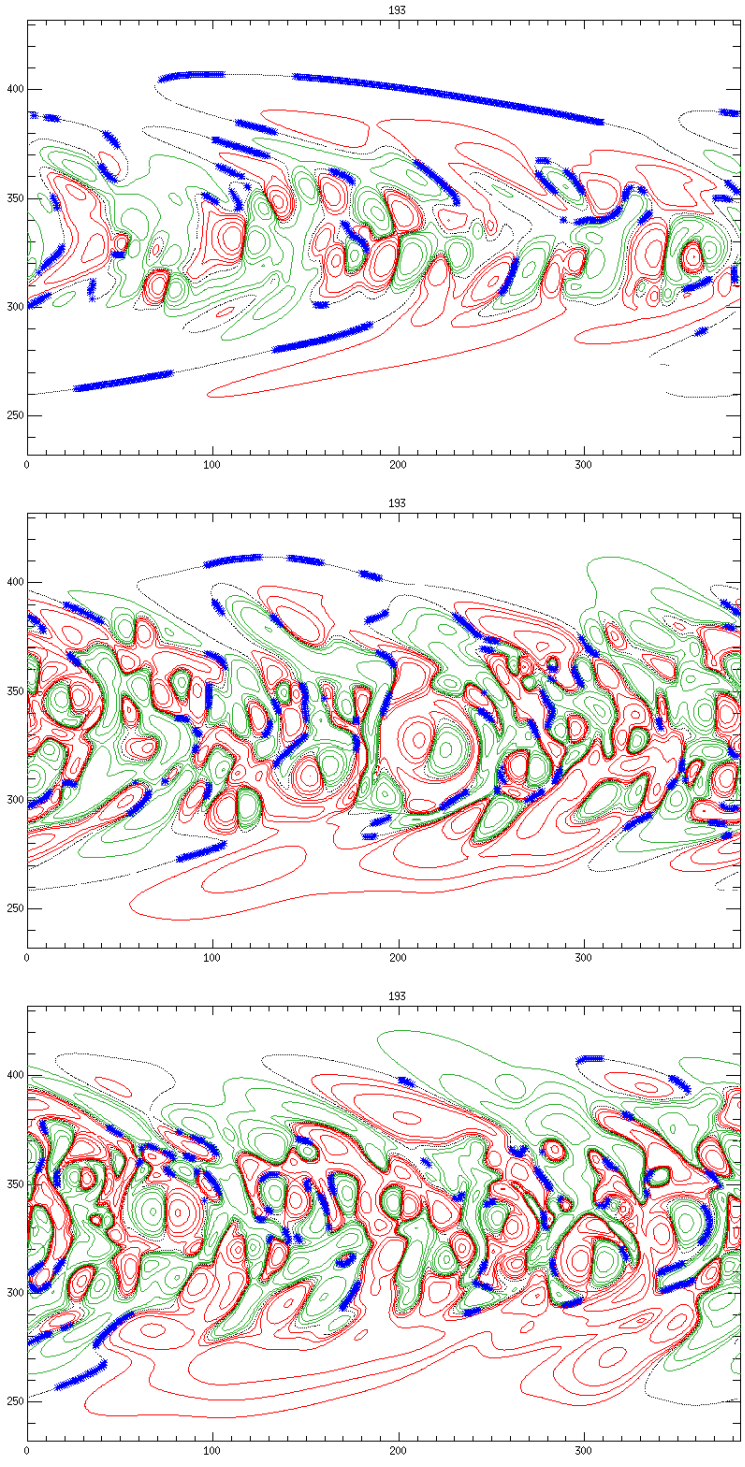

Figure 7.25: Flux rope locations (blue crosses) as determined by PILfinder for the simulations with 1 (top), 3 (centre) and 5 (bottom) times the solar flux emergence rate on day 193. The green and red contours denote negative and positive magnetic flux respectively. The grey lines denote the polarity inversion lines.

Manually counting the flux ropes is very time consuming, and the likelihood for human error is high. It is therefore desirable to develop an automated procedure for counting the flux ropes. PILfinder only finds the locations along a PIL where the shear angle is greater than 90°. A flux rope detected by PILfinder thus consists of many points, and not just one. In order to count the number of flux ropes, a clustering algorithm needs to be used to group the number of points belonging to a flux rope together. The simple clustering algorithm we employ is described below:

1. Flux rope points with fewer than 2 neighbours within a 5 grid cell radius are discarded. This is to remove small regions which could either be false positives (i.e. not a flux rope) or the residual areas of shear angle greater than 90° which can occur just after a flux rope has erupted (e.g. see the bottom panels of Figure 6.13).

2. We then construct a 2-dimensional array with one element per grid cell (in the x and y directions). For grid cells with flux ropes present, the corresponding elements in the array are set to one. Elements corresponding to grid cells without flux ropes are set to zero.

3. We then apply the IDL `SMOOTH` function to the array with a smoothing width of 5 grid cells. This acts to smear out and 'join up' the discrete flux rope points to make one continuous region. Points in the array that are non-zero are set to 1. An example tv image of this smoothed array is shown in Figure 7.26.

4. The array is then contoured using the IDL `CONTOUR` command, and the number of flux ropes is taken to be the number of closed contoured regions.

This method, though generally good at determining the number of flux ropes has some shortcomings. Firstly, if the region of shear angle greater than 90° along the length of a flux rope has a gap of more than 5 grid cells, then the algorithm counts two flux ropes instead of one, thus overestimating the number of flux ropes. An example of this case is visible in the top panel of Figure 7.25 where the two southern-most flux ropes in fact belong to the same flux rope (according to field line plots). If two distinct flux ropes are in close proximity to each other, the smoothing process may merge the two flux ropes into one object, thereby causing the algorithm to underestimate the number of flux ropes. Although these shortcomings exist, upon comparing the number of flux ropes as determined by the algorithm with the number of flux ropes counted by eye for several randomly chosen times, the two numbers were in agreement to within an error of 20%.

In Figure 7.27 the number of flux ropes as a function of time in the simulations with 1 (red), 3 (green) and 5 (blue) times the solar flux emergence rate is plotted. In the figure, the initial number of flux ropes is zero, and quickly rises up to a reasonably constant number. For the solar flux emergence rate the mean number of flux ropes is 44, with a standard deviation of 5. For 3 and 5 times the solar flux emergence rate the mean number of flux ropes is 52 and 55, with standard deviations of 6 and 7 respectively. The mean number of flux ropes present in the simulations with 3 and 5 times the solar flux emergence rate are very similar. It is noted that in each simulation, flux ropes only begin to be counted in the simulation 15 days after the it has started. This is comparable to the formation time for flux ropes on a star with solar differential rotation found in Chapter 6.

We also investigate the latitudinal distribution of flux ropes. To do this, we get the flux rope counting algorithm to count the number of flux ropes present in a series of latitudinal bins. Flux ropes which span multiple latitudinal bins are included in the counts for each bin. Figure 7.28 displays the latitudinal distribution of flux ropes for the simulations. In

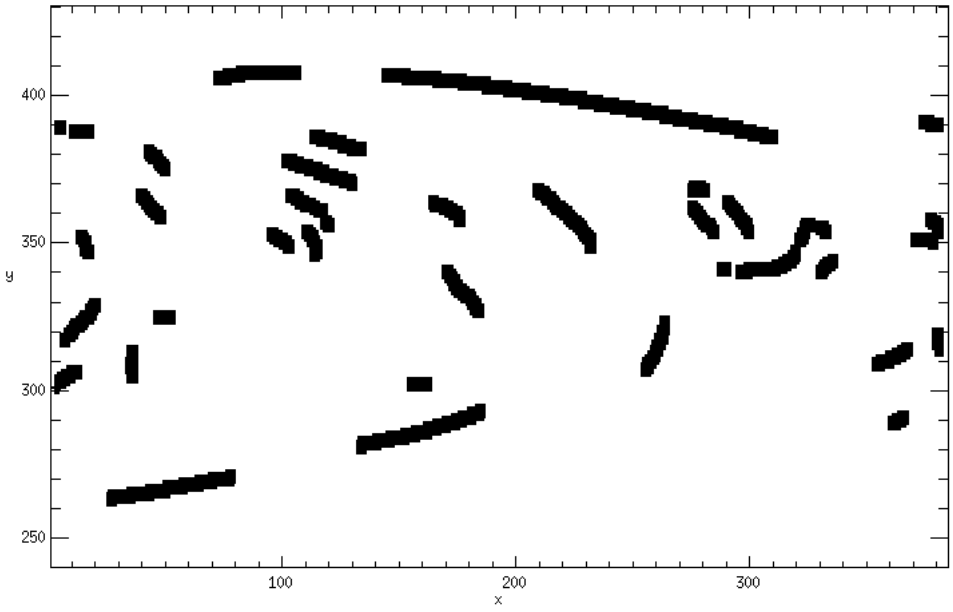

Figure 7.26: Smoothed array of the flux rope positions, which is contoured to count the number of flux ropes. This image corresponds to the flux ropes displayed in the top panel of Figure 7.25.

all the simulations, the shape of the distributions are similar, and the distributions peak between 10° and 30° latitude. No flux ropes are present at latitudes greater than 60°, though this is most likely due to the simulations not having been run for long enough for the meridional flow to transport flux beyond ±60° latitude. Similar to the total number of flux ropes, the simulations with 3 and 5 times the solar flux emergence rate have a similar number of flux ropes present in each bin.

The origin of the similarity between the number of flux ropes in the simulations with 3 and 5 times the solar flux emergence rate is now speculated upon. The similarities suggest that the number of flux ropes in the corona has saturated, and further increases of the flux emergence rate will not significantly increase the number of flux ropes within the corona. This could be a consequence of the saturation of the surface field found in Section 7.4.2, whereby newly emerging bipoles emerge underneath (or in close proximity to) a pre-existing flux rope, causing it to destabilise and erupt. This apparent saturation effect could in part, however, be due to the flux rope counting algorithm underestimating the number of flux ropes present in the simulations with high rates of flux emergence due to the close proximity of flux ropes to each other.

The number of flux ropes in the corona per day reaches a steady state. Therefore, the number of flux ropes that form per day must be roughly equal to the number of flux ropes that erupt per day. Considering that the mean number of flux ropes present per day on the star is 44 to 55 (depending upon the flux emergence rate), keeping count of the appearance and disappearance of flux ropes as determined by PILfinder is time consuming. We therefore instead use FRfinder to look for flux rope eruptions. To do this, we use a method based upon that developed by Yeates & Mackay (2009), which involves looking for flux ropes which are moving upwards with $v_z \geq 0.5$ km s^{-1}. As previously stated, flux ropes may take several days to completely leave the computational box once they have

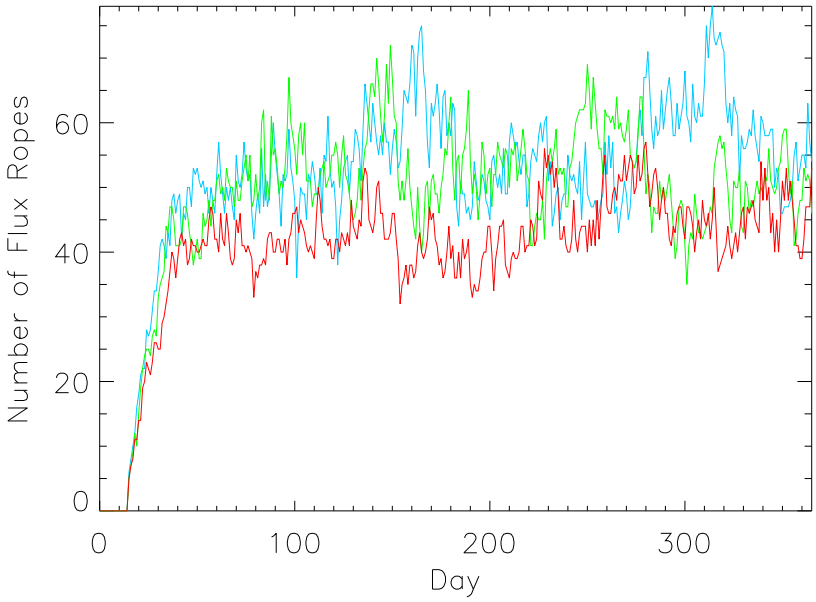

Figure 7.27: The number of flux ropes as a function of time in the simulations with 1 (red), 3 (green) and 5 (blue) times the solar flux emergence rate.

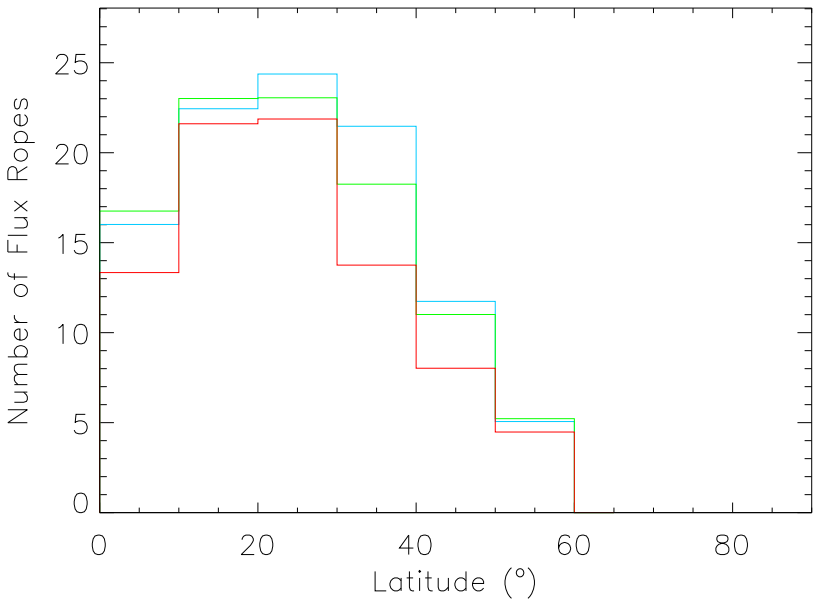

Figure 7.28: The latitudinal number distribution of flux ropes for the simulations with 1 (red), 3 (green) and 5 (blue) times the solar flux emergence rate.

'erupted.' On any two consecutive days, FRfinder may hence identify the same erupting flux rope. We therefore are interested in the number of 'new' erupting flux ropes on each day. This is done manually. Though this is time consuming, it is far less time consuming than checking for the disappearances of flux ropes in the output from PILfinder. Figure 7.29 displays the erupting flux ropes determined by FRfinder for two consecutive days (222 and 223). We have circled the new erupting flux ropes found on day 223 in red.

For each simulation, we determined the number of 'new' erupting flux ropes per day for a 50 day period from day 184 to 233. The mean number of new erupting flux ropes per day (and their standard deviations) are 2.94 ± 1.43, 3.66 ± 1.59 and 3.70 ± 1.70 for the simulations with 1, 3 and 5 times the solar flux emergence rate respectively. As the flux emergence rate increases, the number of eruptions per day increases, however, the number appears to be saturating, as happens with the total number of flux ropes in the corona and the surface magnetic field filling factor. As the number of flux ropes in the corona remains roughly constant in every simulation, the rate at which flux ropes form must be roughly equal to the rate that they erupt, so the mean eruption rates above also correspond to the mean formation rates. Therefore, the formation rates increase with increasing flux emergence rate, however, they saturate.

We may also crudely estimate the mean lifetime of flux ropes. We know that the mean formation rate is roughly equal to the mean eruption rate. So in any one day, on average n_f flux ropes form, and $n_e = n_f$ erupt, keeping the total number of flux ropes in the corona, N, constant. If each flux rope has a mean lifetime of l days, and every day n_f flux ropes form, then the total number of flux ropes in the corona at any one time is approximately

$$N \approx n_f l \tag{7.26}$$

and therefore the lifetime, l, can be approximated by N/n_f. Using this, we find the mean lifetime to be 14.8, 14.2 and 14.9 days for 1, 3 and 5 times the solar flux emergence rate. The mean lifetime found in each simulation is similar to the value of 16 days found in Chapter 6 for stars with solar differential rotation, however it is important to note that given the large error (standard deviation) in the eruption rates and number of flux ropes, the mean lifetimes found here also have a large error. This will be investigated in more detail in the future.

7.5 Varying Differential Rotation

We now investigate the coronal response to the differential rotation rate. Two additional simulations were run with the solar flux emergence rate, but with 3 and 5 times the solar differential rotation rate respectively. These are compared with the simulation with solar differential rotation and flux emergence rate from Section 7.4. As with Section 7.4, we investigate the open and surface flux, energy, heating and the distribution of flux ropes. Each simulation presented in this section has an identical flux emergence profile, so in each simulation the bipoles are emerged at the same time and with the same properties.

7.5.1 Flux

Figures 7.30, 7.31 and 7.32 display the surface flux, open flux, and the ratio of open to surface flux as a function of time respectively for the three simulations. Considering the surface flux (Figure 7.30), it is clear that increasing the differential rotation decreases the surface flux. This is because the stronger differential rotation stretches out the polarity inversion lines, thereby increasing the length of the regions where flux cancellation may

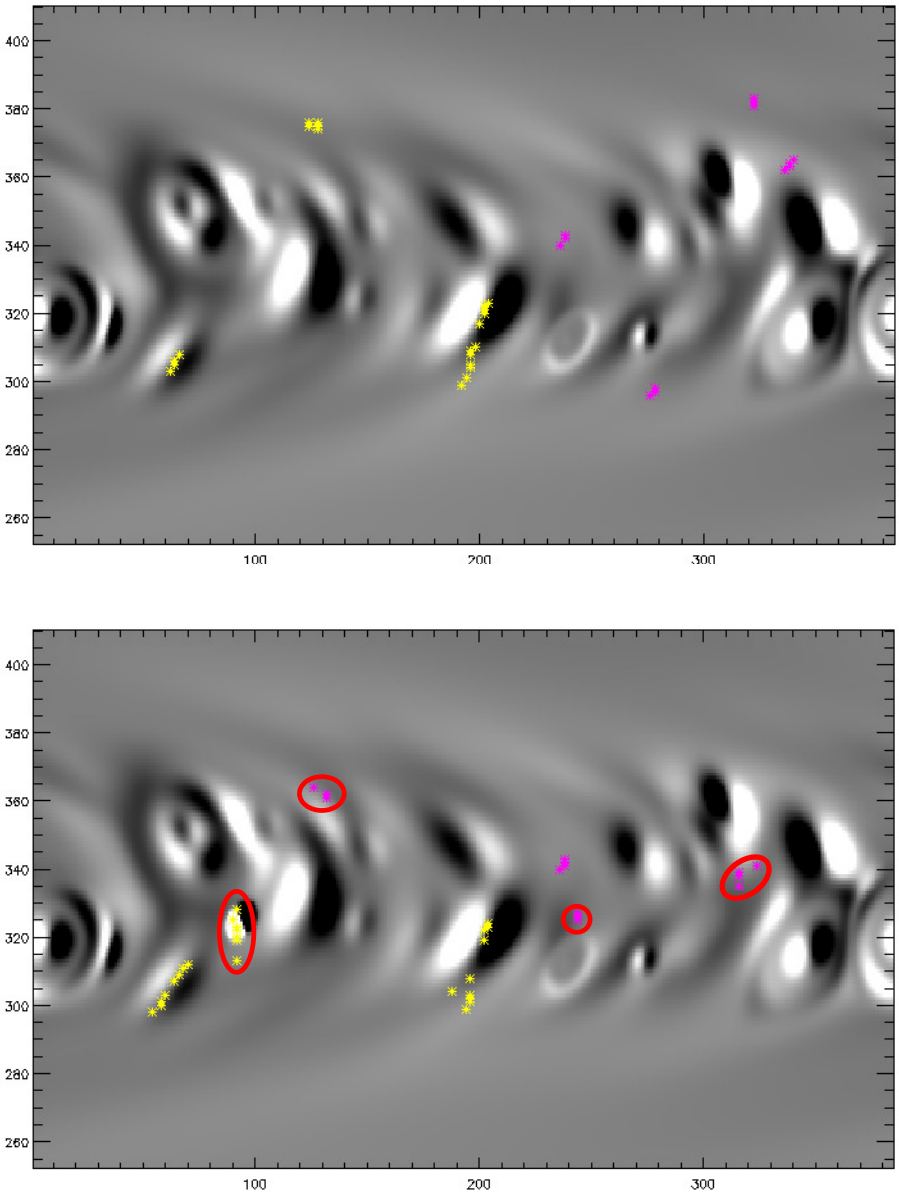

Figure 7.29: Erupting flux ropes ($v_z \geq 0.5$km s^{-1}) determined by FRfinder for days 222 (top) and 223 (bottom) in the simulation with the solar flux emergence rate. The flux ropes circled in red are 'new' erupting flux ropes. The yellow and magenta crosses denote locations of flux rope axes with positive and negative force-free parameter, α.

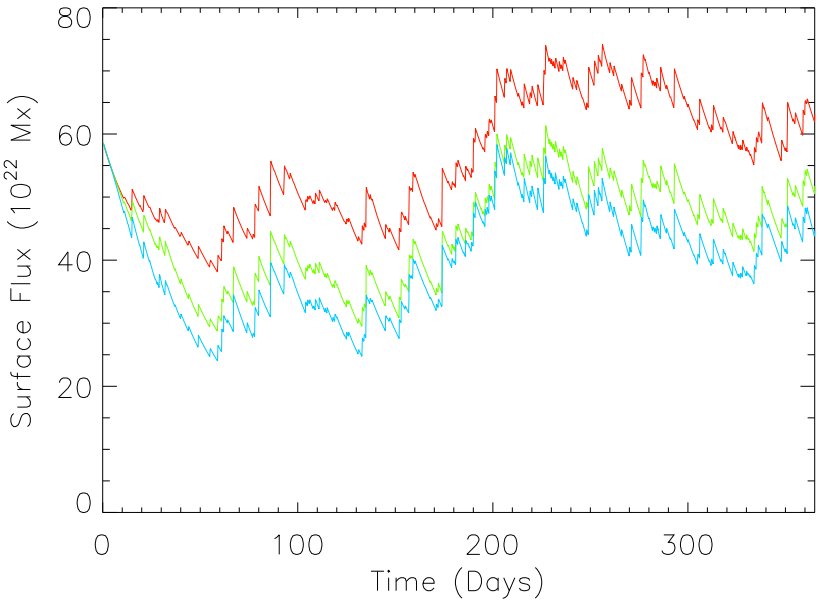

Figure 7.30: Evolution of the surface flux ($\oint |B| \cdot d\mathbf{a}$ at $R = R_*$) as a function of time for the simulations with 1 (red) 3 (green) and 5 (blue) times the solar differential rotation rate.

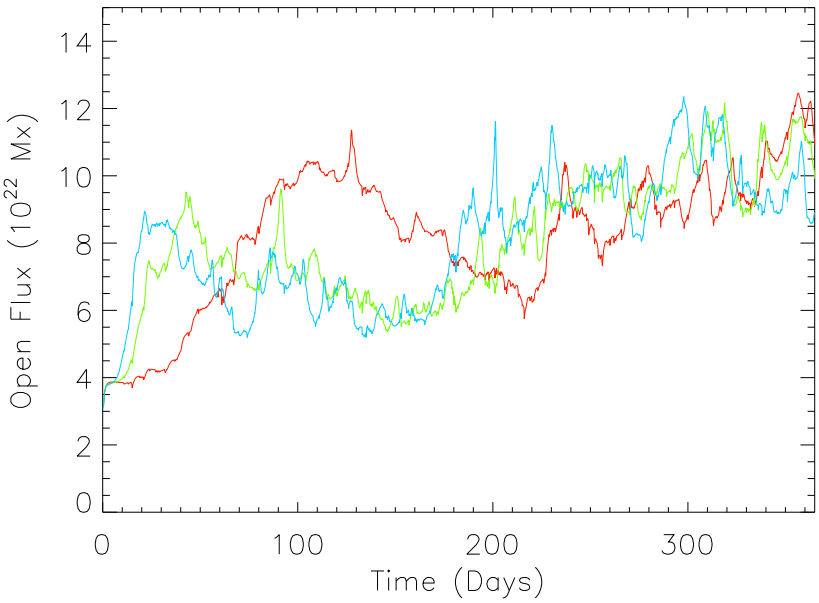

Figure 7.31: Evolution of the open flux ($\oint |B| \cdot d\mathbf{a}$ at $R = 2.5R_*$) as a function of time for the simulations with 1 (red) 3 (green) and 5 (blue) times the solar differential rotation rate.

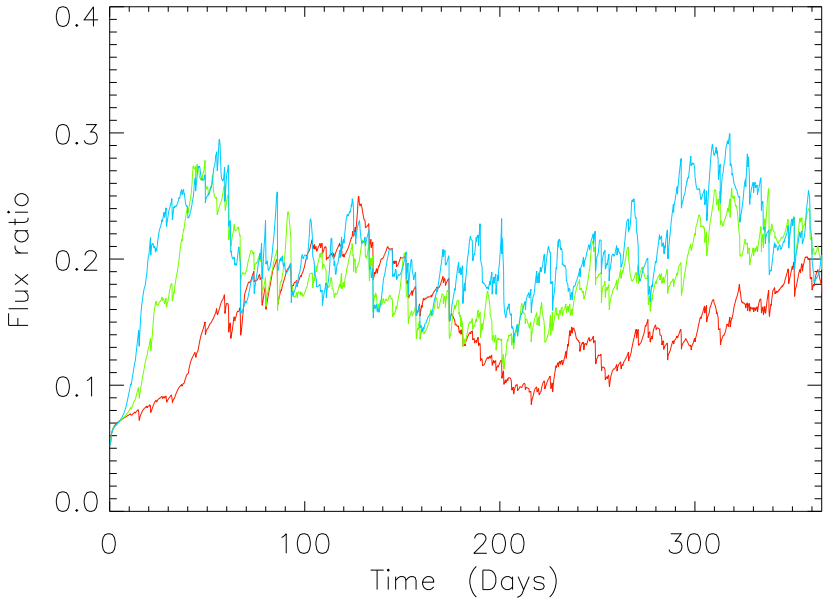

Figure 7.32: Ratio of the open flux to the surface flux as a function of time for the simulations with 1 (red) 3 (green) and 5 (blue) times the solar differential rotation rate.

occur. For the simulations with 1, 3 and 5 times solar differential rotation, the mean surface fluxes (after day 200) are 64×10^{22} Mx, 50×10^{22} Mx and 45×10^{22} Mx respectively. Whilst the mean surface flux decreases with increasing differential rotation, the open flux (Figure 7.31) appears to be independent of differential rotation. Indeed, the mean open fluxes are 9.3×10^{22} Mx, 9.9×10^{22} Mx, and 9.9×10^{22} Mx in the simulations with 1, 3 and 5 times solar differential rotation. The ratio of open to surface flux is thus dependent upon the differential rotation, and increases with increasing differential rotation. The mean ratio is 0.15, 0.20 and 0.23 for 1, 3 and 5 times solar differential rotation. This implies that increasing the differential rotation alters the coronal structure, causing the corona to become more open.

7.5.2 Surface Magnetic Fields

Figure 7.33 displays maps of the photospheric magnetic field on day 193 of the simulations. All three images look similar. Considering the evolution of the mean surface magnetic fields (Figure 7.34), it is apparent that they decrease with increasing differential rotation. This is due to the lengthened polarity inversion lines allowing more flux cancellation to take place, reducing the amount of photospheric field. The mean surface magnetic field is 9.5 G, 7.4 G and 6.6 G for 1, 3 and 5 times the solar differential rotation. The whole-surface filling factor (Figure 7.35) and the filling factor in the active latitudes (Figure 7.36) both decrease with increasing differential rotation, again reflecting the increased lengths of polarity inversion lines leading to more flux cancellation.

7.5.3 Free Magnetic Energy

Figure 7.37 displays the free magnetic energy built up within the simulations. The differential rotation does not seem to have much of an effect on the magnitude of the free

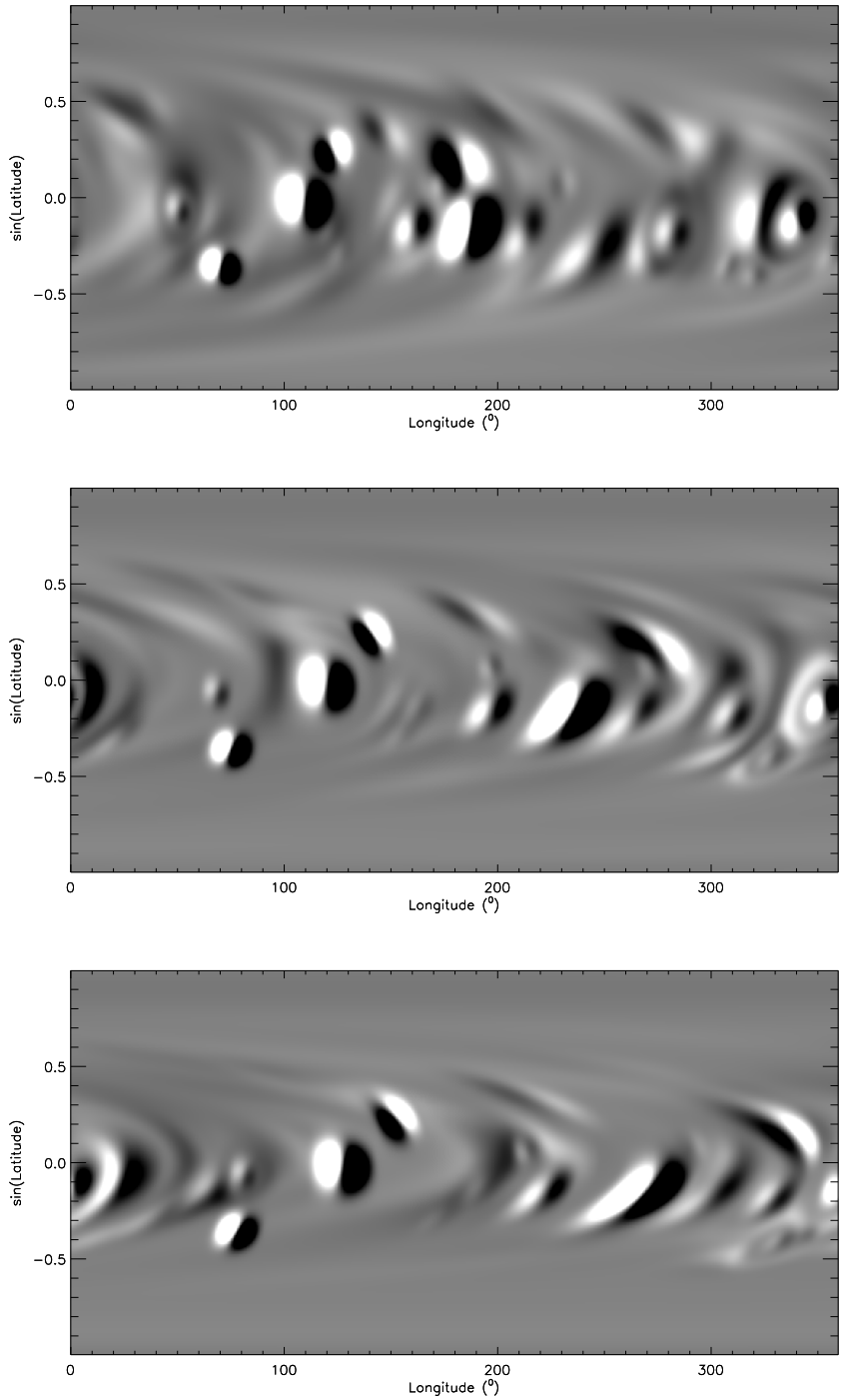

Figure 7.33: Surface maps of the photospheric magnetic field for the simulations with 1 (top), 3 (middle) and 5 (bottom) times the solar differential rotation rate on day 193 of the simulations. The images saturate at ±50 G.

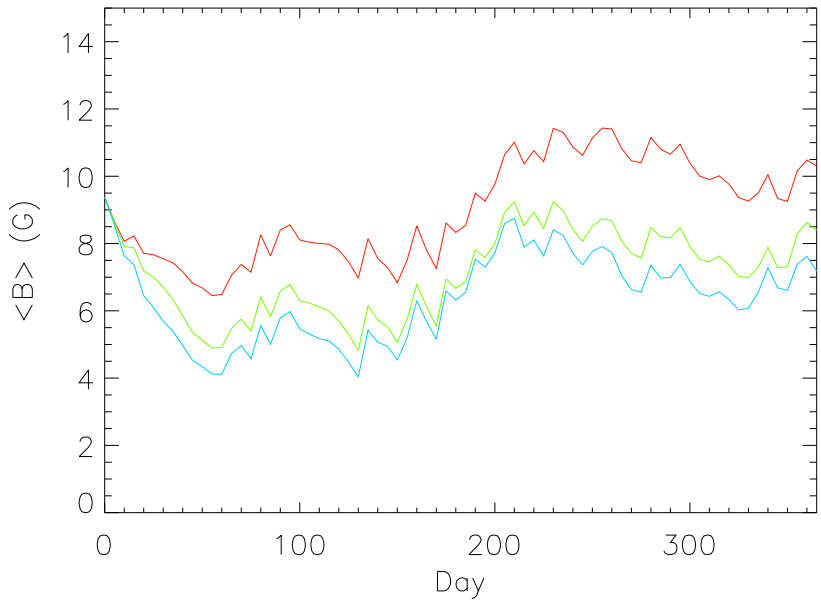

Figure 7.34: Mean surface magnetic field as a function of time for the simulations with 1 (red), 3 (green) and 5 (blue) times the differential rotation rate.

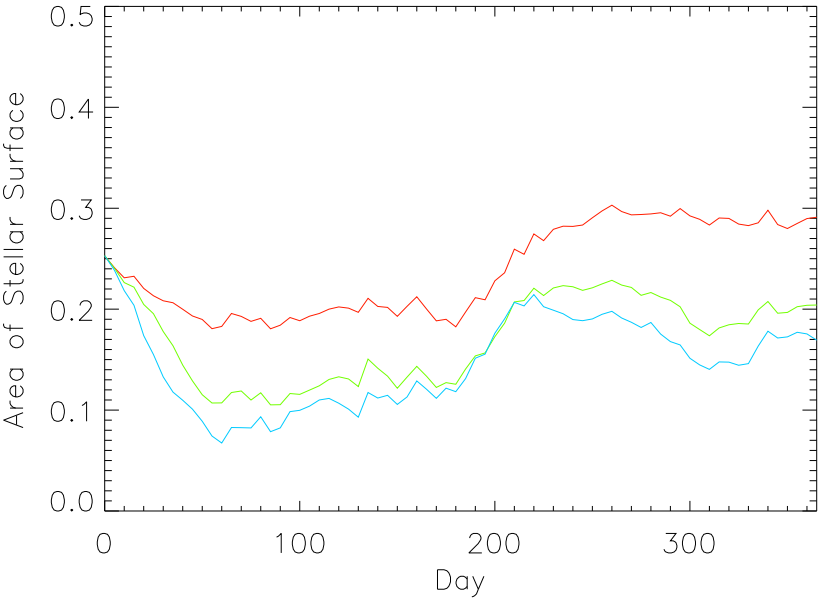

Figure 7.35: Fraction of the area between ±40° latitude covered by magnetic fields greater than 10G for the simulations with 1 (red), 3 (green) and 5 (blue) times the solar differential rotation rate.

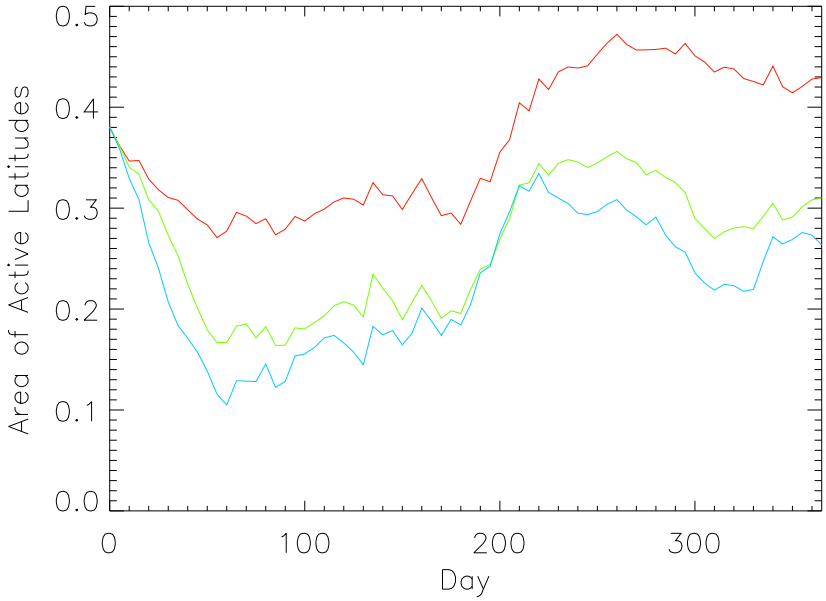

Figure 7.36: Fraction of the stellar surface covered by magnetic fields greater than 10G for the simulations with 1 (red), 3 (green) and 5 (blue) times the solar flux emergence rate.

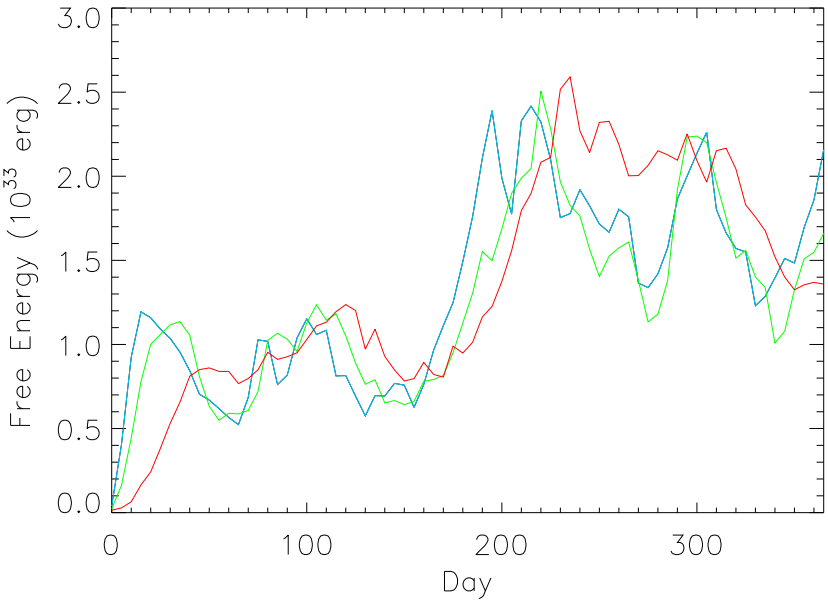

Figure 7.37: Evolution of the free magnetic energy with time in the simulations with 1 (red), 3 (green) and 5 (blue) times the solar differential rotation rate.

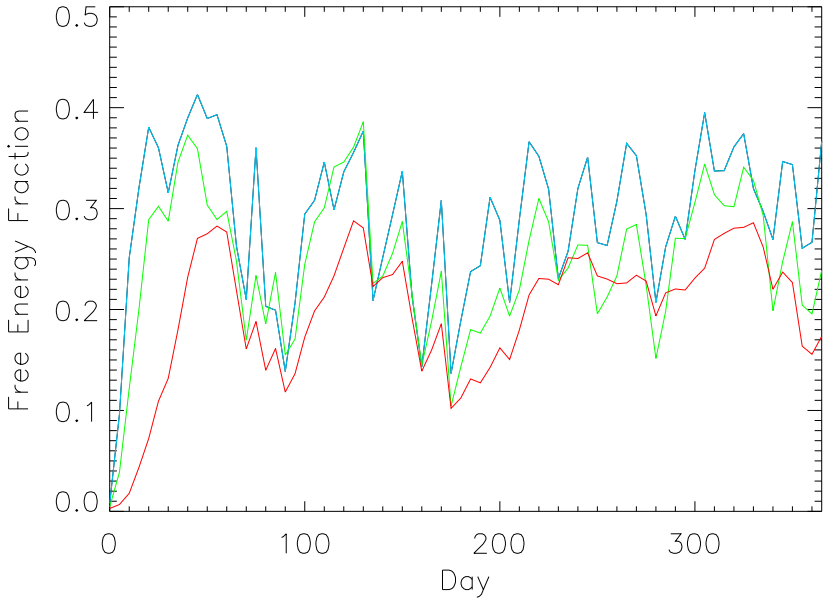

Figure 7.38: Evolution of the ratio of the free magnetic energy to the total magnetic energy in the simulations with 1 (red), 3 (green) and 5 (blue) times the solar differential rotation rate.

magnetic energy. The ratio of the free magnetic energy to the total magnetic energy is plotted in Figure 7.38. The plot shows that the ratio of the free to total magnetic energy slightly increases with increasing differential rotation. The mean ratio of free to total magnetic energy is 0.23, 0.27 and 0.32 for 1, 3 and 5 times the solar differential rotation rate respectively. This, along with the increasing ratio of open to surface flux (Figure 7.32) suggests that the differential rotation has an effect on the structuring of the corona.

7.5.4 Global Currents

Figure 7.39 displays the volume integrated j^2 (which we take to be proxy of heating) as a function of time in the simulations. In all three simulations, the evolution of the volume integrated j^2 is similar, though it appears to slightly decrease with increasing differential rotation. The differential rotation therefore has a small effect on the amount of current within the corona.

7.5.5 Emission Proxy Images of the Stellar Corona

We now present emission proxy images of the simulated coronae, constructed in the manner described in Section 7.4.5. These are shown in Figure 7.40 for day 193, along with field line plots corresponding to the emission proxy images. As with the images presented in Section 7.4.5, features such as coronal holes and sigmoids are visible, and the flux ropes (plotted in the field line plots) correspond to areas of bright emission in the emission proxy images. For greater than solar differential rotation (middle and bottom rows in Figure 7.40), the bright structures visible in the emission proxy images tend to preferentially be aligned east-west. On the stars with solar differential rotation (top row of Figure 7.40 and Figure 7.24) the emission features have no strong preference to their orientation. The east-west alignment

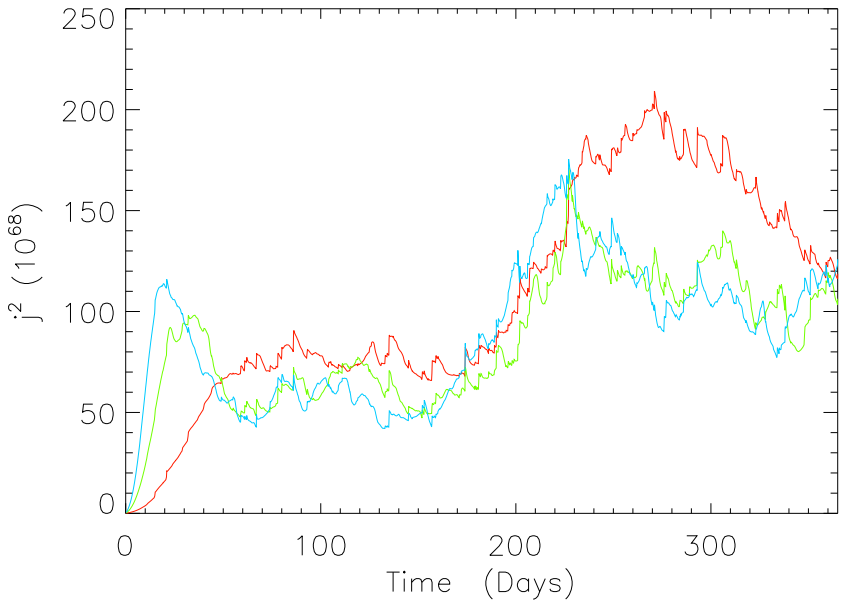

Figure 7.39: Volume-integrated j^2 heating proxy for the simulations with 1 (red), 3 (green) and 5 (blue) times the solar differential rotation rate.

of the emission features in the higher differential rotation stars is a manifestation of the differential rotation stretching photospheric features out in the east-west direction. *The files 'solar_evolution.mp4', '3dr_evolution.mp4' and '5dr_evolution.mp4' in the 'chapter7' directory of the accompanying CD display movies of the emission proxy images for the simulations with 1, 3 and 5 times the solar differential rotation rate respectively.*

7.5.6 Flux Ropes

In this section we study the number of flux ropes, their latitudinal distribution and their eruption rates using the same methods as described in Section 7.4.6. Figure 7.41 displays the flux rope locations determined by PILfinder for the simulations with 1 (top), 3 (centre) and 5 (bottom) times the solar differential rotation rate on day 193 of the simulations. Upon visual inspection the total number of flux ropes seems to be similar. Figure 7.42, which plots the number of non-erupting flux ropes in the corona as a function of time for the three simulations, confirms that the number of flux ropes in each simulation is similar. The mean number of flux ropes in the corona is 44, 41 and 37 for 1, 3 and 5 times the solar differential rotation rate, so increasing differential rotation results in a slight decrease in flux rope number. Flux ropes are first detected 15, 9 and 6 days after the simulation has started in the simulations with 1, 3 and 5 times the solar differential rotation rate respectively. These values are consistent with the formation times found in Chapter 6 of 15, 8 and 6 days for 1, 3 and 5 times the solar differential rotation rate respectively. The latitudinal distribution of flux ropes for each simulation is displayed in Figure 7.43. The distribution of flux ropes is similar in each simulation.

Applying the same technique as described in Section 7.4.6, the mean number of flux ropes erupting per day was calculated for a 50 day period between days 184 to 233 for the simulations. The eruption rates were found to be 2.94 ± 1.43, 3.38 ± 1.86 and 3.84 ± 1.80 per day for 1, 3 and 5 times the solar differential rotation respectively. The eruption

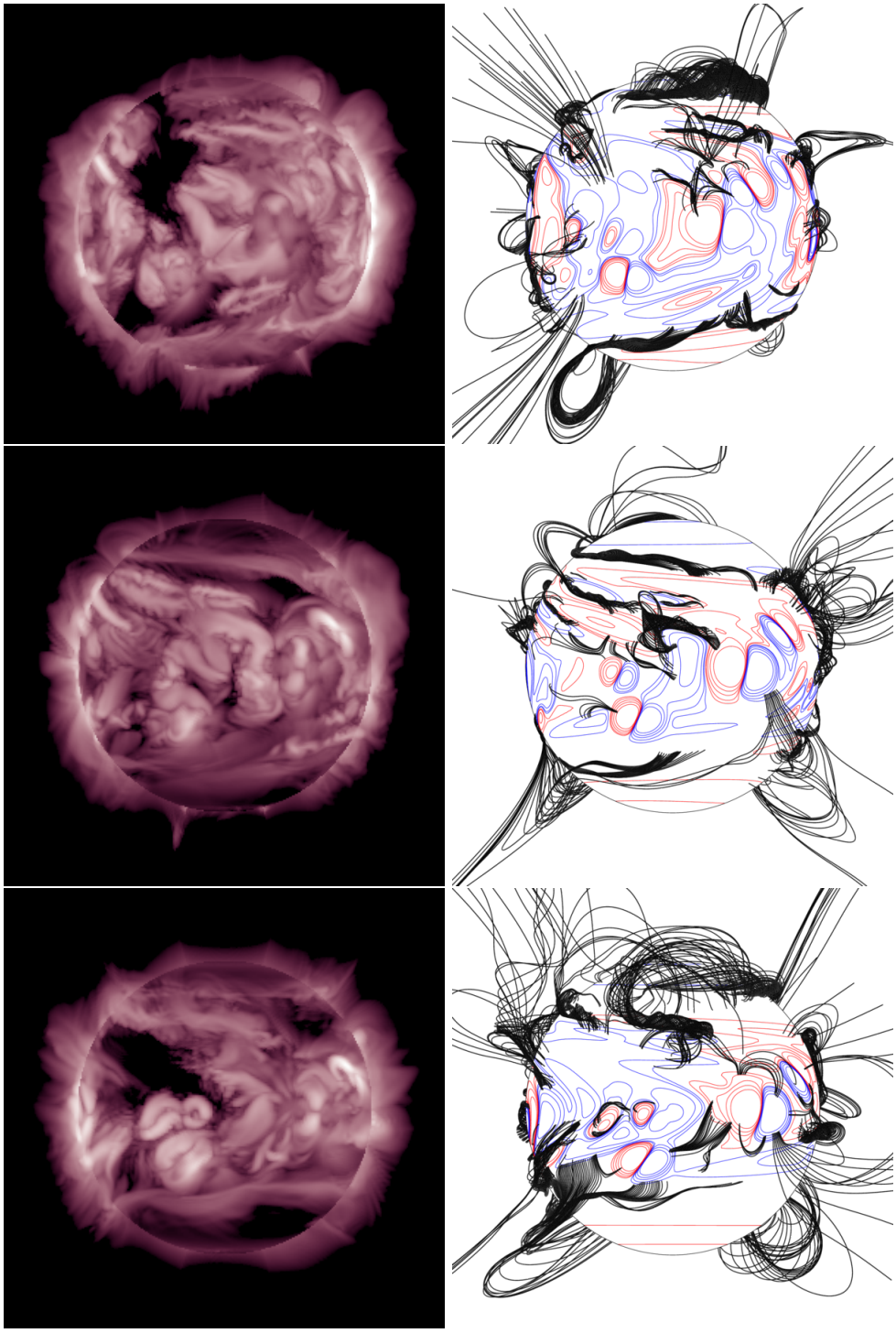

Figure 7.40: Emission proxy images (left) and the corresponding field line plots (right) of the stars with 1 (top), 3 (centre) and 5 (bottom) times the solar differential rate on day 193 of the simulations. The emission proxy images display the natural logarithm of the line-of-sight integrated emission proxy, and the colour scalings are identical in each image. On the field line plots, red and blue contours denote positive and negative magnetic field respectively, and the black lines are field lines.

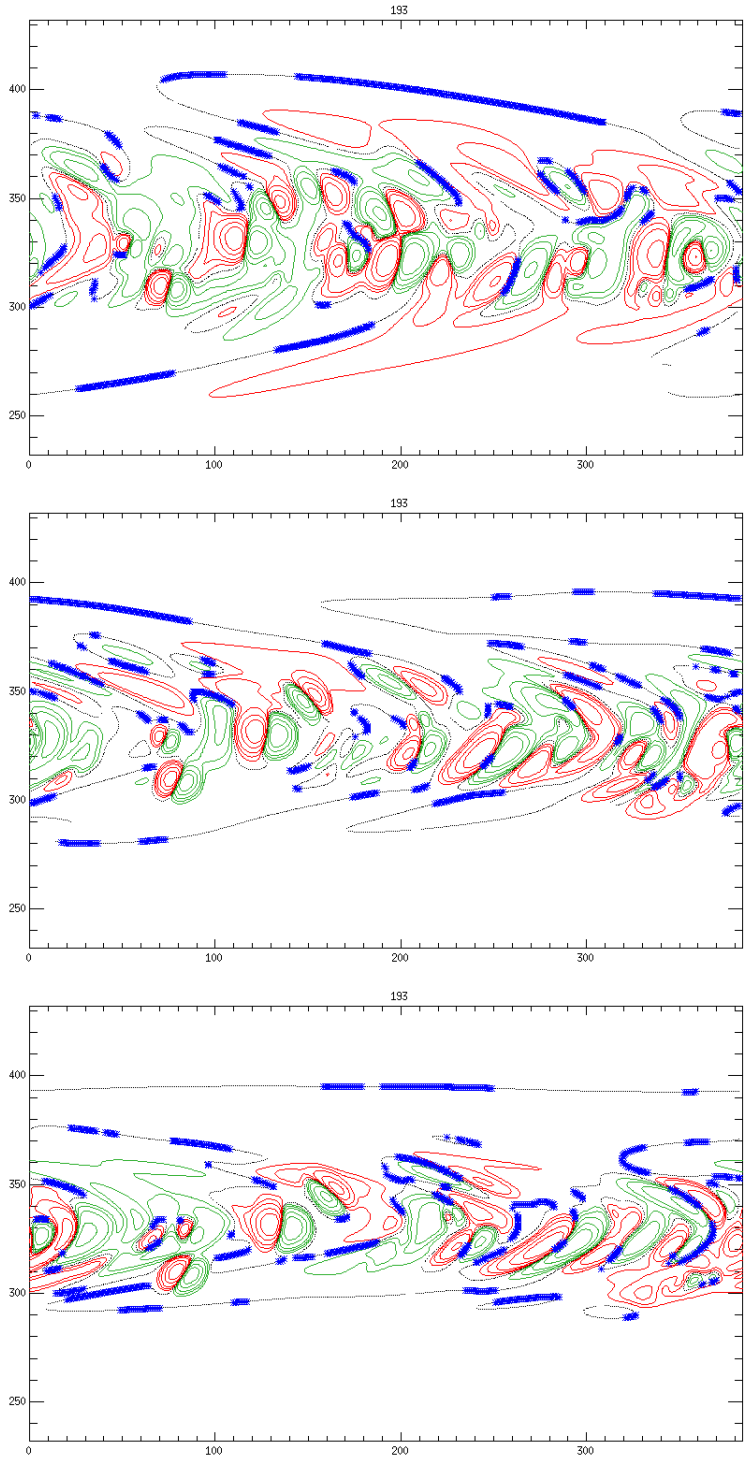

Figure 7.41: Flux rope locations (blue crosses) as determined by PILfinder for the simulations with 1 (top), 3 (centre) and 5 (bottom) times the solar differential rotation rate on day 193. The green and red contours denote negative and positive magnetic flux respectively. The grey lines denote the polarity inversion lines.

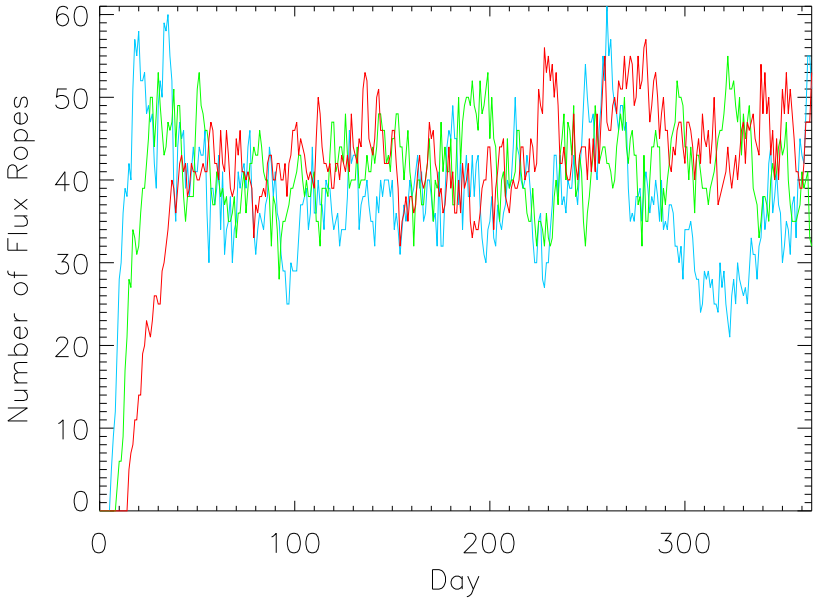

Figure 7.42: The number of flux ropes as a function of time in the simulations with 1 (red), 3 (green) and 5 (blue) times the solar differential rotation rate.

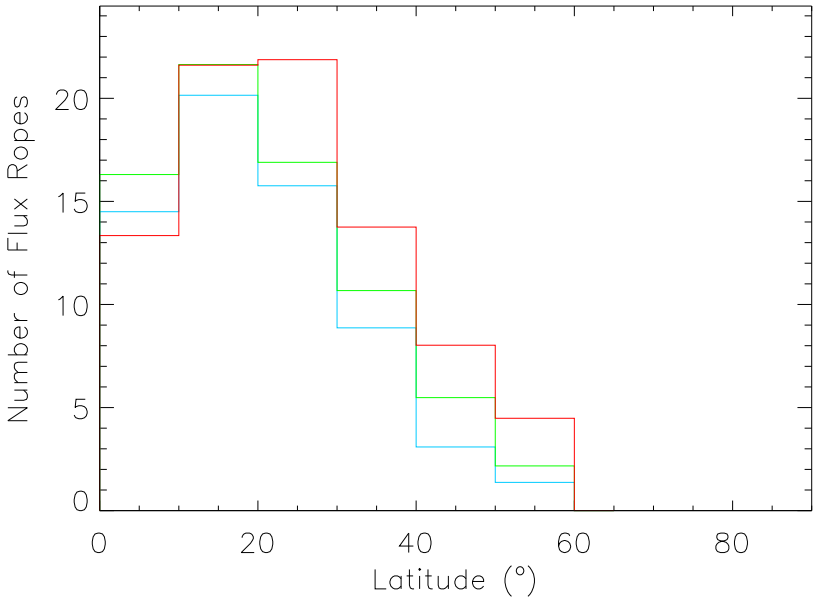

Figure 7.43: The latitudinal number distribution of flux ropes for the simulations with 1 (red), 3 (green) and 5 (blue) times the solar differential rotation rate.

D	K	Φ_S (10^{22} Mx)	Φ_O (10^{22} Mx)	Φ_O/Φ_S	$\langle B \rangle$ (G)	f	E_F (10^{33} erg)	E_f/E_T	j^2
1	1	64	9.3	0.15	9.5	0.39	1.9	0.23	155
3	1	126	20.2	0.16	20	0.70	5.9	0.23	589
5	1	175	30.4	0.17	28	0.78	10.5	0.25	1175
1	1	64	9.3	0.15	9.5	0.39	1.9	0.23	155
1	3	50	9.9	0.20	7.4	0.27	1.7	0.27	113
1	5	45	9.9	0.23	6.6	0.24	1.7	0.32	114

Table 7.1: The time-averaged global quantities of surface flux Φ_S, open flux Φ_O, the mean surface magnetic field $\langle B \rangle$, the filling factor between $\pm 40^\circ$ latitude f, the free energy E_F, the ratio of the free energy to the total energy E_F/E_T and the heating proxy j^2 determined from the simulations. D and K are the scaling factors for the flux emergence and differential rotation relative to solar respectively.

rates therefore increase with increasing differential rotation. Using these eruption rates with the mean number of flux ropes in the corona, the mean lifetime of flux ropes in each simulation can be calculated, and is 14.9, 12.1 and 9.7 days for 1, 3 and 5 times the solar differential rotation respectively. In Chapter 6 the lifetimes of the flux ropes were found to be 16, 6 and 3.5 days for 1, 3 and 5 times the solar differential rotation respectively. In the simulations carried out in this chapter, the lifetimes of the flux ropes are longer than those predicted in Chapter 6. This is likely to be due to the more complex field configuration where above each flux rope there is more overlying flux to provide it stability.

7.6 Discussion

In this chapter global simulations of the evolution of stellar coronae over one year of time have been run. In these simulations the effects of the flux emergence and differential rotation rates on the time-averaged flux, surface magnetic field, free magnetic energy and a heating proxy (current) were investigated. The number and spatial distributions of flux ropes in the coronae were investigated, and a technique to produce emission proxy images of the corona was developed.

In each simulation, the flux, mean surface magnetic fields, magnetic energies and heating proxy reached approximate steady states. These steady state values are displayed in Table 7.1. As the flux emergence rate is increased, the surface flux and open flux both increase, however the ratio of open to surface flux remains roughly constant. The near constant ratio of open to surface flux suggests that though the corona contains more flux, the general coronal configuration is unaffected by the increased flux emergence rate. As the differential rotation rate is increased, the surface flux decreases due to the increased length of polarity inversion lines, allowing flux cancellation to occur more efficiently. Whilst the surface flux decreases, the open flux remains almost constant, and thus the ratio of open to surface flux increases. This suggests that the differential rotation has an effect on the coronal structure, causing it to become more open. A more open corona may lead to a faster stellar wind, which may prove detrimental to exoplanetary atmospheres (See et al. 2014).

The mean surface field is found to increase with increasing flux emergence rate but decreases with increasing differential rotation rate. The increased flux emergence rate increases the mean surface field by adding more field to the photosphere, whilst the increasing differential rotation rate decreases the mean surface field by lengthening polarity

D	K	N	n_e (per day)	t_f (days)	t_l (days)	τ_{form} (days)	τ_{life} (days)
1	1	44	2.94	15	14.8	15	16
3	1	52	3.66	15	14.2	15	16
5	1	55	3.70	15	14.9	15	16
1	1	44	2.94	15	14.8	15	16
1	3	41	3.38	9	12.1	8	6
1	5	37	3.84	6	9.7	6	3.5

Table 7.2: The mean number of flux ropes N, mean number of erupting flux ropes n_e, formation time t_f and mean lifetime t_l for the simulations with D times the solar flux emergence rate and K times the solar differential rotation rate. Also provided are the formation times τ_{form} and the lifetimes τ_{life} determined in Chapter 6.

inversion lines, allowing more flux cancellation to occur. The filling factor (proportion of the stellar surface covered with field $> |10|$ G) increases with increasing flux emergence rate, and decreases with increasing differential rotation rate.

The free magnetic energy increases with increasing flux emergence rate. Whilst this is the case, the ratio of the free magnetic energy to the total magnetic energy remains relatively unchanged. The constant ratio of energies, along with the constant ratio of fluxes agrees with the interpretation made that the increased flux emergence does not affect the general configuration of the corona. Increasing the differential rotation rate has little effect on the free magnetic energy, however it increases the ratio of the free magnetic energy to the total energy. This along with the increasing ratio of open to surface flux agrees with the interpretation made that the increased differential rotation alters the coronal structure.

The volume integrated square of the current in the corona, which is used as a proxy for the coronal heating in this chapter, increases with increasing flux emergence rate. Increasing the differential rotation rate slightly decreases the heating proxy. If a link between the heating and coronal X-ray luminosity is assumed, the X-ray luminosity may increase with increasing flux emergence rate, and decrease slightly with increasing differential rotation rate. While at present this is speculation, it will be considered in more detail in future.

For all the quantities mentioned above, increasing the flux emergence rate by a factor of 5 has a far greater effect on their values than increasing the differential rotation rate by a factor of 5. It can thus be concluded that the flux emergence rate plays a far greater role in the coronal energetics, flux and heating than the differential rotation.

Similar to Chapters 3 and 4, emission proxy images of the stellar coronae were produced. The images were constructed by assuming the emission at each point in the corona was due to the local heating (j^2) and the plasma density (prescribed by assuming an isothermal, hydrostatic corona). These images, though crude, were able to reproduce features observed on the Sun, such as sigmoids and coronal holes. When the emission proxy images were compared to field line plots, the coronal holes were associated with open field regions, and the sigmoids were associated with flux ropes.

The flux ropes formed in the simulations were investigated. Various properties of the flux ropes for each simulation are displayed in Table 7.2. Also displayed are the lifetimes and formation times determined in Chapter 6. Using PILfinder, the mean number of flux ropes present on the stars at any given time were determined, along with their latitudinal distribution. Increasing the flux emergence rate slightly increased the number of flux ropes present in the corona, whilst increasing the differential rotation rate slightly decreased the number of flux ropes in the corona. Varying the flux emergence and differential rotation

rates had little effect on the latitudinal distribution of flux ropes, which peaked between 10° and 30° latitude. By measuring the length of time between the start of the simulation and the time that the first flux ropes formed, the formation times of the flux ropes could be estimated. These times were in agreement with the formation times determined in Chapter 6.

The flux rope eruption rates were determined by using FRfinder to locate flux ropes moving faster than 0.5 km s^{-1} upwards (Yeates & Mackay 2009). The eruption rates increased slightly with increasing flux emergence and differential rotation rates. These results suggest that planets situated around stars with low flux emergence and/or differential rotation rates may be exposed to fewer CMEs, and therefore their magnetospheres and atmospheres will be at lower risk of being eroded away (Khodachenko et al. 2007, Lammer et al. 2012). Since the number of flux ropes in the corona reached an approximate steady state, the formation rate of flux ropes had to be approximately equal to the eruption rate. Using the eruption rate and the number of flux ropes in the corona, it was possible to estimate the mean lifetime of the flux ropes. Increasing the emergence rate had little effect on the lifetime of the flux ropes, however increasing the differential rotation rate decreased the lifetime.

In this chapter an initial analysis on the results of the simulations has been presented. A more in-depth analysis of the results will be carried out in the future. Simulations have also only been run with solar differential rotation but varying the flux emergence rate, and with the solar flux emergence rate but varying the differential rotation. No simulations have been run with non-solar flux emergence and differential rotation rates at present. In the future a more complete parameter study of the effects of differential rotation and flux emergence on the coronal response will be carried out.

Chapter 8

Conclusions and Future Work

In this thesis a magnetofrictional method has been used to simulate time-evolving non-linear force-free coronal magnetic fields. In particular the formation and eruption of magnetic flux ropes that form in the simulations has been investigated. Both solar and stellar coronae were simulated, using observed magnetograms (for the solar case) and a surface flux transport model (for the stellar case) as a driver for the coronal magnetic field's evolution. The main results from each chapter will now be summarised.

In Chapter 2 the magnetofrictional method is described, along with the two FORTRAN codes used to carry out the simulations, Hexa and FFF3. Both these codes solve the induction equation, where the velocity is set to be proportional to the Lorentz force in accordance with the magnetofrictional method (Yang et al. 1986). Hexa solves the induction equation in a Cartesian coordinate system, and thus is applicable for use when simulating a small portion of the corona, where the size of the region being simulated is much smaller than the solar radius. FFF3, on the other hand, solves the induction equation in spherical coordinates, and can be used to simulate either a portion of, or the global corona. In addition to Hexa and FFF3, in Chapter 2 two IDL flux rope detection routines, FRfinder and PILfinder are described. FRfinder locates points belonging to a flux rope's axes by considering the tension and pressure components of the Lorentz force. Alternatively, PILfinder finds locations along a polarity inversion line where the horizontal component of the magnetic field is directed in the opposite direction to the normal to the polarity inversion line. As a result, FRfinder can locate flux ropes anywhere in the coronal volume, whilst PILfinder locates flux ropes low-down in the corona which are in contact with the photosphere.

Chapters 3 and 4 simulate the coronal evolution of the NOAA active region AR10977. Cleaned line of sight magnetograms from SOHO/MDI were used to drive the coronal evolution. Accompanying the magnetogram observations of AR10977 were X-ray observations from Hinode/XRT, which showed the formation of a sigmoid, a flare, and the sigmoid's subsequent eruption. The cleaning method was applied to remove noise and small-scale magnetic features such as network magnetic elements found at the boundaries of supergranular cells. The primary simulation was run using a potential field initial condition, and did not use any non-ideal effects such as Ohmic or hyper-diffusion. In this simulation, a flux rope formed at the location of the observed sigmoid. A number of days later the flux rope's field lines became too twisted for their evolution to be described by the magnetofrictional method. This behaviour suggests that the flux rope had become unstable. Interestingly, this occurred just a few hours after the observed flare. The flux within the flux rope at the time of the observed flare was determined to be 20% of the active region's flux. This was lower than the minimum amount of flux within the flux rope (30%) as

determined by Green et al. (2011). A method to produce emission proxy images of the coronal volume was developed so that the simulation could be directly compared to the X-ray images of the active region. The emission proxy images predicted emission at the same location as the observed X-ray sigmoid. The energy contained within the flux rope at the time of the observed flare was found to be 6.10×10^{30} erg. This amount was more than sufficient to account for the flare, and is in agreement with the flux rope's energy as determined by Savcheva et al. (2012). The evolution of the active region's helicity with time was found to be directly correlated with the observed rotation of the active region.

In addition to the primary simulation, several other simulations were run to bound the results of the primary simulation. One simulation was carried out using uncleaned magnetograms to determine the effect that the cleaning process had on the coronal evolution. In this simulation, the qualitative evolution of the corona was similar, though more noisy. Importantly, the formation (and subsequent instability) of the flux rope, in addition to its magnetic flux and the evolution of the magnetic helicity were all similar to the primary simulation. This demonstrated that driving the coronal evolution with cleaned magnetograms, though resulting in less noise, did not alter the large-scale evolution of the coronal field. Simulations were also run with hyperdiffusion and Ohmic diffusion. The results of the simulation with hyperdiffusion were very similar to the results of the primary simulation, though the emission proxy images appeared smoother due to the effect of the hyperdiffusion smoothing out gradients in the force-free parameter, α. In the simulation with Ohmic diffusion – which used a very large diffusive constant – no flux rope formed due to the strong diffusion.

Various simulations were run using different initial conditions to determine how sensitive the coronal evolution was to the initial condition. One simulation was run with a potential initial condition but starting two days later than the primary simulation, and two simulations were run with linear force-free initial conditions – one with positive force-free parameter, α, and one with negative α. In each of these simulations the coronal evolution was qualitatively similar to that of the primary simulation's. In the simulation with the later start time, and the simulation with the positive-α linear force-free initial condition the flux within the flux rope was found to be roughly 30% of the active region's flux. This is in agreement with the findings of Green et al. (2011). The flux contained within the flux rope in the simulation with the negative-α linear force-free initial condition was found to be only 10% of the active region's flux. The emission proxy images and field line plots were compared to the X-ray observations and showed that the simulation with the later start time, and the simulation with the positive-α linear force-free initial condition provided a far better fit to the observations than the simulation with the negative-α linear force-free initial condition. Finally, simulations were run at a higher resolution to determine the effects that numerical diffusion may have on the coronal evolution. In these simulations, the coronal evolution was qualitatively similar to the primary simulation, however the flux rope's field lines contained more twists, and the free magnetic energy was consistently higher.

In all simulations (save for the one with Ohmic diffusion) a flux rope formed at the location of the observed X-ray sigmoid, and the flux rope in every simulation became unstable at approximately the same time as the flare and eruption of the observed sigmoid. This demonstrates that the general results (formation and subsequent instability of the flux rope, etc...) are robust since they are relatively insensitive to the initial condition chosen.

In Chapter 5 the development of a procedure to produce proxy SOLIS synoptic magnetograms from SOHO/MDI and SDO/HMI magnetograms is presented. This is motivated

by the SOLIS telescopes being relocated from Kitt Peak to a new site, and thus SOLIS magnetograms are not available for the period of time when the telescopes are being re-located. The ongoing work of Yeates et al. (2007) employs SOLIS synoptic magnetograms to determine the properties of bipoles to be emerged into their long-term global simulations of the Sun's magnetic field. For the continuity of these simulations, synoptic magnetograms that are similar to those of SOLIS' must be available to fill the gaps in time where the SOLIS magnetograms are unavailable. This includes the present time when SOLIS is being relocated from Kitt Peak, but can also include times in the past when several synoptic magnetograms are unavailable for various reasons. To that end, synoptic magnetograms produced from SOHO/MDI (to fill in gaps in the data occurring prior to 2010) and SDO/HMI (to fill in the present gaps) are produced in a manner consistent to SOLIS synoptic magnetograms. These synoptic magnetograms are compared with the SOLIS synoptic magnetograms. The properties of bipoles as determined from SOLIS synoptic magnetograms are compared with the properties determined from the MDI and HMI synoptic magnetograms. Scaling factors (if required) were determined to ensure the properties determined from MDI or HMI synoptic magnetograms match those determined from the SOLIS synoptic magnetograms. As a demonstration, the list of bipoles to be emerged during Carrington Rotation 2152 as determined from HMI synoptic magnetograms was presented. Finally, it was concluded that HMI synoptic magnetograms may be a better source of synoptic magnetograms for the ongoing work of Yeates et al. (2007) than SOLIS' as they are not affected by poor weather and so possess fewer gaps.

In Chapter 6 the formation timescale and lifetime of flux ropes as a function of the surface transport effects of differential rotation and surface diffusion were investigated. This way the timescales of evolution of stellar coronae may be investigated. To achieve this, a portion of a stellar corona was simulated by FFF3. Situated in the corona was a decaying bipolar active region. Several simulations were run with different differential rotation rates and surface diffusion coefficients, and the times for flux ropes to form, and then erupt were determined for each simulation. It was found that the formation time of flux ropes scaled with the equator-pole lap time of differential rotation and the timescale of surface diffusion by

$$\tau_{\text{Form}} \propto \sqrt{\tau_{\text{Lap}}\tau_{\text{Diff}}}, \tag{8.1}$$

whilst the lifetime of the flux ropes was found to be

$$\tau_{\text{Life}} \approx \tau_{\text{shear}} \propto \tau_{\text{Lap}}. \tag{8.2}$$

The above relations state that as the differential rotation rate of a star increases (lap time decreases) the formation and lifetimes of flux ropes decrease. Given the link between differential rotation and effective temperature (e.g. Barnes et al. (2005)), flux ropes on hotter (earlier) stars will have shorter formation times and lifetimes. For stars with more than eight times the solar differential rotation rate the lifetimes of flux ropes are less than two days. On such stars it was proposed that features such as quiescent prominences are unlikely to be observed as the flux ropes that likely support them are short-lived. The initial tilt angle of the bipole was found to have little effect on the formation times of flux ropes as long as the tilt angle was less than $\sim 45°$. The effects of the meridional flow on the formation and lifetimes were discussed. For low differential rotation stars the meridional flow rate would have to be $\gtrsim 10$ times the solar flow rate to significantly alter the formation or lifetimes of the flux ropes. On high differential rotation stars, the meridional flow rate would have to be even higher.

Chapter 7 extended the work of Chapter 6 to long-term global simulations of stellar coronae. These simulations were run using a modified version of FFF3 which employed a

variable resolution grid. In these simulations, the coronal response to differential rotation and flux emergence was investigated. A bipole emergence model was developed to mimic the flux emergence profile of the Sun between January 2000 and January 2001. This bipole emergence model could have its flux emergence rate varied, so that different emergence rates could be studied. In the simulations, the evolution of the surface and open flux, mean surface magnetic fields, free magnetic energy and the formation/eruption of flux ropes was investigated. In each simulation these quantities reached steady states after 100-200 days. In the simulations where the flux emergence rate was varied, it was found that increasing the flux emergence rate increased the surface and open flux, though the ratio of the surface to the open flux remained unchanged. The mean surface magnetic field and filling factor were also found to increase with increasing flux emergence rate, along with the free magnetic energy and the j^2 proxy for the amount of coronal heating. While the free magnetic energy increased, the ratio of free magnetic energy to the total energy remained unchanged. The number of flux ropes in the corona at any one time was found to increase slightly with increasing flux emergence rate, as did their eruption rate. The formation times and lifetimes of flux ropes were found to be insensitive to the flux emergence rate, and were in agreement with the timescales found in Chapter 6. As the differential rotation rate was increased, the surface flux decreased and the open flux remained unchanged. The ratio of the open to surface flux thus increased. The mean surface magnetic fields and filling factor also decreased with increasing differential rotation rate. The free magnetic energy was insensitive to the differential rotation rate, though the ratio of free to total magnetic energy increased with increasing differential rotation rate. The j^2 proxy for heating slightly decreased with increasing differential rotation rate. The number of flux ropes present in the corona at any one time slightly decreased with increasing differential rotation rate, whilst the eruption rate slightly increased. The formation times for the flux ropes were found to be in agreement with the times found in Chapter 6. The lifetimes, although displaying the same trend (decreasing lifetime with increasing differential rotation rate), were higher than those found in Chapter 6. This is attributed to the coronal field providing stability to the flux ropes. Emission proxy images were produced of the simulated coronae. Visible in the emission proxy images were features such as sigmoids and coronal holes. These were associated with flux ropes and large, monopolar open field regions respectively. In summary, the flux emergence rate plays a much greater role in the energetics of stellar coronae than the differential rotation. The differential rotation does, however lead to a more open coronal configuration. Stars with low flux emergence rates and low differential rotation were postulated to be the most ideal for exoplanets to be situated around to protect their magnetospheres and atmospheres from stellar winds/CMEs.

8.1 Future Work

There are many possible avenues for future work. Firstly, given that in Chapters 3 and 4 it was demonstrated that the magnetofrictional method is able to simulate the formation of a flux rope in an active region using observed magnetograms, it would be interesting to run similar simulations of other active regions and compare them with coronal observations to test how robust the modelling technique is. If it is found that the magnetofrictional method is able to correctly predict the formation (and instability) of flux ropes in the majority of cases, it could be used in the future to model the coronal fields of active regions in real time. This could allow for the prediction of solar flares and eruptions.

In Chapter 6, the effects of the meridional flow on the coronal timescales were only

speculated at. Running simulations to determine the effects would be useful, since Mackay et al. (2004) found that the meridional flow on some stars (such as AB Doradus) may be around ten times the solar rate. Additionally, many stars (AB Doradus included) possess strong polar fields, and thus investigating the longevity of flux ropes on such stars may be of interest.

In Chapter 7 the coronal response to the flux emergence rate was investigated for stars with solar differential rotation, and the coronal response to the differential rotation rate was investigated for stars with the solar flux emergence rate. The next logical step is to study the effects of enhanced flux emergence and differential rotation rates simultaneously. It would also be interesting to study the effects of the surface diffusion and meridional flow on the coronal evolution. The coronal evolution could also be investigated for non-solar flux emergence profiles (e.g. a different latitudinal distribution of emerging bipoles, different tilt angle distribution). This work could also be extended to study the coronal evolution over a whole stellar activity cycle.

The emission proxy method developed in Chapter 7 was used to visualise the stellar coronae, and produced features that are present in coronal observations of the Sun. A good test for this emission proxy technique would be to use it to produce images of the solar corona as simulated by Yeates (2014) and compare these to the corresponding coronal observations. This would allow a direct comparison between the simulations of Yeates (2014) and solar coronal observations.

Finally, the magnetofrictional method produces a force-free coronal magnetic field. It may be possible to include plasma into magnetofriction, such that instead of finding force-free equilibria (e.g. $\mathbf{j}\times\mathbf{B} = 0$) it finds magnetohydrostatic equilibria (e.g. $\rho\mathbf{g} - \nabla p + \mathbf{j}\times\mathbf{B} = 0$). This is more applicable for a global model than the current magnetofrictional technique used, as the force-free approximation is strictly only valid for length scales shorter than the pressure scale height. For such a model, the plasma density and temperature must be included. The inclusion of density and temperature opens up the possibility of producing more physically realistic emission proxies.

Appendices

Appendix A

Detailed Description of the Calculations Carried Out in Hexa and FFF3

In this appendix the calculations carried out by Hexa and FFF3 on their numerical grids are given in full. Firstly, the Hexa calculations will be given. Secondly, the FFF3 calculations will be given, however we only describe the FFF3 calculations that differ significantly from Hexa.

A.1 Hexa

A.1.1 Calculation of B

Firstly the magnetic field is calculated on the cell faces within the grid (i.e. neglecting ghost cells). B_x is calculated by:

$$B_x(i, j+\tfrac{1}{2}, k+\tfrac{1}{2}) = \frac{A_z(i, j+1, k+\frac{1}{2}) - A_z(i, j, k+\frac{1}{2})}{\Delta y} - \frac{A_y(i, j+\frac{1}{2}, k+1) - A_z(i, j+\frac{1}{2}, k)}{\Delta z} \quad \text{(A.1)}$$

for $i = 1 : N_x + 1$; $j = 1 : N_y$ and $k = 1 : N_z$. Similarly:

$$B_y(i+\tfrac{1}{2}, j, k+\tfrac{1}{2}) = \frac{A_x(i+\frac{1}{2}, j, k+1) - A_x(i+\frac{1}{2}, j, k)}{\Delta z} - \frac{A_z(i+1, j, k+\frac{1}{2}) - A_z(i, j, k+\frac{1}{2})}{\Delta x} \quad \text{(A.2)}$$

for $i = 1 : N_x$, $j = 1 : N_y + 1$ and $k = 1 : N_z$. Finally:

$$B_z(i+\tfrac{1}{2}, j+\tfrac{1}{2}, k) = \frac{A_y(i+1, j+\frac{1}{2}, k) - A_y(i, j+\frac{1}{2}, k)}{\Delta x} - \frac{A_x(i+\frac{1}{2}, j+1, k) - A_x(i+\frac{1}{2}, j, k)}{\Delta y} \quad \text{(A.3)}$$

for $i = 1 : N_x$, $j = 1 : N_y$ and $k = 1 : N_z + 1$.

Secondly the boundary conditions are applied. These are

$$B_x(i,\tfrac{1}{2},k+\tfrac{1}{2}) = B_x(i,1+\tfrac{1}{2},k+\tfrac{1}{2}) \tag{A.4}$$
$$B_x(i,N_y+\tfrac{1}{2},k+\tfrac{1}{2}) = B_x(i,N_y-\tfrac{1}{2},k+\tfrac{1}{2}) \tag{A.5}$$
$$B_x(i,j+\tfrac{1}{2},\tfrac{1}{2}) = B_x(i,j+\tfrac{1}{2},1+\tfrac{1}{2}) - \Delta z\frac{B_z(i+1-\frac{1}{2},j+\frac{1}{2},1+\frac{1}{2}) - B_z(i-\frac{1}{2},j+\frac{1}{2},1+\frac{1}{2})}{\Delta x} \tag{A.6}$$
$$B_x(i,j+\tfrac{1}{2},N_z+1+\tfrac{1}{2}) = B_x(i,j+\tfrac{1}{2},N_z+\tfrac{1}{2}) \tag{A.7}$$

for all i; $j = 0 : N_y + 1$ and $k = 1 : N_z$. Similarly

$$B_y(\tfrac{1}{2},j,k+\tfrac{1}{2}) = B_y(1+\tfrac{1}{2},j,k+\tfrac{1}{2}) \tag{A.8}$$
$$B_y(N_x+1+\tfrac{1}{2},j,k+\tfrac{1}{2}) = B_y(N_x+\tfrac{1}{2},j,k+\tfrac{1}{2}) \tag{A.9}$$
$$B_y(i+\tfrac{1}{2},j,\tfrac{1}{2}) = B_y(i+\tfrac{1}{2},j,1+\tfrac{1}{2}) - \Delta z\frac{B_z(i+\frac{1}{2},j+1+\frac{1}{2},1+\frac{1}{2}) - B_z(i+\frac{1}{2},j+\frac{1}{2},1+\frac{1}{2})}{\Delta y} \tag{A.10}$$
$$B_y(i+\tfrac{1}{2},j,N_z+1+\tfrac{1}{2}) = B_y(i+\tfrac{1}{2},j,N_z+\tfrac{1}{2}) \tag{A.11}$$

for $i = 0 : N_x + 1$, all j and $k = 1 : N_z$. Finally

$$B_z(\tfrac{1}{2},j+\tfrac{1}{2},k) = B_z(1+\tfrac{1}{2},j+\tfrac{1}{2},k) \tag{A.12}$$
$$B_z(N_x+1+\tfrac{1}{2},j+\tfrac{1}{2},k) = B_z(N_x+\tfrac{1}{2},j+\tfrac{1}{2},k) \tag{A.13}$$
$$B_z(i+\tfrac{1}{2},\tfrac{1}{2},k) = B_z(i+\tfrac{1}{2},1+\tfrac{1}{2},k) \tag{A.14}$$
$$B_z(i+\tfrac{1}{2},N_y+\tfrac{1}{2},k) = B_z(i+\tfrac{1}{2},N_y-\tfrac{1}{2},k) \tag{A.15}$$

for $i = 0 : N_x + 1$, $y = 0 : N_y + 1$ and all k.

Lastly the magnetic field is averaged onto cell corners. For B_z the magnetic field at a corner is calculated by:

$$B_x(i,j,k) = \frac{B_x(i,j-\frac{1}{2},k-\frac{1}{2}) + B_x(i,j+\frac{1}{2},k-\frac{1}{2}) + B_x(i,j-\frac{1}{2},k+\frac{1}{2}) + B_x(i,j+\frac{1}{2},k+\frac{1}{2})}{4} \tag{A.16}$$

$$B_y(i,j,k) = \frac{B_y(i-\frac{1}{2},j,k-\frac{1}{2}) + B_y(i+\frac{1}{2},j,k-\frac{1}{2}) + B_y(i-\frac{1}{2},j,k+\frac{1}{2}) + B_y(i+\frac{1}{2},j,k+\frac{1}{2})}{4} \tag{A.17}$$

$$B_z(i,j,k) = \frac{B_z(i-\frac{1}{2},j-\frac{1}{2},k) + B_z(i+\frac{1}{2},j-\frac{1}{2},k) + B_z(i-\frac{1}{2},j+\frac{1}{2},k) + B_z(i+\frac{1}{2},j+\frac{1}{2},k)}{4} \tag{A.18}$$

for $i = 1 : N_x + 1$; $j = 1 : N_y + 1$ and $k = 1 : N_z + 1$.

A.1.2 Calculation of j

The current density is calculated by $\mathbf{j} = \nabla \times \mathbf{B}$. It is calculated from the face values of $\mathbf{B}$, and is calculated onto the ribs - including ribs located in the ghost cells. The calculation is carried out as follows:

$$j_x(i+\tfrac{1}{2},j,k) = \frac{B_z(i+\frac{1}{2},j+\frac{1}{2},k) - B_z(i+\frac{1}{2},j-\frac{1}{2},k)}{\Delta y} - \frac{B_y(i+\frac{1}{2},j,k+\frac{1}{2}) - B_y(i+\frac{1}{2},j,k-\frac{1}{2})}{\Delta z} \quad \text{(A.19)}$$

for $i = 0 : N_x + 1$; $j = 1 : N_y + 1$ and $k = 1 : N_z + 1$;

$$j_y(i,j+\tfrac{1}{2},k) = \frac{B_x(i,j+\frac{1}{2},k+\frac{1}{2}) - B_x(i,j+\frac{1}{2},k-\frac{1}{2})}{\Delta z} - \frac{B_z(i+\frac{1}{2},j+\frac{1}{2},k) - B_z(i-\frac{1}{2},j+\frac{1}{2},k)}{\Delta x} \quad \text{(A.20)}$$

for $i = 1 : N_x + 1$; $j = 0 : N_y + 1$ and $k = 1 : N_z + 1$;

$$j_z(i,j,k+\tfrac{1}{2}) = \frac{B_y(i+\frac{1}{2},j,k+\frac{1}{2}) - B_y(i-\frac{1}{2},j,k+\frac{1}{2})}{\Delta x} - \frac{B_x(i,j+\frac{1}{2},k+\frac{1}{2}) - B_x(i,j-\frac{1}{2},k+\frac{1}{2})}{\Delta y} \quad \text{(A.21)}$$

for $i = 1 : N_x + 1$; $j = 1 : N_y + 1$ and $k = 0 : N_z + 1$.

The values of $\mathbf{j}$ are then averaged onto cell corners. Each component of $\mathbf{j}$ at the cell corner is calculated from the average of the two nearest rib values. The calculation is carried out as follows:

$$j_x(i,j,k) = \frac{j_x(i+\frac{1}{2},j,k) + j_x(i-\frac{1}{2},j,k)}{2} \quad \text{(A.22)}$$

$$j_y(i,j,k) = \frac{j_y(i,j+\frac{1}{2},k) + j_y(i,j-\frac{1}{2},k)}{2} \quad \text{(A.23)}$$

$$j_z(i,j,k) = \frac{j_z(i,j,k+\frac{1}{2}) + j_z(i,j,k-\frac{1}{2})}{2} \quad \text{(A.24)}$$

for $i = 1 : N_x + 1$; $j = 1 : n_y + 1$ and $k = 1 : N_z + 1$.

A.1.3 Magnetofrictional Velocity

In order to calculate the magnetofrictional velocity,

$$\mathbf{v} = \frac{1}{\nu}\frac{\mathbf{j} \times \mathbf{B}}{B^2}, \quad \text{(A.25)}$$

we first need to calculate B^2 at the cell corners. Since all the components of $\mathbf{B}$ have already been averaged onto cell corners, the calculation is simply:

$$B^2(i,j,k) = B_x(i,j,k)^2 + B_y(i,j,k)^2 + B_z(i,j,k)^2 \quad \text{(A.26)}$$

for $i = 1 : N_x + 1$; $j = 1 : N_y + 1$ and $k = 1 : N_z + 1$. The maximum value of B^2, $B^2_{\max}$ is determined. At any point on the grid where B^2 is less than $0.0001B^2_{\max}$, the value of B^2 at this point is set to $0.0001B^2_{\max}$.

The magnetofrictional velocity is then calculated on cell corners by:

$$v_x(i,j,k) = \frac{1}{\nu}\left(\frac{j_y(i,j,k)B_z(i,j,k) - j_z(i,j,k)B_y(i,j,k)}{B^2(i,j,k)}\right) \tag{A.27}$$

$$v_y(i,j,k) = \frac{1}{\nu}\left(\frac{j_z(i,j,k)B_x(i,j,k) - j_x(i,j,k)B_z(i,j,k)}{B^2(i,j,k)}\right) \tag{A.28}$$

$$v_z(i,j,k) = \frac{1}{\nu}\left(\frac{j_x(i,j,k)B_y(i,j,k) - j_y(i,j,k)B_x(i,j,k)}{B^2(i,j,k)}\right) \tag{A.29}$$

for $i = 1 : N_x + 1$; $j = 1 : N_y + 1$ and $k = 1 : N_z + 1$.

$\mathbf{v} \times \mathbf{B}$, the advective term, is then calculated at the corners by

$$(\mathbf{v} \times \mathbf{B})_x(i,j,k) = v_y(i,j,k)B_z(i,j,k) - v_z(i,j,k)B_y(i,j,k) \tag{A.30}$$

$$(\mathbf{v} \times \mathbf{B})_y(i,j,k) = v_z(i,j,k)B_x(i,j,k) - v_x(i,j,k)B_z(i,j,k) \tag{A.31}$$

$$(\mathbf{v} \times \mathbf{B})_z(i,j,k) = v_x(i,j,k)B_y(i,j,k) - v_y(i,j,k)B_x(i,j,k) \tag{A.32}$$

for $i = 1 : N_x + 1$; $j = 1 : N_y + 1$ and $k = 1 : N_z + 1$.

This must now be averaged onto cell ribs. This is achieved by

$$(\mathbf{v} \times \mathbf{B})_x(i + \tfrac{1}{2}, j, k) = \frac{(\mathbf{v} \times \mathbf{B})_x(i+1,j,k) + (\mathbf{v} \times \mathbf{B})_x(i,j,k)}{2} \tag{A.33}$$

for $i = 1 : N_x$; $j = 1 : N_y + 1$ and $k = 1 : N_z + 1$;

$$(\mathbf{v} \times \mathbf{B})_y(i, j + \tfrac{1}{2}, k) = \frac{(\mathbf{v} \times \mathbf{B})_y(i,j+1,k) + (\mathbf{v} \times \mathbf{B})_y(i,j,k)}{2} \tag{A.34}$$

for $i = 1 : N_x + 1$; $j = 1 : N_y$ and $k = 1 : N_z + 1$; and

$$(\mathbf{v} \times \mathbf{B})_z(i, j, k + \tfrac{1}{2}) = \frac{(\mathbf{v} \times \mathbf{B})_z(i,j,k+1) + (\mathbf{v} \times \mathbf{B})_z(i,j,k)}{2} \tag{A.35}$$

for $i = 1 : N_x + 1$; $j = 1 : N_y + 1$ and $k = 1 : N_z$.

A.1.4 Hyperdiffusion

The hyperdiffusive term is

$$\frac{\mathbf{B}}{B^2}\nabla \cdot \left(\eta_4 B^2 \nabla \alpha\right). \tag{A.36}$$

First, α must be determined. This is achieved by calculating

$$\alpha(i,j,k) = \frac{j_x(i,j,k)B_x(i,j,k) + j_y(i,j,k)B_y(i,j,k) + j_z(i,j,k)B_z(i,j,k)}{B^2(i,j,k)} \tag{A.37}$$

for $i = 1 : N_x + 1$; $j = 1 : N_y + 1$ and $k = 1 : N_z + 1$ at cell corners. Next the gradient of α is calculated on the ribs by:

$$(\nabla\alpha)_x(i + \tfrac{1}{2}, j, k) = \frac{\alpha(i+1,j,k) - \alpha(i,j,k)}{\Delta x} \tag{A.38}$$

for $i = 1 : N_x$; $j = 1 : N_y + 1$ and $k = 1 : N_z + 1$;

$$(\nabla\alpha)_y(i, j + \tfrac{1}{2}, k) = \frac{\alpha(i, j + 1, k) - \alpha(i, j, k)}{\Delta y} \tag{A.39}$$

for $i = 1 : N_x + 1$; $j = 1 : N_y$ and $k = 1 : N_z + 1$;

$$(\nabla\alpha)_z(i, j, k + \tfrac{1}{2}) = \frac{\alpha(i, j, k + 1) - \alpha(i, j, k)}{\Delta z} \tag{A.40}$$

for $i = 1 : N_x + 1$; $j = 1 : N_y + 1$ and $k = 1 : N_z$. B^2 must then be averaged onto the cell ribs. This is carried out by the same process as that for averaging the advective term onto the ribs (Equations A.33 to A.35). Next the quantity $\eta_4 B^2 \nabla\alpha$ is determined. As its divergence must be calculated, ghost cells are required on the boundary. These ghost cells are set so that the gradients of $\eta_4 B^2 \nabla\alpha$ normal to the boundaries are set to zero. The divergence of this quantity is calculated on the cell corners (where we have written $\eta_4 B^2 \nabla\alpha$ as Ψ for brevity) by:

$$\nabla \cdot \Psi(i, j, k) = \frac{\Psi(i + \frac{1}{2}, j, k) - \Psi(i + \frac{1}{2} - 1, j, k)}{\Delta x} + \frac{\Psi(i, j + \frac{1}{2}, k) - \Psi(i, j + \frac{1}{2} - 1, k)}{\Delta y} + \frac{\Psi(i, j, k + \frac{1}{2}) - \Psi(i, j, k + \frac{1}{2} - 1)}{\Delta z} \tag{A.41}$$

for $i = 1 : N_x + 1$; $j = 1 : N_y + 1$ and $k = 1 : N_z + 1$. Next $\frac{\mathbf{B}}{B^2}\nabla \cdot \left(\eta_4 B^2 \nabla\alpha\right)$ is calculated on the cell corners by:

$$\left(\frac{B_x}{B^2}\nabla \cdot \left(\eta_4 B^2 \nabla\alpha\right)\right)(i, j, k) = \frac{B_x(i, j, k)}{B^2(i, j, k)}\left[\nabla \cdot \left(\eta_4 B^2 \nabla\alpha\right)(i, j, k)\right] \tag{A.42}$$

$$\left(\frac{B_y}{B^2}\nabla \cdot \left(\eta_4 B^2 \nabla\alpha\right)\right)(i, j, k) = \frac{B_y(i, j, k)}{B^2(i, j, k)}\left[\nabla \cdot \left(\eta_4 B^2 \nabla\alpha\right)(i, j, k)\right] \tag{A.43}$$

$$\left(\frac{B_z}{B^2}\nabla \cdot \left(\eta_4 B^2 \nabla\alpha\right)\right)(i, j, k) = \frac{B_z(i, j, k)}{B^2(i, j, k)}\left[\nabla \cdot \left(\eta_4 B^2 \nabla\alpha\right)(i, j, k)\right] \tag{A.44}$$

Finally the hyperdiffusive term is averaged onto the cell ribs, in the same manner as averaging the advective term onto the ribs (Equations A.33 to A.35).

A.1.5 Diffusion of $\nabla \cdot \mathbf{A}$

The diffusive term is

$$\eta_0 \nabla(\nabla \cdot \mathbf{A}) \tag{A.45}$$

In order to calculate this term, first the divergence of the vector potential is found at cell corners within the computational box by

$$\nabla \cdot \mathbf{A}(i, j, k) = \frac{\mathbf{A}(i + \frac{1}{2}, j, k) - \mathbf{A}(i + \frac{1}{2} - 1, j, k)}{\Delta x} + \frac{\mathbf{A}(i, j + \frac{1}{2}, k) - \mathbf{A}(i, j + \frac{1}{2} - 1, k)}{\Delta y} + \frac{\mathbf{A}(i, j, k + \frac{1}{2}) - \mathbf{A}(i, j, k + \frac{1}{2} - 1)}{\Delta z}. \tag{A.46}$$

for $i = 2 : N_x$; $j = 2 : N_y$ and $k = 2 : N_z$. $\nabla \cdot \mathbf{A}$ is set to zero along the top and sides of the computational box, and is calculated to be

$$\nabla \cdot \mathbf{A}(i,j,1) = \frac{\mathbf{A}(i+\frac{1}{2},j,1) - \mathbf{A}(i+\frac{1}{2}-1,j,1)}{\Delta x} + \frac{\mathbf{A}(i,j+\frac{1}{2},1) - \mathbf{A}(i,j+\frac{1}{2}-1,1)}{\Delta y} \tag{A.47}$$

along the base of the computational box for $i = 2 : N_x$ and $j = 2 : N_y$. Finally, the gradient of this quantity is calculated on the cell ribs (in the same way as it is achieved in Equations A.38 to A.40) and is then multiplied by η_0.

A.2 FFF3

FFF3 employs a uniformly spaced numerical grid using the variables (x, y, z) defined by:

$$x(\phi) = \frac{\phi}{\Delta} \tag{A.48}$$

$$y(\theta) = \frac{-\ln\left(\tan\frac{\theta}{2}\right)}{\Delta} \tag{A.49}$$

$$z(r) = \frac{\ln\left(\frac{r}{R_*}\right)}{\Delta} \tag{A.50}$$

and therefore

$$\phi(x) = x\Delta \tag{A.51}$$

$$\theta(y) = 2\arctan\left(e^{-y\Delta}\right) \tag{A.52}$$

$$r(z) = R_\odot e^{z\Delta} \tag{A.53}$$

where Δ is the grid spacing in radians.

A.2.1 Grid Spacing

Since the grid spacing in FFF3 $(h_x, h_y, h_z) = (r\Delta\sin\theta, r\Delta\sin\theta, r\Delta)$ is dependent upon r and θ, this must be taken into account in derivatives. On the staggered grid, since different quantities are located on different points of a grid cell, each quantity has its own (h_x, h_y, h_z) value. At a cell corner (integer value of (x, y, z)), these variables are

$$h_x(i,j,k) = r(k)\Delta\sin\theta(j), \tag{A.54}$$

$$h_y(i,j,k) = r(k)\Delta\sin\theta(j), \tag{A.55}$$

$$h_z(i,j,k) = r(k)\Delta, \tag{A.56}$$

for $i = 1 : N_x + 1$; $j = 1 : N_y + 1$ and $k = 1 : N_z + 1$. At the x-ribs we have

$$h_{x_{A_x}}(i+\tfrac{1}{2},j,k) = r(k)\Delta\sin\theta(j), \tag{A.57}$$

$$h_{y_{A_x}}(i+\tfrac{1}{2},j,k) = r(k)\Delta\sin\theta(j), \tag{A.58}$$

$$h_{z_{A_x}}(i+\tfrac{1}{2},j,k) = r(k)\Delta, \tag{A.59}$$

for $i = 1 : N_x$; $j = 1 : N_y + 1$ and $k = 1 : N_z + 1$. At the y-ribs:

$$h_{x_{A_y}}(i,j+\tfrac{1}{2},k) = r(k)\Delta\sin\theta(j+\tfrac{1}{2}), \tag{A.60}$$

$$h_{y_{A_y}}(i,j+\tfrac{1}{2},k) = r(k)\Delta\sin\theta(j+\tfrac{1}{2}), \tag{A.61}$$

$$h_{z_{A_y}}(i,j+\tfrac{1}{2},k) = r(k)\Delta, \tag{A.62}$$

for $i = 1 : N_x + 1$; $j = 1 : N_y$ and $k = 1 : N_z + 1$. At the z-ribs:

$$h_{x_{A_z}}(i, j, k + \tfrac{1}{2}) = r(k + \tfrac{1}{2})\Delta \sin\theta(j), \tag{A.63}$$
$$h_{y_{A_z}}(i, j, k + \tfrac{1}{2}) = r(k + \tfrac{1}{2})\Delta \sin\theta(j), \tag{A.64}$$
$$h_{z_{A_z}}(i, j, k + \tfrac{1}{2}) = r(k + \tfrac{1}{2})\Delta, \tag{A.65}$$

for $i = 1 : N_x + 1$; $j = 1 : N_y + 1$ and $k = 1 : N_z$. Finally, the length variables must also be defined at cell faces. At an x-face:

$$h_{x_{B_x}}(i, j + \tfrac{1}{2}, k + \tfrac{1}{2}) = r(k + \tfrac{1}{2})\Delta \sin\theta(j + \tfrac{1}{2}), \tag{A.66}$$
$$h_{y_{B_x}}(i, j + \tfrac{1}{2}, k + \tfrac{1}{2}) = r(k + \tfrac{1}{2})\Delta \sin\theta(j + \tfrac{1}{2}), \tag{A.67}$$
$$h_{z_{B_x}}(i, j + \tfrac{1}{2}, k + \tfrac{1}{2}) = r(k + \tfrac{1}{2})\Delta, \tag{A.68}$$

for $i = 1 : N_x + 1$; $j = 1 : N_y + 1$ and $k = 1 : N_z + 1$. At a y-face:

$$h_{x_{B_y}}(i, j, k + \tfrac{1}{2}) = r(k + \tfrac{1}{2})\Delta \sin\theta(j), \tag{A.69}$$
$$h_{y_{B_y}}(i, j, k + \tfrac{1}{2}) = r(k + \tfrac{1}{2})\Delta \sin\theta(j), \tag{A.70}$$
$$h_{z_{B_y}}(i, j, k + \tfrac{1}{2}) = r(k + \tfrac{1}{2})\Delta, \tag{A.71}$$

for $i = 1 : N_x + 1$; $j = 1 : N_y + 1$ and $k = 1 : N_z + 1$. Finally, at a z-face:

$$h_{x_{B_z}}(i, j + \tfrac{1}{2}, k) = r(k)\Delta \sin\theta(j + \tfrac{1}{2}), \tag{A.72}$$
$$h_{y_{B_z}}(i, j + \tfrac{1}{2}, k) = r(k)\Delta \sin\theta(j + \tfrac{1}{2}), \tag{A.73}$$
$$h_{z_{B_z}}(i, j + \tfrac{1}{2}, k) = r(k)\Delta, \tag{A.74}$$

for $i = 1 : N_x + 1$; $j = 1 : N_y + 1$ and $k = 1 : N_z + 1$.

A.2.2 Calculation of B

The magnetic field is calculated using Stokes' theorem. The x, y and z components of the magnetic field are calculated by

$$B_x(i, j + \tfrac{1}{2}, k + \tfrac{1}{2}) = \frac{[A_y h_{y_{A_y}}](i,j+\frac{1}{2},k)+[A_z h_{z_{A_z}}](i,j+1,k+\frac{1}{2})-[A_y h_{y_{A_y}}](i,j+\frac{1}{2},k+1)-[A_z h_{z_{A_z}}](i,j,k+\frac{1}{2})}{[h_{z_{B_x}} h_{y_{B_x}}](i,j+\frac{1}{2},k+\frac{1}{2})}, \tag{A.75}$$

for $i = 1, ...N_x + 1$, $j = 1, ..., N_y$ and $k = 1, ..., N_z$.

$$B_y(i + \tfrac{1}{2}, j, k + \tfrac{1}{2}) = \frac{[A_x h_{x_{A_x}}](i+\frac{1}{2},j,k+1)-[A_z h_{z_{A_z}}](i+1,j,k+\frac{1}{2})-[A_x h_{x_{A_x}}](i+\frac{1}{2},j,k)+[A_z h_{z_{A_z}}](i,j,k+\frac{1}{2})}{[h_{x_{B_y}} h_{z_{B_y}}](i+\frac{1}{2},j,k+\frac{1}{2})}, \tag{A.76}$$

for $i = 1, ...N_x$, $j = 1, ..., N_y + 1$ and $k = 1, ..., N_z$.

$$B_z(i + \tfrac{1}{2}, j + \tfrac{1}{2}, k) = \frac{[A_y h_{y_{A_y}}](i+1,j+\frac{1}{2},k)-[A_x h_{x_{A_x}}](i+\frac{1}{2},j+1,k)-[A_y h_{y_{A_y}}](i,j+\frac{1}{2},k)+[A_x h_{x_{A_x}}](i+\frac{1}{2},j,k)}{[h_{x_{B_z}} h_{y_{B_z}}](i+\frac{1}{2},j+\frac{1}{2},k)} \tag{A.77}$$

for $i = 1, ...N_x$, $j = 1, ..., N_y$ and $k = 1, ..., N_z + 1$, where we have used the shorthand $[AB](i, j, k) = A(i, j, k)B(i, j, k)$.

Boundary conditions are then applied to fill the ghost cells. At the top and bottom boundaries:

$$B_x(i,j+\tfrac{1}{2},\tfrac{1}{2}) = \frac{[B_x h_{x_{B_x}}](i,j+\frac{1}{2},1+\frac{1}{2}) - [B_z h_{z_{B_z}}](i+\frac{1}{2},j+\frac{1}{2},1) + [B_z h_{z_{B_z}}](i-\frac{1}{2},j+\frac{1}{2},1)}{[h_{x_{B_x}}](i,j+\frac{1}{2},\frac{1}{2})} \tag{A.78}$$

$$B_x(i,j+\tfrac{1}{2},N_z+1+\tfrac{1}{2}) = B_x(i,j+\tfrac{1}{2},N_z+\tfrac{1}{2}) \tag{A.79}$$

$$B_y(i+\tfrac{1}{2},j,\tfrac{1}{2}) = \frac{[B_z h_{z_{B_z}}](i+\frac{1}{2},j+\frac{1}{2},1) + [B_y h_{y_{B_y}}](i+\frac{1}{2},j,1+\frac{1}{2}) - [B_z h_{z_{B_z}}](i+\frac{1}{2},j-\frac{1}{2},1)}{[h_{y_{B_y}}](i+\frac{1}{2},j,\frac{1}{2})} \tag{A.80}$$

$$B_y(i+\tfrac{1}{2},j,N_z+1+\tfrac{1}{2}) = B_y(i+\tfrac{1}{2},j,N_z+\tfrac{1}{2}) \tag{A.81}$$

At the latitudinal boundaries:

$$B_x(i,\tfrac{1}{2},k+\tfrac{1}{2}) = B_x(i,1+\tfrac{1}{2},k+\tfrac{1}{2})\frac{h_{x_{B_x}}(i,1+\frac{1}{2},k+\frac{1}{2})}{h_{x_{B_x}}(i,\frac{1}{2},k+\frac{1}{2})} \tag{A.82}$$

$$B_x(i,N_y+1+\tfrac{1}{2},k+\tfrac{1}{2}) = B_x(i,N_y+\tfrac{1}{2},k+\tfrac{1}{2})\frac{h_{x_{B_x}}(i,N_y+\frac{1}{2},k+\frac{1}{2})}{h_{x_{B_x}}(i,N_y+\frac{1}{2}+1,k+\frac{1}{2})} \tag{A.83}$$

$$B_z(i+\tfrac{1}{2},\tfrac{1}{2},k) = B_z(i+\tfrac{1}{2},1+\tfrac{1}{2},k)\frac{h_{z_{B_z}}(i+\frac{1}{2},1+\frac{1}{2},k)}{h_{z_{B_z}}(i+\frac{1}{2},\frac{1}{2},k)} \tag{A.84}$$

$$B_z(i+\tfrac{1}{2},N_y+1+\tfrac{1}{2},k) = B_z(i+\tfrac{1}{2},N_y+\tfrac{1}{2},k)\frac{h_{z_{B_z}}(i+\frac{1}{2},N_y+\frac{1}{2},k)}{h_{z_{B_z}}(i+\frac{1}{2},N_y+1+\frac{1}{2},k)} \tag{A.85}$$

At the longitudinal boundaries:

$$B_y(\tfrac{1}{2},j,k+\tfrac{1}{2}) = B_y(N_x+\tfrac{1}{2},j,k+\tfrac{1}{2}) \tag{A.86}$$

$$B_y(N_x+1+\tfrac{1}{2},j,k+\tfrac{1}{2}) = B_y(1+\tfrac{1}{2},j,k+\tfrac{1}{2}) \tag{A.87}$$

and

$$B_z(\tfrac{1}{2},j+\tfrac{1}{2},k) = B_y(N_x+\tfrac{1}{2},j+\tfrac{1}{2},k) \tag{A.88}$$

$$B_z(N_x+1+\tfrac{1}{2},j+\tfrac{1}{2},k) = B_y(1+\tfrac{1}{2},j+\tfrac{1}{2},k) \tag{A.89}$$

A.2.3 Calculation of j

The current density (**j**) is calculated at the ribs using Stokes' theorem. Numerically this is achieved by:

$$j_x(i+\tfrac{1}{2},j,k) = \frac{[B_y h_{y_{B_y}}](i+\frac{1}{2},j,k-\frac{1}{2}) + [B_z h_{z_{B_z}}](i+\frac{1}{2},j+\frac{1}{2},k) - [B_y h_{y_{B_y}}](i+\frac{1}{2},j,k+\frac{1}{2}) - [B_z h_{z_{B_z}}](i+\frac{1}{2},j-\frac{1}{2},k)}{[h_{z_{A_x}} h_{y_{A_x}}](i+\frac{1}{2},j,k)} \tag{A.90}$$

for $i = 0, ...N_x + 1$, $j = 1, ..., N_y + 1$ and $k = 1, ..., N_z + 1$.

$$j_y(i, j + \tfrac{1}{2}, k) = \frac{[B_x h_{x_{B_x}}](i,j+\frac{1}{2},k+\frac{1}{2}) - [B_z h_{z_{B_z}}](i+\frac{1}{2},j+\frac{1}{2},k) - [B_x h_{x_{B_x}}](i,j+\frac{1}{2},k-\frac{1}{2}) + [B_z h_{z_{B_z}}](i-\frac{1}{2},j+\frac{1}{2},k)}{[h_{z_{A_y}} h_{x_{A_y}}](i,j+\frac{1}{2},k)} \tag{A.91}$$

for $i = 1, ...N_x + 1$, $j = 0, ..., N_y + 1$ and $k = 1, ..., N_z + 1$.

$$j_z(i, j, k + \tfrac{1}{2}) = \frac{[B_y h_{y_{B_y}}](i+\frac{1}{2},j,k+\frac{1}{2}) - [B_x h_{x_{B_x}}](i,j+\frac{1}{2},k+\frac{1}{2}) - [B_y h_{y_{B_y}}](i-\frac{1}{2},j,k+\frac{1}{2}) + [B_x h_{x_{B_x}}](i,j-\frac{1}{2},k+\frac{1}{2})}{[h_{x_{A_z}} h_{y_{A_z}}](i,j,k+\frac{1}{2})} \tag{A.92}$$

for $i = 1, ...N_x+1$, $j = 1, ..., N_y+1$ and $k = 0, ..., N_z+1$, where we have used the shorthand $[AB](i, j, k) = A(i, j, k)B(i, j, k)$.

Appendix B

Maximum Likelihood

In this Appendix the maximum likelihood method fit a model to data is described. Firstly, the Likelihood function and the method to determine the maximum likelihood estimators for parameters will be outlined. Secondly, some properties of the chi-squared statistic are described. Then a method to estimate the error in the maximum likelihood parameters is outlined. Lastly the maximum likelihood method is demonstrated by applying it to fit a straight line to data.

B.1 The Likelihood Function

Let us suppose we have a set of N data points, $\mathbf{X} = \{X_i\}$, with associated Normal errors $\boldsymbol{\sigma} = \{\sigma_i\}$ (where $i = 1, N$). These errors are such that if we were to take an ensemble of measurements of X_i, the variance of the ensemble would be σ_i^2. Say we want to fit a model $\mu_i(\boldsymbol{\alpha})$ with a set of M parameters, $\boldsymbol{\alpha} = \{\alpha_k\}$ (where $k = 1, M$) to the data. The model is assumed to be the true representation of the data – in other words if we could measure X_i to infinite precision then $X_i = \mu_i(\boldsymbol{\alpha})$. In order to fit the model, let us consider the Likelihood function, $L(\boldsymbol{\alpha})$. The likelihood function is the probability of the data, $\mathbf{X}$, given the parameters, $\boldsymbol{\alpha}$. In other words $L(\boldsymbol{\alpha}) = P(\mathbf{X}|\boldsymbol{\alpha})$. The likelihood function is mathematically expressed by

$$L(\boldsymbol{\alpha}) = \exp\left(-\frac{\chi^2}{2}\right) \prod_{i=1}^{N} \left(\frac{1}{\sigma_i}\right) (2\pi)^{-N/2}, \tag{B.1}$$

where

$$\chi^2 = \sum_{i=1}^{N} \left(\frac{X_i - \mu_i(\boldsymbol{\alpha})}{\sigma_i}\right)^2. \tag{B.2}$$

The chi-squared, $\chi^2 = \chi^2(\mathbf{X}, \boldsymbol{\alpha}, \boldsymbol{\sigma})$ is the dimensionless distance between the model and the data, normalised to the errors. It is as such a measure of the badness of fit, as the larger the χ^2 is, the worse the model parameters represent the data.

B.2 The Maximum Likelihood Method

In order to find the parameter values that best describe the data, we must maximise the likelihood with respect to these parameters. To simplify the calculation, first we take the

logarithm of the likelihood,

$$\ln L = -\frac{\chi^2}{2} - \sum_{i=1}^{N} \ln \sigma_i - \frac{N}{2} \ln 2\pi. \tag{B.3}$$

To determine the maximum likelihood estimate for each parameter, $\hat{\alpha}_k$ we solve

$$\frac{\partial L}{\partial \alpha_k} = -\frac{1}{2}\frac{\partial \chi^2}{\partial \alpha_k} - \sum_{i=1}^{N} \frac{\partial}{\partial \alpha_k} \ln \sigma_i = 0 \tag{B.4}$$

for α_k. Frequently the errors, σ_i are independent of the parameters, α_k and the above relation simplifies to

$$\frac{\partial \chi^2}{\partial \alpha_k} = 0. \tag{B.5}$$

It is important to note that though the maximum likelihood estimators, $\hat{\alpha}_k$, provide the best fit of the model to the data, they may not be the true values of α_k. Taking a new sample of $\mathbf{X}$ will change the values of $\hat{\alpha}_k$. As such, an error on the maximum likelihood estimator $\sigma_{\hat{\alpha}_k}$ exists, where we have a $1-\sigma$ (68.3%) confidence the true value of α_k lies within the range $[\hat{\alpha}_k - \sigma_{\hat{\alpha}_k}, \hat{\alpha}_k + \sigma_{\hat{\alpha}_k}]$.

B.3 Properties of the Chi-Squared

We will briefly consider the chi-squared (Equation B.2). If the model, $\mu_i(\boldsymbol{\alpha})$, is a good representation of the data, then the expected value of each term

$$\left\langle (X_i - \mu_i(\boldsymbol{\alpha}))^2 \right\rangle = \sigma_i^2, \tag{B.6}$$

where $\boldsymbol{\alpha}$ are the true values of the parameters. Thus the expected value of the chi-squared (with the true values of $\boldsymbol{\alpha}$) is

$$\left\langle \chi^2(\mathbf{X}, \boldsymbol{\alpha}, \boldsymbol{\sigma}) \right\rangle = \sum_{i=1}^{N} \left\langle \left(\frac{X_i - \mu_i(\boldsymbol{\alpha})}{\sigma_i} \right)^2 \right\rangle = \sum_{i=1}^{N} 1 = N. \tag{B.7}$$

When fitting the model to the data, we do not obtain the true values of $\boldsymbol{\alpha}$, but instead obtain the maximum likelihood estimates of the parameters, $\hat{\boldsymbol{\alpha}}$, which have the associated errors $\sigma_{\hat{\alpha}_k}$. Each maximum likelihood estimate parameter, which is dependent upon the data removes one degree of freedom from the chi-squared such that

$$\left\langle \chi^2(\mathbf{X}, \hat{\boldsymbol{\alpha}}, \boldsymbol{\sigma}) \right\rangle = N - M. \tag{B.8}$$

If we define the reduced chi-squared as $\chi^2_R = \chi^2/(N-M)$, then $\left\langle \chi^2_R \right\rangle = 1$. Therefore if the model we choose is appropriate for the data then the $\chi^2_R \approx 1$. If $\chi^2_R \gg 1$ then the model chosen is not appropriate for the data.

B.4 Estimating the Error on the Maximum Likelihood Estimators

As is mentioned above, the maximum likelihood estimator for a parameter is not necessarily the true value of the parameter, and is associated with an error, $\sigma_{\hat{\alpha}}$. We can estimate this error by applying the following method. Consider the chi-squared, which for

a given dataset is a function of the parameters, $\boldsymbol{\alpha}$. We can take a Taylor expansion of the chi-squared about the point $\hat{\alpha}_k$ as

$$\chi^2(\alpha_k) = \chi^2(\hat{\alpha}_k) + \cancelto{0}{\frac{\partial \chi^2}{\partial \alpha_k}\bigg|_{\hat{\alpha}_k}}(\alpha_k - \hat{\alpha}_k) + \frac{1}{2}\frac{\partial^2 \chi^2}{\partial \alpha_k^2}\bigg|_{\hat{\alpha}_k}(\alpha_k - \hat{\alpha}_k)^2. \tag{B.9}$$

Evaluating this expression at $\alpha_k = \hat{\alpha_k} \pm \sigma_{\hat{\alpha}_k}$ and defining $\Delta\chi^2 = \chi^2(\alpha_k) - \chi^2(\hat{\alpha}_k)$ we get

$$\Delta\chi^2 = \frac{1}{2}\frac{\partial^2 \chi^2}{\partial \alpha_k^2}\bigg|_{\hat{\alpha}_k}\sigma^2_{\hat{\alpha}_k} \tag{B.10}$$

and thus

$$\sigma^2_{\hat{\alpha}_k} = \frac{2}{\frac{\partial^2 \chi^2}{\partial \alpha_k^2}}\Delta\chi^2. \tag{B.11}$$

For the $1-\sigma$ confidence interval on $\hat{\alpha}_k$, $\Delta\chi^2 = 1$. This is not trivial to prove rigorously, but below an intuitive argument will be given. Consider a model for which there is only one parameter, α. The expected value of the chi-squared is $N-1$ for $\alpha = \hat{\alpha}$, and N for the true value of α. The true value of α is thus expected to provide a χ^2 which is one unit greater than the χ^2 for $\alpha = \hat{\alpha}$, in other words where $\Delta\chi^2 = 1$. It is thus reasonably likely to find the true value of α in the region where $\Delta\chi^2 \leq 1$.

B.5 Fitting a Straight Line to Data Using the Maximum Likelihood Method

Say we have a set of data $\{y_i\}$, with errors $\{\sigma_i\}$. Each value of y_i is associated with x_i. We want to fit the model $\mu_i(m,c) = mx_i + c$ such that $\mu_i = \langle y_i \rangle$. We can use the maximum likelihood method to determine the values of m and c that provide the best fit to the data. Firstly, we note that the errors are not dependent upon m and c. Therefore we can determine the maximum likelihood estimators for m and c by solving equation B.5. For this problem, the chi-squared is

$$\chi^2 = \sum_{i=1}^{N}\left(\frac{y_i - mx_i - c}{\sigma_i}\right)^2 \tag{B.12}$$

and therefore the maximum likelihood estimators are

$$\hat{m} = \frac{\sum_{i=1}^{N}(y_i - c)x_i/\sigma_i^2}{\sum_{i=1}^{N} x_i^2/\sigma_i^2}. \tag{B.13}$$

$$\hat{c} = \frac{\sum_{i=1}^{N}(y_i - mx_i)/\sigma_i^2}{\sum_{i=1}^{N} 1/\sigma_i^2}. \tag{B.14}$$

These can be solved to determine $\hat{m}$ and $\hat{c}$, however since $\hat{m}$ is dependent upon c and $\hat{c}$ is dependent upon m, trial values of m and c must be chosen. The above two equations must then be iterated to determine the correct values of the maximum likelihood estimators.

Using Equation B.11 we may now determine the uncertainty in $\hat{m}$ and $\hat{c}$ by

$$\sigma^2_{\hat{m}} = \frac{1}{\sum_{i=1}^{N}\left(\frac{x_i}{\sigma_i}\right)^2} \tag{B.15}$$

$$\sigma^2_{\hat{c}} = \frac{1}{\sum_{i=1}^{N}\left(\frac{1}{\sigma_i}\right)^2} \tag{B.16}$$

Appendix C

Probability Distributions

In this Appendix we describe the probability distribution functions used in this thesis, the nomenclature we use for random variables, and then outline the method we use to draw random numbers from arbitrary probability distribution functions.

C.1 Probability Distribution Functions

Consider that we take a measurement of a quantity, x. The probability distribution function (PDF) describes the probability that the value of x obtained by the measurement lies between the values a and b. Mathematically,

$$P(a < x \leq b) = \int_a^b f(x')dx', \tag{C.1}$$

where $f(x)$ is the probability distribution function. The PDF has the property that

$$\int_{-\infty}^{+\infty} f(x)dx = 1. \tag{C.2}$$

From the PDF, we may determine the expected value of the parameter x, $\langle x \rangle$ and its variance $\mathrm{Var}(x)$ by

$$\langle x \rangle = \int_{-\infty}^{+\infty} x' f(x')dx', \tag{C.3}$$

and

$$\mathrm{Var}(x) = \left\langle x^2 \right\rangle - \langle x \rangle^2 = \int_{-\infty}^{+\infty} \left(x - \langle x \rangle\right)^2 f(x)dx. \tag{C.4}$$

Another related function is the cumulative distribution function (CDF) defined as

$$F(x) = \int_{-\infty}^{x} f(x')dx', \tag{C.5}$$

Whose values range from 0 to 1. There are a number of probability distribution functions which will be used in this thesis. In the following subsections they will be described.

C.1.1 Uniform Distribution

The uniform distribution is a PDF which describes the case where there's an equal probability of x being measured between some values, a and b, and zero probability elsewhere.

Mathematically the uniform distribution's PDF is given by

$$f(x) = \begin{cases} \frac{1}{b-a} & a < x < b \\ 0 & \text{otherwise} \end{cases} \tag{C.6}$$

and its CDF is

$$F(x) = \begin{cases} 0 & x < a \\ \frac{x-a}{b-a} & a \leq x < b \\ 1 & x > b \end{cases} \tag{C.7}$$

The distribution's expected value and variance are given by

$$\frac{1}{2}(a+b), \tag{C.8}$$

and

$$\frac{1}{12}(b-a)^2, \tag{C.9}$$

respectively. In the top row of Figure C.1 the PDF (left) and CDF (right) for a uniform distribution between -1 and 1 is displayed.

C.1.2 Normal Distribution

The normal distribution (also known as the Gaussian distribution) is one of the most common distributions to use. This is because of the central limit theorem, which states that the distribution of a sum of independent random variables (drawn from the same distribution) will resemble a normal distribution. Measurement errors, for example, tend to take on a normal distribution, so if one was to take the same measurement many times, the distribution of the values measured will be approximately normal. The normal distribution is expressed by

$$f(x) = \frac{1}{\sigma\sqrt{2\pi}} \exp\left(\frac{(x-\mu)^2}{2\sigma^2}\right), \tag{C.10}$$

and its CDF is

$$F(x) = \frac{1}{2}\left(1 + \operatorname{erf}\left(\frac{x-\mu}{\sqrt{2}\sigma}\right)\right). \tag{C.11}$$

The expected value of the normal distribution is μ, and its variance is σ^2. In the middle row of Figure C.1 the PDF (left) and CDF (right) for a normal distribution with $\mu = 0$ and $\sigma = 1$ is displayed.

C.1.3 Exponential Distribution

The exponential distribution describes the time between events that occur independently of each other, but which occur at a constant rate. As such it is only defined for $x > 0$. For example the time between raindrops hitting a roof can be described by an exponential distribution. The exponential distribution's PDF is given by

$$f(x) = \frac{1}{\tau} \exp\left(\frac{-x}{\tau}\right), \tag{C.12}$$

and its CDF is

$$F(x) = 1 - \exp\left(\frac{-x}{t}\right). \tag{C.13}$$

The mean and variance of the exponential distribution are τ and τ^2 respectively. In the bottom row of Figure C.1 the PDF (left) and CDF (right) for an exponential distribution with $\tau = 1$ is displayed.

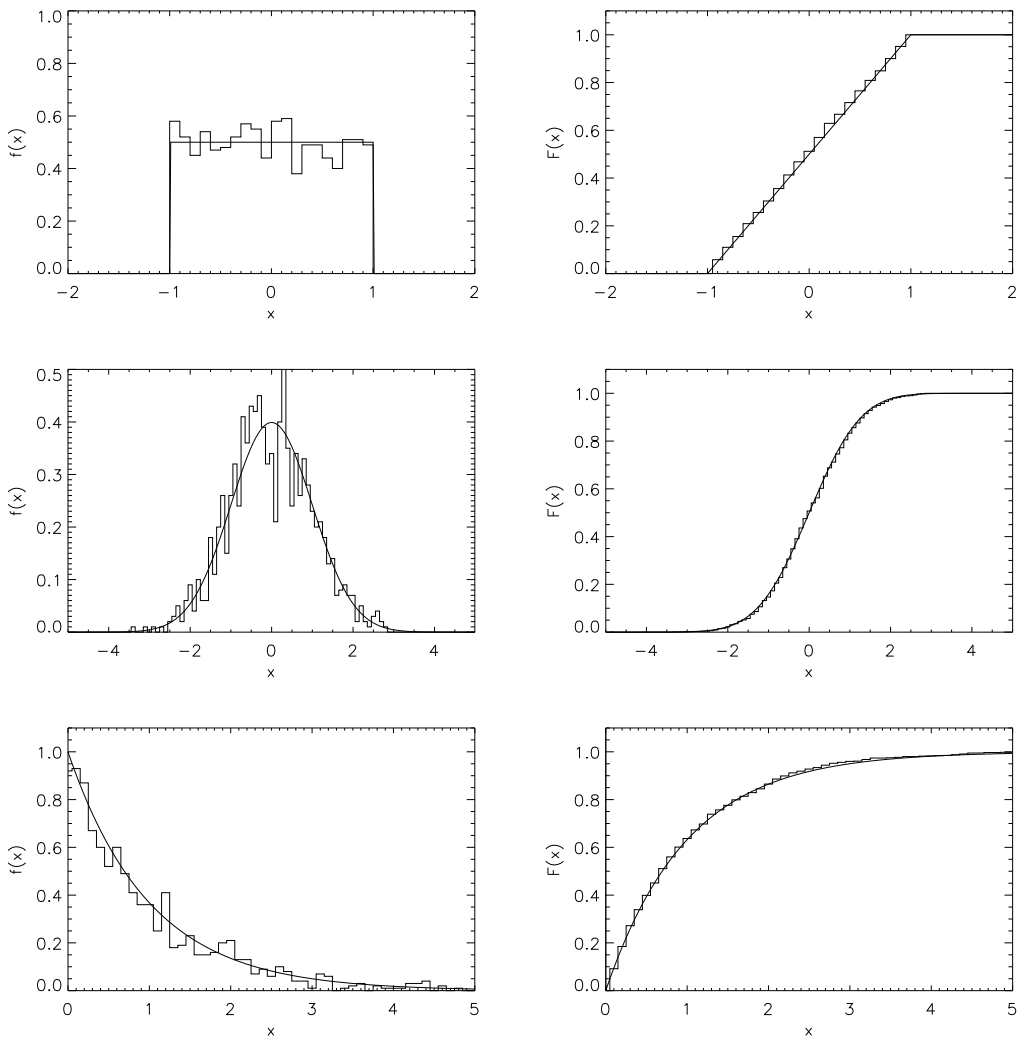

Figure C.1: The probability distribution functions (left) and cumulative distribution functions (right) for the uniform (top row), normal (middle row) and exponential (bottom row) distributions. Also shown are histograms of a set of 1000 random numbers drawn from the distributions (scaled to fit on the plot).

C.2 Random variables

A random variable is a variable whose value is random, but is associated with a probability distribution function. In chapter 7 random variables are used in the flux emergence model to produce randomly selected bipole properties. We use the following shorthands to describe random variables. Say x is a random variable which is drawn from a uniform distribution between a and b. Then we write

$$x = U[a, b] \tag{C.14}$$

to denote the random variable. Similarly, if x is drawn from a normal distribution with expected value μ and variance σ^2 then we express this number as

$$x = N[\mu, \sigma]. \tag{C.15}$$

Finally, if x is drawn from an exponential distribution with expected value τ then we express x as

$$x = E[\tau]. \tag{C.16}$$

C.3 Constructing a Set of Random Numbers Drawn from a Distribution

Say we need to obtain a set of n random numbers which are distributed according to a PDF, $f(x)$. Computers are only capable of producing 'pseudo'-random numbers. The numbers produced are described as pseudo-random because they are not in fact random, but are obtained using a deterministic algorithm. For a particular start point (seed), the set of 'random' numbers produced is identical, however a different seed will produce a different set of 'random' numbers. Pseudo-random number generators on computers generally produce random numbers according to the uniform distribution, $u = U[0, 1]$. Thus, in order to obtain a series of numbers, x, which obey an arbitrary PDF, $f(x)$, a transformation must be applied to u. This is achieved using the CDF ($F(x)$) corresponding to $f(x)$, by calculating

$$x = F^{-1}(u). \tag{C.17}$$

Therefore, if we know the CDF of the distribution we wish to sample from, then we can obtain this sample by applying Equation C.17 to a set of uniformly distributed random numbers. To illustrate this, in Figure C.1 we have overplotted histograms (scaled to fit on the axes) of sets of 1000 random numbers drawn from the relevant distributions.

Appendix D

List of Movies

Several movies are included with this thesis and are held on the accompanying CD. On the CD, the movies are placed into directories according to the chapter they are mentioned in. The following is a short description of each of them.

D.1 Chapter 3

- *raw.mpg*
  The timeseries of raw magnetograms of AR10977. The images are saturated at ±100 G.

- *xrt.mpg*
  The timeseries of XRT observations of AR10977.

- *cleaning.mpg*
  A comparison of no time averaging (top left), uniform (boxcar – top centre) and Gaussian (top right) time averaging for the timeseries of magnetograms. Also displayed are the raw frames (repeated three times on the bottom row) for comparison. The green and red stars are the centres of flux for the positive and negative flux regions. The images are saturated at ±100 G.

- *compare.mpg*
  A comparison of the cleaned magnetograms (left) and the lower boundary condition (right) for the whole timeseries. The images are saturated at ±100 G.

- *emission_proxy.mp4*
  The evolution of the emission proxy of the active region over the whole simulation.

D.2 Chapter 6

- *eruption.mp4*
  The evolution of the simulation with $d\Omega_*/d\Omega_\odot = 3$ and $D = 450$ km^{2}s^{-1} outlining the sheared arcade transforming into a flux rope, the eruption of the flux rope then the formation of a second flux rope. Red and blue contours represent positive and negative surface flux respectively. The contour levels are the same throughout the movie.

D.3 Chapter 7

- *solar_evolution.mp4*
  The time-evolution of the coronal emission proxy for the simulation with solar differential rotation and flux emergence rate. The star is shown from three viewing angles, with the central meridians corresponding to $-120°$ (left), $0°$ (centre) and $120°$ (right) longitude respectively.

- *3em_evolution.mp4*
  The time-evolution of the coronal emission proxy for the simulation with solar differential rotation and three times the solar flux emergence rate. The star is shown from three viewing angles, with the central meridians corresponding to $-120°$ (left), $0°$ (centre) and $120°$ (right) longitude respectively.

- *5em_evolution.mp4*
  The time-evolution of the coronal emission proxy for the simulation with solar differential rotation and five times the solar flux emergence rate. The star is shown from three viewing angles, with the central meridians corresponding to $-120°$ (left), $0°$ (centre) and $120°$ (right) longitude respectively.

- *3dr_evolution.mp4*
  The time-evolution of the coronal emission proxy for the simulation with three times the solar differential rotation rate and the solar flux emergence rate. The star is shown from three viewing angles, with the central meridians corresponding to $-120°$ (left), $0°$ (centre) and $120°$ (right) longitude respectively.

- *5dr_evolution.mp4*
  The time-evolution of the coronal emission proxy for the simulation with five times the solar differential rotation rate and the solar flux emergence rate. The star is shown from three viewing angles, with the central meridians corresponding to $-120°$ (left), $0°$ (centre) and $120°$ (right) longitude respectively.

References

Aarnio, A. N., Stassun, K. G., Hughes, W. J. & McGregor, S. L. (2011), 'Solar Flares and Coronal Mass Ejections: A Statistically Determined Flare Flux - CME Mass Correlation', Sol. Phys. **268**, 195–212. 147

Aigrain, S., Llama, J., Ceillier, T., Chagas, M. L. d., Davenport, J. R. A., García, R. A., Hay, K. L., Lanza, A. F., McQuillan, A., Mazeh, T., de Medeiros, J. R., Nielsen, M. B. & Reinhold, T. (2015), 'Testing the recovery of stellar rotation signals from Kepler light curves using a blind hare-and-hounds exercise', MNRAS **450**, 3211–3226. 15

Altschuler, M. D. & Newkirk, G. (1969), 'Magnetic Fields and the Structure of the Solar Corona. I: Methods of Calculating Coronal Fields', Sol. Phys. **9**, 131–149. 13, 123

Antiochos, S. K. (2013), 'Helicity Condensation as the Origin of Coronal and Solar Wind Structure', ApJ **772**, 72. 7, 87, 120

Antiochos, S. K. & Klimchuk, J. A. (1991), 'A model for the formation of solar prominences', ApJ **378**, 372–377. 8

Archontis, V. (2008), 'Magnetic flux emergence in the Sun', *Journal of Geophysical Research (Space Physics)* **113**, 3. 22

Archontis, V. & Hood, A. W. (2010), 'Flux emergence and coronal eruption', AAP **514**, A56. 22

Archontis, V., Moreno-Insertis, F., Galsgaard, K., Hood, A. & O'Shea, E. (2004), 'Emergence of magnetic flux from the convection zone into the corona', AAP **426**, 1047–1063. 22

Archontis, V. & Török, T. (2008), 'Eruption of magnetic flux ropes during flux emergence', AAP **492**, L35–L38. 22

Arge, C. N., Luhmann, J. G., Odstrcil, D., Schrijver, C. J. & Li, Y. (2004), 'Stream structure and coronal sources of the solar wind during the May 12th, 1997 CME', *Journal of Atmospheric and Solar-Terrestrial Physics* **66**, 1295–1309. 123

Aulanier, G. & Demoulin, P. (1998), '3-D magnetic configurations supporting prominences. I. The natural presence of lateral feet', AAP **329**, 1125–1137. 7

Ayres, T. R. (1997), 'Evolution of the solar ionizing flux', J. Geophys. Res. **102**, 1641–1652. 14

Babcock, H. W. (1961), 'The Topology of the Sun's Magnetic Field and the 22-YEAR Cycle.', ApJ **133**, 572. 9

Bai, T. (1988), 'Distribution of flares on the sun during 1955-1985 - 'Hot spots' (active zones) lasting for 30 years', ApJ **328**, 860–874. 5

Baraffe, I., Chabrier, G., Allard, F. & Hauschildt, P. H. (1998), 'Evolutionary models for solar metallicity low-mass stars: mass-magnitude relationships and color-magnitude diagrams', AAP **337**, 403–412. 10

Barnes, J. R., Collier Cameron, A., Donati, J.-F., James, D. J., Marsden, S. C. & Petit, P. (2005), 'The dependence of differential rotation on temperature and rotation', MNRAS **357**, L1–L5. 15, 16, 176, 225

Benz, A. O. (2008), 'Flare Observations', *Living Reviews in Solar Physics* **5**, 1. 5

Berdyugina, S. V. (2005), 'Starspots: A Key to the Stellar Dynamo', *Living Reviews in Solar Physics* **2**, 8. 13

Berger, M. A. (1999), 'Introduction to magnetic helicity', *Plasma Phys. Control. Fusion* **41**, B167. 21, 69

Berger, M. A. & Field, G. B. (1984), 'The topological properties of magnetic helicity', *Journal of Fluid Mechanics* **147**, 133–148. 21

Bobra, M. G., van Ballegooijen, A. A. & DeLuca, E. E. (2008), 'Modeling Nonpotential Magnetic Fields in Solar Active Regions', ApJ **672**, 1209–1220. 22, 85

Brown, S. F., Donati, J.-F., Rees, D. E. & Semel, M. (1991), 'Zeeman-Doppler imaging of solar-type and AP stars. IV - Maximum entropy reconstruction of 2D magnetic topologies', AAP **250**, 463–474. 13

Burlaga, L., Sittler, E., Mariani, F. & Schwenn, R. (1981), 'Magnetic loop behind an interplanetary shock - Voyager, Helios, and IMP 8 observations', J. Geophys. Res. **86**, 6673–6684. 21

Canfield, R. C., Hudson, H. S. & McKenzie, D. E. (1999), 'Sigmoidal morphology and eruptive solar activity', Geophys. Res. Lett. **26**, 627–630. 5, 7

Canfield, R. C., Kazachenko, M. D., Acton, L. W., Mackay, D. H., Son, J. & Freeman, T. L. (2007), 'Yohkoh SXT Full-Resolution Observations of Sigmoids: Structure, Formation, and Eruption', ApJL **671**, L81–L84. 22

Chae, J. (2001), 'Observational Determination of the Rate of Magnetic Helicity Transport through the Solar Surface via the Horizontal Motion of Field Line Footpoints', ApJL **560**, L95–L98. 7

Cheung, M. C. M. & DeRosa, M. L. (2012), 'A Method for Data-driven Simulations of Evolving Solar Active Regions', ApJ **757**, 147. 24, 50, 68, 86, 116, 121

Cohen, O., Drake, J. J., Kashyap, V. L., Hussain, G. A. J. & Gombosi, T. I. (2010), 'The Coronal Structure of AB Doradus', ApJ **721**, 80–89. 147

Collier Cameron, A. (2007), 'Differential rotation on rapidly rotating stars', *Astronomische Nachrichten* **328**, 1030. 15, 176

Collier Cameron, A. & Robinson, R. D. (1989), 'Fast H-alpha variations on a rapidly rotating cool main sequence star. I - Circumstellar clouds', MNRAS **236**, 57–87. 147

Crooker, N. U., Antiochos, S. K., Zhao, X. & Neugebauer, M. (2012), 'Global network of slow solar wind', *Journal of Geophysical Research (Space Physics)* **117**, 4104. 123

Dahlburg, R. B., Antiochos, S. K. & Klimchuk, J. A. (1998), 'Prominence Formation by Localized Heating', ApJ **495**, 485. 8

Deng, Y. Y., Schmieder, B., Engvold, O., DeLuca, E. & Golub, L. (2000), 'Emergence of sheared magnetic flux tubes in an active region observed with the SVST and TRACE', Sol. Phys. **195**, 347–366. 7

DeVore, C. R. & Antiochos, S. K. (2000), 'Dynamical Formation and Stability of Helical Prominence Magnetic Fields', ApJ **539**, 954–963. 7, 86

DeVore, C. R., Sheeley, Jr., N. R., Boris, J. P., Young, Jr., T. R. & Harvey, K. L. (1985), 'Simulations of magnetic-flux transport in solar active regions', Sol. Phys. **102**, 41–49. 9, 10

Donahue, R. A., Saar, S. H. & Baliunas, S. L. (1996), 'A Relationship between Mean Rotation Period in Lower Main-Sequence Stars and Its Observed Range', ApJ **466**, 384. 15, 16

Donati, J.-F. & Brown, S. F. (1997), 'Zeeman-Doppler imaging of active stars. V. Sensitivity of maximum entropy magnetic maps to field orientation.', AAP **326**, 1135–1142. 13

Donati, J.-F. & Collier Cameron, A. (1997), 'Differential rotation and magnetic polarity patterns on AB Doradus', MNRAS **291**, 1–19. 15, 177

Donati, J.-F., Collier Cameron, A., Hussain, G. A. J. & Semel, M. (1999), 'Magnetic topology and prominence patterns on AB Doradus', MNRAS **302**, 437–456. 177

Donati, J.-F., Collier Cameron, A., Semel, M., Hussain, G. A. J., Petit, P., Carter, B. D., Marsden, S. C., Mengel, M., López Ariste, A., Jeffers, S. V. & Rees, D. E. (2003), 'Dynamo processes and activity cycles of the active stars AB Doradus, LQ Hydrae and HR 1099', MNRAS **345**, 1145–1186. 177

Donati, J.-F., Jardine, M. M., Gregory, S. G., Petit, P., Bouvier, J., Dougados, C., Ménard, F., Collier Cameron, A., Harries, T. J., Jeffers, S. V. & Paletou, F. (2007), 'Magnetic fields and accretion flows on the classical T Tauri star V2129 Oph', MNRAS **380**, 1297–1312. 13

Donati, J.-F. & Landstreet, J. D. (2009), 'Magnetic Fields of Nondegenerate Stars', ARAA **47**, 333–370. 14

Donati, J.-F., Mengel, M., Carter, B. D., Marsden, S., Collier Cameron, A. & Wichmann, R. (2000), 'Surface differential rotation and prominences of the Lupus post T Tauri star RX J1508.6-4423', MNRAS **316**, 699–715. 13, 15

Donati, J.-F., Morin, J., Delfosse, X., Forveille, T., Farès, R., Moutou, C. & Jardine, M. (2009), Large-scale magnetic topologies of cool stars, *in* E. Stempels, ed., '15th Cambridge Workshop on Cool Stars, Stellar Systems, and the Sun', Vol. 1094 of *American Institute of Physics Conference Series*, pp. 130–139. 14

Donati, J.-F., Moutou, C., Farès, R., Bohlender, D., Catala, C., Deleuil, M., Shkolnik, E., Collier Cameron, A., Jardine, M. M. & Walker, G. A. H. (2008), 'Magnetic cycles of the planet-hosting star τ Bootis', MNRAS **385**, 1179–1185. 13, 14, 15, 180

Drake, J. J., Cohen, O., Yashiro, S. & Gopalswamy, N. (2013), 'Implications of Mass and Energy Loss due to Coronal Mass Ejections on Magnetically Active Stars', ApJ **764**, 170. 147

Fan, Y. (2001), 'The Emergence of a Twisted Ω-Tube into the Solar Atmosphere', ApJL **554**, L111–L114. 5, 22

Fan, Y. (2009), 'The Emergence of a Twisted Flux Tube into the Solar Atmosphere: Sunspot Rotations and the Formation of a Coronal Flux Rope', ApJ **697**, 1529–1542. 22

Fares, R., Donati, J.-F., Moutou, C., Bohlender, D., Catala, C., Deleuil, M., Shkolnik, E., Collier Cameron, A., Jardine, M. M. & Walker, G. A. H. (2009), 'Magnetic cycles of the planet-hosting star τ Bootis - II. A second magnetic polarity reversal', MNRAS **398**, 1383–1391. 13, 14, 180

Favata, F. & Micela, G. (2003), 'Stellar Coronal Astronomy', Space Sci. Rev. **108**, 577–708. 12

Feigelson, E. D. & Montmerle, T. (1999), 'High-Energy Processes in Young Stellar Objects', ARAA **37**, 363–408. 12

Finn, J. M. & Antonsen, T. M. (1985), 'Magnetic helicity: What is it and what it is good for?', *Comments Plasma Phys. Control. Fusion* **9(3)**, 111. 21

Finn, J. M., Guzdar, P. N. & Usikov, D. (1994), 'Three-dimensional force-free looplike magnetohydrodynamic equilibria', ApJ **427**, 475–482. 60, 61

Gibb, G. P. S., Jardine, M. M. & Mackay, D. H. (2014), 'Stellar differential rotation and coronal time-scales', MNRAS **443**, 3251–3259. 148

Gibb, G. P. S., Mackay, D. H., Green, L. M. & Meyer, K. A. (2014), 'Simulating the Formation of a Sigmoidal Flux Rope in AR10977 from SOHO/MDI Magnetograms', ApJ **782**, 71. 50

Gibson, S. E. & Fan, Y. (2006), 'The Partial Expulsion of a Magnetic Flux Rope', ApJL **637**, L65–L68. 7

Glover, A., Ranns, N. D. R., Harra, L. K. & Culhane, J. L. (2000), 'The onset and association of CMEs with sigmoidal active regions', Geophys. Res. Lett. **27**, 2161–2164. 7

Gondoin, P., Gandolfi, D., Fridlund, M., Frasca, A., Guenther, E. W., Hatzes, A., Deeg, H. J., Parviainen, H., Eigmüller, P. & Deleuil, M. (2012), 'From CoRoT 102899501 to the Sun. A time evolution model of chromospheric activity on the main sequence', AAP **548**, A15. 14

Green, L. M., Kliem, B., Török, T., van Driel-Gesztelyi, L. & Attrill, G. D. R. (2007), 'Transient Coronal Sigmoids and Rotating Erupting Flux Ropes', Sol. Phys. **246**, 365–391. 22

Green, L. M., Kliem, B. & Wallace, A. J. (2011), 'Photospheric flux cancellation and associated flux rope formation and eruption', AAP **526**, A2. 49, 53, 85, 89, 92, 117, 118, 120, 121, 224

Güdel, M. (2007), 'The Sun in Time: Activity and Environment', *Living Reviews in Solar Physics* **4**, 3. 14

Hale, G. E. (1908), 'On the Probable Existence of a Magnetic Field in Sun-Spots', ApJ **28**, 315. 3

Hale, G. E., Ellerman, F., Nicholson, S. B. & Joy, A. H. (1919), 'The Magnetic Polarity of Sun-Spots', ApJ **49**, 153. 8, 180

Hannah, I. G., Hudson, H. S., Battaglia, M., Christe, S., Kasparová, J., Krucker, S., Kundu, M. R. & Veronig, A. (2011), 'Microflares and the Statistics of X-ray Flares', Space Sci. Rev. **159**, 263–300. 69

Hathaway, D. H., Wilson, R. M. & Reichmann, E. J. (2002), 'Group Sunspot Numbers: Sunspot Cycle Characteristics', Sol. Phys. **211**, 357–370. 8

Henry, G. W., Eaton, J. A., Hamer, J. & Hall, D. S. (1995), 'Starspot evolution, differential rotation, and magnetic cycles in the chromospherically active binaries lambda andromedae, sigma Geminorum, II Pegasi, and V711 Tauri', ApJS **97**, 513–549. 16

Hood, A. & Anzer, U. (1988), 'Thermal condensations in coronal magnetic fields', Sol. Phys. **115**, 61–80. 8

Hood, A. W. & Priest, E. R. (1981), 'Critical conditions for magnetic instabilities in force-free coronal loops', *Geophysical and Astrophysical Fluid Dynamics* **17**, 297–318. 22

Jardine, M., Collier Cameron, A. & Donati, J.-F. (2002), 'The global magnetic topology of AB Doradus', MNRAS **333**, 339–346. 13

Khodachenko, M. L., Ribas, I., Lammer, H., Grießmeier, J.-M., Leitner, M., Selsis, F., Eiroa, C., Hanslmeier, A., Biernat, H. K., Farrugia, C. J. & Rucker, H. O. (2007), 'Coronal Mass Ejection (CME) Activity of Low Mass M Stars as An Important Factor for The Habitability of Terrestrial Exoplanets. I. CME Impact on Expected Magnetospheres of Earth-Like Exoplanets in Close-In Habitable Zones', *Astrobiology* **7**, 167–184. 222

Kippenhahn, R. & Schlüter, A. (1957), 'Eine Theorie der solaren Filamente. Mit 7 Textabbildungen', Z. Astrophys. **43**, 36. 7

Kliem, B. & Török, T. (2006), 'Torus Instability', *Physical Review Letters* **96**(25), 255002. 22

Korhonen, H., Berdyugina, S. V., Strassmeier, K. G. & Tuominen, I. (2001), 'The first close-up of the "flip-flop" phenomenon in a single star', AAP **379**, L30–L33. 13

Krall, J., Chen, J., Santoro, R., Spicer, D. S., Zalesak, S. T. & Cargill, P. J. (1998), 'Simulation of Buoyant Flux Ropes in a Magnetized Solar Atmosphere', ApJ **500**, 992–1002. 193

Küker, M. & Rüdiger, G. (2011), 'Differential rotation and meridional flow on the lower zero-age main sequence: Reynolds stress versus baroclinic flow', *Astronomische Nachrichten* **332**, 933. 15, 176

Kuperus, M. & Raadu, M. A. (1974), 'The Support of Prominences Formed in Neutral Sheets', AAP **31**, 189. 7

Lammer, H., Güdel, M., Kulikov, Y., Ribas, I., Zaqarashvili, T. V., Khodachenko, M. L., Kislyakova, K. G., Gröller, H., Odert, P., Leitzinger, M., Fichtinger, B., Krauss, S., Hausleitner, W., Holmström, M., Sanz-Forcada, J., Lichtenegger, H. I. M., Hanslmeier, A., Shematovich, V. I., Bisikalo, D., Rauer, H. & Fridlund, M. (2012), 'Variability of solar/stellar activity and magnetic field and its influence on planetary atmosphere evolution', *Earth, Planets, and Space* **64**, 179–199. 222

Lang, P., Jardine, M., Morin, J., Donati, J.-F., Jeffers, S., Vidotto, A. A. & Fares, R. (2014), 'Modelling the hidden magnetic field of low-mass stars', MNRAS **439**, 2122–2131. 13

Leake, J. E., Linton, M. G. & Török, T. (2013), 'Simulations of Emerging Magnetic Flux. I. The Formation of Stable Coronal Flux Ropes', ApJ **778**, 99. 22

Leamon, R. J., Canfield, R. C. & Pevtsov, A. A. (2002), 'Properties of magnetic clouds and geomagnetic storms associated with eruption of coronal sigmoids', *Journal of Geophysical Research (Space Physics)* **107**, 1234. 21

Leighton, R. B. (1964), 'Transport of Magnetic Fields on the Sun.', ApJ **140**, 1547. 10

Leka, K. D., Canfield, R. C., McClymont, A. N. & van Driel-Gesztelyi, L. (1996), 'Evidence for Current-carrying Emerging Flux', ApJ **462**, 547. 7, 178

Lites, B. W. & Low, B. C. (1997), 'Flux Emergence and Prominences: a New Scenario for 3-DIMENSIONAL Field Geometry Based on Observations with the Advanced Stokes Polarimeter', Sol. Phys. **174**, 91–98. 7

Lites, B. W., Low, B. C., Martinez Pillet, V., Seagraves, P., Skumanich, A., Frank, Z. A., Shine, R. A. & Tsuneta, S. (1995), 'The Possible Ascent of a Closed Magnetic System through the Photosphere', ApJ **446**, 877. 7

Liu, Y., Zhao, X. P., Hoeksema, J. T., Scherrer, P. H., Wang, J. & Yan, Y. (2002), 'On Formation of the Sigmoidal Structure in Solar Active Region NOAA 8100', Sol. Phys. **206**, 333–346. 20

Llama, J., Jardine, M., Mackay, D. H. & Fares, R. (2012), 'Using Kepler transit observations to measure stellar spot belt migration rates', MNRAS **422**, L72. 180

Longbottom, A. (1998), Force-Free Models of Filament Channels, *in* D. F. Webb, B. Schmieder & D. M. Rust, eds, 'IAU Colloq. 167: New Perspectives on Solar Prominences', Vol. 150 of *Astronomical Society of the Pacific Conference Series*, p. 274. 60

Low, B. C. & Lou, Y. Q. (1990), 'Modeling solar force-free magnetic fields', ApJ **352**, 343–352. 20

Mackay, D. H., DeVore, C. R. & Antiochos, S. K. (2014), 'Global-scale Consequences of Magnetic-helicity Injection and Condensation on the Sun', ApJ **784**, 164. 7

Mackay, D. H., Green, L. M. & van Ballegooijen, A. (2011), 'Modeling the Dispersal of an Active Region: Quantifying Energy Input into the Corona', ApJ **729**, 97. 7, 24, 49, 50, 56, 61, 68, 69, 84, 85, 116, 120, 121

Mackay, D. H., Jardine, M., Collier Cameron, A., Donati, J.-F. & Hussain, G. A. J. (2004), 'Polar caps on active stars: magnetic flux emergence and transport', MNRAS **354**, 737–752. 147, 180, 227

Mackay, D. H., Karpen, J. T., Ballester, J. L., Schmieder, B. & Aulanier, G. (2010), 'Physics of Solar Prominences: II Magnetic Structure and Dynamics', Space Sci. Rev. **151**, 333–399. 7

Mackay, D. H. & van Ballegooijen, A. A. (2006), 'Models of the Large-Scale Corona. I. Formation, Evolution, and Liftoff of Magnetic Flux Ropes', ApJ **641**, 577–589. 7, 22, 24, 124, 147, 148

Mackay, D. & Yeates, A. (2012), 'The Sun's Global Photospheric and Coronal Magnetic Fields: Observations and Models', *Living Reviews in Solar Physics* **9**, 6. 147

Magara, T. (2006), 'Dynamic and Topological Features of Photospheric and Coronal Activities Produced by Flux Emergence in the Sun', ApJ **653**, 1499–1509. 22

Manchester, IV, W., Gombosi, T., DeZeeuw, D. & Fan, Y. (2004), 'Eruption of a Buoyantly Emerging Magnetic Flux Rope', ApJ **610**, 588–596. 22

Marsden, S. C., Donati, J.-F., Semel, M., Petit, P. & Carter, B. D. (2006), 'Surface differential rotation and photospheric magnetic field of the young solar-type star HD 171488 (V889 Her)', MNRAS **370**, 468–476. 13, 15

Marsden, S. C., Jardine, M. M., Ramírez Vélez, J. C., Alecian, E., Brown, C. J., Carter, B. D., Donati, J.-F., Dunstone, N., Hart, R., Semel, M. & Waite, I. A. (2011), 'Magnetic fields and differential rotation on the pre-main sequence - II. The early-G star HD 141943 - coronal magnetic field, Hα emission and differential rotation', MNRAS **413**, 1939–1948. 13, 15

Marubashi, K. (1986), 'Structure of the interplanetary magnetic clouds and their solar origins', *Advances in Space Research* **6**, 335–338. 21

Maunder, E. W. (1904), 'Note on the distribution of sun-spots in heliographic latitude, 1874-1902', MNRAS **64**, 747–761. 8

Meyer, K. A., Mackay, D. H., van Ballegooijen, A. A. & Parnell, C. E. (2013), 'Solar Magnetic Carpet III: Coronal Modelling of Synthetic Magnetograms', Sol. Phys. . 68

Meyer, K. A., Sabol, J., Mackay, D. H. & van Ballegooijen, A. A. (2013), 'The Storage and Dissipation of Magnetic Energy in the Quiet Sun Corona Determined from SDO/HMI Magnetograms', ApJL **770**, L18. 24

Mok, Y., Drake, J. F., Schnack, D. D. & van Hoven, G. (1990), 'Prominence formation in a coronal loop', ApJ **359**, 228–231. 8

Moreno-Insertis, F. (2004), 'The Emergence of Magnetic Field into Stellar Atmospheres', Astrophys. and Space Science **292**, 587–597. 22

Morin, J., Donati, J.-F., Petit, P., Delfosse, X., Forveille, T., Albert, L., Aurière, M., Cabanac, R., Dintrans, B., Fares, R., Gastine, T., Jardine, M. M., Lignières, F., Paletou, F., Ramirez Velez, J. C. & Théado, S. (2008), 'Large-scale magnetic topologies of mid M dwarfs', MNRAS **390**, 567–581. 16

Nakariakov, V. M. & Ofman, L. (2001), 'Determination of the coronal magnetic field by coronal loop oscillations', AAP **372**, L53–L56. 5

Nakariakov, V. M., Ofman, L., Deluca, E. E., Roberts, B. & Davila, J. M. (1999), 'TRACE observation of damped coronal loop oscillations: Implications for coronal heating', *Science* **285**, 862–864. 5

Noyes, R. W., Hartmann, L. W., Baliunas, S. L., Duncan, D. K. & Vaughan, A. H. (1984), 'Rotation, convection, and magnetic activity in lower main-sequence stars', ApJ **279**, 763–777. 14

Pagano, P., Mackay, D. H. & Poedts, S. (2013), 'Magnetohydrodynamic simulations of the ejection of a magnetic flux rope', AAP **554**, A77. 65

Parker, E. N. (1955), 'Hydromagnetic Dynamo Models.', ApJ **122**, 293. 14

Parker, E. N. (1972), 'Topological Dissipation and the Small-Scale Fields in Turbulent Gases', ApJ **174**, 499. 4

Petit, P., Donati, J.-F. & Collier Cameron, A. (2002), 'Differential rotation of cool active stars: the case of intermediate rotators', MNRAS **334**, 374–382. 15

Pevtsov, A. A., Canfield, R. C. & Metcalf, T. R. (1995), 'Latitudinal variation of helicity of photospheric magnetic fields', ApJL **440**, L109–L112. 7, 70, 178

Pevtsov, A. A., Fisher, G. H., Acton, L. W., Longcope, D. W., Johns-Krull, C. M., Kankelborg, C. C. & Metcalf, T. R. (2003), 'The Relationship Between X-Ray Radiance and Magnetic Flux', ApJ **598**, 1387–1391. 147

Pietarila, A., Bertello, L., Harvey, J. W. & Pevtsov, A. A. (2013), 'Comparison of Ground-Based and Space-Based Longitudinal Magnetograms', Sol. Phys. **282**, 91–106. 135, 136

Platten, S. J., Parnell, C. E., Haynes, A. L., Priest, E. R. & Mackay, D. H. (2014), 'The solar cycle variation of topological structures in the global solar corona', AAP **565**, A44. 123

Pneuman, G. W. (1983), 'The formation of solar prominences by magnetic reconnection and condensation', Sol. Phys. **88**, 219–239. 7

Pointer, G. R., Jardine, M., Collier Cameron, A. & Donati, J.-F. (2002), 'Modelling surface magnetic field evolution on AB Doradûs due to diffusion and surface differential rotation', MNRAS **330**, 160–166. 147

Pont, F., Gilliland, R. L., Moutou, C., Charbonneau, D., Bouchy, F., Brown, T. M., Mayor, M., Queloz, D., Santos, N. & Udry, S. (2007), 'Hubble Space Telescope time-series photometry of the planetary transit of HD 189733: no moon, no rings, starspots', AAP **476**, 1347–1355. 12

Priest, E. R. (1982), *Solar Magneto-Hydrodynamics*, Springer. 3, 5, 7, 19

Priest, E. R., Hood, A. W. & Anzer, U. (1989), 'A twisted flux-tube model for solar prominences. I - General properties', ApJ **344**, 1010–1025. 7

Rabus, M., Alonso, R., Belmonte, J. A., Deeg, H. J., Gilliland, R. L., Almenara, J. M., Brown, T. M., Charbonneau, D. & Mandushev, G. (2009), 'A cool starspot or a second transiting planet in the TrES-1 system?', AAP **494**, 391–397. 12

Régnier, S., Amari, T. & Kersalé, E. (2002), '3D Coronal magnetic field from vector magnetograms: non-constant-alpha force-free configuration of the active region NOAA 8151', AAP **392**, 1119–1127. 20

Reiners, A. (2012), 'Observations of Cool-Star Magnetic Fields', *Living Reviews in Solar Physics* **9**, 1. 14

Reinhold, T., Reiners, A. & Basri, G. (2013), 'Rotation and differential rotation of active Kepler stars', AAP **560**, A4. 15

Robinson, R. D., Worden, S. P. & Harvey, J. W. (1980), 'Observations of magnetic fields on two late-type dwarf stars', ApJL **236**, L155–L158. 13

Rust, D. M. & Kumar, A. (1994), 'Helical magnetic fields in filaments', Sol. Phys. **155**, 69–97. 7, 22

Rust, D. M. & Kumar, A. (1996), 'Evidence for Helically Kinked Magnetic Flux Ropes in Solar Eruptions', ApJL **464**, L199. 7, 22, 202

Savcheva, A. S., Green, L. M., van Ballegooijen, A. A. & DeLuca, E. E. (2012), 'Photospheric Flux Cancellation and the Build-up of Sigmoidal Flux Ropes on the Sun', ApJ **759**, 105. 24, 49, 85, 86, 89, 117, 118, 120, 121, 224

Savcheva, A. & van Ballegooijen, A. (2009), 'Nonlinear Force-free Modeling of a Long-lasting Coronal Sigmoid', ApJ **703**, 1766–1777. 22, 85

Schatzman, E. (1949), 'The heating of the solar corona and chromosphere', *Annales d'Astrophysique* **12**, 203. 4

Schwabe, M. (1844), 'Sonnenbeobachtungen im Jahre 1843. Von Herrn Hofrath Schwabe in Dessau', *Astronomische Nachrichten* **21**, 233. 8

Schwadron, N. A., McComas, D. J. & DeForest, C. (2006), 'Relationship between Solar Wind and Coronal Heating: Scaling Laws from Solar X-Rays', ApJ **642**, 1173–1176. 147

See, V., Jardine, M., Vidotto, A. A., Petit, P., Marsden, S. C., Jeffers, S. V. & do Nascimento, J. D. (2014), 'The effects of stellar winds on the magnetospheres and potential habitability of exoplanets', AAP **570**, A99. 220

Seehafer, N. (1978), 'Determination of constant alpha force-free solar magnetic fields from magnetograph data', Sol. Phys. **58**, 215–223. 20

Semel, M. (1989), 'Zeeman-Doppler imaging of active stars. I - Basic principles', AAP **225**, 456–466. 13

Serio, S., Peres, G., Vaiana, G. S., Golub, L. & Rosner, R. (1981), 'Closed coronal structures. II - Generalized hydrostatic model', ApJ **243**, 288–300. 8

Sheeley, Jr., N. R. (2005), 'Surface Evolution of the Sun's Magnetic Field: A Historical Review of the Flux-Transport Mechanism', *Living Reviews in Solar Physics* **2**, 5. 33

Shibata, K., Masuda, S., Shimojo, M., Hara, H., Yokoyama, T., Tsuneta, S., Kosugi, T. & Ogawara, Y. (1995), 'Hot-Plasma Ejections Associated with Compact-Loop Solar Flares', ApJL **451**, L83. 21

Skumanich, A. (1972), 'Time Scales for CA II Emission Decay, Rotational Braking, and Lithium Depletion', ApJ **171**, 565. 14

Snodgrass, H. B. (1983), 'Magnetic rotation of the solar photosphere', ApJ **270**, 288–299. 9

Strassmeier, K. G. (1996), 'Doppler imaging of stellar surface structure. I. The rapidly-rotating RS CVn binary UZ Librae.', AAP **314**, 558–566. 13

Strassmeier, K. G. (2002), 'Doppler images of starspots', *Astronomische Nachrichten* **323**, 309–316. 13

Su, Y., van Ballegooijen, A., Lites, B. W., Deluca, E. E., Golub, L., Grigis, P. C., Huang, G. & Ji, H. (2009), 'Observations and Nonlinear Force-Free Field Modeling of Active Region 10953', ApJ **691**, 105–114. 22, 85

Tandberg-Hanssen, E. (1995), *The Nature of Solar Prominences*, Springer. 7

Titov, V. S. & Démoulin, P. (1999), 'Basic topology of twisted magnetic configurations in solar flares', AAP **351**, 707–720. 22, 85

Valori, G., Kliem, B. & Keppens, R. (2005), 'Extrapolation of a nonlinear force-free field containing a highly twisted magnetic loop', AAP **433**, 335–347. 24

van Ballegooijen, A. A. (2004), 'Observations and Modeling of a Filament on the Sun', ApJ **612**, 519–529. 24, 49

van Ballegooijen, A. A., Cartledge, N. P. & Priest, E. R. (1998), 'Magnetic Flux Transport and the Formation of Filament Channels on the Sun', ApJ **501**, 866. 123, 147

van Ballegooijen, A. A. & Martens, P. C. H. (1989), 'Formation and eruption of solar prominences', ApJ **343**, 971–984. 7, 21, 22, 44, 49, 64, 84, 86, 154

van Ballegooijen, A. A., Priest, E. R. & Mackay, D. H. (2000), 'Mean Field Model for the Formation of Filament Channels on the Sun', ApJ **539**, 983–994. 7, 24, 147, 154

Vidotto, A. A., Gregory, S. G., Jardine, M., Donati, J. F., Petit, P., Morin, J., Folsom, C. P., Bouvier, J., Cameron, A. C., Hussain, G., Marsden, S., Waite, I. A., Fares, R., Jeffers, S. & do Nascimento, J. D. (2014), 'Stellar magnetism: empirical trends with age and rotation', MNRAS **441**, 2361–2374. 14

Vilhu, O. (1984), 'The nature of magnetic activity in lower main sequence stars', AAP **133**, 117–126. 14

Vogt, S. S. & Penrod, G. D. (1983), 'Doppler Imaging of spotted stars - Application to the RS Canum Venaticorum star HR 1099', PASP **95**, 565–576. 13

Waite, I. A., Marsden, S. C., Carter, B. D., Hart, R., Donati, J.-F., Ramírez Vélez, J. C., Semel, M. & Dunstone, N. (2011), 'Magnetic fields and differential rotation on the pre-main sequence - III. The early-G star HD 106506', MNRAS **413**, 1949–1960. 13, 15

Wang, Y.-M. (1999), 'The Jetlike Nature of HE II lambda304 Prominences', ApJL **520**, L71–L74. 7

Wang, Y.-M., Nash, A. G. & Sheeley, Jr., N. R. (1989), 'Magnetic flux transport on the sun', *Science* **245**, 712–718. 10

Wang, Y.-M., Sheeley, Jr., N. R. & Lean, J. (2002), 'Meridional Flow and the Solar Cycle Variation of the Sun's Open Magnetic Flux', ApJ **580**, 1188–1196. 10

Weber, E. J. & Davis, Jr., L. (1967), 'The Angular Momentum of the Solar Wind', ApJ **148**, 217–227. 14, 147

Wheatland, M. S., Sturrock, P. A. & Roumeliotis, G. (2000), 'An Optimization Approach to Reconstructing Force-free Fields', ApJ **540**, 1150–1155. 20

Wilson, O. C. (1978), 'Chromospheric variations in main-sequence stars', ApJ **226**, 379–396. 12, 180

Wilson, R. M. & Hildner, E. (1984), 'Are interplanetary magnetic clouds manifestations of coronal transients at 1 AU?', Sol. Phys. **91**, 169–180. 21

Yan, Y. & Sakurai, T. (1997), 'Analysis of it YOHKOH SXT Coronal Loops and Calculated Force-Free Magnetic Field Lines from Vector Magnetograms', Sol. Phys. **174**, 65–71. 20

Yan, Y. & Sakurai, T. (2000), 'New Boundary Integral Equation Representation for Finite Energy Force-Free Magnetic Fields in Open Space above the Sun', Sol. Phys. **195**, 89–109. 20

Yang, W. H., Sturrock, P. A. & Antiochos, S. K. (1986), 'Force-free magnetic fields - The magneto-frictional method', ApJ **309**, 383–391. 23, 24, 223

Yeates, A. R. (2008), Development and Application of a Global Magnetic Field Evolution Model for the Solar Corona, PhD thesis, University of St Andrews. 138, 193

Yeates, A. R. (2014), 'Coronal Magnetic Field Evolution from 1996 to 2012: Continuous Non-potential Simulations', Sol. Phys. **289**, 631–648. 180, 191, 227

Yeates, A. R., Constable, J. A. & Martens, P. C. H. (2010), 'Solar Cycle Variation of Magnetic Flux Ropes in a Quasi-Static Coronal Evolution Model', Sol. Phys. **263**, 121–134. 180

Yeates, A. R. & Mackay, D. H. (2009), 'Initiation of Coronal Mass Ejections in a Global Evolution Model', ApJ **699**, 1024–1037. 206, 222

Yeates, A. R. & Mackay, D. H. (2012), 'Chirality of High-latitude Filaments over Solar Cycle 23', ApJL **753**, L34. 124, 133, 147

Yeates, A. R., Mackay, D. H. & van Ballegooijen, A. A. (2007), 'Modelling the Global Solar Corona: Filament Chirality Observations and Surface Simulations', Sol. Phys. **245**, 87–107. 10, 24, 123, 124, 125, 128, 138, 142, 144, 145, 180, 225

Yeates, A. R., Mackay, D. H. & van Ballegooijen, A. A. (2008), 'Modelling the Global Solar Corona II: Coronal Evolution and Filament Chirality Comparison', Sol. Phys. **247**, 103–121. 147, 191, 193

Yokoyama, T. & Shibata, K. (1996), 'Numerical Simulation of Solar Coronal X-Ray Jets Based on the Magnetic Reconnection Model', PASJ **48**, 353–376. 193